The Impact of Inelastic Deformation, Radiation Effects, and Fatigue Damage on Fusion Reactor First Wall Lifetime

Robert David Watson

December 1981

UWFDM-460

Ph.D thesis.

FUSION TECHNOLOGY INSTITUTE

UNIVERSITY OF WISCONSIN

MADISON WISCONSIN

The Impact of Inelastic Deformation, Radiation Effects, and Fatigue Damage on Fusion Reactor First Wall Lifetime

Robert David Watson

Fusion Technology Institute
University of Wisconsin
1500 Engineering Drive
Madison, WI 53706

http://fti.neep.wisc.edu

December 1981

UWFDM-460

Ph.D thesis.

THE IMPACT OF INELASTIC DEFORMATION, RADIATION EFFECTS, AND FATIGUE DAMAGE ON FUSION REACTOR FIRST WALL LIFETIME

by

ROBERT DAVID WATSON

A thesis submitted in partial fulfillment of the requirements for the degree of

DOCTOR OF PHILOSOPHY

(Nuclear Engineering)

at the

UNIVERSITY OF WISCONSIN-MADISON

1981

UWFDM-460

THE IMPACT OF INELASTIC DEFORMATION, RADIATION EFFECTS, AND FATIGUE DAMAGE ON FUSION REACTOR FIRST WALL LIFETIME

Robert David Watson

Under the supervision of Professor W.G. Wolfer

The growth of undetected surface flaws is believed to be a dominant failure mechanism for first wall components in fusion reactors. A methodology has been developed to model crack growth which accounts for the synergism between the material's response to 14 MeV neutron irradiation and the structure's response to pulsed surface heat loads, coolant pressure, and bombardment from energetic particles.

The method consists of two parts. First, a 1-D inelastic stress analysis code, TSTRESS, calculates the long-term redistribution of the stresses in a generic thin-walled plate element that is subjected to membrane loads. The plate is free to expand but is constrained from bending. This redistribution is caused by inelastic deformation from thermal expansion, thermal and irradiation creep, and swelling. The code also models wall thinning due to surface erosion.

Next, the stress history computed by TSTRESS serves as input to a 2-D, linear elastic fracture mechanics code, WISECRACK, that calculates the two-dimensional growth of a semi-elliptical surface flaw. Two failure modes are considered: leak-through and catastrophic fracture. The effects of temperature, R-ratio, flaw shape changes,

threshold ΔK_o, short crack correction, neutron irradiation, wall thinning, crack erosion, and creep crack growth are included.

A parametric study was performed with these codes on a 316 stainless steel cylindrical blanket module with a hemispherical cap facing the plasma. The effects of changing the wall thickness, surface heat flux, coolant temperature, and wall erosion rate were studied. The sensitivity of the predictions to the initial flaw depth, initial flaw aspect ratio, data scatter in da/dN, irradiated fracture toughness level, and changes in crack shape (1-D or 2-D) was also investigated.

The reduction in fracture toughness due to radiation hardening was found to be a primary factor that reduces the lifetime, and experiments are needed to measure this critical property.

A major conclusion of this research is that in a pulsed fusion device, where crack propagation is a life-limiting failure mechanism, the synergisms that result from the interaction between inelastic deformation and radiation damage effects cannot be neglected if realistic lifetime predictions are to be achieved.

APPROVED:

Dec. 14, 1981
Date

Professor Wilhelm G. Wolfer
Nuclear Engineering

ACKNOWLEDGEMENTS

I would like to express my sincere appreciation to my advisor, Professor Wilhelm G. Wolfer, for his patience, keen insight, and dedication to teaching and research. Without his guidance and continuous encouragement this work would not have been possible. I would also like to acknowledge Professors R.W. Conn (now at UCLA) and G.L. Kulcinski for the leadership and motivation provided for the students and staff of the Fusion Research Program at the University of Wisconsin. I am especially indebted to Dr. Robert R. Peterson who programmed the computer code TSTRESS and assisted me with numerous computer problems.

I would like to thank Bruce Cramer, Dave Bowers, John Davis and the rest of the staff of the Fusion Engineering Program at McDonnell Douglas Co. for their friendship and many valuable discussions. I also benefited from discussions with Rich Mattas at Argonne Labs, Tom Prevenslick at Westinghouse, Wilhelm Daenner at the Max Planck Institute for Plasma Physics, John Dalessandro at INESCO, and Gene Lucas at the University of California-Santa Barbara.

Special thanks go to Mrs. Helga Fack and her staff for the excellent drawings, and to Dennis Bruggink for his helpful assistance. My greatest admiration goes to Mary Jo Biechler for her diligence and excellence in typing this manuscript. Also, I would like to thank Tom McCarville, Ahmed Hassanein, and Abderrahmane Si-Ahmed

for their friendship and valuable discussions.

Last, but not least, I am grateful to my parents for their continuous support and understanding in this endeavor.

Table Of Contents

List of Symbols

a	crack depth into plate
a_o	initial crack depth
a_f	final crack depth
Δa	increment in crack growth in a-direction
a/c	aspect ratio
A, A_o	various constants
α	coefficient of thermal expansion
$\vec{B}$	magnetic field vector
B_T	toroidal magnetic field
B_p	poloidal magnetic field
BOL	beginning-of-life
B, b	various constants
β_p	ratio of plasma pressure to B_p
$2c$	crack length along surface
$2c_o$	initial crack length
Δc	increment in crack growth in c-direction
C	constant, also plate width
c_p	specific heat
da/dN	fatigue crack growth rate in a-direction
dc/dN	fatigue crack growth rate in c-direction
da/dt	creep crack growth rate in a-direction
dc/dt	creep crack growth rate in c-direction
$(da/dN)_{total}$	total crack growth rate in a-direction
$(dc/dN)_{total}$	total crack growth rate in c-direction

dh/dt	time rate-of-change of wall thickness
dpa	displacement-per-atom, a unit of radiation damage
D	flexural rigidity
D_o	constant
E	Young's modulus of elasticity
EOL	end-of-life
e_r	surface erosion rate
e^{th}	thermal strain
e^{sw}	swelling strain
e_x^c, e_y^c	creep strain in x and y directions
e_x, e_y, e_z	total inelastic strain in x, y and z directions
$\dot{e}_x^c$, $\dot{e}_y^c$	creep strain rates in x and y directions
$\dot{e}_{eq}^c$	Von Mises equivalent creep strain rate
$\dot{e}_{ij}^c$	creep strain rate tensor
ε	fractional change in crack size per iteration
$\varepsilon_x, \varepsilon_y, \varepsilon_z$	total strains in x, y and z directions
ε_x^e, ε_y^e, ε_z^e	elastic strains in x, y and z directions
ε_u	uniform elongation strain
ε_f	fracture strain
f	modulus ratio for temperature correction, $E(T_o)/E(T)$
$\dot{F}$	neutron damage in dpa
F	neutron damage rate in dpa/sec
F_b	magnification factor for pure bending moment
F_m	magnification factor for pure tension load
FPY	full power year
FCG	fatigue crack growth

h	thickness of first wall
I_p	plasma current
ICFR	inertial confinement fusion reactor
$\vec{J}_p$	eddy current in first wall from plasma disruptions
K_I or K	stress intensity factor for mode I
K_{II}	stress intensity factor for mode II
K_{III}	stress intensity factor for mode III
K_{Ic}	plane strain fracture toughness
K_{mean}	mean (average) stress intensity factor
K_{max}	maximum stress intensity factor
K_{min}	minimum stress intensity factor
ΔK_o or K_{th}	threshold stress intensity factor
ΔK_{oo}	threshold stress intensity factor at R = 0
ΔK	stress intensity factor range
K_o	constant
K_x, K_y	deflection constants for stretching in x and y direction
ℓ	constant
ℓ_o	short crack correction factor
L_x, L_y	deflection constants for bending in x and y directions
λ	1/(1-R)
m	exponent in Walker correction
M_m	membrane correction factor
M_b	bending correction factor
M_x, M_y	bending moments in x and y direction
μ_o	magnetic permeability

N	number of fatigue cycles
N_f	number of cycles to failure
ΔN	increment in fatigue cycles per iteration
n	Paris exponent in fatigue crack growth rate equations
N_x, N_y	membrane loads in x and y directions
ν	Poisson's Ratio
p	creep crack growth rate exponent
P, P_o	coolant pressure
p_m^{max}	maximum magnetic pressure
P_{NW}	neutron wall loading
ψ	total creep compliance
ψ_{irr}	irradiation creep compliance
ψ_{th}	thermal creep compliance
ϕ_o	toroidal magnetic flux
$\Delta\phi$	change in magnetic flux
ϕ	neutron flux in n/cm^2- sec
Q	activation energy
q_s''	surface heat flux
q_o'''	volumetric nuclear heating rate
R	R-ratio, equal to K_{min}/K_{max}
ρ	density, g/cm^3
σ_{ij}	stress tensor
$\sigma_x, \sigma_y, \sigma_z$	stress in x, y and z direction
σ_Y	yield strength
σ_m	membrane stress
σ_b	bending stress

σ_f	fracture strength
σ_u	ultimate strength
σ_{kk}	$\sigma_x + \sigma_y + \sigma_z$
σ_{eq}	Von Mises equivalent stress
$\dot{\sigma}_x$, $\dot{\sigma}_y$	stress rates in x and y directions
σ_x^{ss}, σ_y^{ss}	steady-state stress in x and y direction
$\Delta\sigma_o$ or $\Delta\sigma_{th}$	threshold cyclic stress
$\Delta\sigma_e$	S-N fatigue endurance limit
$\Delta\sigma_{thermal}$	cyclic thermal stress
S_{ij}	deviatoric stress tensor
S	swelling ($\Delta V/V$)
$\dot{S}$	swelling rate
$\dot{S}_{ss}$	steady-state swelling rate
$\dot{S}_{max}$	maximum swelling rate
$\dot{S}_{ave}$	average swelling rate
$\Delta\dot{S}$	differential swelling rate across wall
t	time
t_{on}	time while plasma is on (burn time)
t_{off}	time while plasma is off (down time)
t_{pulse}	time for one complete plasma on-off cycle
T	temperature
T_b	temperature on backside of first wall facing coolant
ΔT	temperature difference across wall thickness
τ	decay constant for stress relaxation
τ_s	incubation dose for swelling
τ_d	plasma disruption time

τ_w	current decay constant
θ	angle along crack front
W	plate width
x, y	coordinate directions in the plane of the first wall
z	coordinate perpendicular to the surface of the wall

List of Tables

List of Figures

CHAPTER 1

Introduction

The production of electricity from controlled thermonuclear fusion offers the promise of unlimited energy supply. However, to achieve this goal fusion reactors must be economically competitive with alternative energy sources, environmentally acceptable and safe for workers inside the plant. One of the most important factors that affects each of these concerns is the lifetime of first wall components. The replacement of failed components is likely to be an expensive, time-consuming, and potentially hazardous operation, requiring the disposal of radioactive wastes. Even the certification and licensing of these reactors will require detailed failure analysis for both normal and off-normal or accident conditions. Therefore, the eventual success of fusion power may ultimately depend upon the safety and reliability of first wall components for many years of operation.

Reliability will most likely be the controlling factor, because failure of a single component will prevent ignition of the plasma by degradation of the vacuum. This is quite a different situation than in a LWR fission reactor, where normal operation is possible even with 1% of the core containing failed fuel rods. Also, the design lifetime of the cladding is shorter since new fuel is added approximately every two years. A better analogy

can be made between the lifetime requirements of the first wall and the LWR pressure vessel, the latter having to survive for the entire life of the plant (30 years).

Unfortunately, early studies of fusion reactors discovered that excessive swelling and loss-of-ductility caused by neutron irradiation might limit the first wall lifetime to less than 6 and 2 years, respectively, for a neutron wall loading of 1 MW/m^2. On the other hand, later studies predicted lifetimes in excess of 30 years (for the same wall loading) by neglecting the effects of radiation damage. This wide range of variation is typical of all first wall studies in the literature and is the direct result of three factors. First, the effect of neutron irradiation on mechanical properties is not adequately understood, especially for fracture toughness measurements and *in-reactor* tests of fatigue crack growth. Secondly, uncertainties in the plasma physics prevent an accurate specification of the surface heat fluxes and wall erosion rates, in addition to plasma disruptions (which are only briefly considered in this thesis). And thirdly, each investigator has used substantially different methods of analysis, mainly due to the fact that an appropriate lifetime code for fusion reactors simply does not exist at the present time, unlike the situation in the fast breeder reactor community where the failure analysis of fuel pin cladding is almost always performed by a single unified code.

Accordingly, the primary objective of this project is the

development of an integrated and self-consistent methodology for life-time analysis that accounts for any synergistic effects that may exist between the materials behavior, structural response and damage processes which occur in a fusion environment, and to make available an appropriate set of design codes to the community.

Recognizing that the accuracy of a single prediction is limited by the lack of data for materials response to neutrons, a second objective is to use these codes to study parametrically the impact of different correlations for radiation damage and surface effects. In this way, by modelling the physical process of crack propagation through the wall, we will be able to identify the critical materials properties that still need to be measured. This parametric study will also allow us to study what possible combinations of design variables and operating conditions would give the longest lifetime. The fourth, and final, objective of this project is to use these codes to investigate the sensitivity of the results to different assumptions and uncertainties in the fracture mechanics analysis of crack propagation.

This thesis is organized into four main parts. First, the literature on first wall analysis is reviewed, followed by a discussion of the proposed method of solution. Next, the theory of inelastic stress analysis and the associated computer code, TSTRESS, are presented. The third section presents models for crack propagation that are used in the fracture mechanics code, WISECRACK. Finally, both of these codes are coupled together and

used to study parametrically the effects of different variables and assumptions on the lifetime of a specific first wall design for a tokamak power reactor.

The results of this study are intended to guide future research in the areas of both materials behavior and alloy development, as well as fusion reactor technology, towards the ultimate goal of safe and reliable fusion power.

CHAPTER 2

Literature Review

Industrial Standards for Electric Power Components

In order to better understand the rationale behind the proposed lifetime methodology, it is useful to survey the existing methods which are currently being used in the electric power industry. These methods make up a set of rules that the engineer must follow in order for the component to satisfy specified design limits on stress, strain, deflections and cycles-to-failure. Table 1 lists the various standards and codes which apply to power plants.

Table 1. Industrial Standards and Codes

Application	Standard of Code
* Fossil-fueled power plant	* ASME Boiler & Pressure Vessel Code, Sections I & II [152]
* Light water reactor (LWR)	* ASME B&PV Code, Section III [152] and Code Case 1592 "Class 1 Components in Elevated Temperature Service" [148]
* Liquid metal fast breeder (LMFBR)	* RDT Standards F9-7,8,9 "Structural Design Guidelines for FBR Core Components" [27]
* Fusion reactor (CTR)	* nothing exists as yet

ASME Boiler & Pressure Vessel Code

Back in 1914, it was proposed in the ASME Boiler code that the membrane stress produced by pressure in the wall of a vessel should not be allowed to exceed one-fifth of the ultimate strength of the material, as determined by a tensile test [150]. This rule successfully prevented many boiler explosions. Today, for fossil-fueled power plants, the ASME Boiler and Pressure Vessel Code [152] contains many more design rules to protect against three fundamental failure modes, including: 1) ductile rupture (short-term tensile instability), 2) gross distortion from buckling or incremental collapse and 3) fatigue failure. The first two modes protect against failure upon the initial loading, whereas the third mode, fatigue, is a long-term phenomena.

The rules for fatigue failure essentially provide a check on whether or not the calculated life for a given cyclic stress level will exceed the desired service life. The ASME fatigue design curve is generated by reducing the nominal curve through the data points on a S-N plot (for smooth, uniaxial specimen) by a factor of 2 on stress and 20 on life (cycles-to-failure). These safety factors are intended to account for possible detrimental effects of mean stresses, multiaxial stresses, environment, etc. The code allows the fatigue life to be calculated based on the elastic stresses only because the operating temperatures are low enough.

The rules for design of light water reactor components, as given in section III of the ASME B&PV Code, also protect against the same three failure modes as above. However, two more sets of rules were

added because of the greater potential hazards of radioisotope release from a nuclear power plant accident.

The first set is contained in Appendix G, subsection NA of section III, which provides for "Protection Against Nonductile Failure" (brittle fracture) [151]. This was necessary because of the potential for catastrophic fracture of the ferritic steel used in pressure vessels. Also, since ferritic steels experience an irradiation-induced shift upwards in the transition temperature for brittle-to-ductile fracture, the so-called Nil-Ductility Temperature, the Appendix A of Section XI called "Evaluation of Flaw Indicators" [25] was written to protect against this. Finally, the development of Section XI, "Rules for Inservice Inspection of Nuclear Power Plant Components" [25] reflects a greater concern about the fracture potential of previously undetected flaws, especially in weld areas. The "safe-life" used for LWR design is, therefore, more conservative than the earlier rules for fatigue life which basically protected against the initiation of flaws.

Code Case 1592

With the operating temperatures of LWR components exceeding 800°F (427°C), it became necessary to develop rules to protect against high temperature, long-term, time-dependent failure modes. These standards are now called the Code Case 1592, "Class 1 Components for Elevated Temperature Service", Section III, Division 1 of the ASME B&PV Code [148]. Specifically, they protect against seven types of failure modes, as listed in Table 2.

Table 2. Failure Modes for Code Case 1592

Short-Term Failure Modes

1. Ductile rupture (tensile instability)
2. Buckling

Long-Term Failure Modes

3. Creep rupture
4. Creep-fatigue interaction
5. Gross distortion due to incremental collapse and ratcheting
6. Loss of function due to excessive dimensional changes
7. Creep buckling

The detailed design rules for Code Case 1592 are contained in Appendix T, entitled "Rules for Strain, Deformation and Fatigue Limits at Elevated Temperatures" [148]. A major limitation of these rules is that they include no irradiation effects. Also, the use of Code Case 1592 requires a much broader data base, as well as the capability to perform inelastic stress analysis, including plasticity and creep. Nevertheless, according to Langer [150], some of the advantages of using Code Case 1592 include:

* Long-lived components do not use the same allowable stress limit as short-lived components.
* Different stress limits for transients and accidents are used than limits based on 100,000 hour rupture properties.

* More efficient use of the metal's strength and ductility capabilities can be attained.

RDT Standards

Over the past ten to fifteen years, the United States has been trying to commercialize the liquid metal fast breeder reactor (LMFBR). Concurrent with this has been the development of a new set of design rules, the RDT Standards F9-7,8,9 entitled: "Structural Design Guidelines for FBR Core Components" [27]. Although it is still only a draft, these RDT Standards represent a significant increase in the sophistication for the design of components which operate in an elevated temperature (300-700°C) and fast neutron environment ($3 \times 10^{23} n/cm^2$, $E > 0.1$ MeV). The major difference, then, between these new Standards and the previous Code Case 1592 is in the inclusion of irradiation effects on mechanical properties and how they affect failure modes. Also, the RDT Standards place greater emphasis on the 304 and 316 type stainless steels than on the ferritic steels used in LWR's. The data base used in the Standards is the Nuclear Systems Materials Handbook (NSMH) [32]. Table 3 lists the eleven different failure modes which are protected against by the RDT Standards.

Table 3. Failure Modes Used in RDT Standards

Short-Term Failure Modes

1. Tensile plastic instability, necking, thinning (ductile rupture)
2. Structural instability (buckling)
3. Localized rupture

Long-Term Failure Modes

4. Creep instability, necking, thinning
5. Creep buckling
6. Ratcheting (incremental growth)
7. Thermal creep rupture
8. Fatigue (crack initiation)
9. Creep-fatigue interaction
10. Excessive deformation
11. Crack growth leading to brittle fracture

These failure modes are essentially the same as outlined for the Code Case 1592, except that the RDT Standards permit three different types of structural analyses, namely

* Elastic Analysis
* Elastic-Irradiation Creep-Swelling Analysis (EISCA)
* Inelastic Analysis.

For each type of analysis, a different set of design rules, limits and criteria are specified. A strictly elastic analysis is often used for preliminary design and the criteria in this case limit the stresses to

specified strength levels. However, when plastic and thermal creep strains are small, but irradiation creep and swelling strains are large, then an EISCA is performed. But even in this case, the same design rules are applied as for the Elastic Analysis.

The third approach requires a fully inelastic stress analysis to be done when thermal creep and/or plastic strains are significant. In this case, the criteria limit the strains (not stresses) to appropriate levels of ductility, e.g. uniform elongation, fracture strain, etc. Finally, in all three types of stress analysis, there are some rules which always must be satisfied in order to protect against:

* Thermal creep and fatigue damage
* Crack propagation
* Buckling
* Structural instability.

The RDT Standards do not consider swelling or irradiation creep to be damaging or ductility-limiting. Also, due to the higher level of sophistication and knowledge contained in a fully inelastic stress analysis, the design rules and limits are less restrictive than for an EISCA or strictly Elastic Analysis. The engineer must weigh the cost of doing a detailed inelastic analysis against the benefits gained from using less restrictive design rules and, hence, more efficient use of the material. Table 4 presents a summary of the different failure mechanisms and design rules used by the RDT Standards, as taken from Ref. [149].

Table 4. Summary of Failure Mechanisms and Associated Design Rules [149]

Potential Failure Mechanism	DESIGN RULE	
	Elastic or Elastic-Irradiation Creep-Swelling Analysis	Inelastic Analysis
Tensile Plastic or Creep Instability (Incl. Ratcheting) Leading to Gross Rupture Structural Instability/Buckling/ Gross Deformation	Stress Intensity Limits On:* P_m; $P_m + P_b$; $P_m + P_b + Q$ Limits on Load/Strain For Short-Time and Long-Time Instability/Buckling	Membrane Plastic and Thermal Creep Strain Fraction Summation Rule Limits on Load/Strain For Short-Time and Long-Time Instability/Buckling
Localized Rupture (Short-Time)	Limit on Maximum Principal (Tensile) Stress	Total Strain Fraction Summation Rule
Thermal Creep Damage + Fatigue Damage (Incl. Creep-Fatigue Interaction)	Limit On: Time Fraction Summation + Cycle Fraction Summation	Limit On: Time Fraction Summation + Cycle Fraction Summation
Unstable Crack Propagation	Limit on Linear Elastic Fracture Mechanics Stress Intensity	Limit on J-Integral
Excessive Deformation	Deformation Limits for Functional Adequacy	Deformation Limits for Functional Adequacy

* P_m = primary membrane stress intensity
P_b = primary bending stress intensity
Q = secondary stress intensity

In many aspects, there are similarities between the RDT Standards for LMFBR's and the Code Case 1592 for LWR's. However, Nelson [149] has identified four important differences where the RDT Standards account for the special effects of fast neutron irradiation. According to him, these improvements are:

1. Revised stress intensity limits based on a review of limit load and shakedown concepts in view of the reduction of ductility with irradiation.
2. Plastic and thermal creep strain fraction summation rules for membrane, bending and peak strains, which utilize strain limits that vary to account for time-dependent changes in material ductility.
3. A combined thermal creep and fatigue damage rule, which considers changes in time-to-rupture and cycles-to-failure due to irradiation.
4. Fluence-dependent limits on fracture toughness.

Assuming that the damage from fast neutrons is qualitatively similar to that from 14 MeV fusion neutrons, it would appear that the RDT Standards are generally applicable to fusion reactor first wall design and lifetime analysis. However, the two major areas where the RDT Standards fail to apply are:

* Inapplicability of the breeder correlations (NSMH) to a fusion environment, and
* Lack of specific guidelines for wall erosion or plasma disruptions.

First Wall Designs

We shall define the first wall as "any pressure retaining boundary that is located closest to the plasma". Its primary function is to intercept the surface energy flux, which contains roughly 20% of the total fusion power (the other 80% is deposited volumetrically in the blanket by neutrons). A bare, unprotected first wall is subjected to a severe environment, including 14 MeV neutron irradiation, pulsed surface heat fluxes, bombardment by energetic particles, magnetic forces and possibly coolant corrosion. Even with some form of protection, such as thick graphite tiles, radiation damage will degrade the mechanical properties.

Since 1972, when researchers first began to focus on the unique problems of the first wall, many different materials, coolants, and geometries have been proposed. In general, we can classify various first wall designs into two categories, namely, those which are either thin-walled or thick-walled and those which are either separated from the blanket structure or integrated with it. The most common feature among all of them is the choice of thin-walled, metallic structures 1-10 mm thick, which permits efficient removal of the surface heat flux with low thermal stresses. Almost all of the early designs consisted of a helium gas or liquid lithium cooled 316 stainless steel structure that was an integral part of the blanket, as shown in Fig. 1. Later designs utilized refractory metals or ceramics for either their high temperature capability or radiation damage resistance (or both). Type 316 stainless steel remains,

however, the preferred choice because of its extensive materials properties data base, industrial experience, etc. With the advent of solid breeder pellets (e.g. Li_2O) and lithium-lead compounds that are less chemically reactive in water than in pure lithium, the choice of pressurized water or steam as a coolant has gained in popularity. Also, the use of a flowing bed of small pellets (Li_2O, for example) to transport the heat out of the system has also been suggested [197]. An excellent study of the relative merits of various first wall/blanket designs has been published by Smith et al [198].

Among the various types of geometries that have been proposed for the integral first wall, the most common choices are:

1. U-bend module,
2. cylindrical canister with either a hemispherical or ellipsoidal end cap, or
3. rectangular plate module.

Figures 1 through 6 show examples of each of these types.

In recent years, the trend has been to physically separate the first wall from the blanket. This allows the wall to be operated at a much lower temperature than the blanket which is believed to enhance its resistance to radiation damage (except possibly for ferritic steels, which exhibit a ductile-to-brittle fracture transition at low temperatures [199]). It also enhances the blanket lifetime by removing the pulsed heat flux from its surface.

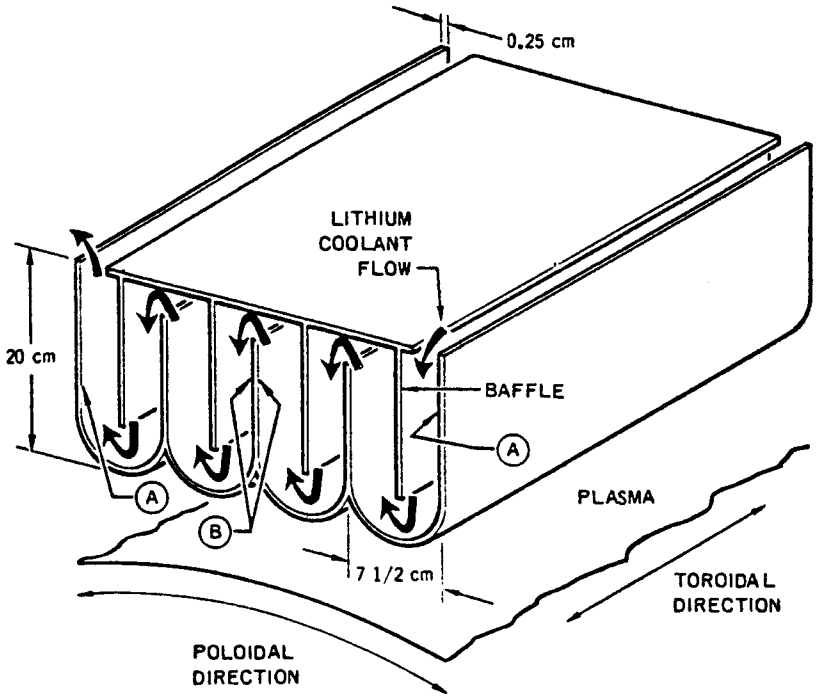

(a)

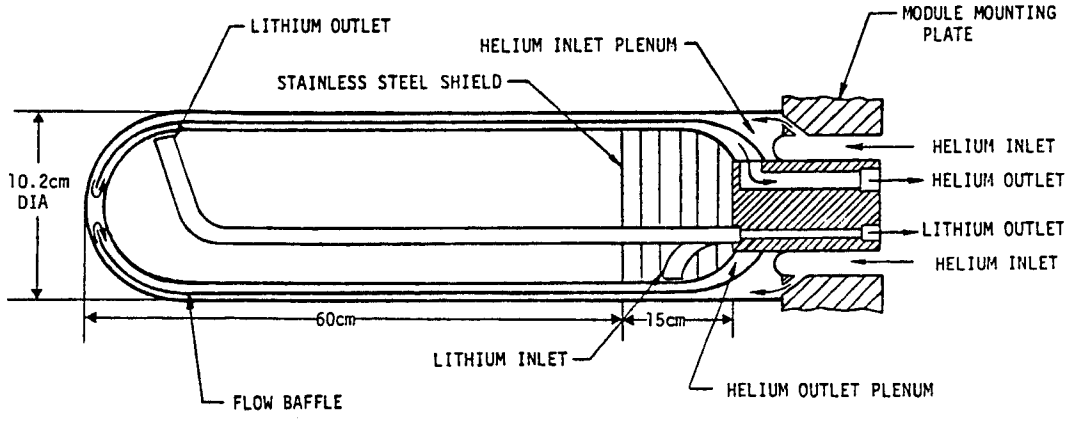

(b)

Figure 1. Common first wall designs: (a) U-bend blanket module [161], (b) cylindrical blanket module [19].

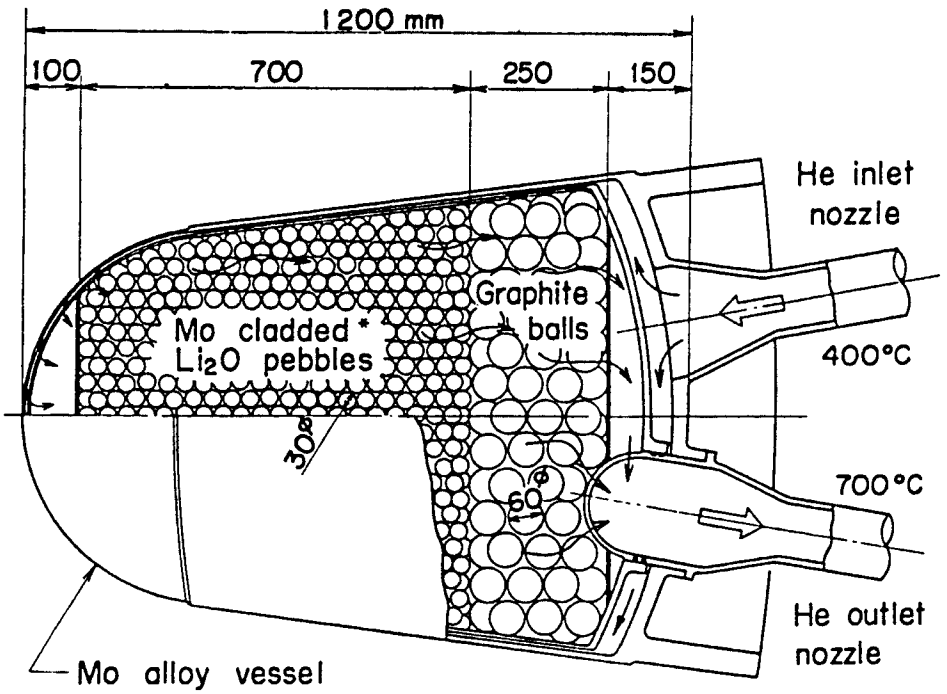

Figure 2. Conical blanket module with ellipsoidal end closure [203].

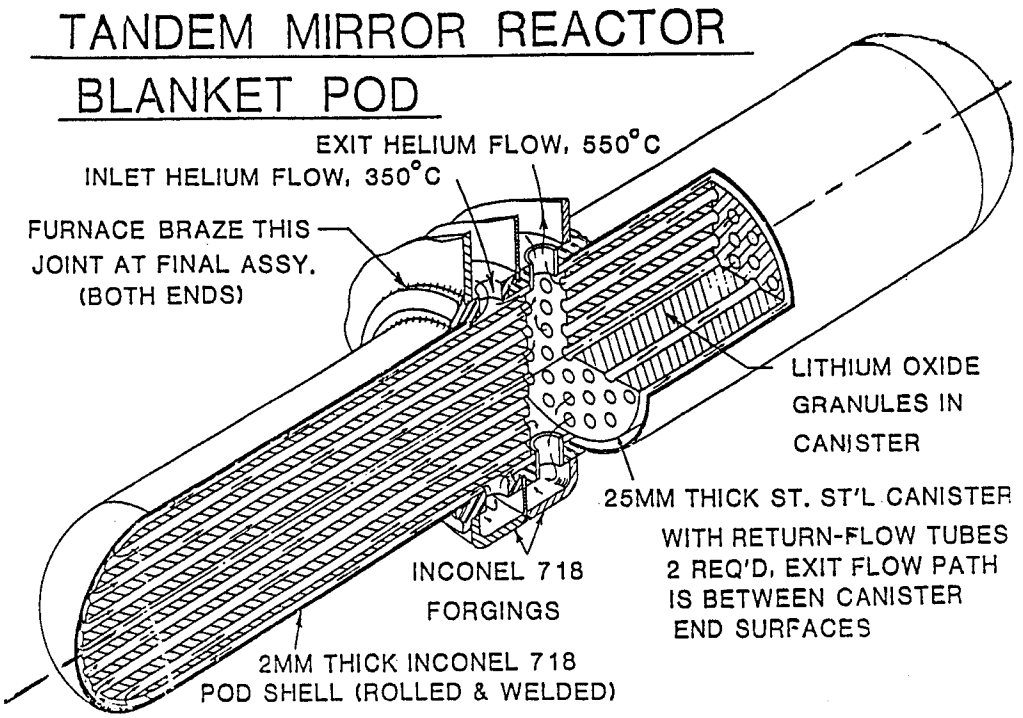

Figure 3. Cylindrical blanket module for a tandem mirror reactor [204].

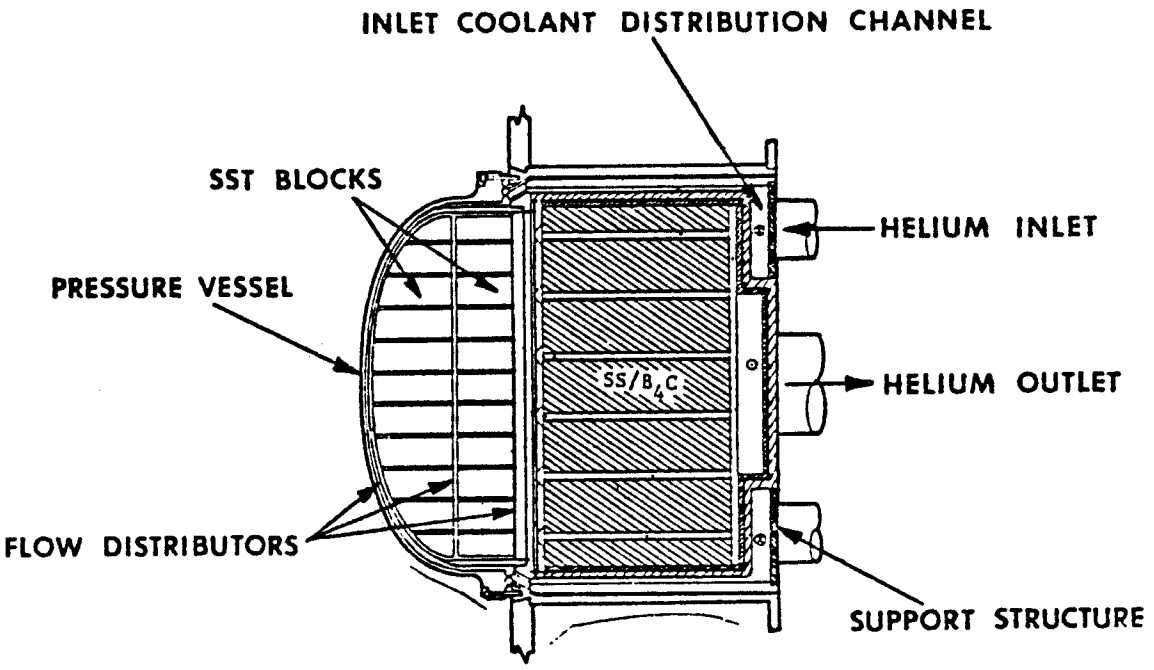

Figure 4. Cylindrical blanket module with ellipsoidal end closure [17].

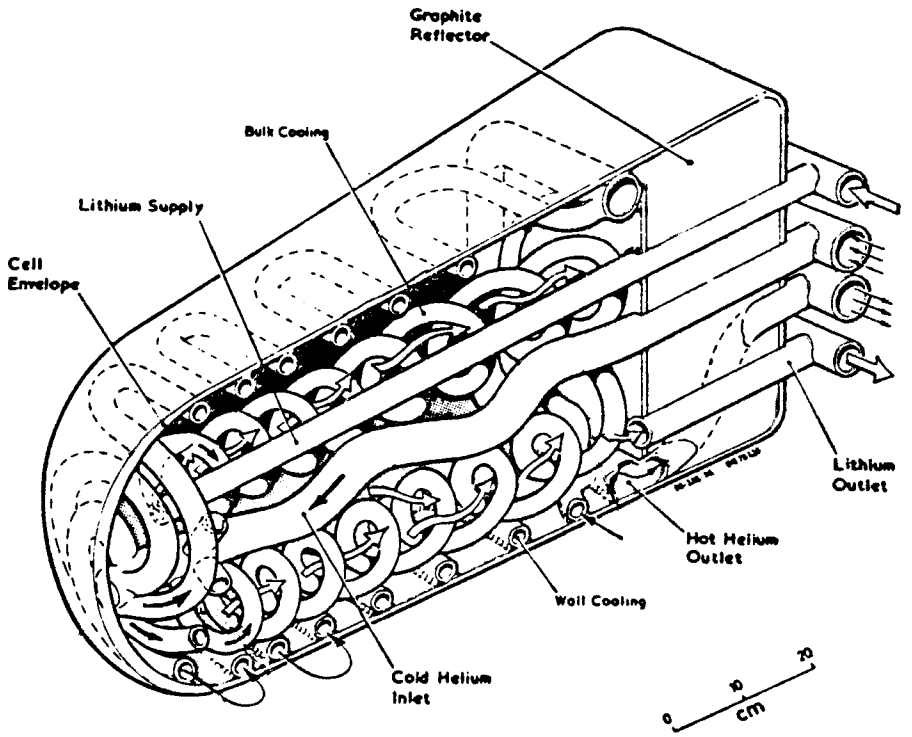

Figure 5. Semi-rectangular blanket module with ellipsoidal end closure [203].

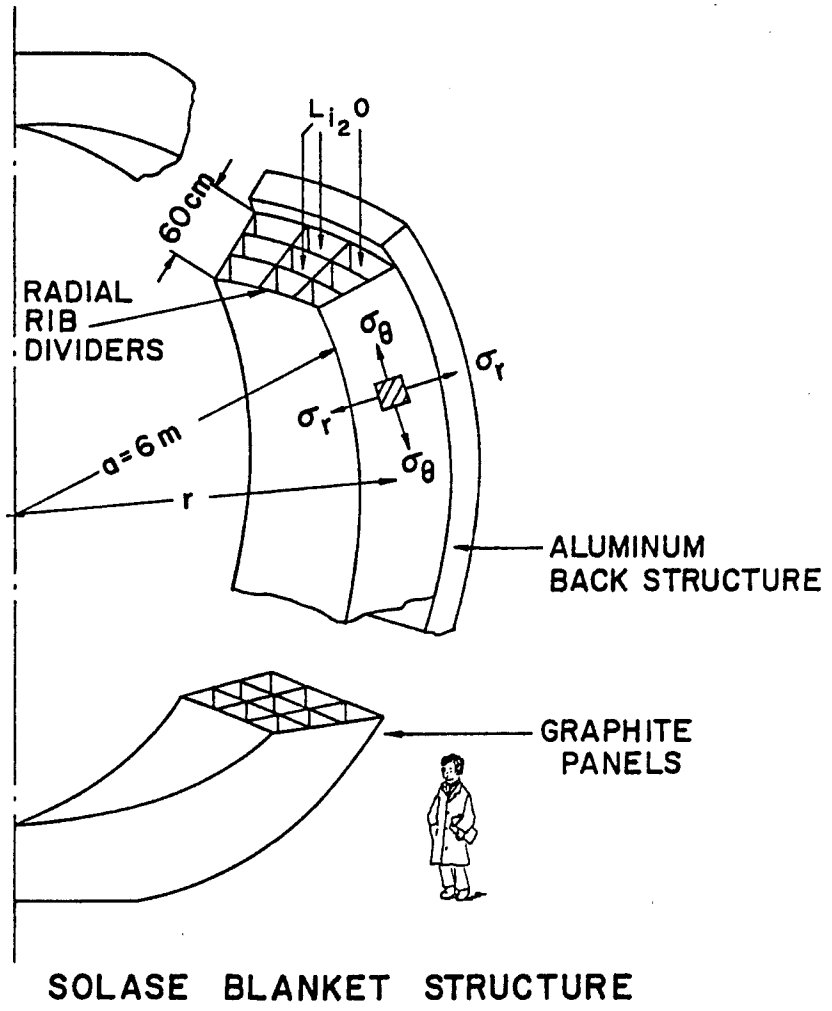

Figure 6. All-graphite blanket structure consisting of flat plates [169].

These designs fit into four basic categories, namely

1. tube sheet
2. plate with tubes bonded on either side
3. plate with corrugated panel attached on either side
4. plate with internal coolant channels

Figures 7 through 8 illustrate each of these designs.

Up to this point, all of the figures have shown only thin-walled designs. Only recently have concerns over surface erosion forced designers to use thick-walled components in order to retain an acceptable thickness after many years. These walls are typically 1 cm or thicker. Figure 9 illustrates this type of design. The analysis used in this thesis does not treat this particular case, however.

The other approach which is more commonly used to protect the first wall involves placing a passively-cooled, high melting-point material in between the actively-cooled wall and the plasma. Refractory metals or ceramics such as SiC or graphite are typically used. These protection systems take many different forms, including armor (tiles), woven liners, falling balls of metal or streams of liquid metal (ICFR). Although the lifetime of these components is not addressed in this thesis, the methods that have been developed can, in principle, be applied to these structures as well.

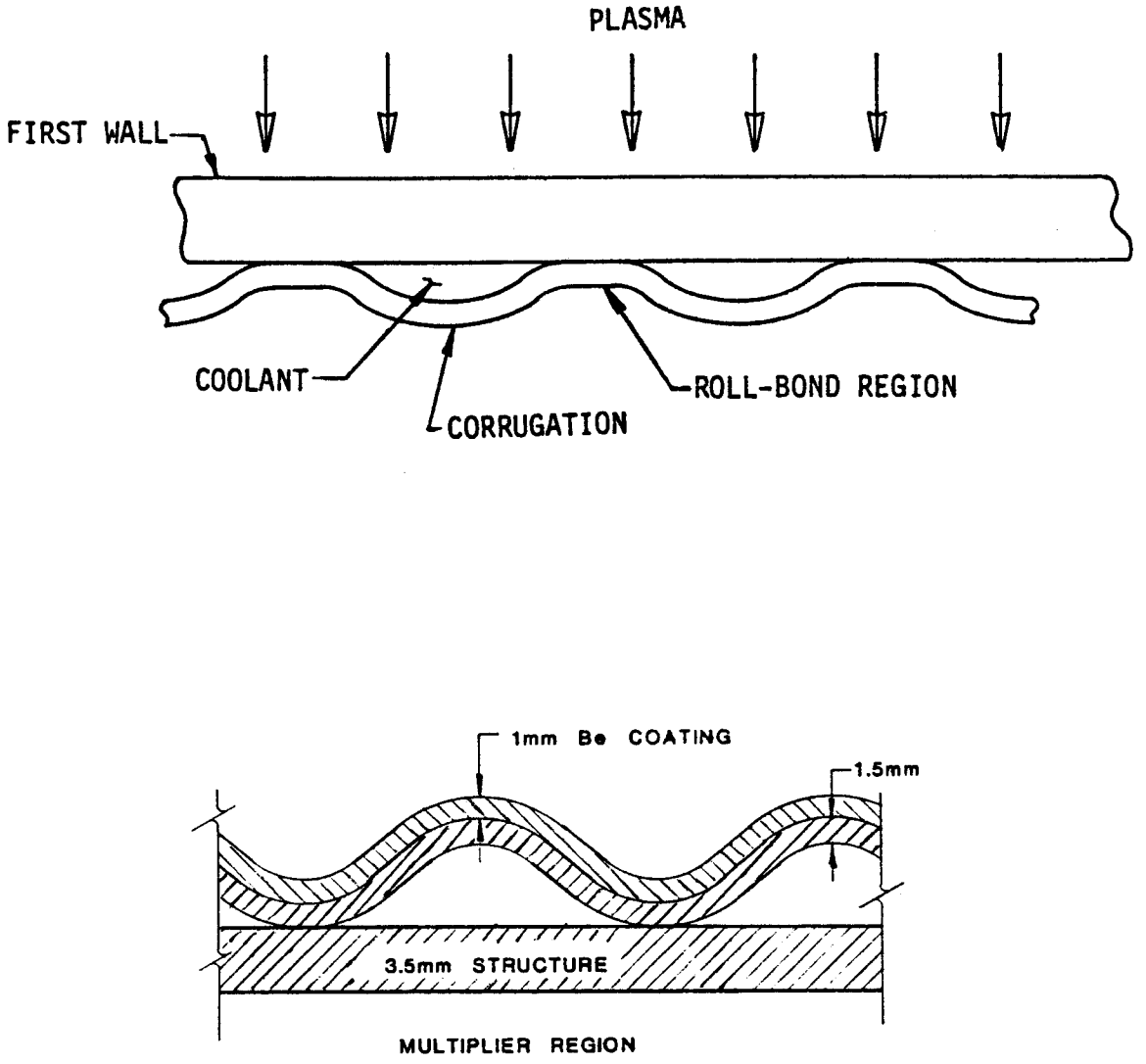

Figure 7. Corrugated panel first wall designs [154,155].

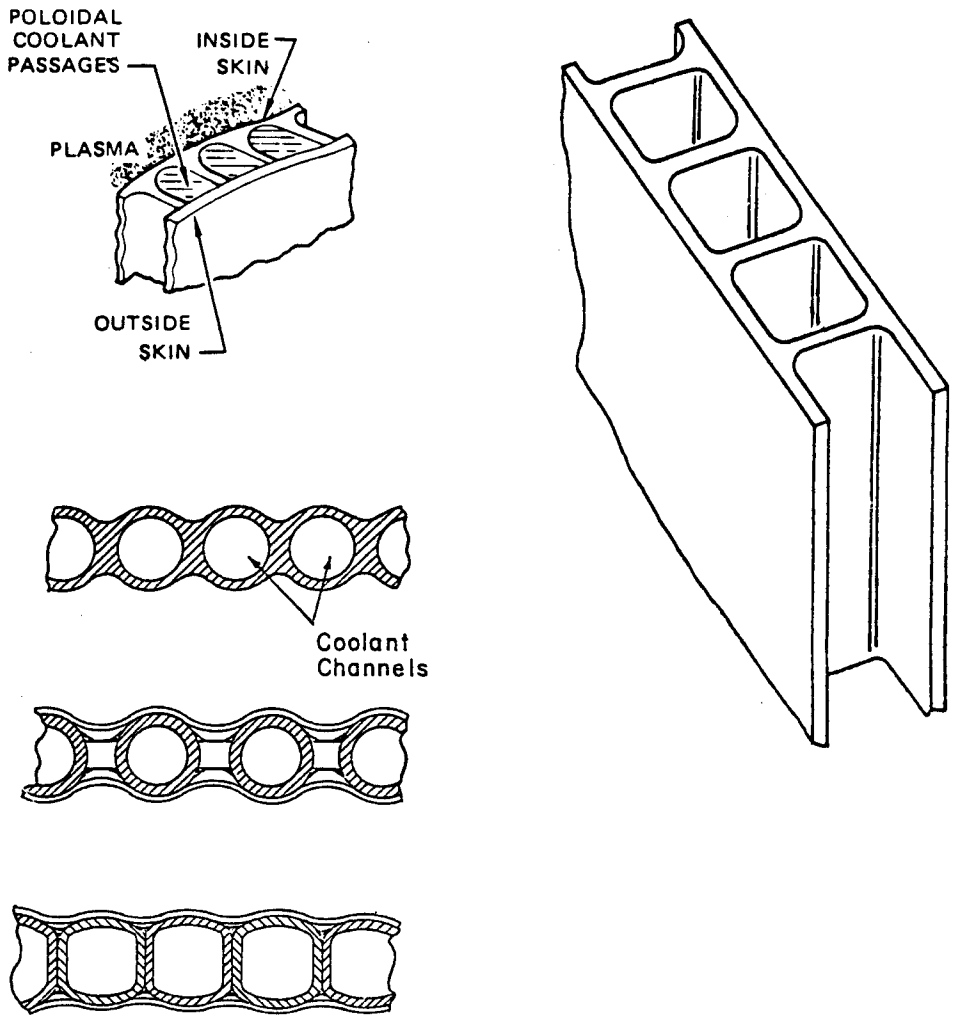

Figure 8. Double-wall first wall design with internal coolant channels [20,165].

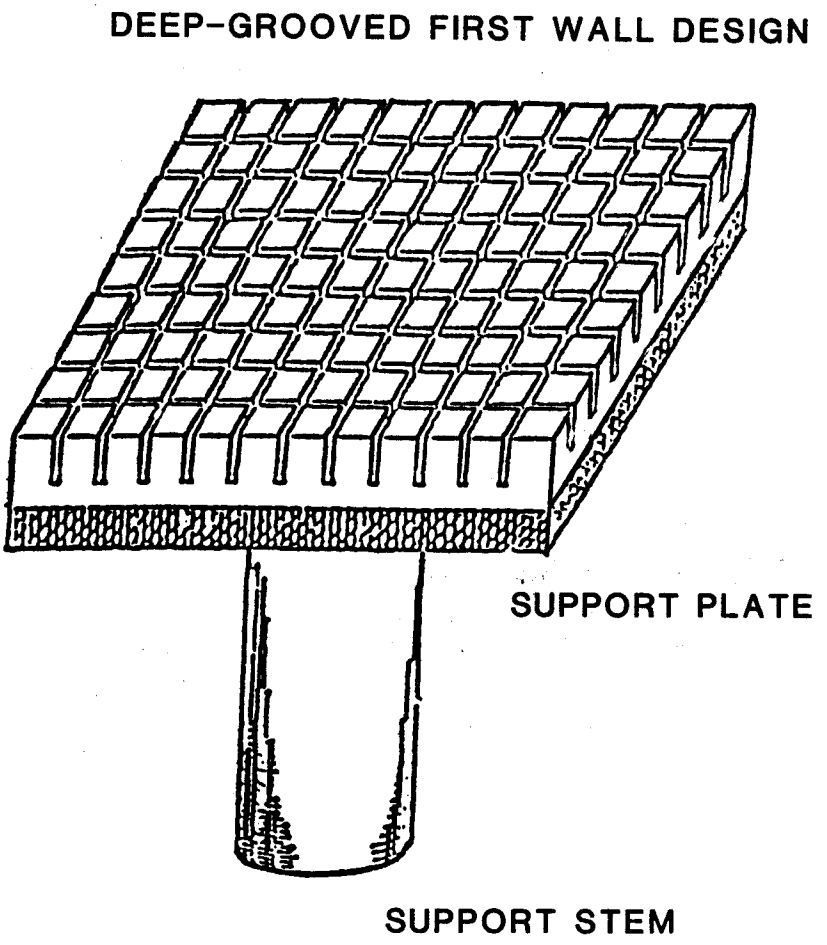

Figure 9. Deep-grooved first wall design [155].

Previous Lifetime Studies

Since 1972, roughly forty-five papers have been published in which the problems associated with first wall lifetime analysis were studied. Excellent reviews have been written by Conn [179], Harkness and Cramer [157], Cramer [15], and Powell and Reich [172]. It is difficult to summarize the body of knowledge represented by these papers not only because the field is nine years old, but also due to the fact that fusion technology, overall, has changed dramatically over that period of time. To illustrate this, Table 5 presents the evolution of first wall designs and lifetime analysis since 1972, primarily for the tokamak concept. Since thirty out of the forty-five papers mentioned above appear in this list, it is apparent that roughly two-thirds of all the papers represented a significant advance in the field. The two most common features in the literature is the obvious preference for a 316 stainless steel first wall in a tokamak reactor (the same choices as for the example used in this thesis).

From the beginning, in 1972, the effects of irradiation-induced swelling, loss-of-ductility (embrittlement) and surface erosion (sputtering) were identified as serious first wall problems. Early predictions by Kulcinski [178] in 1974 put the lifetime of a 316 SS wall at one to two years for a neutron wall loading of 0.25 MW/m^2 because of severe embrittlement. Researchers typically used end-of-life (EOL) limits on swelling of 2 - 10% $\Delta V/V$ and on uniform elongation of 0.5 - 2.0% strain. The severe effects of radiation damage therefore motivated a search for better materials, and designs or operating condi-

tions that would extend the lifetime. Low swelling metals, such as HT-9, first wall designs with armor protection, and low-temperature structures are all examples of innovative ideas for longer-life components.

At the same time these improvements were being made, however, "new" sources of damage such as fatigue, creep cavitation, corrosion, blistering, and vaporization/melting due to plasma disruptions were being investigated. It seemed as if new problems were being created as fast as better designs or stronger materials could be developed. Concurrent with a better understanding of the materials response was the use of more sophisticated methods of structural analysis and fracture mechanics, as characterized by a shift from elastic to inelastic stress analyses and from smooth speciman fatigue life to fatigue crack propagation. Failure modes were extended to include coolant leak-through due to crack growth, in addition to the existing modes of excessive deformation from swelling or catastrophic fracture due to embrittlement or creep cavitation.

Over the past nine years, predicted lifetimes have generally increased as the result of better data on irradiated materials properties, innovative first wall designs, and more accurate methods of lifetime assessment. Verification of these predictions, however, will not be possible for at least ten years until in-reactor tests can be performed in an INTOR or TASKA-type reactor [155, 180]. Therefore, the next ten years can be used to improve the predictive capabilities.

Table 5. Highlights of First Wall Lifetime Studies

1972	Reference
First lifetime analysis published. (INTERATOM)	[134]
Irradiation swelling and loss-of-ductility are identified as special problems. (INTERATOM)	[134]
First use of ASME Boiler & Pressure Vessel Codes. (UW)	[160]
Helium gas production and dpa rates are calculated for a fusion environment. (UW)	[160]
First use of EOL limits on surface erosion. (UW)	[160]
First use of liquid lithium cooled, 316 stainless steel first wall (INTERATOM, UW)	[134,160]
Excessive deformation considered as possible failure mode. (UW)	[160]
1973	
First use of EOL limits on swelling, loss-of-ductility and surface erosion. (UW)	[161]
1974	
First inelastic analysis to calculate inelastic strains, using thermal and irradiation creep and swelling. (CULHAM)	[163]
First use of creep rupture as a failure mode. (CULHAM)	[163]
First consideration of irradiation creep phenomena. (CULHAM)	[163]
First assessment of problems from mechanical interactions between modules caused by swelling. (CULHAM)	[163]
First use of fatigue (S-N) curves to calculate life. (IOWA STATE)	[162]
First use of creep-fatigue and crack growth concepts. (IOWA STATE)	[162]

1975	Reference
First design of a first wall which is separate from blanket. (UW)	[164]
First design with a protective liner. (UW)	[164]
First design with helium gas as a first wall coolant. (UW)	[164]
1976	
First use of the finite element method for elastic stress analysis. (GA)	[17]
First use of ASME Code Case 1592. (GA)	[17]
First use of a first wall metal other than 316 S.S. (TZM). (UW)	[165]
First high temperature first wall (1000°C). (UW)	[165]
First design with a ceramic coating on the first wall (LASL)	[10]
First use of fracture mechanics to calculate brittle fracture and leak-through failure modes from crack growth. (LASL)	[10]
First use of H_2O as a first wall coolant. (ARGONNE)	[166]
First buckling analysis of a first wall (ARGONNE)	[166]
First calculation of the damage from vaporization/ ablation. (GA)	[167]
First design of a low temperature first wall (350°C). (UW)	[168]
First calculation of decrease in fracture toughness caused by neutron irradiation. (UW)	[143]
1977	
First calculation of the saturation stress level from combined irradiation creep and swelling deformations. (UW)	[143]
First consideration of forces from electromagnetic loads. (JAERI)	[127]
First calculation of stress history from doing a self-consistent inelastic stress analysis. (MDAC - McDonnell Douglas Astronautics Co.)	[14]

1977 (cont.)	Reference
First use of inelastic finite element code (ANSYS). (MDAC)	[14]
First calculation of plastic/shakedown behavior. (MDAC)	[14]
First calculation of performance goals for alloy development. (ARGONNE)	[159]
First completely non-metallic first wall (graphite). (UW)	[169]
First use of Li_2O particles as a first wall coolant. (UW)	[169]
First lifetime analysis of a graphite FW/blanket. (UW)	[135]
1978	
First major use of the RDT Standards. (WESTINGHOUSE)	[19]
First assessment of creep crack growth (WESTINGHOUSE)	[19]
First consideration of off-normal scenarios and plasma disruption loads for lifetime predictions. (WESTINGHOUSE)	[19]
First use of EOL limits on deflection which is based on loss-of-function criteria. (WESTINGHOUSE)	[19]
1979	
First approach to first wall design by working backwards from the limits required by Code Case 1592. (ARGONNE)	[158]
First crack growth analysis of an all-ceramic, SiC FW/blanket module. (GE)	[200]
First use of martensitic steel, HT-9, in a first wall. (GA)	[21]
First review article of first wall lifetimes. (ARGONNE)	[157]
First conference on fusion reactor materials. (MIAMI BEACH, FL)	[170]
First complete session on fusion reactor problems at the SMIRT V conference. (WEST BERLIN, GERMANY)	[171]
Second review article of first wall lifetimes. (MDAC)	[15]

1980	Reference
First lifetime assessment due to creep crack growth in a steady-state tokamak. (ARGONNE)	[154]
First self-consistent fatigue (S-N) calculation including wall erosion. (INTOR)	[155]
Major shift in emphasis towards greater survivability of first wall armor, limiters, beam dumps and divertor collector plates. (9th SYMP. On ENGR. PROB. OF FUSION RESEARCH, CHICAGO)	[156]

This is necessary because the literature review revealed that no one has done a self-consistent, integrated lifetime assessment. No computer code exists for first walls similar to the LIFE-III code for fast breeder reactor fuel pin cladding [181]. To illustrate this, the remainder of this section presents a more detailed review of five studies that represent the state-of-the-art in lifetime methodology.

By coupling an inelastic stress analysis to fatigue crack growth in the UWMAK-I blanket module first wall, Cramer [12-14] achieved the first integrated lifetime analysis. His results, shown in Fig. 10, identified flaw growth as the life-limiting failure mechanism. Cramer used a finite element code, ANSYS, to calculate the 2-D stress history due to irradiation creep, swelling and plasticity. This was coupled to a 1-D crack growth calculation of a surface flaw. However, the most serious omission from this study was not including any effects of embrittlement in the fracture mechanics analysis. Wall erosion was also omitted, as well as off-normal loads such as plasma disruptions.

Another important study is the lifetime analysis done by Wolfer and Watson [135] of a graphite first wall and blanket structure. They integrated the reduction in fracture strength due to porosity changes with a one-dimensional inelastic stress analysis to compute the brittle fracture lifetime. Although no crack growth or erosion was calculated, the analysis was self-consistent because the irradiation-induced dimensional changes directly affected both the fracture stress via changes in the elastic modulus and the stress history via swelling and creep.

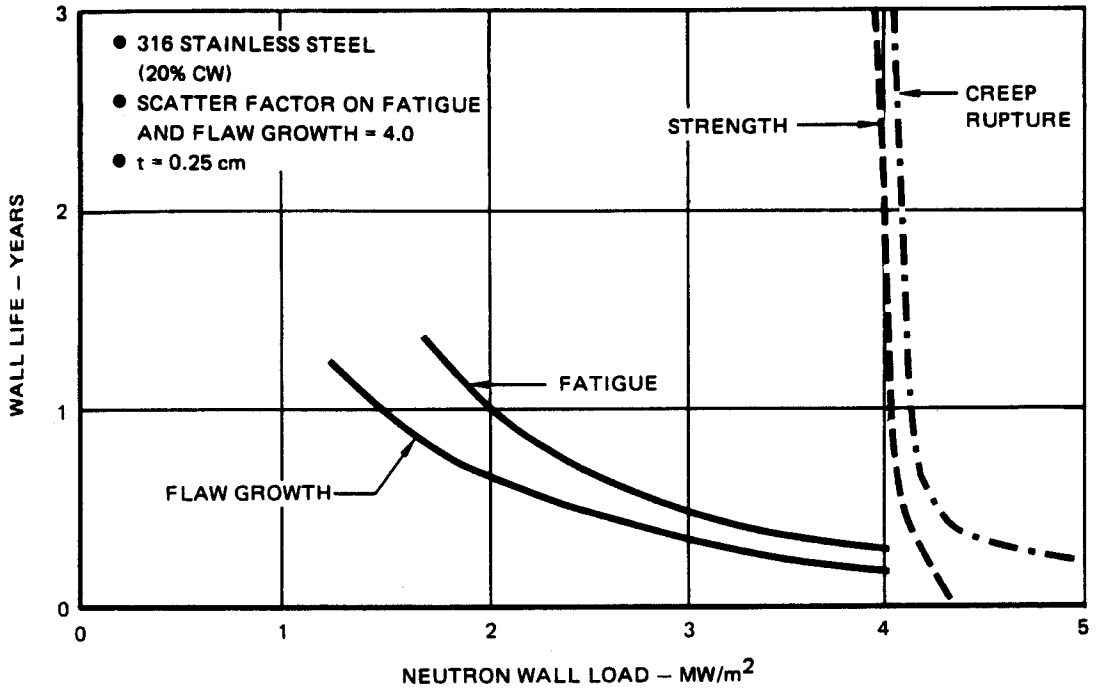

Figure 10. First wall life prediction comparison for a tokamak U-bend first wall configuration [12].

Another significant lifetime study is the analysis of the Westinghouse cylindrical blanket module done by Prevenslick, et al [19,147]. Particularly notable is the detailed structural analysis done with a 1-D ANSYS inelastic model. Off-normal loads were considered, including electromagnetic forces from plasma disruptions. Prevenslick was the first to include a drop in K_{IC} and creep crack growth. The governing failure mode was excessive deformation of the coolant channel due to creep and swelling. Crack growth was found to be negligible due to small thermal stresses. He also concluded that a single plasma disruption of sufficient intensity to melt the surface would also cause catastrophic fracture of an embrittled first wall. His analysis, however, did not include surface erosion effects.

Surface erosion effects have been considered recently by Cramer [176] in his fatigue (S-N) analysis of the INTOR first wall coolant channels on the outboard wall. He found that by including the reduction in cyclic thermal stresses due to wall thinning the fatigue life could be extended from 4×10^5 cycles to greater than 10^7 cycles. No crack growth was performed for this design, however.

Another important work is the lifetime analysis of the STARFIRE first wall tubes done by Mattas [22]. His work is notable because it integrated a 2-D inelastic stress analysis with a crack growth analysis. A very long lifetime was found since STARFIRE is a steady-state tokamak and, hence, only creep crack growth was present. Some limitations of his work is due to the neglect of wall erosion and neutron embrittlement.

From the literature review we have identified that crack growth

is one of the dominant life-limiting failure mechanisms for cyclic tokamak fusion reactors. Excessive deformation due to irradiation creep and swelling is another. Most first wall analysts have concentrated on phenomena which are unique to the fusion environment and, therefore, are not included in the Standards or Codes currently used by the nuclear power industry. However, no one has included all of these effects within a single, self-consistent methodology.

Also, none of the papers surveyed included any effects of threshold ΔK on fatigue crack growth (FCG), effects of embrittlement on FCG, or effects of wall erosion on crack propagation. Finally, a critical area for lifetime analysis appears to be the damage done to an embrittled, unprotected first wall caused by a plasma disruption. There is nothing quantitative in the literature about this scenario and, unfortunately, it is also beyond the scope of this thesis. Nevertheless, the author believes this to be a critical area for future study. A final observation can be made that, in general, our ability to predict first wall lifetimes is limited more by the lack of irradiated materials' data than by our ability to mathematically model the structural response and damage mechanisms, such as crack growth.

In the next chapter we shall discuss the methodology of lifetime assessment, which integrates a 1-D inelastic stress analysis with a 2-D crack propagation analysis, while including the effects of embrittlement and wall erosion in a self-consistent fashion.

CHAPTER 3

Method of Solution

As stated in the Introduction, the primary objective of this research was the development of an integrated method of lifetime assessment that would account for the synergisms between the structural response and the damage processes. Fundamental to this task is an understanding of the materials behavior in a fusion environment. Accordingly, an appropriate methodology for lifetime analysis consists of the following three parts:

1. a materials analysis
2. a structural analysis, and
3. a fracture mechanics analysis.

This procedure is illustrated schematically in Fig. 11, which shows the various computer codes that were developed at the University of Wisconsin for this purpose.

Each of these codes, which are described in more detail later on, contain subroutines for materials behavior. In particular, TSTRESS contains models for inelastic deformation caused by thermal creep, irradiation creep and swelling. Instantaneous plasticity, however, is not accounted for in the code due to the complexity of such an analysis. In addition, surface erosion is modelled as a continuous reduction in wall thickness. The other code, WISECRACK, models fatigue and creep crack growth phenomena. Also, the effect

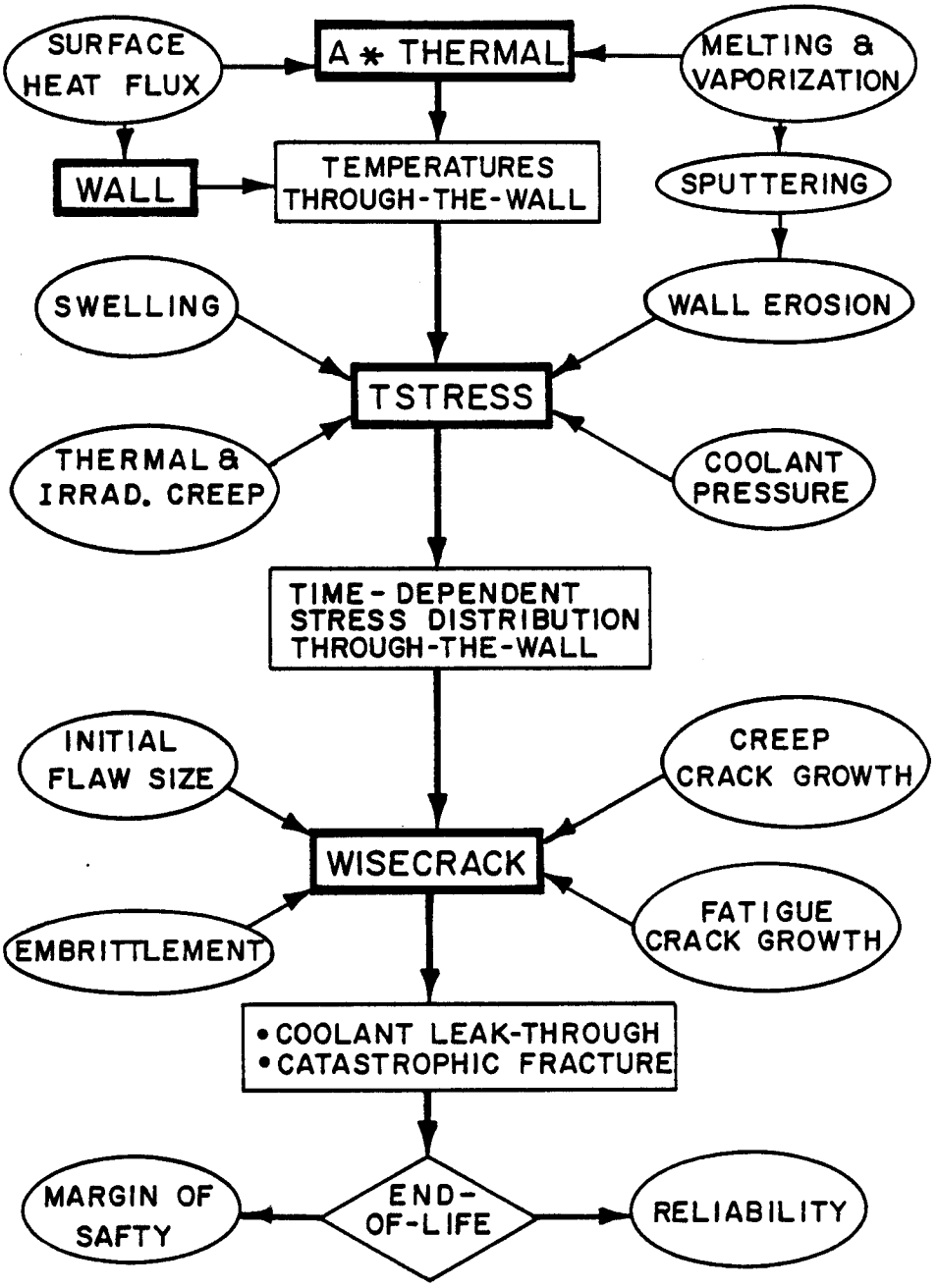

Figure 11. Methodology of first wall lifetime analysis.

of neutron-induced embrittlement is modelled as a reduction in the fracture toughness as a function of dose (dpa). It will be shown later on that the primary source of uncertainty in the lifetime predictions is the lack of sufficient data on radiation effects to crack propagation.

The second stage of the lifetime methodology consists of a structural analysis. A computer code is needed for this because inelastic deformation will cause the stresses to relax and redistribute in a non-uniform way over a period of time due to creep and swelling. To predict this would require, in general, a fully three-dimensional, inelastic global stress analysis of the entire structure. However, two reasons advise us against doing this. First, the depth and detail of such an analysis is not yet warranted because of uncertainties in not only the materials behavior, but also in the fusion environment (e.g. surface heat flux, erosion rate, etc.). And secondly, it will be shown that a global structural analysis is not actually needed in order to answer many of the generic questions that are of interest.

Therefore, for these two reasons, a less complicated method was sought that would still retain all of the important features of a global analysis. A review of previous structural analyses, especially those by Cramer [12] and Prevenslick [19], indicated that the variations in stress along the surface of the first wall were

typically much smaller than the variations through the thickness. Therefore, the computer code TSTRESS was written (see Chapter 5) to perform only a one-dimensional inelastic analysis of the stresses through the thickness of the wall at a critical location.

Use of the TSTRESS code requires a knowledge of the bending moments and membrane loads at a specific location in the structure, as shown in Fig. 12. Although this is discussed in more detail in Chapter 4, these loads can be determined by a variety of methods. The most detailed (and most accurate) method would be a 2-D inelastic shell analysis, probably with finite elements. However, for the vast majority of thin-walled designs shown in Chapter 2, this is not required because the N_x, N_y, M_x and M_y are mainly determined by the coolant pressure and constraints with respect to bending. In this case, these loads can be simply determined by doing an elastic structural analysis. As a result, one discovers that only the membrane loads are of importance, which greatly simplifies the analysis. Nevertheless, by splitting the stress analysis from a 3-D code into separate 2-D shell and 1-D through-the-thickness codes, we have reduced the overall effort and increased the flexibility without any significant loss in accuracy.

As shown in Fig. 11, a thermal analysis is also required as input to the strucutral analysis. The same arguments concerning a global vs. local approach apply to this as well. We have found that a 1-D analysis of the temperature distribution through the wall gives sufficient accuracy (see Chapter 4).

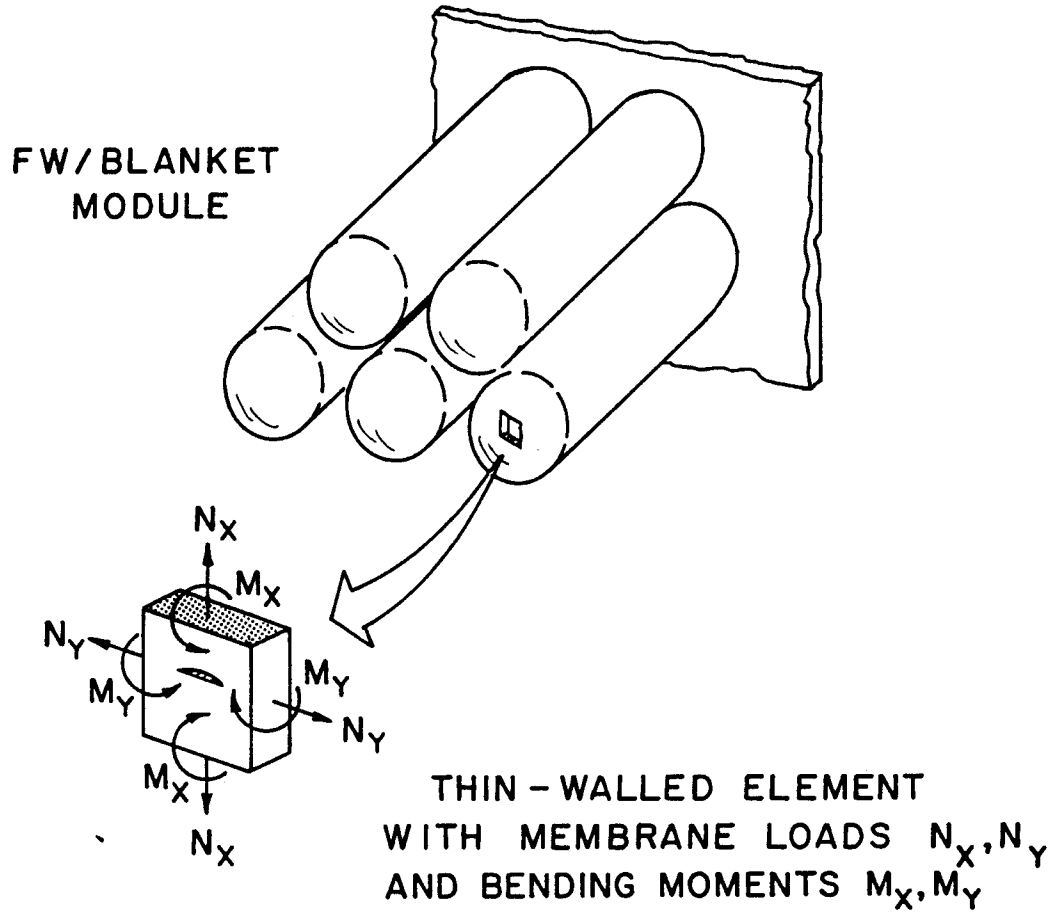

Figure 12. Use of a thin-walled plate element with membrane loads and bending moments to model the behavior of a critical position in the first wall structure.

For the problems that are solved by TSTRESS in this thesis, only normal operating conditions were considered. However, off-normal loads, such as those caused by plasma disruptions, loss-of-cooling accidents or seismic events may also cause large stresses. Although TSTRESS could handle these scenarios, nevertheless, they were judged to be beyond the scope of this project.

The third and final stage of the lifetime methodology involves coupling both the materials and structural analyses to a fracture mechanics analysis. Fundamental to this entire treatment is the assumption of the existance of a flaw or defect in the structure that has escaped detection. It is this feature that distinguishes the fracture mechanics approach from the fatigue life (S-N) approach, which is based upon smooth-speciman uniaxial tests of cycles-to-failure. Fracture mechanics will always predict a shorter lifetime than the traditional S-N appraoch because the initiation period is neglected. Therefore, it is more conservative. Clearly, this is desireable because high reliability is a primary concern for first wall components that will be difficult and expensive to repair and to replace. A survey of existing fracture mechanics codes indicated that nothing was available that could handle the effects of radiation damage and wall erosion. Therefore, an in-house code called WISECRACK was written that was specifically designed to couple to the TSTRESS code. Through this connection, the lifetime analysis can be performed in a self-consistent manner.

In the next two chapters, the theory of inelastic stress

analysis is presented and is followed by the application of the theory to a specific first wall design, a cylindrical blanket module. This specific design is used throughout the thesis to provide a basis for comparison of the various predictions by TSTRESS and WISECRACK.

CHAPTER 4

Theory of Inelastic Stress Analysis

Introduction

The inelastic deformation of fuel pin cladding in fast breeder reactors due to irradiation creep and swelling (e.g. bowing of fuel rod assemblies) has been a serious problem for the industry and a great deal of research has gone into developing swelling resistant alloys. First wall components in fusion reactors, on the other hand, are generally much more tolerant to swelling or "bowing"; there simply is more space in which to expand. Nevertheless, irradiation creep and swelling will cause a redistribution of the stresses over a period of time (e.g. years). Knowing the history of these stresses, then, allows for a much more accurate calculation of the propagation of a surface flaw. In contrast, most of the first wall designers use only the initial elastic stresses to calculate crack growth, which may or may not be a conservative approach. A major objective, then, of this research was to develop a method of inelastic stress analysis of a first wall component that could be easily coupled to a crack growth analysis.

A survey of the existing finite element computer codes revealed that none of them had the capability to handle wall thinning due to surface erosion and irradiation creep and swelling at the same time. Therefore, an in-house code was developed, called TSTRESS.

As discussed in Chapter 3, it was decided that a two- or three-dimensional inelastic global structural analysis code was beyond the scope of this project. Instead, a one-dimensional analysis of the stress distribution through the wall, at only a critical location, would provide sufficient detail to subsequently perform an accurate crack growth analysis. An extension of TSTRESS to two or three dimensions, TSTRESS-2D or TSTRESS-3D, would be the next logical step.

This chapter presents the theory which is used in the TSTRESS code. It begins with a review of previous first wall structural analyses. Then, equations for the initial elastic stresses in a thin-walled plate element are derived, which depend on the temperature distribution through the wall and on the applied membrane loads and bending moments. Next, the four different sources of inelastic strains are discussed and included in a constitutive law for inelastic deformation. Instantaneous plasticity is not considered in this development because a design requirement for normal operation would be to keep the stresses from exceeding the yield stress. Next, the time-dependent inelastic stress equations are derived for the plate element. Finally, a method for solving these equations directly for the steady-state stresses is presented, along with a complete analytic solution for the stress history of a clamped flat plate.

Review of Previous Work

A review of previous first wall structural analyses can be divided into two classes: by their dimensionality (1-D, 2-D, or 3-D) and by their type (elastic or inelastic). Structural analyses of limiters, armored tiles or other high heat flux components are not reviewed here.

Every first wall designer performs a one-dimensional elastic stress analysis, which is useful for initial scoping design studies. However, to satisfy ASME code limits, other investigators prefer to use 2-D axisymmetric and 3-D finite element elastic methods. For example, Biggio, et al [126] used BERSAFE-II to model the cylindrical blanket module used in the FINTOR tokamak design. Cramer [12] used SAAS III and Prevenslick [19] used ANSYS to model a cylindrical blanket module with hemispherical end cap. Sako and Minato [127] used a 3-D flat plate shell element from SAP-IV to model a semi-rectangular blanket module with ellipsoidal head closure. Finally, Streibl et al [128] used a specially designed macro-element in the CASTEM code to model the D-shaped bellows which connect sectors of the JET vacuum vessel. Detailed 3-D elastic analyses of actively cooled first wall designs have not appeared in the literature and probably are not warranted at this stage due to inelastic deformation.

A more realistic assessment of the structural response can be obtained with a 1-D inelastic analysis. Here, the variations in stress only through the thickness are considered for a long period of

time. Daenner [129-134] has used a finite difference program which is very similar to TSTRESS. On the other hand, both Cramer [12] and Prevenslick [19] have used the finite element code ANSYS with only a few elements through the thickness to predict the stress history. Qualitatively, the responses obtained by each investigator are all very similar; the differences between them arise from different swelling correlations.

While all of the analyses described so far have used stainless steel or some other metal, Watson and Wolfer [136] have studied the inelastic behavior of graphite as a structural material. They performed a 1-D inelastic finite difference analysis of the SOLASE blanket design [135] by modelling it as a thin disk subjected to radial temperature and flux gradients.

To date, only two investigators have performed 2-D inelastic analysis and no one has done a 3-D study. Mattas [22] has developed a 2-D finite difference program to predict the response of an infinitely long, thick-walled tube (plane strain) which sees an internal coolant pressure and a non-axisymmetric surface heat flux. A sample of his results is shown in Fig. 13. He apparently has only used it for scoping studies on the INTOR project and is currently writing [137] instead a 1-D inelastic code similar to TSTRESS.

Cramer [12-14] used the finite element code ANSYS to perform a 2-D inelastic stress analysis of the UWMAK-I U-bend blanket module and first wall. He used a 2-D plastic beam element (STIF-23), which models non-linear plasticity with kinematic hardening, irradiation

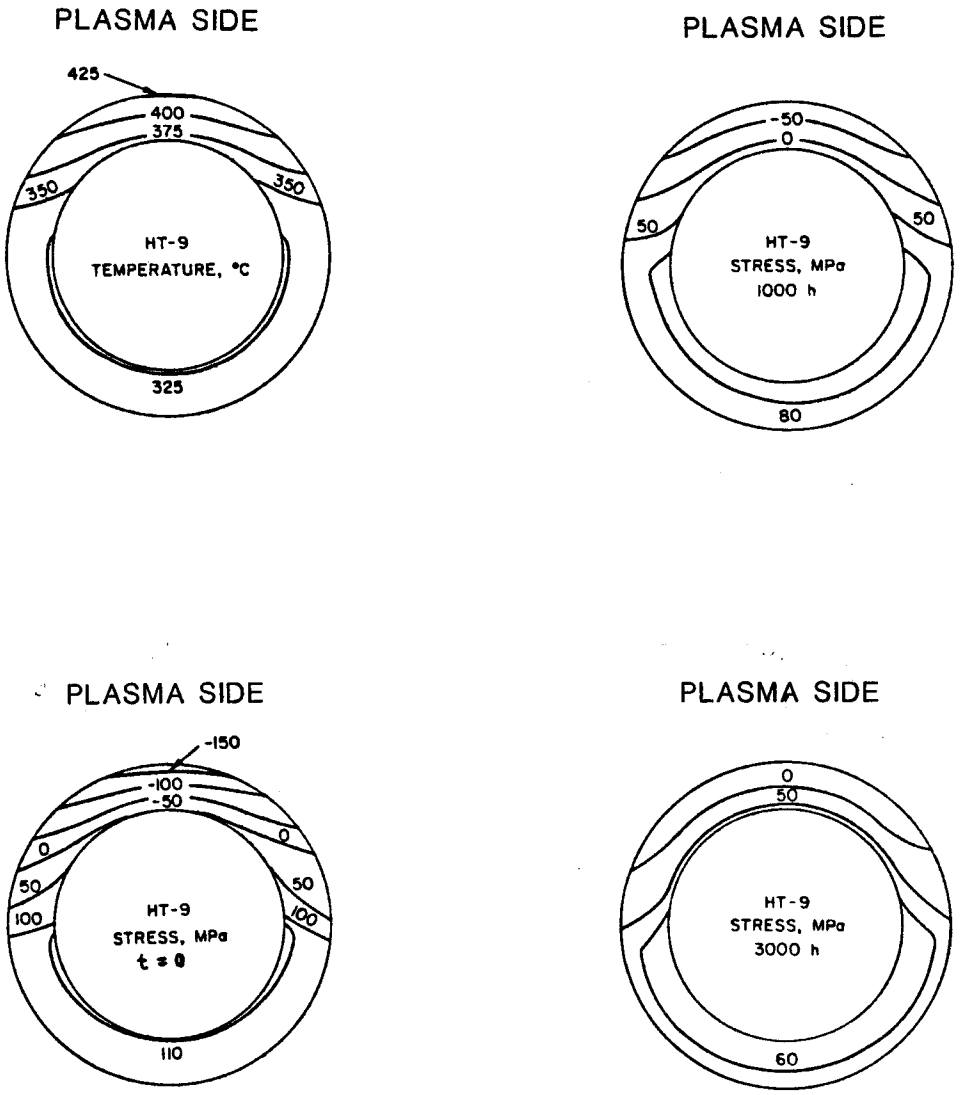

Figure 13. Two-dimensional stress history predictions for HT-9 first wall tube in the STARFIRE reactor [22].

creep, swelling and thermal creep effects. His results, shown in Figure 14, are plotted for plasma-on stresses on the plasma side. Note that the trends are very similar to the TSTRESS results (a 1-D model) plotted in Figure 29, for the same neutron wall loading (P_{nw} = 2.5 MW/m^2). This gives us some confidence in the application of the one-dimensional TSTRESS code to an actual three-dimensional structure.

From this review, we see that only a small number of investigators have attempted inelastic structural analyses of first wall components. The 1-D TSTRESS model presented in this report is believed to be a state-of-the-art program for fusion applications. However, there are many questions that remain to be answered concerning the impact of global variations in temperature, swelling, creep or erosion on the local stress history at a specific location. The developemnt of an in-house inelastic shell code that would then couple to TSTRESS could provide not only a more accurate stress analysis, but also the ability to determine the critical location with more precision.

One-Dimensional Inelastic Stress Equations

In this section we shall derive the equations for the biaxial stress distribution, $\sigma_x(z)$ and $\sigma_y(z)$, through the thickness of a thin-walled plate element which are caused by the action of externally applied mechanical loads and inelastic deformations. The plate element, shown in Fig. 15, models a critical location within a thin-walled high heat flux component where failure is expected to occur

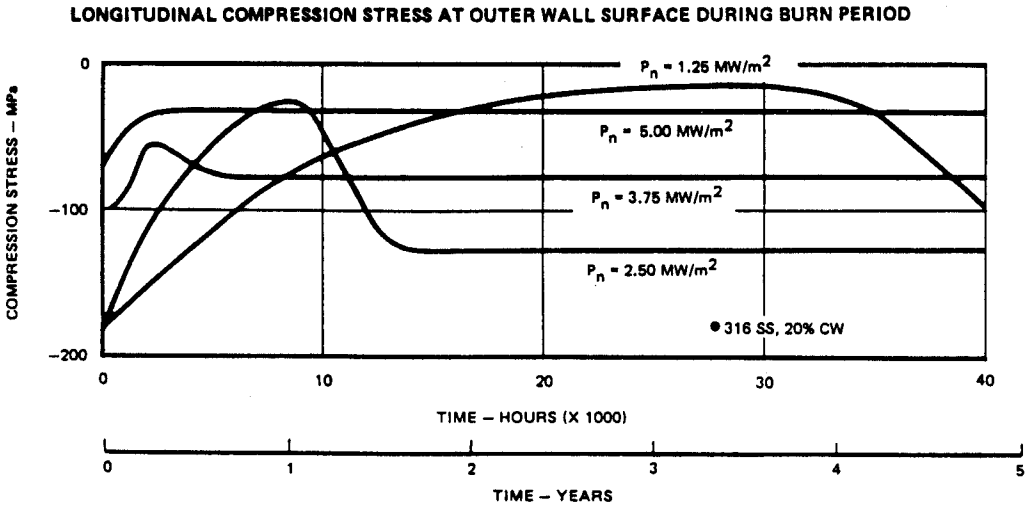

Figure 14. Stress history of the longitudinal stresses on the plasma side of a U-bend blanket module during the plasma-on period [14].

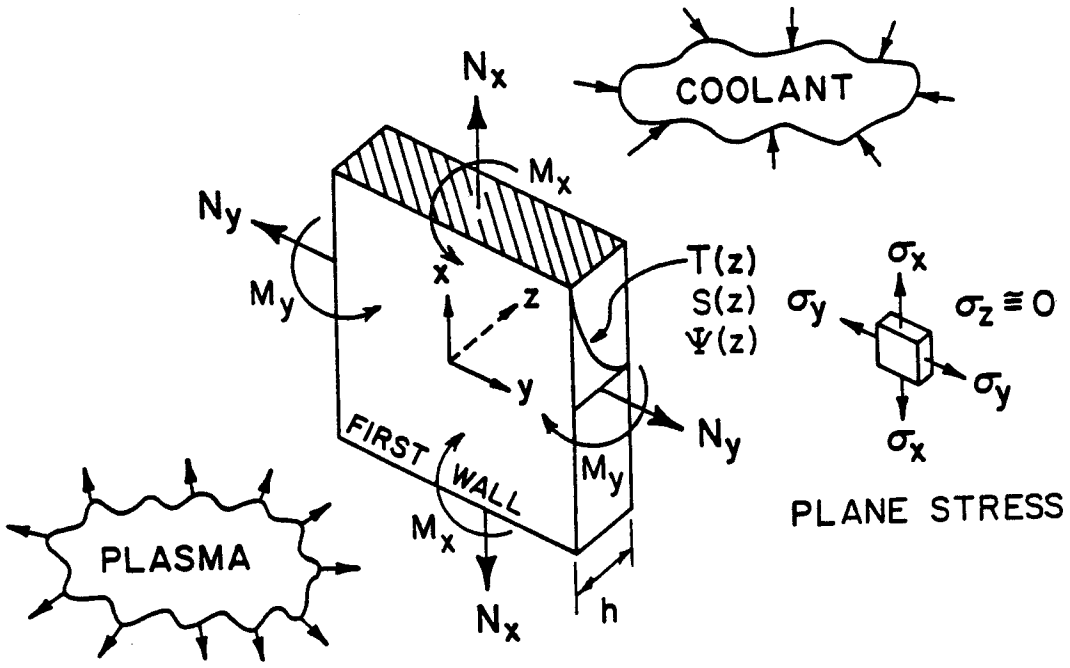

Figure 15. TSTRESS thin-walled plate element model of a first wall.

due to crack growth. The externally applied membrane loads N_x, N_y and bending moments M_x, M_y must be specified in addition to distribution of temperature, swelling and creep constants through the thickness.

Figure 16 shows that the coordinate system is chosen appropriately to coincide with the directions of maximum principal stress. We then assume that the plate element is initially flat, but when loaded is free to bend and expand, as shown in Figure 17. Furthermore, we assume small deflection plate theory (Szilard [138]) and that plane cross-sections which are perpendicular to the element midplane will remain plane after deformation.

Because the thickness of the plate element is assumed to be much smaller than the radii of curvature of the global structure at the critical location, this allows us to neglect any variation in the normal stress, σ_z, through the thickness. Since the boundary conditions at the two surfaces require that: $\sigma_z(z = h/2) = -P_o$ and $\sigma_z(z = -h/2) = 0$, then we conclude that σ_z cannot exceed the coolant pressure $P_o \approx 1 - 14$ MPa (150-2000 psi). Since the thermal stresses range from 70 to 700 MPa (10-100 ksi), we can neglect the contribution of σ_z to the stress state and assume it is one of plane stress.

Assuming, then, that $\sigma_z = 0$, we can state Hooke's laws for plane stress in an isotropic medium (see Timoshenko and Goodier [139]) as:

$$\sigma_x = \frac{E}{1-\nu^2} \left(\varepsilon_x^e + \nu \varepsilon_y^e \right) \qquad (1)$$

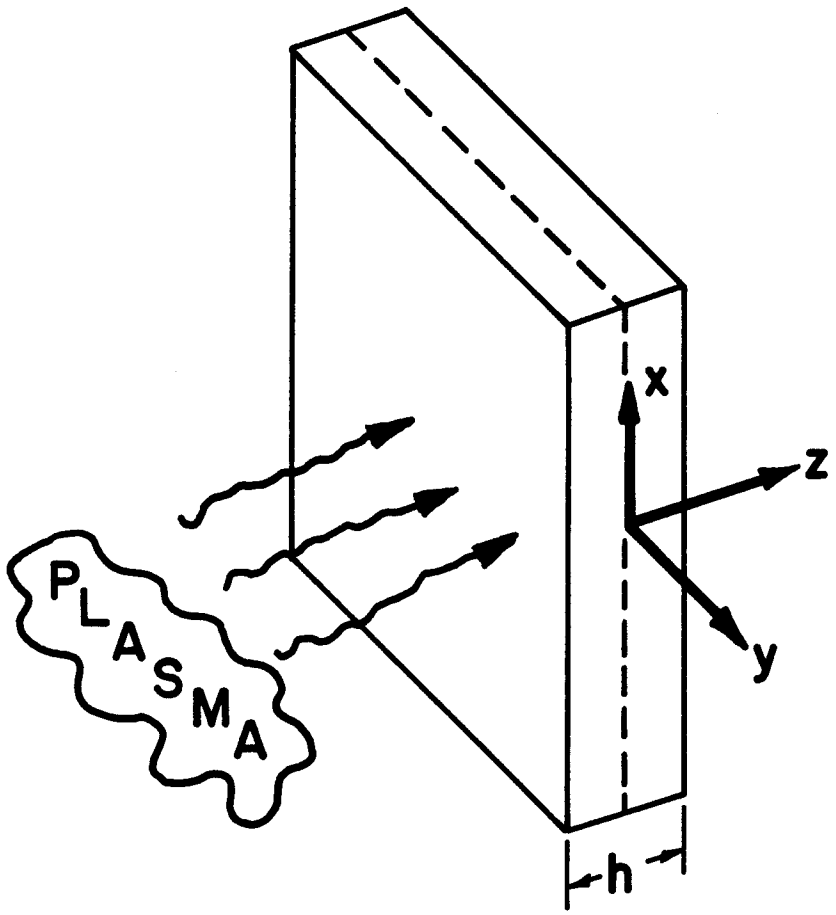

Figure 16. Coordinate system for the inelastic stress analysis.

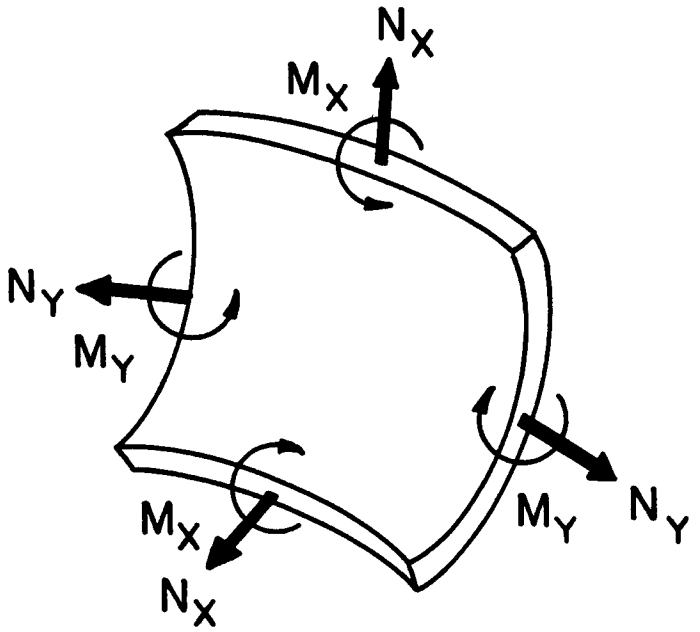

Figure 17. Deflected geometry of the thin-walled plate element.

and

$$\sigma_y = \frac{E}{1-\nu^2} (\varepsilon_y^e + \nu\varepsilon_x^e) , \tag{2}$$

where E = Young's modulus of elasticity and ν = Poisson's ratio. ε_x^e and ε_y^e are the elastic strain components in the x and y directions, respectively.

However, to solve the inelastic problem, we must rewrite these equations in terms of the total strains ε_x, ε_y and the inelastic strains e_x, e_y. Following the work of Lin [140], we assume that the total strain is a sum of these two components:

$$\varepsilon_x(z) = \varepsilon_x^e(z) + e_x(z) \tag{3}$$

and

$$\varepsilon_y(z) = \varepsilon_y^e(z) + e_y(z) . \tag{4}$$

Substituting back into Eqs. (1) and (2) yields:

$$\sigma_x = \frac{E}{1-\nu^2} (\varepsilon_x - e_x) + \frac{E\nu}{1-\nu^2} (\varepsilon_y - e_y) \tag{5}$$

and

$$\sigma_y = \frac{E}{1-\nu^2} (\varepsilon_y - e_y) + \frac{E\nu}{1-\nu^2} (\varepsilon_x - e_x) . \tag{6}$$

The next step in this derivation is to choose an appropriate strain field, $\varepsilon_x(z)$ and $\varepsilon_y(z)$, which is compatible with the assumed deformations (e.g. bending and stretching). When the element is stretched only in the x-y plane due to membrane loads, the total

strain should not be a function of the z-coordinate; rather, it should be a constant. We assume, therefore, that for pure membrane loads

$$\varepsilon_x(z) = K_x \tag{7}$$

and

$$\varepsilon_y(z) = K_y \ , \tag{8}$$

where K_x and K_y are constants.

However, in pure bending the basic kinematic assumption of plane sections remaining plane is equivalent to assuming that the strain varies linearly with its distance from the neutral axis (z=0) (see Popov [173]). Therefore, for pure bending moments, we can assume

$$\varepsilon_x(z) = L_x z \tag{9}$$

and

$$\varepsilon_y(z) = L_y z \ , \tag{10}$$

where L_x and L_y are constants. Linear elasticity theory allows us to superimpose these deformation states to generate a linear strain field, namely:

$$\varepsilon_x(z) = K_x + L_x z \tag{11}$$

and

$$\varepsilon_y(z) = K_y + L_y z \ . \tag{12}$$

Here, we can identify K_x, K_y as the strain of the neutral membrane (e.g. element midplane) due to stretching and L_x, L_y as a measure of the rotation of plane cross-sections due to bending. If, for example, we set $K_x = K_y = 0$, then we prevent the plate element from expanding in the x-y plane. Or, if we set $L_x = L_y = 0$, then we prevent any bending (rotation) from occurring. Therefore, many different geometries and kinematic boundary conditions can be easily modeled by adjusting the deflection constants K_x,K_y, L_x, and L_y to be either zero or non-zero.

Substitution of the total strain components (given by Eqs. (11) and (12)) back into Eqs. (5) and (6) for Hooke's Laws yields

$$\sigma_x = \frac{E}{1-\nu^2}(K_x + L_x z - e_x) + \frac{E\nu}{1-\nu^2}(K_y + L_y z - e_y) \qquad (13)$$

and

$$\sigma_y = \frac{E}{1-\nu^2}(K_y + L_y z - e_y) + \frac{E\nu}{1-\nu^2}(K_x + L_x z - e_x) \; . \qquad (14)$$

Next, we must use the four boundary conditions to solve for the four unknown deflection constants: K_x, K_y, L_x and L_y. The boundary conditions consist of a set of equivalent forces and moments which can replace the actual stress distribution, $\sigma_x(z)$ and $\sigma_y(z)$, while still preserving static equilibrium of the plate element. The membrane loads N_x, N_y and bending moments M_x, M_y are assumed to be known because they have already been calculated by a separate, global structural analysis program. If an *inelastic* global analysis is done, then the membrane loads and bending moments may, in general,

be time-dependent functions. In either case, in order to preserve the laws of equilibrium, we must require that

$$\int_{-h/2}^{h/2} \sigma_x(z)\, dz = N_x \tag{15}$$

$$\int_{-h/2}^{h/2} \sigma_y(z)\, dz = N_y \tag{16}$$

$$\int_{-h/2}^{h/2} \sigma_x(z) z dz = M_x \tag{17}$$

$$\int_{-h/2}^{h/2} \sigma_y(z) z dz = M_y \quad . \tag{18}$$

These equations provide the necessary and self-consistent link between the 1-D local stress analysis and the two-dimensional global structural analysis.

Next, we substitute the two stress equations into the four boundary conditions to eliminate σ_x and σ_y from the equations. For example, inserting $\sigma_x(z)$ from Eq. (13) into the integral in Eq. (15) yields

$$\int_a^b \frac{E}{1-\nu^2} (K_x + L_x z - e_x) dz + \int_a^b \frac{E\nu}{1-\nu^2} (K_y + L_y z - e_y) dz = N_x \tag{19}$$

where a = h/2 and b = -h/2. Solving the integrals gives

$$K_x + \nu K_y = \left(\frac{1-\nu^2}{E}\right) \frac{N_x}{h} - \frac{1}{h} \int_a^b (e_x - \nu e_y) dz \quad . \tag{20}$$

We have tacitly assumed that the elastic properties E and ν are only weak functions of temperatures and can be brought outside of the integrals. For very steep temperature gradients, however, they would have to be kept inside.

The second boundary condition is satisfied in a similar way, namely, by substituting Eq. (13) into Eq. (16). This produces an equation similar to Eq. (19) and can be integrated in closed form to give

$$L_x + \nu L_y = \left(\frac{1-\nu^2}{E}\right) \frac{12M_x}{h^3} - \frac{12}{h^3} \int_a^b (e_x + \nu e_y) z dz \quad . \tag{21}$$

Because no special preference has been given to the choice of the x-y coordinates, we can simply generate the other two equilibrium equations by interchanging the "x" and "y" subscripts in Eqs. (20) and (21). This then yields

$$K_y + \nu K_x = \left(\frac{1-\nu^2}{E}\right) \frac{N_y}{h} - \frac{1}{h} \int_a^b (e_y - \nu e_x) dz \tag{22}$$

and

$$L_y + \nu L_x = \left(\frac{1-\nu^2}{E}\right) \frac{12M_y}{h^3} - \frac{12}{h^3} \int_a^b (e_y - \nu e_x) z dz \quad . \tag{23}$$

We can now solve Eqs. (20,21,22,23) for the four unknowns K_x, K_y, L_x and L_y by applying Cramer's Rule to this linear system of

equations. This then yields

$$K_x = \frac{N_x - \nu N_y}{Eh} + \frac{1}{h}\int_a^b e_x dz \tag{24}$$

$$K_y = \frac{N_y - \nu N_x}{Eh} + \frac{1}{h}\int_a^b e_y dz \tag{25}$$

$$L_x = \frac{12(M_x - \nu M_y)}{Eh^3} + \frac{12}{h^3}\int_a^b e_x z dz \tag{26}$$

$$L_y = \frac{12(M_y - \nu M_x)}{Eh^3} + \frac{12}{h^3}\int_a^b e_y z dz \quad . \tag{27}$$

The first term in each of the equations represents the elastic strain, or rotation, due to the externally applied mechanical loads, whereas the second term is the contribution from inelastic deformations. Note that the factor $12/Eh^3$ which appears in Eqs. (26) and (27) is related to the flexural rigidity

$$D = \frac{Eh^3}{12(1 - \nu^2)} \tag{28}$$

commonly found in classic plate bending theory [138].

The final step in this derivation of the general 1-D inelastic stress equation involves substituting the expressions just given for K_x, K_y, L_x, and L_y into Hooke's Laws: Eqs. (13) and (14). After some algebra, this then yields the desired results.

$$\sigma_x(z) = \frac{N_x}{h} + \frac{12M_x z}{h^3} + \frac{E}{(1-\nu^2)h}\int_{-h/2}^{h/2}(e_x + \nu e_y)dz \qquad (29)$$

$$- \frac{E}{(1-\nu^2)}(e_x + \nu e_y) + \frac{12Ez}{(1-\nu^2)h^3}\int_{-h/2}^{h/2}(e_x + \nu e_y)zdz$$

$$\sigma_y(z) = \frac{N_y}{h} + \frac{12M_y z}{h^3} + \frac{E}{(1-\nu^2)h}\int_{-h/2}^{h/2}(e_y + \nu e_x)dz \qquad (30)$$

$$- \frac{E}{(1-\nu^2)}(e_y + \nu e_x) + \frac{12\,Ez}{(1-\nu^2)h^3}\int_{-h/2}^{h/2}(e_y + \nu e_x)zdz$$

The first two terms in these equations represent the elastic stresses which are caused by the externally applied membrane loads, N_x and N_y, and bending moments, M_x and M_y. The last three terms, then, represent the self-equilibrating, "inelastic" stresses which are caused by the internally generated inelastic strains, $e_x(z)$ and $e_y(z)$.

Sources of Membrane Loads and Bending Moments

The 1-D inelastic stress equations (29) and (30) that were derived in the previous section each contain two terms, N_x/h and $12\ M_x z/h^3$, and N_y/h and $12\ M_y z/h^3$, that represent the elastic stresses which are caused by externally applied membrane loads, N_x and N_y, and bending moments, M_x and M_y. These loads, which are calculated, in general, by a three-dimensional global structural analysis code (such as NASTRAN or ANSYS), are caused by the application of temperatures, pressures, magnetic forces or specified displacements to the structure. The purpose, then, of this section is to discuss the sources of these loads and moments in fusion reactors.

As an example, consider the simple case of a thin-walled tube of radius R, free to expand, with an internal pressure P. The axial stress σ_x will equal PR/2h and the hoop stress σ_y will be PR/h. Therefore, the membrane loads would be identified as $N_x = PR/2$ and $N_y = PR$ (note that N_x and N_y have the units of N/m, while M_x and M_y have units of N·m/m). As another example, consider the case of a square, clamped flat plate of width W subjected to a time-dependent pressure P(t) from an ICFR shock blast wave. Here, for small deflections, the membrane loads are zero, but the time-dependent bending moments, at the center of the plate for example, are given by: $M_x(t) = M_y(t) = .023\ p(t)W^2$ [138].

Another source of pressure is the $\vec{j} \times \vec{B}$ magnetic force in tokamaks produced by the interaction of the magnetic field at the

wall $\vec{B}$, with the eddy current $\vec{j}$ that is induced by plasma disruptions. The distribution and pattern of eddy currents depends crucially on the shape of, and the insulating barriers in the metallic first wall. Therefore, a general expression for the magnetic loads cannot be given. Nevertheless, by considering a simple example, we can at least obtain a representative value for the magnetic loads. Accordingly, we assume that the first wall consists of toroidal sections separated by insulating barriers. Each section has a metallic wall continuous in the poloidal direction. As the plasma current I_p decays in a disruption over a short time period τ_d, a poloidal eddy current is induced in the first wall of the magnitude given by

$$j_p = \frac{1}{\mu_o} (\Delta\phi/\phi_o) \, B_T \exp(-t/\tau_w). \tag{31}$$

Here, $\mu_o = 1.26 \times 10^{-6}$ m kg s^{-2} A^{-2} is the magnetic permeability, B_T the strength of the toroidal magnetic field at the wall, and τ_w is a current decay constant assumed to be substantially larger than τ_d. Its exact value depends on the electrical resistivity of the wall material, as well as the mutual inductance of the eddy currents, etc. ϕ_o is the toroidal magnetic flux inside the plasma chamber in the absence of the plasma. With the plasma present, its value is reduced by $\Delta\phi$. The latter is approximately given by

$$\Delta\phi \cong \frac{\mu_o^2}{8\pi} \frac{1 - \beta p}{B_T} I_p^2 \tag{32}$$

where the poloidal β_p is the ratio of the plasma pressure to the magnetic field pressure of the poloidal field B_p. Since j_p is perpendicular to the toroidal field B_T, and both are in the plane of the wall, the magnetic pressure produced is perpendicular to the wall and given by

$$P_M = \frac{\mu_o}{8\pi} (1 - \beta_p) \frac{B_T}{\phi_o} I_p^2 \exp(-t/\tau_w) \tag{33}$$

It can be directed towards or away from the plasma depending on the direction of the eddy current. The magnetic pressure is largest at the instant of the disruption, e.g. $t \simeq 0$, and on the inboard side of the first wall where B_T has its maximum value (on the first wall). Hence

$$P_M^{max} \cong \frac{\mu_o}{8\pi} | 1-\beta_p | I_p^2 B_T^{max}/(\overline{B}_T A) \tag{34}$$

where

$$\phi_o = \overline{B}_T A \ . \tag{35}$$

A is the cross-section area of the plasma chamber and $\overline{B}_T$ an appropriate average of the toroidal field over A.

Typical plasma parameters for fusion power reactors are given in Table 6. With these values we find that

$$P_M^{max} \simeq 1.2 \text{ MN/m}^2 = 180 \text{ psi.} \tag{36}$$

Table 6. Plasma Parameters

Parameter	Value
I_p	7 MA
β_p	3.0
A	6 m^2
$B_T^{max}/\bar{B}_T$	1.5

$$P_M^{max} \cong 1.2 \text{ MN/m}^2 = 180 \text{ psi} . \quad (36)$$

It should be noted that the above value for the magnetic pressure is only a typical value, but by no means a conservative estimate. Perhaps the important conclusion is that the magnetic pressure produced in a plasma disruption is of the same order or even greater than the coolant pressure for liquid metals.

Gradients in temperature throughout the structure caused by a non-uniform surface heat flux will induce variations in the membrane loads and bending moments from thermal expansion, swelling and creep. For example, the tip of a hemi-spherical blanket module closest to the plasma will be hotter than the rest of the module and, hence, will swell faster, consequently putting the tip region in compression. In this case, $N_x = N_y = PR/2h$ at time = 0, and then

would become negative after sufficient swelling had occurred.

Finally, the supports of first wall components may be subjected to specified displacements as a function of time due to seismic activity (e.g. earthquakes). Other accident scenarios can be envisioned, although they are not considered further in this work.

In summary, the membrane loads and bending moments which are used in Equations (29) and (30) are, in general, functions of both time and location on the structure. In most cases, a global 2-D inelastic structural analysis code is required to compute N_x, N_y, M_x, and M_y. However, for the reference design of a tokamak first wall that is used extensively in Chapter 8, we assume that $N_x = N_y = PR/2$ (constant w/r time) and that $L_x = L_y = 0$. It is believed that this simple set of N's and M's will allow for a realistic assessment of the important factors that influence the lifetime.

Temperature Distribution Through the Wall

The inelastic strains $e_x(z)$ and $e_y(z)$, which are used in Equations (28) and (29), are composed, in part, of thermal strains equal to $\alpha\, T(z)$, where α is the thermal expansion coefficient. To compute the temperature distribution through the wall, $T(z)$, at any location on the structure, we must solve the heat conduction equation. In general, the surface heat flux is distributed non-uniformly on a first wall component. However, because the wall is thin, we shall assume that any heat flow conducted along the surface

is small as compared to the flow through the thickness. A three-dimensional finite element heat transfer analysis by Lee [144] indicates, indeed, that only small errors are introduced by this approximation. Therefore, we need to solve only the one-dimensional heat conduction equation:

$$K \frac{\partial^2 T}{\partial z^2} + q_o''' = \frac{K}{\rho C_p} \frac{\partial T}{\partial t} \tag{37}$$

where

k = thermal conductivity ($W/cm^2 °K$)

q_o''' = nuclear volumetric heat generation rate (W/cm^3)

ρ = density (g/cm^3)

C_p = specific heat ($J/g°K$) .

The two boundary conditions used in this model are

$$T(z = h/2) = T_b \tag{38}$$

and

$$-K \frac{dT}{dz}\bigg|_{z = -h/2} = q_s''(t) \tag{39}$$

where T_b = backside wall temperature ($°K$)

q_s'' = surface heat flux (W/cm^2).

For an initial condition we shall assume $T(z,0) = T_c$, where T_c is the coolant temperature.

Many different computer programs are available to solve the one-dimensional heat conduction equation. In particular, the code A*THERMAL written by Hassenien at the University of Wisconsin [145] is especially useful for first wall applications because melting and vaporization of the surface are included in the analysis. The emphasis in this thesis, however, is on long burn-time, magnetically-confined fusion devices, such as the tokamak. By "long", we refer to cases where the surface heat flux is turned on long enough for the temperature to reach a steady-state distribution. For tokamaks with burn-times longer than 100 seconds, these conditions are easily satisfied. In this case, it can be shown that the steady-state solution to Equation (37) is given by

$$T(z) = T_b + \frac{q_s''}{K}(h-z) + \frac{q_o'''}{2K}(h^2-z^2). \qquad (40)$$

When $h < 5$ mm, then $q_s'' >> hq_o'''/2$ for tokamaks and we can neglect the last term in this equation, therefore giving the familiar linear temperature distribution:

$$T(z) \cong T_b + \frac{q_s''}{K}(h-z) \quad , \qquad (41)$$

$$\text{for} \quad q_s'' >> \frac{hq_o'''}{2} \quad .$$

When the thermal conductivity, K, is a function of temperature, then Eq. (40) is no longer correct. An accurate representation of K(T) for stainless steel is a linear function, namely

$$K(T) = A + BT \qquad [W/cm°k] \tag{42}$$

where

$$A = 0.10552$$

$$B = 1.355 \times 10^{-4} \quad .$$

It can be shown that an exact solution to the heat conduction equation with a linearly varying conductivity is given by

$$T(z) = \frac{-A}{B} + \frac{1}{B}\left[A^2 - B(2q_s''(z-h) + q_o'''(z^2-h^2) - 2AT_b - BT_b^2)\right]^{1/2} \quad . \tag{43}$$

In summary, two options can be chosen when using TSTRESS to solve the 1-D inelastic stress equations. The first option is to use A*THERMAL, or some other heat transfer computer code (such as HEATRAN or FEM-2D), to compute a file of temperatures for transient heat fluxes. For constant heat fluxes, however, the steady-state temperatures are computed from Eq. (43) directly within TSTRESS.

Initial Elastic Stress Distribution

When the first wall component is first exposed to the plasma at the beginning of life there will be no inelastic strains from either swelling or creep. Therefore, the only inelastic strains will be those caused by thermal expansion, namely

$$e_x(z) = e_y(z) = e^{th}(z) \tag{44}$$

where

$$e^{th}(z) = \alpha(z)\ [T(z)-T_o]\ . \tag{45}$$

T_o is defined as the reference temperature at which the thermal strains are identically zero. Substitution of these equations into Eq. (29) and (30) yields the 1-D initial elastic stress distribution through a plate which is free to bend and expand:

$$\sigma_x(z) = \frac{N_x}{h} + \frac{12M_x z}{h^3} + \frac{E}{(1-\nu)h}\int_{-h/2}^{h/2} \alpha(T-T_o)dz \tag{46}$$

$$- \frac{E\alpha}{(1-\nu)}(T-T_o) + \frac{12\ Ez}{(1-\nu)h^3}\int_{-h/2}^{h/2} \alpha(T-T_o)zdz$$

and

$$\sigma_y(z) = \frac{N_y}{h} + \frac{12M_y z}{h^3} + \frac{E}{(1-\nu)h}\int_{-h/2}^{h/2} \alpha(T-T_o)dz \tag{47}$$

$$- \frac{E\alpha}{(1-\nu)}(T-T_o) + \frac{12\ Ez}{(1-\nu)h^3}\int_{-h/2}^{h/2} \alpha(T-T_o)zdz\ .$$

If, instead, we wish to know the initial elastic stresses in a plate element which is free to expand but is constrained from bending, then we would eliminate the second and last terms from Eqs. (46) and (47) to derive a new set of equations

$$\sigma_x(z) = \frac{N_x}{h} + \frac{E}{(1-\nu)h} \int_{-h/2}^{h/2} \alpha(T-T_o)dz - \frac{E\alpha}{1-\nu}(T-T_o) \qquad (48)$$

and

$$\sigma_y(z) = \frac{N_y}{h} + \frac{E}{(1-\nu)h} \int_{-h/2}^{h/2} \alpha(T-T_o)dz - \frac{E\alpha}{1-\nu}(T-T_o). \qquad (49)$$

Likewise, if the plate is constrained from both bending and expanding, then the initial elastic stresses would be given by:

$$\sigma_x(z) = \sigma_y(z) = -\frac{E\alpha}{1-\nu}[T(z)-T_o] \quad . \qquad (50)$$

Sources of Inelastic Strains

The total inelastic strains, e_x and e_y, are assumed to be composed of three separate sources: thermal expansion, e^{th}, creep strains e_x^c and e_y^c, and swelling strains e^{sw}. Therefore, using superposition, we can add these components together:

$$e_x(z) = e^{th}(z) + e^{sw}(z) + e_x^c(z) \qquad (51)$$

and

$$e_y(z) = e^{th}(z) + e^{sw}(z) + e_y^c(z) \quad . \qquad (52)$$

Instantaneous plasticity is not included in this report due to the

complexity of such an analysis. Although the thermal strain is treated here as an inelastic strain, it is, in fact, reversible deformation which equals

$$e^{th}(z) = \alpha(z)\ [T(z)-T_o] \quad . \tag{53}$$

Swelling, on the other hand, causes deformations which are permanently locked into the structure when the radiation source is removed. Assuming that the swelling behavior is not a function of stress, then e^{sw} is isotropic (like e^{th}) and is given by

$$e^{sw}(z) = \frac{1}{3}\ S(z) \tag{54}$$

where S(z) = total volumetric swelling ($\Delta V/V$) The swelling equation used in TSTRESS is taken from the Nuclear Systems Materials Handbook, revision #7 [32]. It is an empirical correlation originally developed for fast breeder reactor applications:

$$S(t) = R\ [\phi t + \frac{1}{\alpha}\ \ln\ \{\ \frac{1 + e^{\alpha(\tau-\phi t)}}{1 + e^{\alpha\tau}}\ \}\ ] \tag{55}$$

where, for 20% CW 316 S.S.

$$R = 0.01\ \exp[0.0419+1.498\beta+0.122\beta^2-0.332\beta^3-0.441\beta^4] \tag{56}$$

$$\tau_s = (4.742-0.2326\beta+2.717\beta^2)\times 10^{22}\ n/cm^2 \tag{57}$$

α = 0.75

T = temperature in °C

ϕ = neutron flux in n/cm^2-sec

t = time in seconds

$$\beta = (T-500)/100 \quad .$$

The swelling rate, $\dot{S}$ is given by the derivative of Eq. (55):

$$\dot{S}(t) = R\phi \left[1 - \frac{1}{1 + e^{-\alpha(\tau-\phi t)}}\right] \quad [sec^{-1}] \tag{58}$$

In TSTRESS a conversion is made between fluence and dpa for 316 SS:

$$5 \text{ dpa} = 1 \times 10^{22} \text{ n/cm}^2 \text{ (E > 0.1 MeV)} \quad . \tag{59}$$

The steady-state swelling rate, $\dot{S}(t \to \infty)$, is given by

$$\dot{S}_{ss} = R\phi \tag{60}$$

and is plotted in Fig. 18 as a function of temperature for 316 SS. Note that the maximum swelling rate occurs at around 580°C.

Swelling correlations are always being updated as new data is generated by the U.S. materials program. The particular swelling law chosen here is only representative of the kind of behavior that would be expected from stainless steel in a fusion environment. Note, also, that helium bubble swelling was not included, only void swelling. This is because the first wall temperatures are limited to 500-550°C maximum, which is below the range of temperatures where helium swelling is expected to be significant (Glasgow et al [141]).

Irradiation creep and thermal creep are also sources of in-

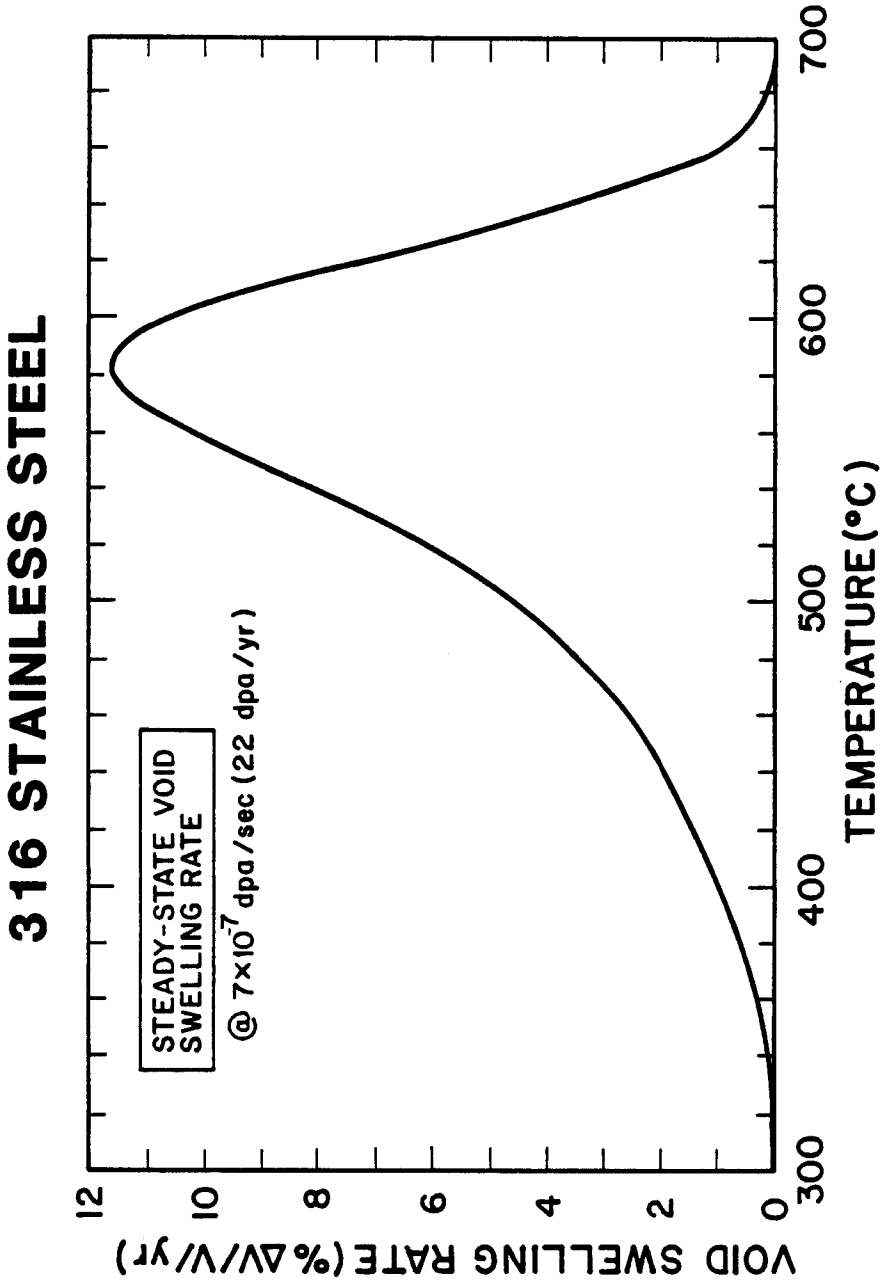

Figure 18. Steady-state void swelling rate for 316 stainless steel as a function of temperature [32].

elastic deformation. Creep, however, is different than swelling or thermal expansion because creep is the deformation of a material in response to an applied stress.

The irradiation creep law used in TSTRESS is taken from experimental measurements by Gilbert and Bates [142] of 20% CW 316 SS irradiated in EBR II from 375 to 575°C and 0-30 dpa. Their results can be written in terms of the irradiation creep compliance, $\psi_{irr} = \frac{\dot{e}^{c}_{eq}}{\sigma_{eq}}$, where

$$\psi_{irr} = K_o \dot{F} \{A + B [1-\text{sech}^2(F/c)]\} \quad [\text{ksi-sec}]^{-1} \tag{61}$$

where

K_o = 9.19307×10^{-6}

$\dot{F}$ = damage rate in dpa/sec

A = 0.67

B = $5.8 \times 10^{4} \exp(-16000/RT)$

T = temperature in °K

c = 8.5

F = dose in dpa .

The thermal creep law, taken from the Nuclear Systems Materials Handbook, revision 0 [32], is written in terms of the equivalent creep rate, $\dot{e}^{c}_{eq}$, as

$$\dot{e}^{c}_{eq} = A_o[\sinh(\alpha \sigma_{eq})]^{n} \exp(-Q/RT) \quad [HR^{-1}] \tag{62}$$

where

$$A_o = 1.609 \times 10^3 \exp(14633/T)$$

$$\alpha = \frac{-5.225 \times 10^{-1} + 8.716 \times 10^{-4} T}{23.55 - 0.01796T} \ [ksi^{-1}]$$

$$n = 24.608 - 0.01923T$$

$$Q = 64{,}000$$

$$R = 1.987$$

T [°K]

applicable range = 538-760°C .

We can also define a thermal creep compliance, ψ_{th}, as

$$\psi_{th} = \frac{e^c_{eq}}{\sigma_{eq}} \tag{63}$$

where

$$\sigma_{eq} = \frac{1}{\sqrt{2}} \left[(\sigma_x - \sigma_y)^2 + (\sigma_x - \sigma_z)^2 + (\sigma_y - \sigma_z)^2 \right]^{1/2} . \tag{64}$$

For the plate element, $\sigma_z = 0$, and σ_{eq} may then be rewritten as

$$\sigma_{eq} = [\sigma_x^2 + \sigma_y^2 - \sigma_x \sigma_y]^{1/2} . \tag{65}$$

Figure 19 illustrates the relative sizes of thermal and irradiation creep rates at a damage rate of 7×10^{-7} dpa/sec (22 dpa/FPY), for different stress levels. As can be seen, irradiation creep dominates over thermal creep for stress and temperature ranges applicable to magnetically-confined devices. The opposite holds true for ICFR's. Finally, we can define a total creep compliance, ψ, which equals the

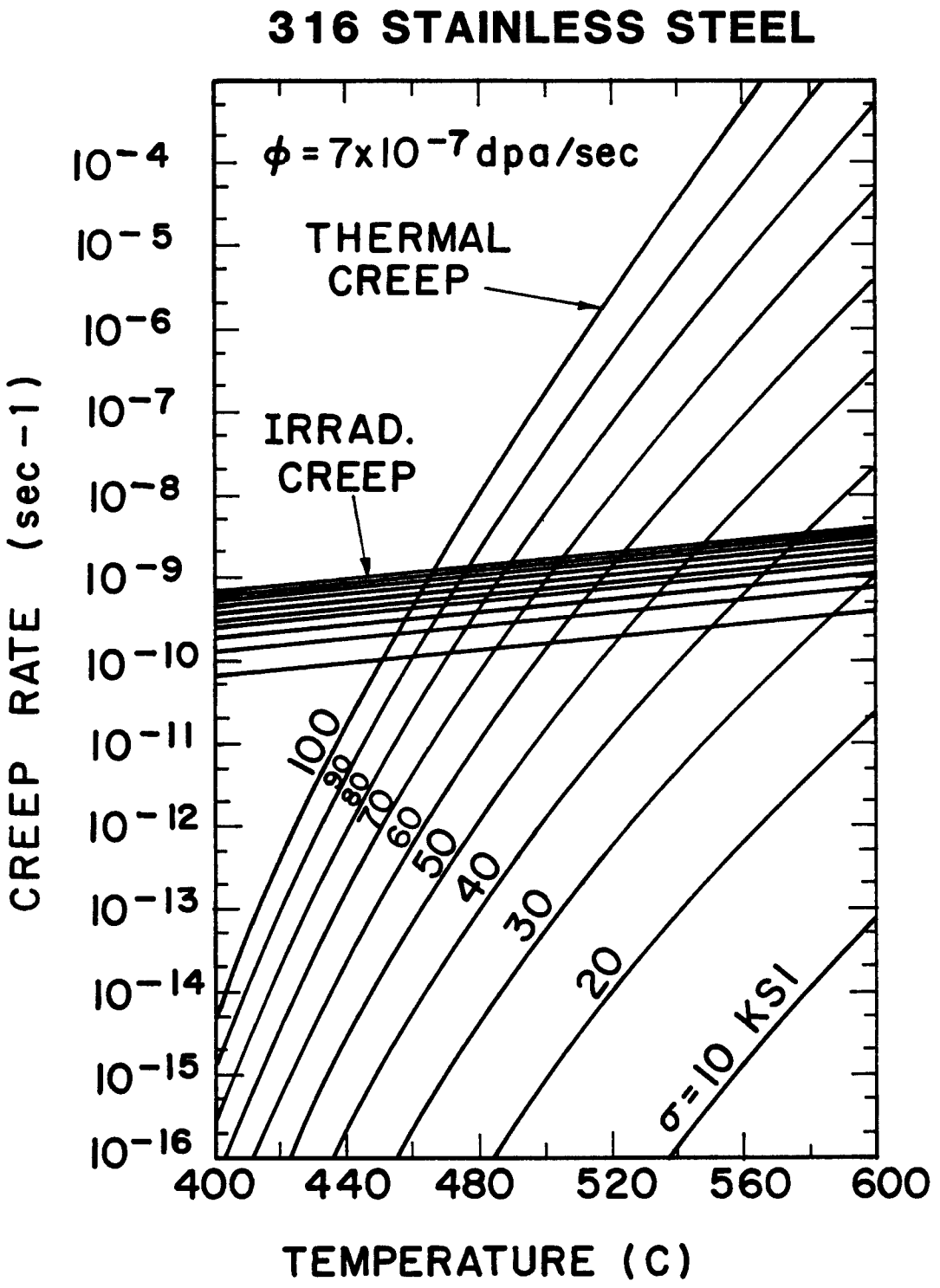

Figure 19. Temperature dependence of the thermal and irradiation creep rates for 316 stainless steel.

sum of the two types, namely

$$\psi = \psi_{irr} + \psi_{th} \cdot \tag{66}$$

Wall thinning due to surface erosion is another source of time-dependent stress changes because the geometry is changing. Assuming, then, a constant erosion rate, e_r, (in cm/FPY), the rate at which the wall thins down is given by

$$\frac{dh}{dt} = - e_r \cdot \tag{67}$$

The surface erosion is caused by physical or chemical sputtering, or by vaporization of material during intense heating, as in a plasma disruption. In the next section we will derive a constitutive law for inelastic deformation that will be used by the TSTRESS code to predict long-term stress histories.

A Constitutive Law for Inelastic Deformation

We assume that the three different sources of inelastic strains, discussed in the preceeding section, may be linearly superimposed, hence

$$e_x(z) = \alpha[T(z)-T_o] + \frac{1}{3} S(z) + e_x^c(z) \tag{68}$$

and

$$e_y(z) = \alpha[T(z)-T_o] + \frac{1}{3} S(z) + e_y^c(z) \tag{69}$$

where

$e_x^c(z)$ = total creep strain in x-direction

and

$e_y^c(z)$ = total creep strain in y-direction.

The difficulty in this formulation arises from the fact that only the creep rates, $\dot{e}_x^c$ and $\dot{e}_y^c$, can be specified at any point in time. Therefore, e_x^c and e_y^c must be expressed as

$$e_x^c(z,t) = \int_o^t \dot{e}_x^c(z)dt' \tag{70}$$

and

$$e_y^c(z,t) = \int_o^t \dot{e}_x^c(z)dt' \ . \tag{71}$$

The creep rates, $\dot{e}_x^c$ and $\dot{e}_y^c$, are calculated by using the Prandtl-Reuss stress-strain relationships for plastic flow [140]:

$$\dot{e}_{ij} = \frac{3}{2} \frac{\dot{e}_{eq}^c}{\sigma_{eq}} S_{ij} \tag{72}$$

where

$$S_{ij} = \sigma_{ij} - \frac{1}{3} \sigma_{kk} S_{ij} \ . \tag{73}$$

Since $\sigma_z = 0$, then $\sigma_{kk} = \sigma_x + \sigma_y + \sigma_z = \sigma_x + \sigma_y$, and the two components of Eq. (72) that we are interested in become

$$\dot{e}_x^c = \frac{3}{2} \frac{\dot{e}_{eq}}{\sigma_{eq}} [\sigma_x - \frac{1}{3} (\sigma_x + \sigma_y)] \tag{74}$$

and

$$\dot{e}_y^c = \frac{3}{2}\frac{\dot{e}_{eq}^c}{\sigma_{eq}}\left[\sigma_y - \frac{1}{3}(\sigma_y + \sigma_x)\right] \tag{75}$$

Using the definition of the creep compliance, $\psi = \dot{e}_{eq}^c/\sigma_{eq}$, Eqs. (74) and (75) can be rewritten as

$$\dot{e}_x^c = \psi(\sigma_x - \frac{1}{2}\sigma_y) \tag{76}$$

and

$$\dot{e}_y^c = \psi(\sigma_y - \frac{1}{2}\sigma_x) \ . \tag{77}$$

Substituting these expressions back into Eqs. (70) and (71) yields

$$e_x^c = \int_o^t \psi(\sigma_x - \frac{1}{2}\sigma_y)dt' \tag{78}$$

and

$$e_y^c = \int_o^t \psi(\sigma_y - \frac{1}{2}\sigma_x)dt' \ . \tag{79}$$

Here, we have explicitly assumed that σ_x and σ_y are functions of time, as well. Substituting these expressions back into Eqs. (68) and (69) then produces the final form of the constitutive law

$$e_x(z) = \alpha[T(z)-T_o] + \frac{1}{3}S(z) + \int_o^t \psi(\sigma_x - \frac{1}{2}\sigma_y)dt' \tag{80}$$

and

$$e_y(z) = \alpha[T(z)-T_o] + \frac{1}{3}S(z) + \int_o^t \psi(\sigma_y - \frac{1}{2}\sigma_x)dt' \ . \tag{81}$$

For some applications, however, the instantaneous rate form of the

constitutive law may be more convenient. Taking the derivative of Eqs. (80) and (81) with respect to time yields

$$\dot{e}_x = \alpha\dot{T} + \frac{1}{3}\dot{S} + \psi(\sigma_x - \frac{1}{2}\sigma_y) \tag{82}$$

and

$$\dot{e}_y = \alpha\dot{T} + \frac{1}{3}\dot{S} + \psi(\sigma_y - \frac{1}{2}\sigma_x) \quad . \tag{83}$$

Time-Dependent Inelastic Stress Equations

In this section we shall derive the one-dimensional, time-dependent inelastic stress equations that will be solved, numerically, by the TSTRESS computer code. The fundamental step used here involves substituting the constitutive law that was derived in the previous section into the integrals in the stress equations. Inserting Eqs. (80) and (81) into Eqs. (29) and (30) yields after some algebra:

$$\sigma_x(z,t) = \frac{N_x}{h} + \frac{12\,M_x z}{h^3} - \frac{E}{1-\nu}\left[\alpha(T-T_o) + \frac{1}{3}S\right] \tag{84}$$

$$+ \frac{E}{(1-\nu)h}\int_{-h/2}^{h/2}\left[\alpha(T-T_o) + \frac{1}{3}S\right]dz'$$

$$+ \frac{12\,Ez}{(1-\nu)h^3}\int_{-h/2}^{h/2}\left[\alpha(T-T_o) + \frac{1}{3}S\right]z'dz'$$

$$- \frac{E}{2(1-\nu^2)}\int_{o}^{t}\psi[\sigma_x(2-\nu) + \sigma_y(2\nu-1)]dt'$$

(Cont. on next page)

$$+ \frac{E}{2(1-\nu^2)h}\int_{-h/2}^{h/2}\int_{o}^{t}\psi[\sigma_x(2-\nu) + \sigma_y(2\nu-1)]dt'dz'$$

$$+ \frac{6Ez}{(1-\nu^2)h^3} \int_{-h/2}^{h/2} \int_{o}^{t} \psi[\sigma_x(2-\nu) + \sigma_y(2\nu-1)]dt'z'dz' \quad .$$

A similar equation can be written for $\sigma_y(z,t)$ by interchanging the x and y subscripts. Likewise, for the case of a plate element free to expand, but constrained from bending ($L_x = L_y = 0$), Equation (84) reduces to:

$$\sigma_x(z,t) = \frac{N_x}{h} - \frac{E}{1-\nu}\left[\alpha(T-T_o) + \frac{1}{3}S\right] \tag{85}$$

$$+ \frac{E}{(1-\nu)h} \int_{-h/2}^{h/2} \left[\alpha(T-T_o) + \frac{1}{3}S\right]dz'$$

$$- \frac{E}{2(1-\nu^2)} \int_{o}^{t} \psi[\sigma_x(2-\nu) + \sigma_y(2\nu-1)]dt'$$

$$+ \frac{E}{2(1-\nu^2)h} \int_{-h/2}^{h/2} \int_{o}^{t} \psi[\sigma_x(2-\nu) + \sigma_y(2\nu-1)]dt'dz' \quad .$$

As before, a similar equation exists for $\sigma_y(z,t)$ by switching the subscripts. The numerical solution of these equations, performed by the TSTRESS code, is presented in Chapter 5.

Steady-State Stress Distribution

When certain simplifying assumptions are made, it becomes possible to solve directly for the steady-state stress distribution. A steady-state situation can only be attained if the swelling rate, $\dot{S}$, and the creep compliance, ψ, have themselves reached steady-state (e.g. constant) values. The only other requirement is that the

plate thickness and temperatures remain constant with respect to time (i.e. no wall erosion). At steady state the stresses, membrane loads and bending moments will not be changing and, hence, their derivatives with respect to time will be zero. In this case, the stress rate, $\dot{\sigma}_x$, from Equation (84) becomes zero, hence

$$0 = -\frac{E}{3(1-\nu)}\dot{S} + \frac{E}{3(1-\nu)h}\int_{-h/2}^{h/2}\dot{S}\,dz' + \frac{12Ez}{3(1-\nu)h^3}\int_{-h/2}^{h/2}\dot{S}\,z'dz' \tag{86}$$

$$-\frac{E\psi}{2(1-\nu^2)}\left[\sigma_x(2-\nu) + \sigma_y(2\nu-1)\right]$$

$$+\frac{E}{2(1-\nu^2)h}\int_{-h/2}^{h/2}\psi\left[\sigma_x(2-\nu) + \sigma_y(2\nu-1)\right]dz'$$

$$+\frac{6Ez}{(1-\nu^2)h^3}\int_{-h/2}^{h/2}\psi\left[\sigma_x(2-\nu) + \sigma_y(2\nu-1)\right]z'dz'$$

A similar equation exists by switching the subscripts x with y. Solution of this pair of equations can, in principle, be performed by replacing the integrals with sums and then solving the simultaneous system of 2N equations for the unknowns σ_x and σ_y. Unfortunately, if thermal creep is large, then the creep compliance, ψ, may depend on σ_x and σ_y, thereby turning equation (85) into a transcendental equation, which is more difficult to solve numerically.

A short program called TSASS (tokamak stresses at steady-state) has been written and used to determine the steady-state stresses for the constrained plate element. TSASS allows the final stresses

from TSTRESS to be checked as to their accuracy. Very good agreement was obtained between the two different methods.

This concept of setting the stress rates to zero can, in principle, be extended to two-or-three-dimensional structures, which may be a useful and inexpensive method of obtaining the steady-state stresses for complicated designs.

Analytic Solution For Clamped Plate

As an example of the general method of analysis used in this chapter, we shall derive a closed-form solution of the entire stress history of a clamped flat plate subjected to swelling, creep and temperature gradients through its thickness. Since the plate is clamped, the total strain components, ε_x and ε_y, are both zero. Therefore, Eqs. (5) and (6) simply reduce to:

$$\sigma_x = \frac{-E}{1-\nu^2} (e_x + \nu e_y) \tag{87}$$

and

$$\sigma_y = \frac{-E}{1-\nu^2} (e_y + \nu e_x) \ . \tag{88}$$

From symmetry, it is assumed that $e_x = e_y$, therefore $\sigma_x = \sigma_y$ and

$$\sigma_x = \frac{-E}{1-\nu} e_x \ . \tag{89}$$

Differentiation of Eq. (89) with respect to time yields

$$\dot{\sigma}_x = \frac{-E}{1-\nu} \dot{e}_x \ . \tag{90}$$

Next, we substitute the rate form of the constitutive law into this equation to produce the governing differential equation, namely

$$\dot{\sigma}_x = \frac{-E}{1-\nu} \left[\frac{1}{3} \dot{S} + \psi(\sigma_x - \frac{1}{2} \sigma_y)\right] . \tag{91}$$

Rearranging this yields

$$\dot{\sigma}_x + \frac{E \psi}{2(1-\nu)} \sigma_x = \frac{-E\dot{S}}{3(1-\nu)} . \tag{92}$$

Assuming that ψ is not a function of stress (no thermal creep), then the general solution of Eq. (92) is:

$$\sigma_x(z,t) = \sigma_o(z) \exp\left(\frac{-E\psi t}{2(1-\nu)}\right) - \frac{2}{3} \frac{\dot{S}(z)}{\psi(z)} \left[1-\exp\left(\frac{-E\psi t}{2(1-\nu)}\right)\right] . \tag{93}$$

The function $\sigma_o(z)$ is identified as the initial stress distribution at time = 0. The steady-state solution is obtained by letting $t \to \infty$, thus producing

$$\sigma_x^{ss}(z) = -\frac{2}{3} \frac{\dot{S}(z)}{\psi(z)} . \tag{94}$$

This result was originally derived by Wolfer in 1977 [143].

This concludes the discussion of inelastic stresses in a first wall. In the next chapter, the computer code, TSTRESS, that is used to solve the time-dependent equations is presented, along with some detailed analyses of a cylindrical first wall/blanket module.

CHAPTER 5

TSTRESS - A Computer Code for 1-D Inelastic Stress Analysis

Introduction

The equations for a one-dimensional stress inelastic analysis which were derived in the previous chapter cannot be solved in closed-form. Therefore, a computer code called TSTRESS was written by R. Peterson at the University of Wisconsin [146]. Originally designed for application to inertial confinement fusion reactor first walls, TSTRESS was subsequently modified by the author to compute stress histories for magnetically-confined devices, such as the tokamak. Specifically, these changes included additional subroutines to calculate (1) the temperature distribution due to a constant surface heat flux, (2) changes in wall thickness due to surface erosion, and (3) stresses in a first wall modelled as a clamped flat plate.

TSTRESS solves only the cases of a clamped plate and a plate constrained from bending and does not model a plate which is free to bend. In principle, however, the code could be easily modified to include this case by adding some extra terms to the stress equations. This was not done in the present version of TSTRESS for two reasons. First, in order to solve the free plate equations this would require, in most cases, performing a 2-D or 3-D global inelastic structural analysis to compute the bending moments M_x and M_y in Eq. (83), which was judged to be beyond the scope of this

project. Secondly, since the majority of first wall designs are curved, thin-walled structures, they can be accurately modelled as a plate constrained from bending. This is due to the fact that the major component of deformation is stretching of the midplane, rather than bending. This would even be true for flat tube sheets, corrugated panel coils or plates with internal coolant passages (see Fig. 8) because the material on one side is still thin with respect to the thickness of the entire wall. Nevertheless, the stress equations were derived for the general case of a totally free plate to allow a future version of TSTRESS to be completely integrated with a global structural analysis code.

Method of Solution

In this section we describe the method used in TSTRESS to solve the 1-D inelastic stress equations for a plate element constrained from bending. The governing equations (see Eq. (85)) are repeated here for convenience:

$$\sigma_x(z,t) = \frac{N_x}{h} - \frac{E}{1-\nu}\left[\alpha(T-To) + \frac{1}{3}S\right] \qquad (95)$$

$$+ \frac{E}{(1-\nu)h}\int_{-h/2}^{h/2}\left[\alpha(T-To) + \frac{1}{3}S\right]dz'$$

$$- \frac{E}{2(1-\nu^2)}\int_{o}^{t}\psi\left[\sigma_x(2-\nu) + \sigma_y(2\nu-1)\right]dt'$$

$$+ \frac{E}{2(1-\nu^2)h}\int_{o}^{t}\int_{-h/2}^{h/2}\psi\left[\sigma_x(2-\nu) + \sigma_y(2\nu-1)\right]dz'dt'$$

and

$$\sigma_y(z,t) = \frac{Ny}{h} - \frac{E}{1-\nu}\left[\alpha(T-To) + \frac{1}{3}S\right] \tag{96}$$

$$+ \frac{E}{(1-\nu)h}\int_{-h/2}^{h/2}\left[\alpha(T-To) + \frac{1}{3}S\right]dz'$$

$$- \frac{E}{2(1-\nu^2)}\int_{o}^{t}\psi\left[\sigma_y(2-\nu) + \sigma_x(2\nu-1)\right]dt'$$

$$+ \frac{E}{2(1-\nu^2)h}\int_{o}^{t}\int_{-h/2}^{h/2}\psi\left[\sigma_y(2-\nu) + \sigma_x(2\nu-1)\right]dz'dt' .$$

Each variable in these two equations is considered to be a function of space (depth through the wall) and time. Note that in the last term of these equations, we have reversed the order of integration from what originally appeared in Eq. (85). This was done to allow the wall thickness, h, to vary as a function of time due to surface erosion processes.

These equations can also be integrated in another way. Because the first three terms depend only upon the instantaneous values of N_x, N_y, h, E, α, ν, T, and S at the current time, they therefore represent a type of forcing function. On the other hand, the last two integrals represent a response function because they both include the prior history of creep deformation within the structure.

The numerical solution to these equations involves two procedures. First, for each time step the spatial integrals are approximated as summations by using Simpson's Rule. The zone spacing is

permitted to be non-uniform in order to more accurately handle steep stress gradients. However, for tokamak reactor first wall components, the stress gradients are not very steep under normal operation and ten zones through the thickness has been found to give adequate accuracy.

The second step involves solving the integrals with respect to time. Let us begin by first rewriting Eqs. (95) and (96) in the following form:

$$\sigma_x(z,t) = Q_x(z,t) + \int_o^t \dot{R}_x dt' \tag{97}$$

and

$$\sigma_y(z,t) = Q_y(z,t) + \int_o^t \dot{R}_y dt' \tag{98}$$

where we have defined Q_x and Q_y to be the sum of the first three terms in Eqs. (95) and (96), respectively. The terms $\dot{R}_x$ and $\dot{R}_y$ are given by

$$\dot{R}_x = \frac{E}{2(1-\nu^2)} \left\{ \frac{1}{h} \int_{-h/2}^{h/2} \psi[\sigma_x(2-\nu) + \sigma_y(2\nu-1)]dz' \right. \tag{99}$$

$$\left. - \psi[\sigma_x(2-\nu) + \sigma_y(2\nu-1)] \right\}$$

and

$$\dot{R}_y = \frac{E}{2(1-\nu^2)} \left\{ \frac{1}{h} \int_{-h/2}^{h/2} \psi[\sigma_y(2-\nu) + \sigma_x(2\nu-1)]dz' \right. \tag{100}$$

$$\left. - \psi[\sigma_y(2-\nu) + \sigma_x(2\nu-1)] \right\} \quad .$$

Equations (97) and (98) are solved simply by replacing the integrals

with summations, which yields

$$\sigma_x(z,t_i) \cong Q_x(z,t_i) + \sum_{k=0}^{i} \dot{R}_x(z,t_k)\,\Delta t_k \tag{101}$$

and

$$\sigma_y(z,t_i) \cong Q_y(z,t_i) + \sum_{k=0}^{i} \dot{R}_y(z,t_k)\,\Delta t_k \quad . \tag{102}$$

The smaller the time step, Δt_k, the more accurate the solution will be. The method of solution used in TSTRESS is summarized as follows:

1. First, compute the initial elastic stresses at time = 0, which are given by $Q_x(z,0)$ and $Q_y(z,0)$.
2. At the current value of time, read in the membrane loads N_x and N_y and compute the current wall thickness h.
3. At the current value of time, calculate the swelling S, temperature T, creep compliance ψ, and elastic properties E, α, ν, for each spatial zone. These quantities may in general be functions of the current values of stress, temperature, dpa, etc.
4. Perform the spatial integrals in Eqs. (97) and (98), using Simpson's Rule.
5. Compute the current values of Q_x and Q_y for each zone.
6. Compute the response rate functions $\dot{R}_x$ and $\dot{R}_y$ for each zone.
7. Choose a stable time step Δt.
8. Use Euler's Rule to approximate the stresses at the new time for each zone by using the following equations:

$$\sigma_x(z,t + \Delta t) = Q_x(z,t) + \dot{R}_x(z,t)\ \Delta t \tag{103}$$

$$\sigma_y(z,t + \Delta t) = Q_y(z,t) + \dot{R}_y(z,t)\ \Delta t \quad . \tag{104}$$

9. Finally, update the time $t = t + \Delta t$, then return to step 2.

Sample Calculations

In order to verify the accuracy of the results from TSTRESS, three different test cases were chosen that have exact, closed-form solutions. The first example is the creep relaxation of a linear initial stress distribution through a flat plate. Note that in all three examples the plate is assumed to be constrained from bending. We assume, then, that the membrane loads are zero ($N_x = N_y = 0$) and irradiation creep and swelling are not included. In addition, the temperature is assumed to be uniform everywhere. Therefore, the only source of inelastic deformation is thermal creep, which is assumed to be given by

$$\dot{e}^{c}_{eq} = A\ \sigma_{eq}^{4} \tag{105}$$

where

A = creep constant

$$\sigma_{eq} = \sqrt{\sigma_x^2 + \sigma_y^2 - \sigma_x\sigma_y} \quad . \tag{106}$$

Since $\sigma_x = \sigma_y$, it can be shown that the general solution to Eq. (95) is given by

$$\sigma_x(z,t) = \left[\frac{3}{2} \frac{A\ E}{(1-\nu)}\ t + \sigma_x^{-3}\ (z,0) \right]^{-1/3} \qquad (107)$$

where $\sigma_x(z,0) = -Bz$ is the linear initial stress distribution at time = 0. Figure 20 shows a comparison between the exact solution as given by Eq. (107), and the TSTRESS results for the following assumptions: $A = 1.5 \times 10^{-14}$ (KSI-HR)$^{-1}$, B = 47.2 KSI/cm, h = 5 cm, E = 295.8 KSI and $\nu = 0.33$. It can be seen that the agreement is excellent.

Instead, if we choose for this same problem a creep law for irradiation creep of the form

$$\dot{e}_{eq}^{c} = \psi_{irr}\ \sigma_{eq} \qquad (108)$$

we will find that the general solution for the stress history becomes

$$\sigma_x(z,t) = \sigma_x(z,0)\ \exp\left(-\frac{E\psi_{irr}}{2(1-\nu)}t\right). \qquad (109)$$

This assumes, however, that ψ_{irr} is not a function of temperature or time. The behavior of this equation is such that as $t \to \infty$, all of the stresses will relax towards zero. The time constant for the relaxation in this case is given by

$$\tau = \frac{2(1-\nu)}{E\ \psi_{irr}} \qquad (110)$$

For the second test case, consider a linear, steady-state

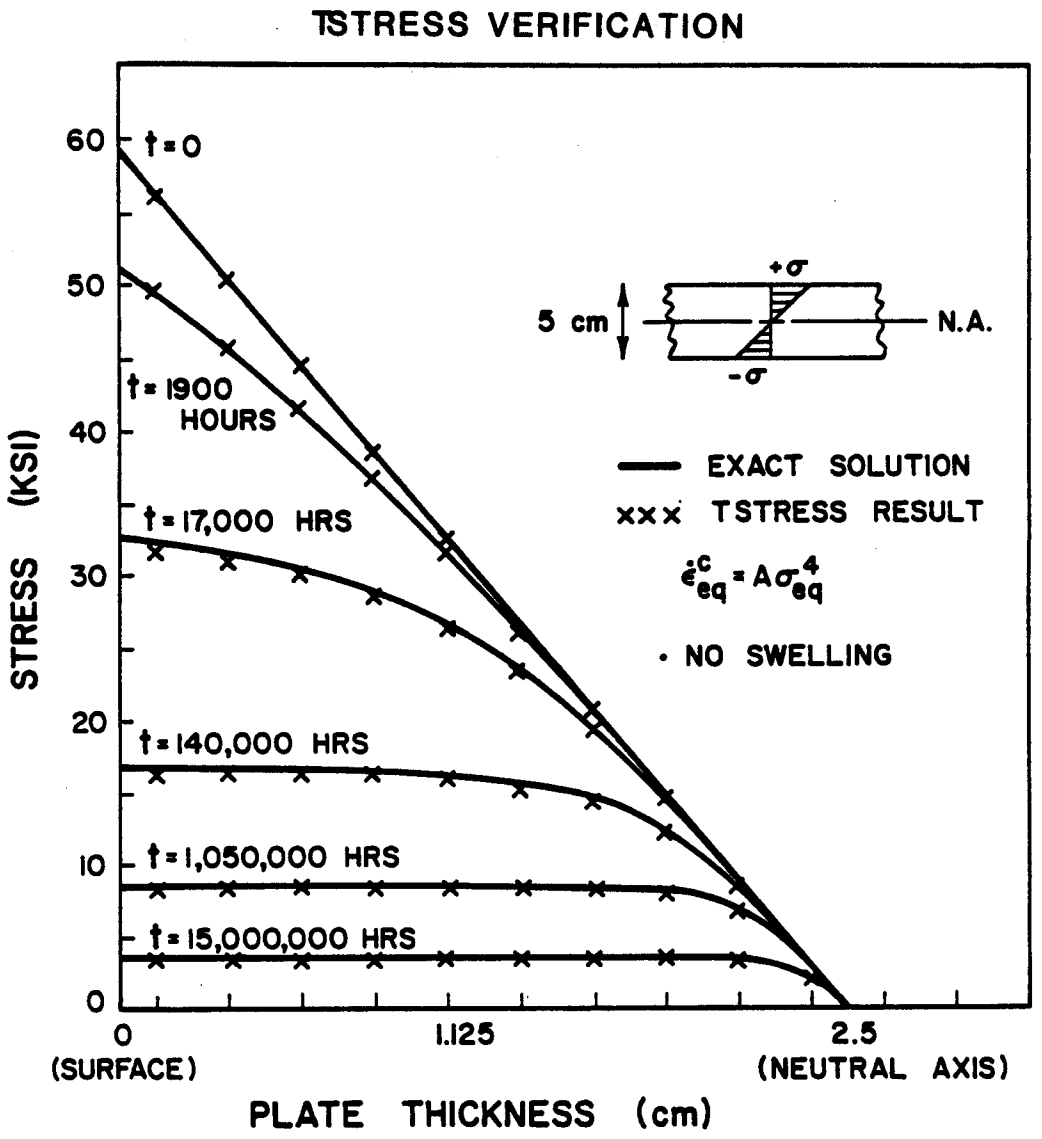

Figure 20. Comparison of TSTRESS predictions with analytical results for the stress relaxation of an initially linear stress distribution through the thickness as caused by creep.

swelling rate, such as

$$\dot{S}(z) = (\dot{S}_{ave} - \dot{S}_{max}) \frac{2z}{h} + \dot{S}_{ave} \tag{111}$$

where $\dot{S}_{max}$ is the swelling rate at the surface and $\dot{S}_{ave}$ is the average swelling rate. If we assume that the temperatures are uniform everywhere and that only irradiation creep is active, then the creep compliance, ψ_o, will be a constant. In this case, the exact solution to the stress history, assuming zero initial stresses, is given by

$$\sigma_x(z,t) = \frac{2}{3} \frac{(\dot{S}_{max}-\dot{S}_{ave})}{\psi_o} \frac{z}{2h} \left[1-\exp\left(-\frac{E\psi_o}{2(1-\nu)}t\right)\right] . \tag{112}$$

This equation along with the TSTRESS results (using 10 zones through the thickness) are plotted in Fig. 21 for the following values: $z = 2.25$ cm, $h = 5$ cm, $E = 4.18 \times 10^4$ KSI, $\nu = 0.33$, $(\dot{S}_{max}-\dot{S}_{ave}) = 1.4 \times 10^{-5}$ $(HR)^{-1}$, and $\psi_o = 9.333 \times 10^{-8}$ $(KSI\text{-}HR)^{-1}$. Again, we find that the agreement between the two solutions is excellent. Note, however, that the average swelling rate does not enter into the solution given by Eq. (112), since the plate element is free to expand and an average amount of swelling should induce no stresses. In this example, the steady-state stresses are given by

$$\sigma_x^{SS}(z) = \frac{2}{3} \frac{(\dot{S}_{max}-\dot{S}_{ave})}{\psi_o} \frac{2z}{h} . \tag{113}$$

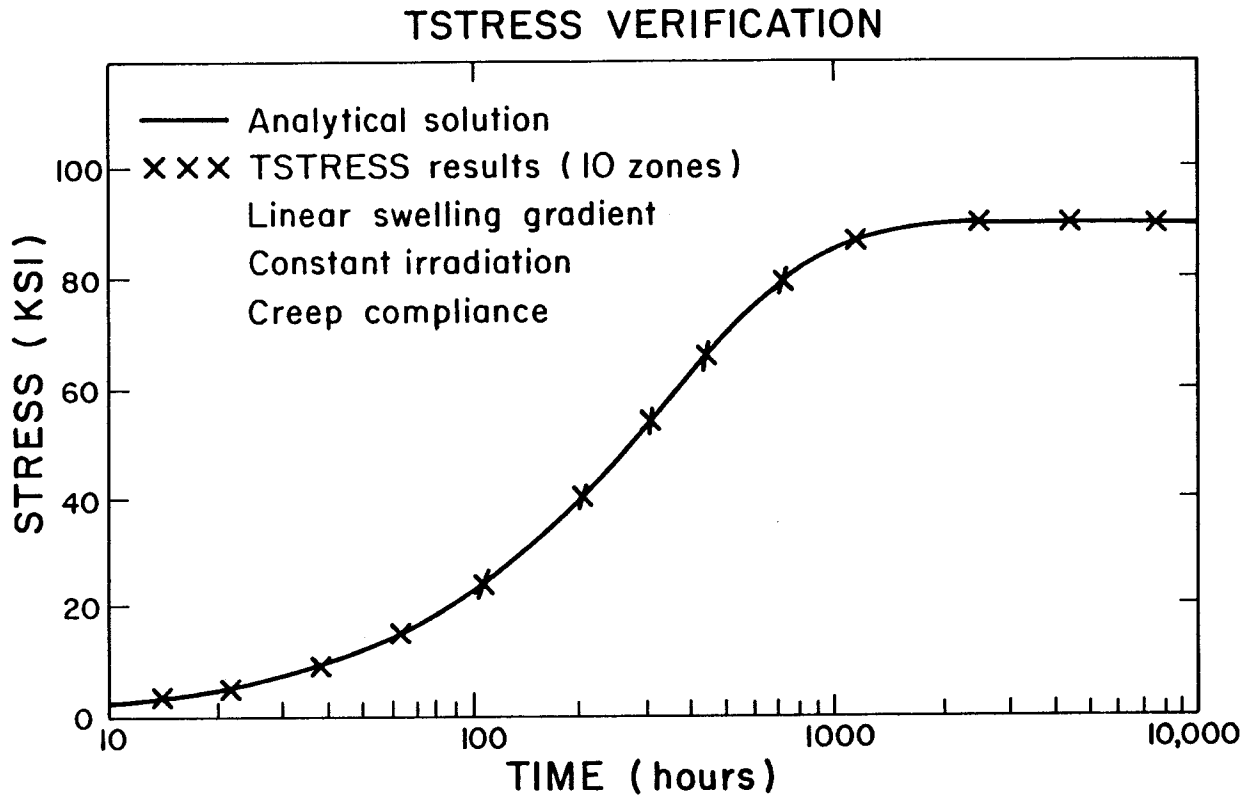

Figure 21. Comparison of TSTRESS predictions with analytical results for the stress redistribution of a thin plate subjected to a linear swelling gradient and constant irradiation creep compliance.

The time constant, τ , which governs the response of this system, is given by

$$\tau = \frac{2(1-\nu)}{E\psi_o} \quad . \tag{114}$$

In this example τ = 343.5 Hours. Note that this equation for the time constant is identical to Eq. (110).

This result can be extended to a more general case where the steady-state swelling rate, $\dot{S}(z)$, is an arbitrary function of depth through the plate. Assuming a constant irradiation creep compliance, ψ_{irr}, it can be shown that the steady-state stresses are given by

$$\sigma_x^{SS}(z) = -\frac{2}{3} \frac{[\dot{S}(z)-\dot{S}_{ave}]}{\psi_{irr}} \tag{115}$$

where $\dot{S}_{ave}$ is the average swelling rate defined by

$$\dot{S}_{ave} = \frac{1}{h} \int_{-h/2}^{h/2} \dot{S}(z)dz \quad . \tag{116}$$

For first wall structures that deform as a flat plate constrained from bending (such as a hemispherical end cap in a cylindrical blanket module), Eq. (115) provides an accurate and convenient estimate of the steady-state stresses. If, however, the irradiation creep compliance varies somewhat with temperature then ψ_{irr} should be replaced by $\overline{\psi}_{irr}$ where

$$\overline{\psi}_{irr} = \frac{1}{h} \int_{-h/2}^{h/2} \psi_{irr}(z)dz \quad . \tag{117}$$

Of course, if thermal creep is large, then Eq. (115) cannot be used at all. Equation (115) also tells us that the steady-state stresses are only a function of the ratio of differential swelling rate, $\Delta\dot{S}$, to the creep compliance, ψ_{irr}. It is also interesting to note that the time constant, τ, is only a function of the elastic properties, E and ν, and the creep compliance ψ_{irr}.

The third test case was used to study the stability of TSTRESS. Here, a linear, sinusoidally-varying swelling rate, $\dot{S}$, given by

$$\dot{S}(z,t) = M_o z\ [1 + A\ \mathrm{Sin}(\omega t)] + C \tag{118}$$

was used where M_o, ω, A, and C are constants. As before, we assume a constant irradiation creep compliance ψ_{irr}. Assuming zero initial stresses the general solution to Eq. (95) is given by

$$\sigma_x(z,t) = G \exp\left[\frac{-E\psi_{irr}}{2(1-\nu)}\, t\right] + g(z) \tag{119}$$

$$+ f(z)\ [a \sin(\omega t) + b \cos(\omega t)]$$

where

$$G = -\frac{2}{3}\ M_o z\left[\frac{AB\omega}{\omega^2 + B^2\psi_{irr}^2} - \frac{1}{\psi_{irr}}\right] \tag{120}$$

$$B = \frac{E}{2(1-\nu)} \tag{121}$$

$$f(z) = \frac{2}{3}\ A\ B\ M_o\ z \tag{122}$$

$$g(z) = -\frac{2}{3}\frac{M_o}{\psi_{irr}} z \tag{123}$$

$$a = -\frac{B\ \psi_{irr}}{\omega^2+B^2\psi_{irr}^2} \tag{124}$$

$$b = \frac{\omega}{\omega^2+B^2\psi_{irr}^2} \tag{125}$$

Figure 22 compares the exact solution given by Eq. (119) with the TSTRESS results for: $M_o = 5.6 \times 10^{-6}$, $\psi_{irr} = 9.333 \times 10^{-8}$, $B = 3.1186 \times 10^{4}$, $\omega = 2\pi/T$, $T = 100$, $z = 2.0$, $h = 5$, $A = 1$ (note: units are in KSI, cm, hours). It can be seen that even for only five zones through the thickness, the TSTRESS results are very accurate. While this example has no particular application to fusion reactors, it, nevertheless, allowed the time-step selection criteria to be "fine-tuned" so as to prevent undesirable numerical oscillations, which appeared in the early development of the code.

Applications: Tokamak First Wall Stress History

To demonstrate the capabilities of TSTRESS, and to illustrate some of the synergistic effects which can occur in a fusion environment, a specific design of a first wall component was chosen to perform a detailed inelastic analysis of the stress variations through the thickness. The Westinghouse cylindrica blanket module with hemispherical end cap [147], shown in Fig. 1, was chosen because

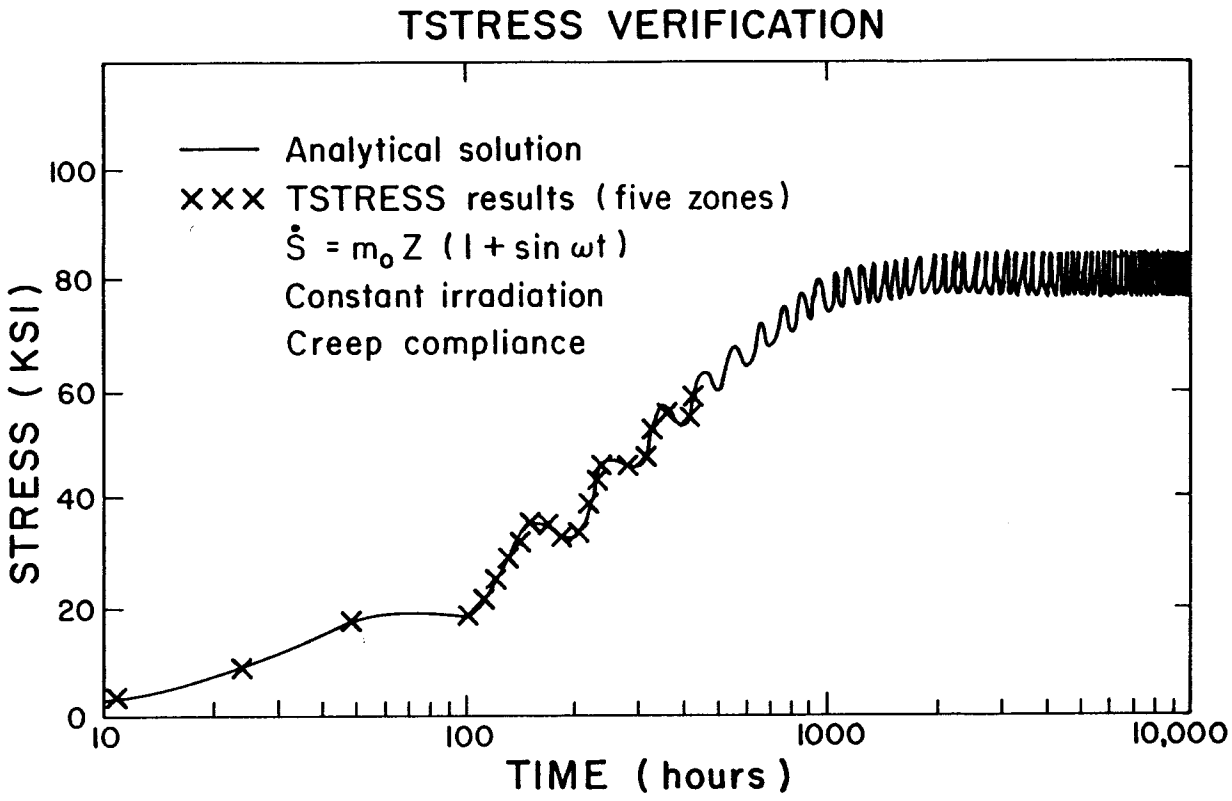

Figure 22. Comparison of TSTRESS predictions with analytical results for the stress redistribution of a thin plate subjected to a sinusoidally varying swelling rate and constant irradiation creep compliance.

a detailed 3-D global structural analysis was not required in order to compute the membrane loads N_x and N_y. Instead, they are simply given by

$$N_x = N_y = \frac{PR}{2} \tag{126}$$

where P is the coolant pressure and R is the radius of curvature of the end closure. Because the entire hemispherically shaped first wall is free to expand outward without constraint, this allows us to accurately model the tip region as a flat plate constrained from bending but free to expand.

We shall neglect any bending stresses caused by the meridional variations in either temperature or swelling. Two observations support this assumption. First, although the temperature difference from the tip to the junction with the cylinder can be as large as 200°C [144], the temperature gradient is much smaller than through the thickness because of the greater distance involved. Secondly, since the entire hemispherical cap is free to expand radially, bending stresses from meridional variations should be small, unlike the bending stresses caused by self-constraint of the inelastic strains through the thickness.

Since, for this example, a global structural analysis is not required to study the detailed behavior of the tip region (assuming that this is the critical location of interest), TSTRESS can then be used to investigate the generic effects of different variables on the long-term stress history. These effects are qualitatively expected to be the same for any other first wall design, rather than

being design-dependent. Specifically, we have studied the impact of coolant temperature, wall thickness, and surface wall erosion on the long-term stress history of the tip region of the cylindrical blanket module. We shall begin, however, with an analysis using only the reference design parameters as listed in Table 7.

Reference Design Stress History

Figure 23 shows the initial stress distribution through the thickness for the 6 mm thick reference wall calculated by TSTRESS using ten zones through the thickness. When the plasma is off for refueling (plasma-off), the only stress present is that due to the internal coolant pressure. However, when the plasma is burning (plasma-on), the constant surface heat flux produces a linear temperature gradient through the wall resulting in 350°C on the backside (e.g. coolant side) and 520°C on the plasma side. Since the hotter side expands more than the cooler side, the plasma side of the wall is put into compression with a stress at the surface equal to -48 ksi (-331 MPa). On the coolant side a large tensile stress of 63 ksi (434 MPa) is developed. Since thermal stresses are self-equilibrating, the integral over the stresses through the thickness must equal the membrane load in that direction, as indeed it does in this example.

Figure 24 shows the long-term stress history for the reference design and plasma-on conditions. The structural response is characterized by three distinct regimes of behavior. During the first year of operation irradiation creep relaxes the stresses towards a limiting value equal to the membrane (hoop) stress. Then, at about

Table 7. Reference Design Parameters

- Tokamak power reactor
- Cylindrical blanket module, 80 cm long
- Hemispherical end cap, 10 cm diameter
- 316 stainless steel structure, 6 mm thick
- Neutron wall loading = 2 MW/m^2
- Surface heat flux = 50 W/cm^2
- Nuclear heating rate = 20 W/cm^3
- Backside wall temperature = 350°C
- Displacement damage rate = 22 dpa/yr
- Helium gas coolant at 1000 psi (6.9 MPa)
- Burn time = 19 minutes
- Refueling time = 1 minute
- On/Off cycles in 30 years = 788,400
- Availability = 100%
- No surface wall erosion
- Initial flaw depth = 1 mm
- Initial flaw aspect ratio = 1.0

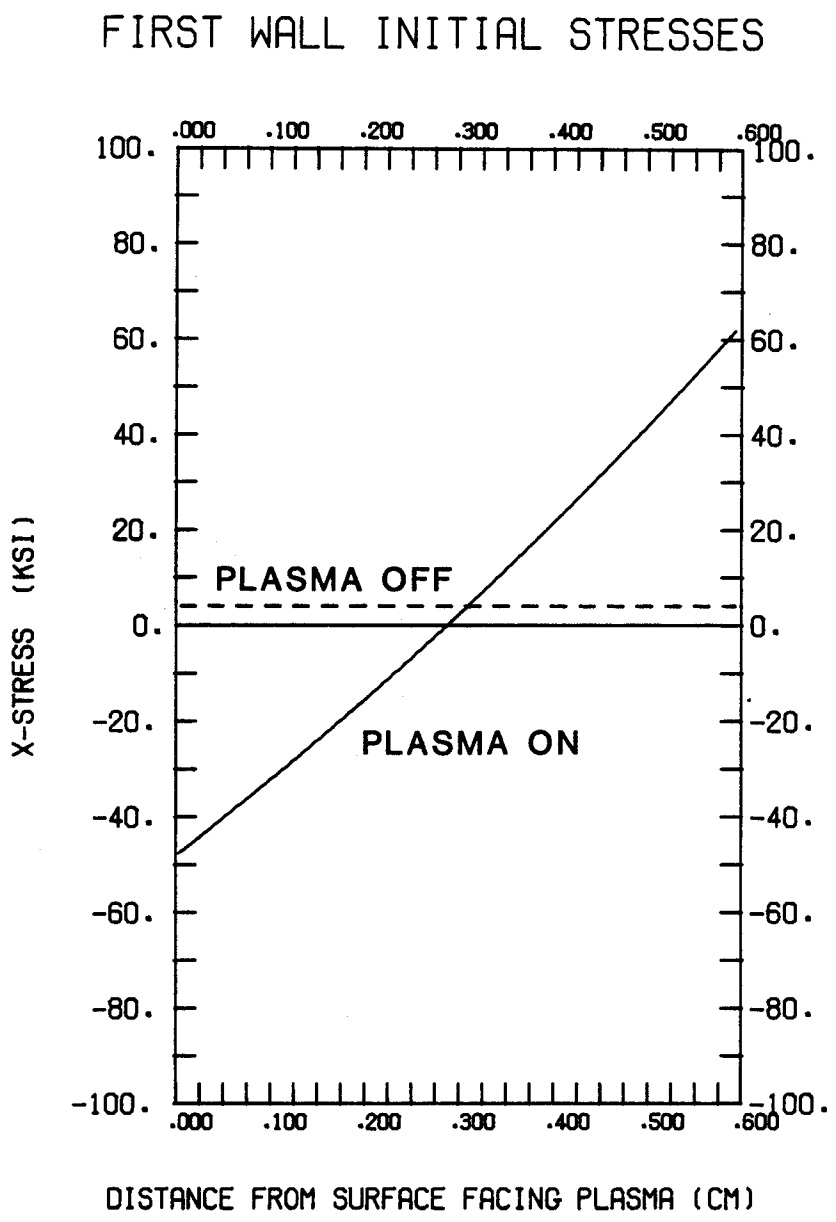

Figure 23. Initial stress distribution through the thickness for the reference design.

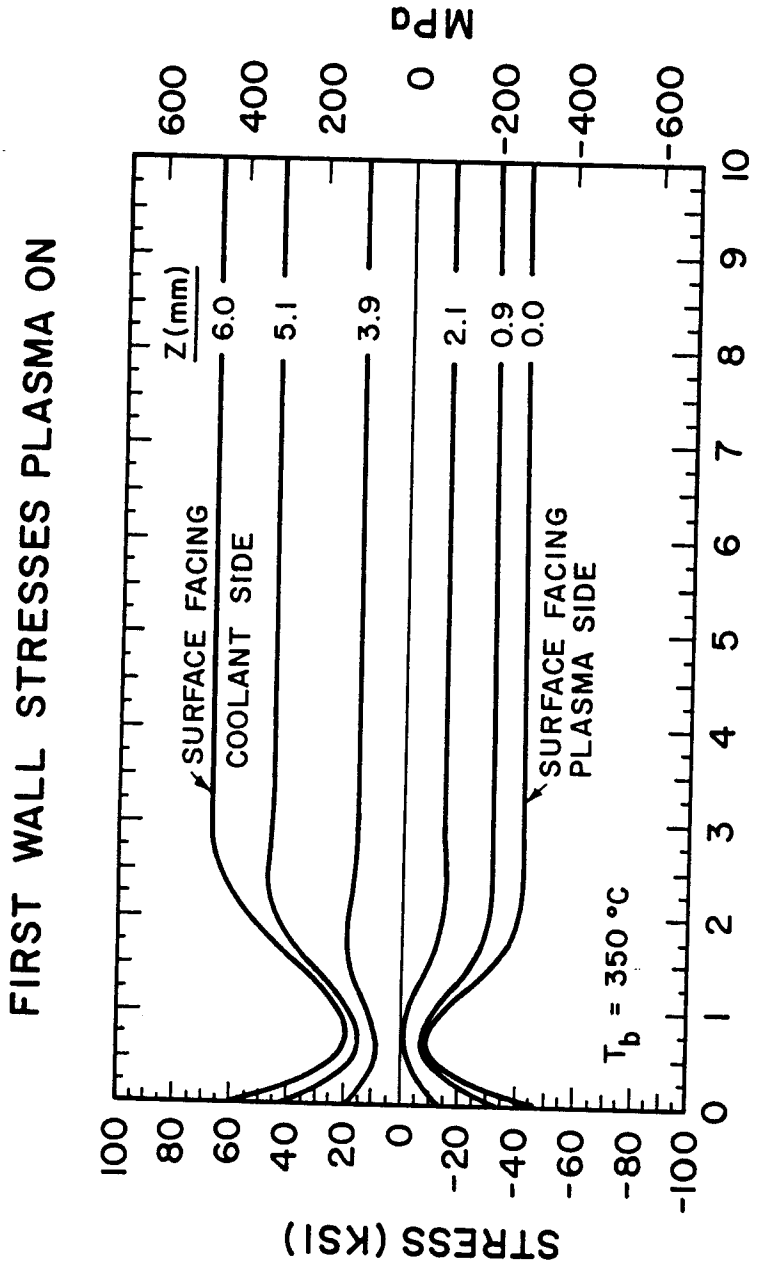

Figure 24. Stress history for the reference design during plasma-on conditions.

one year (22 dpa) the incubation dose for swelling is reached and differential swelling starts to redistribute the stresses for the next 1-2 years. Finally, after roughly three years (66 dpa), we see that a pseudo steady-state is reached where a dynamic balance exists between the buildup of stresses due to swelling and the simultaneous relaxation due to irradiation creep. We use the term "pseudo" as a reminder that the stresses actually cycle elastically between a maximum and minimum value during each plasma on-off cycle.

Figure 25 shows the stress history for plasma-off conditions. Again, three regimes are evident. First, we see an immediate buildup of residual stresses during the first year which is caused by stress relaxation during the burn-time. Note that the plasma-off stresses are calculated simply by subtracting the initial thermo-elastic stress distribution from the current value of the plasma-on stresses. The residual stresses reach a maximum of 44 ksi (303 MPa) on the plasma side at around six months. At this time, swelling turns on and begins to reduce the residual stresses, eventually producing a steady-state distribution after three years.

Figure 26 plots the steady-state stress distribution through the thickness for the reference design. It can be seen that these values are remarkably similar to the initial stresses in Fig. 23. This can be explained by remembering that the saturation stresses are proportional to the ratio of the differential swelling rate to the creep compliance at a specific location (see Eq. (115)). According to Fig. 27 the creep compliance is essentially constant for the

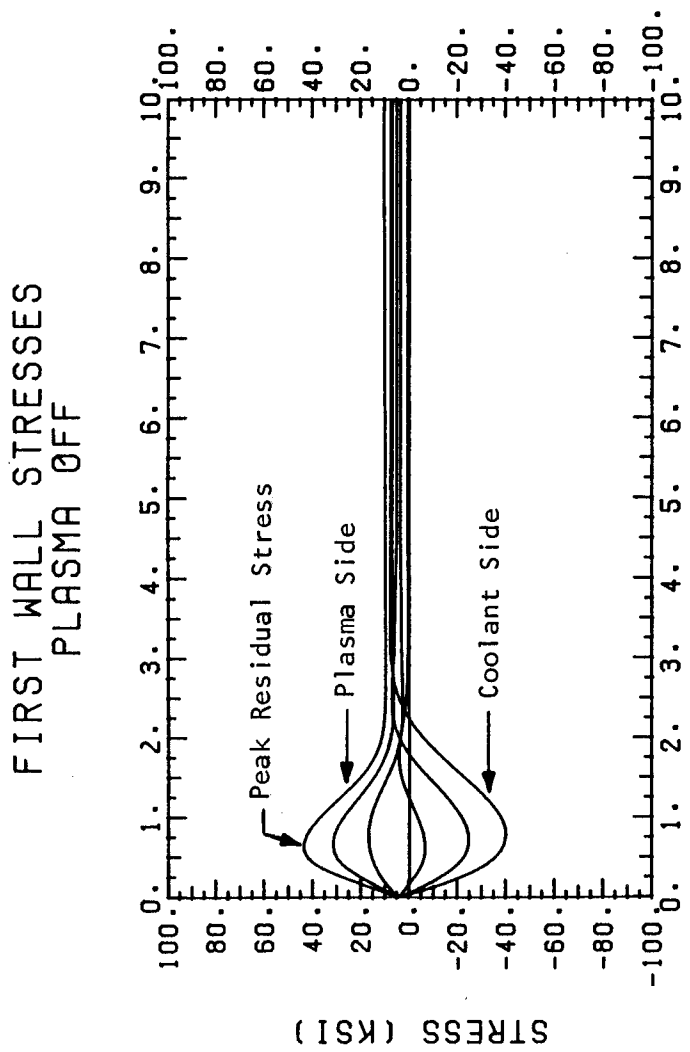

Figure 25. Stress history for the reference design during plasma-off conditions.

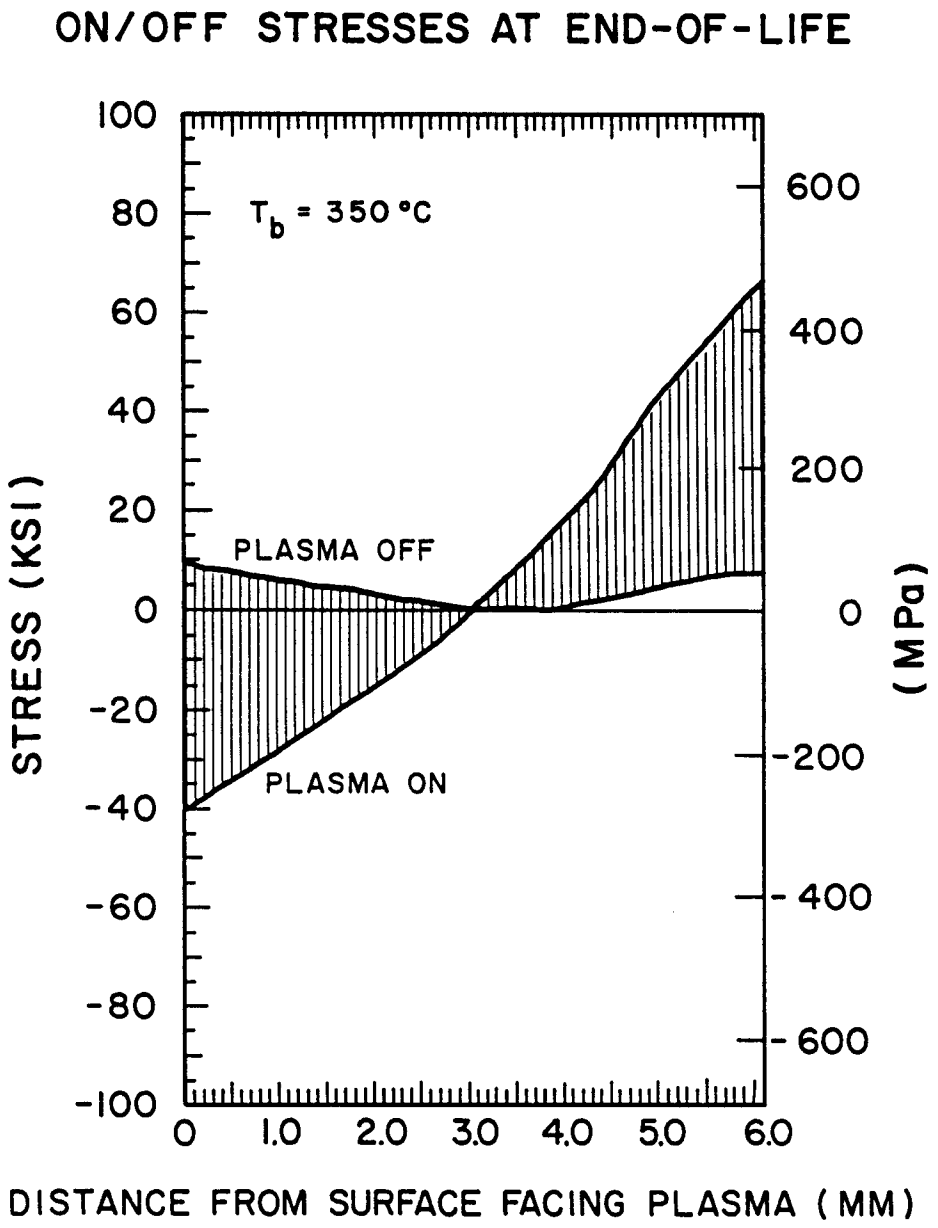

Figure 26. Steady-state stress distribution through the thickness for the reference design. The shaded region indicates the cycling of stress between plasma-on and plasma-off conditions.

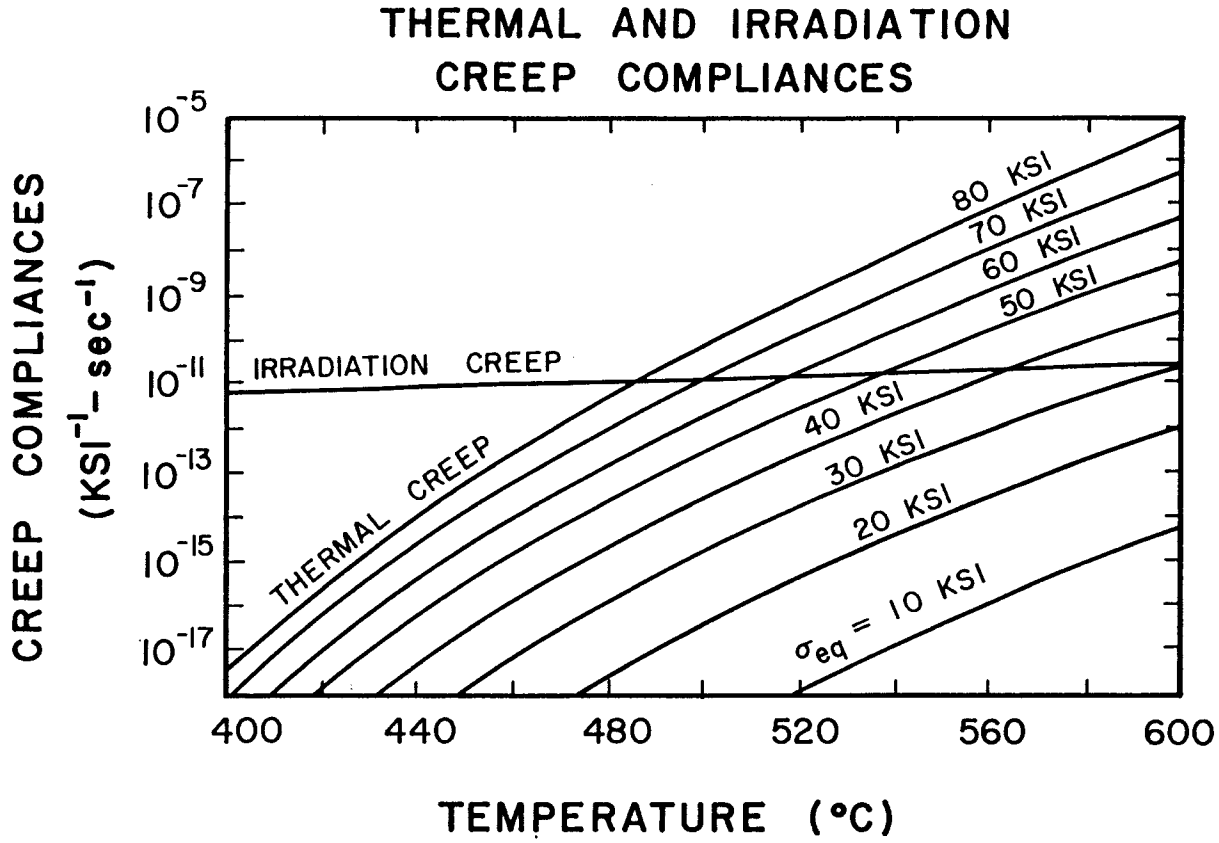

Figure 27. Temperature dependence of the thermal and irradiation creep compliances for 316 stainless steel, for different values of the equivalent stress.

range of interest. However, the steady-state swelling rate is very sensitive to temperature, as can be seen from Figure 18. Therefore, over the temperature range of 350°C to 520°C, the saturation stress, $\sigma_{SS} \sim \dot{S}/\psi$, should vary roughly in a linear fashion. Since the hotter side swells at a faster rate than the cooler side, the plasma side should be placed in compression, which is indeed predicted by TSTRESS in Fig. 26. The fact that the magnitudes of these stresses (-40 ksi @ z = 0 and + 67 ksi @ z = 6 mm) are almost identical to the initial stresses (-48 and + 63 ksi) is only an artifact of the particular average wall temperature used in this example (435°C). There is no direct relationship between the initial and final stress distributions, as will be demonstrated in the next section.

Since the stresses redistribute gradually over a period of years, typically, this is expected to have a significant effect on crack propagation. Although this is discussed in more detail in Chapter 8, we can use Figs. 28 and 29 to identify the controlling factors. To indicate the fatigue cycling, each figure plots the stresses at the surface for plasma-on and plasma-off conditions. First, we observe that the mean stress, $\sigma_{mean} = (\sigma_{on} + \sigma_{off})/2$, varies with time like the other stresses. This affects fatigue crack growth via the R-ratio. Secondly, the cyclic stress, $\Delta\sigma = \sigma_{on} - \sigma_{off}$, remains unchanged for the entire time. Actually, we would not expect $\Delta\sigma$ to change because it equals the thermoelastic component of the total stress (assuming no wall erosion). Other than the mean stress effect, we would expect no effect on crack growth due to the stress redistribution. As it turns out, mean stresses do play an important role.

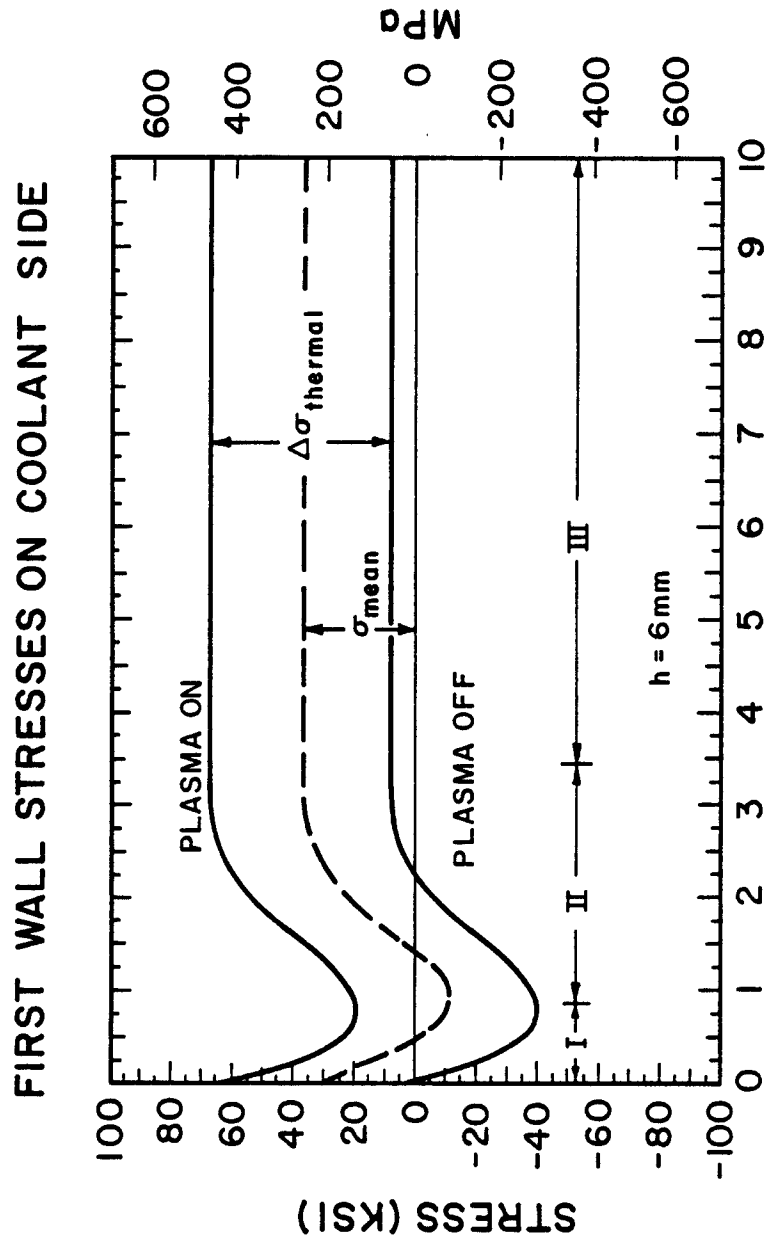

Figure 28. Stress history of plasma-on and off stresses on the coolant side of the reference design.

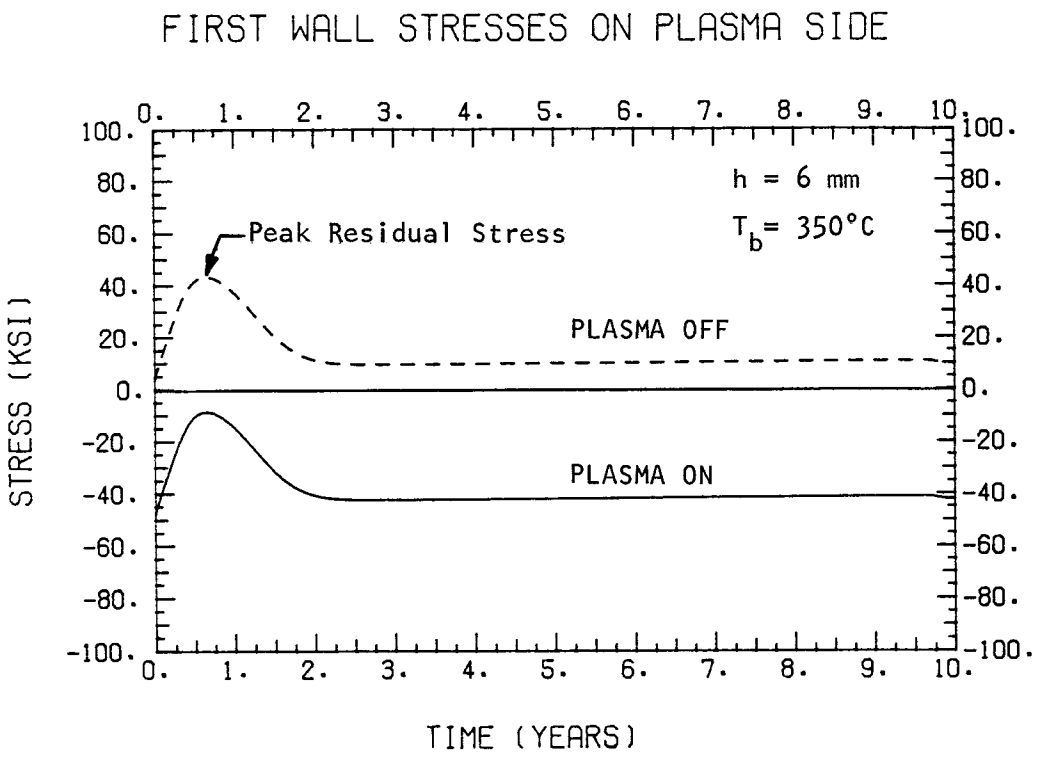

Figure 29. Stress history of plasma-on and off stresses on the plasma side of the reference design.

Figure 14 shows some results of a 2-D inelastic stress analysis of the UWMAK-I U-bend blanket module first wall performed by Cramer [12] with ANSYS. Plotted are the plasma-on stresses on the plasma side for various neutron wall loadings and a wall thickness of 2.5 mm. Cramer's results for a neutron wall loading of 2.5 MW/m^2 compare favorably with the TSTRESS calculations although the conditions are different (P_{NW} = 2 MW/m^2 and h = 6 mm for the TSTRESS analysis).

Effect of Coolant Temperature

In this section, we investigate the effect of varying the coolant temperature, T_c, from 100°C to 500°C (reference value = 350°C) on the long-term stress history of the reference design. Since none of the other parameters are changed, an increase in the coolant temperature will also increase the average wall temperature while having only a slight effect on the temperature drop across the wall. Furthermore, we make the simplifying assumption that the heat transfer coefficient is sufficiently large so that the backside (coolant side) wall temperature, T_b, is approximately equal to the coolant temperature. 400°C is probably the highest coolant temperature one would use for 316 SS in order to keep the maximum structure temperature below 600°C. However, T_c = 500°C is included to illustrate the wide range of effects.

Figures 30 and 31 show the effect of increasing the backside temperature from 100°C to 500°C, for stresses on the plasma side. We see that for low temperatures (100°C) minimal swelling is experienced and irradiation creep dominates the response. At inter-

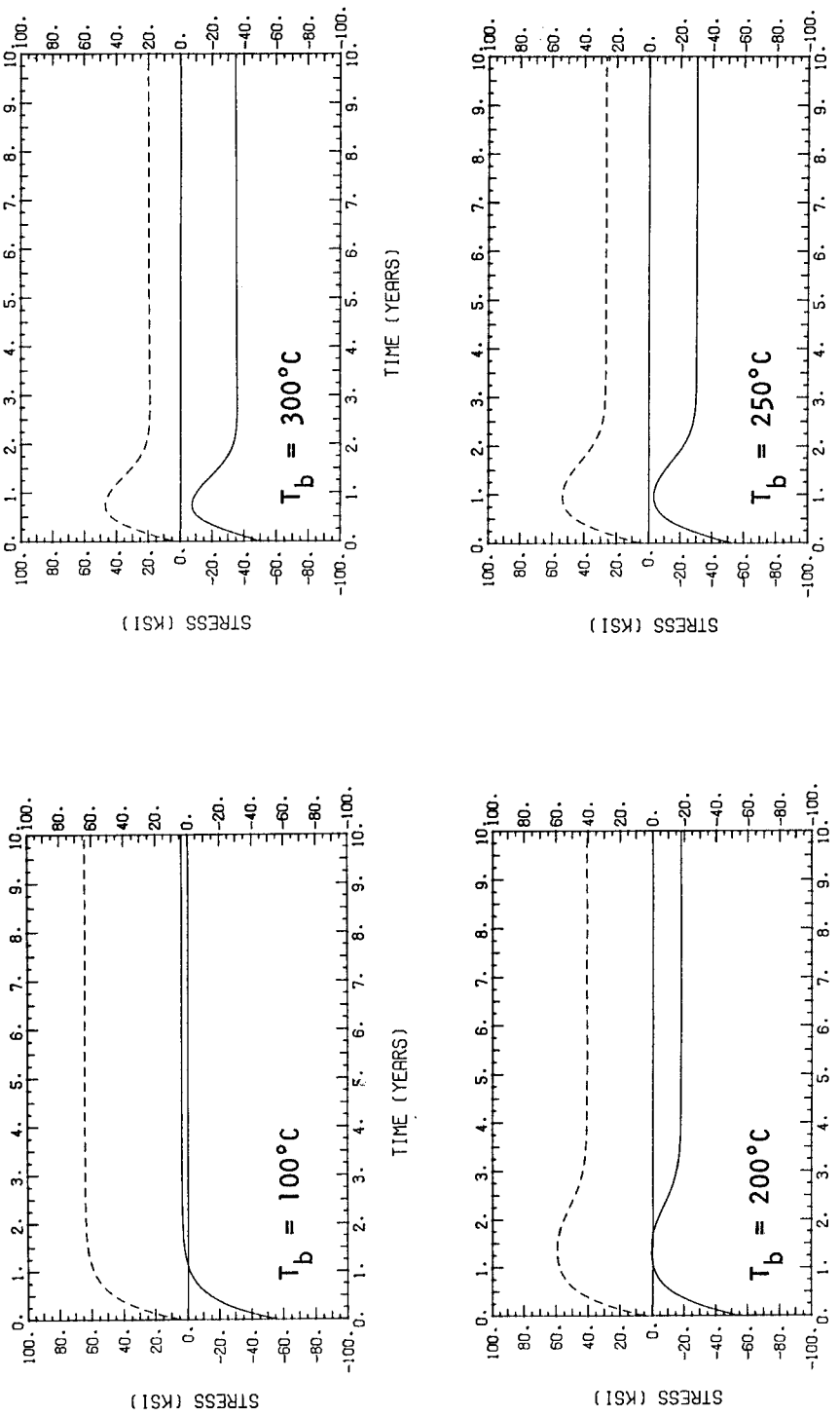

Figure 30. Stress history of plasma-on and off stresses on the plasma side for various backside wall temperatures. The wall thickness equals 6 mm unless otherwise stated.

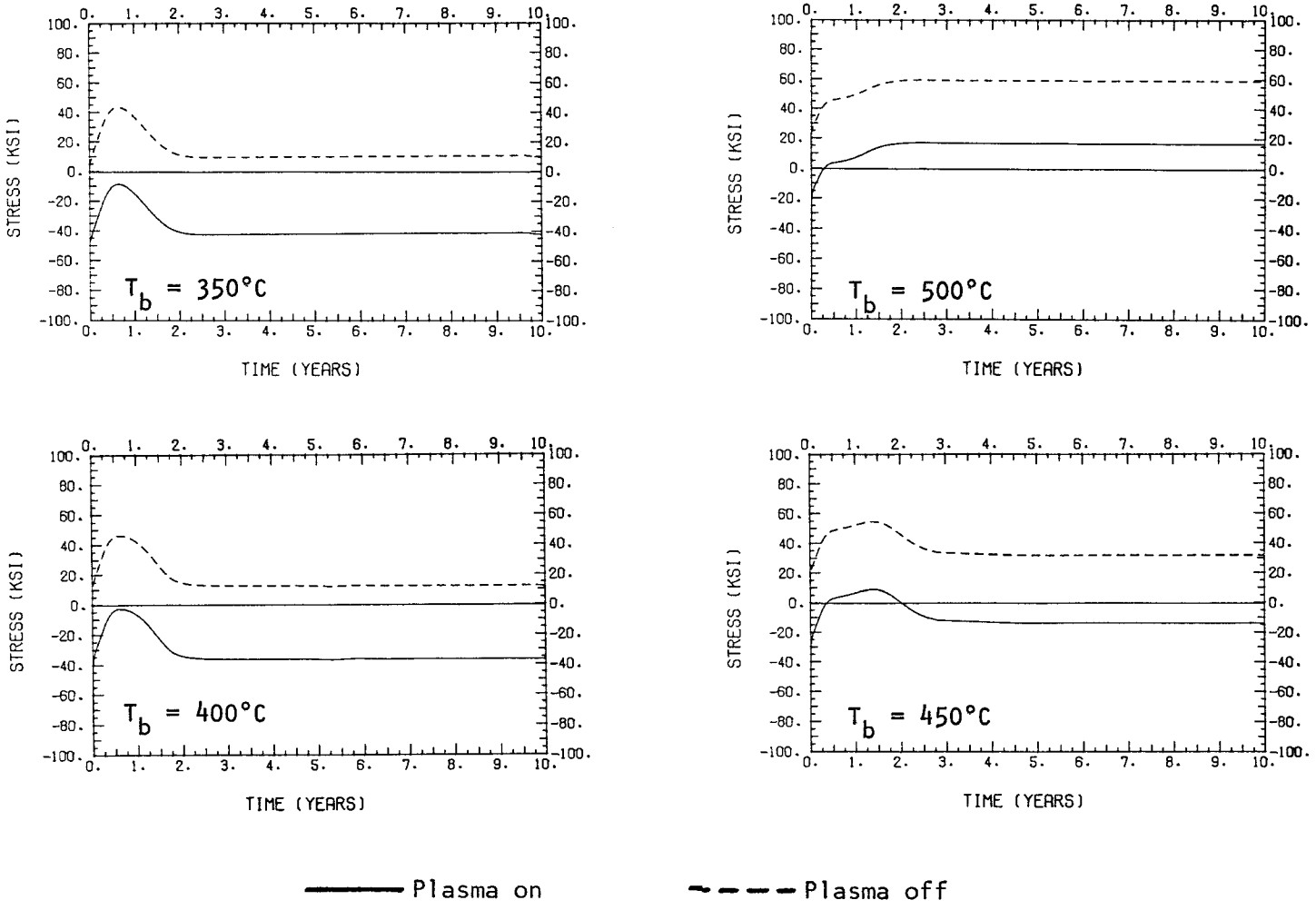

Figure 31. Stress history of plasma-on and off stresses on the plasma side for various backside wall temperatures.

mediate temperatures (350°C) a pronounced peak in the plasma-off curve appears at about one year (20 dpa). Finally, at the higher temperatures (500°C) the behavior resembles the low temperature case because swelling is low in this range. Figure 32 shows a composite plot of the steady-state stress on the plasma side for the eight different temperatures. The shape of these two curves is a function of the temperature dependence of swelling. We see that the largest tensile stresses occur at T_b = 100°C and T_b = 500°C, during the plasma refueling period. It is interesting to note in this figure that the somewhat arbitrary choice of T_b = 350°C as the reference case resulted in the situation where the initial and final stresses are nearly identical.

A general trend that can be observed in Figs. 30 and 31 is that the steady-state stresses on the plasma side during plasma-off conditions are always lower than or equal to the intermediate values in stage II (6 months to 1.5 years). Figure 33 summarizes this effect. The "peak residual stress" can be a large number (in this example 45-65 ksi), and it is only slightly dependent on the backside temperature. This is because swelling does not contribute to the peak residual stress, only stress relaxation by irradiation creep (which is weakly temperature dependent). It is precisely this stress which has been identified by previous investigators as causing early failure in first wall components (see Cramer [12], Wolfer [135]).

Figures 34 and 35 plot the history of stresses on the coolant side for eight different T_b. Of interest are the steady-state stresses, which are summarized in Fig. 36. We can see that at low temperatures

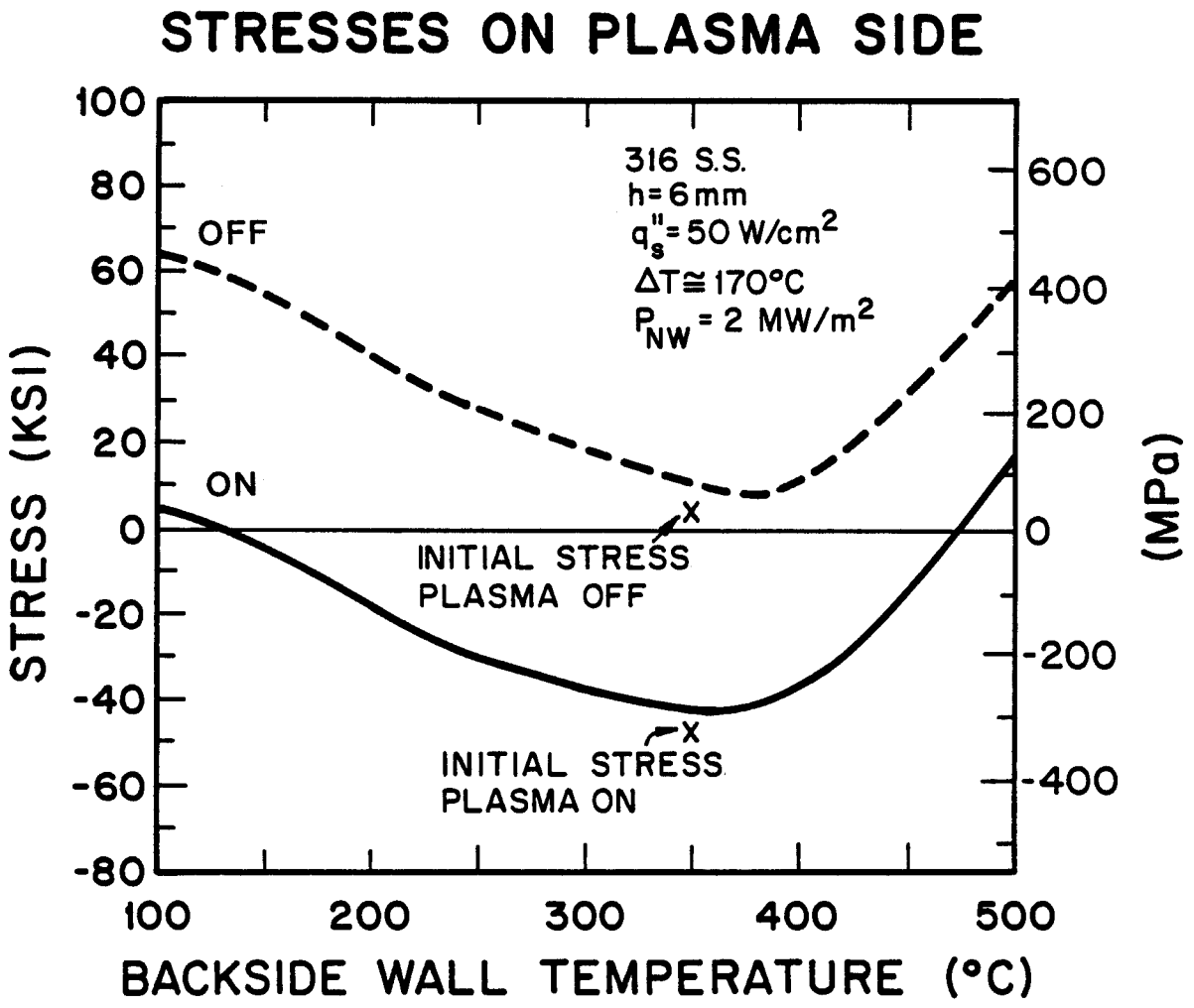

Figure 32. Steady-state stresses on the plasma side for plasma-on and off conditions plotted as a function of the backside wall temperature.

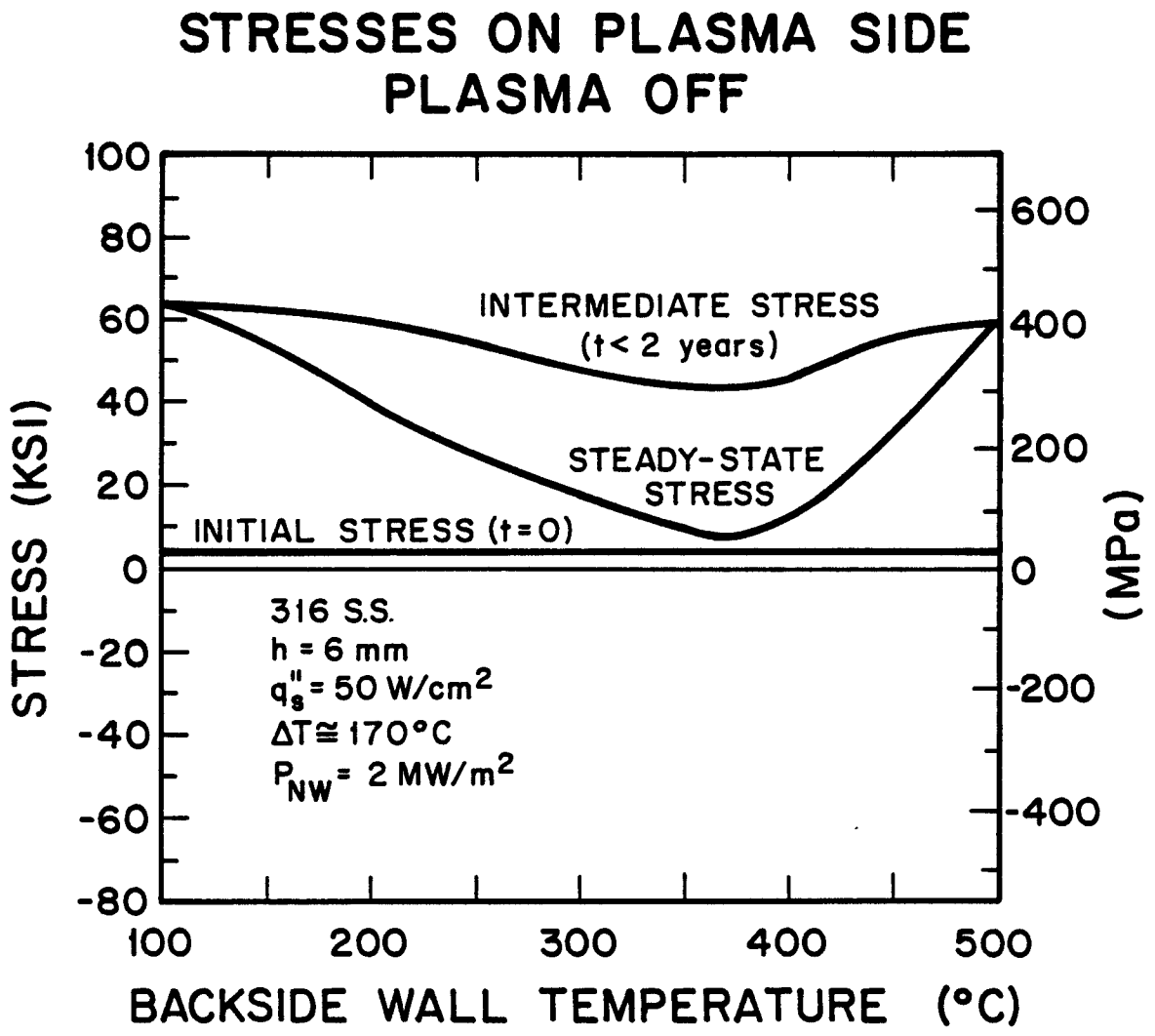

Figure 33. Plasma off stresses on the plasma side plotted as a function of the backside wall temperature for three different times: at t = 0, t < 2 years, and at steady state. The curve labelled "intermediate stress" is also defined as the "peak residual stress" in the text.

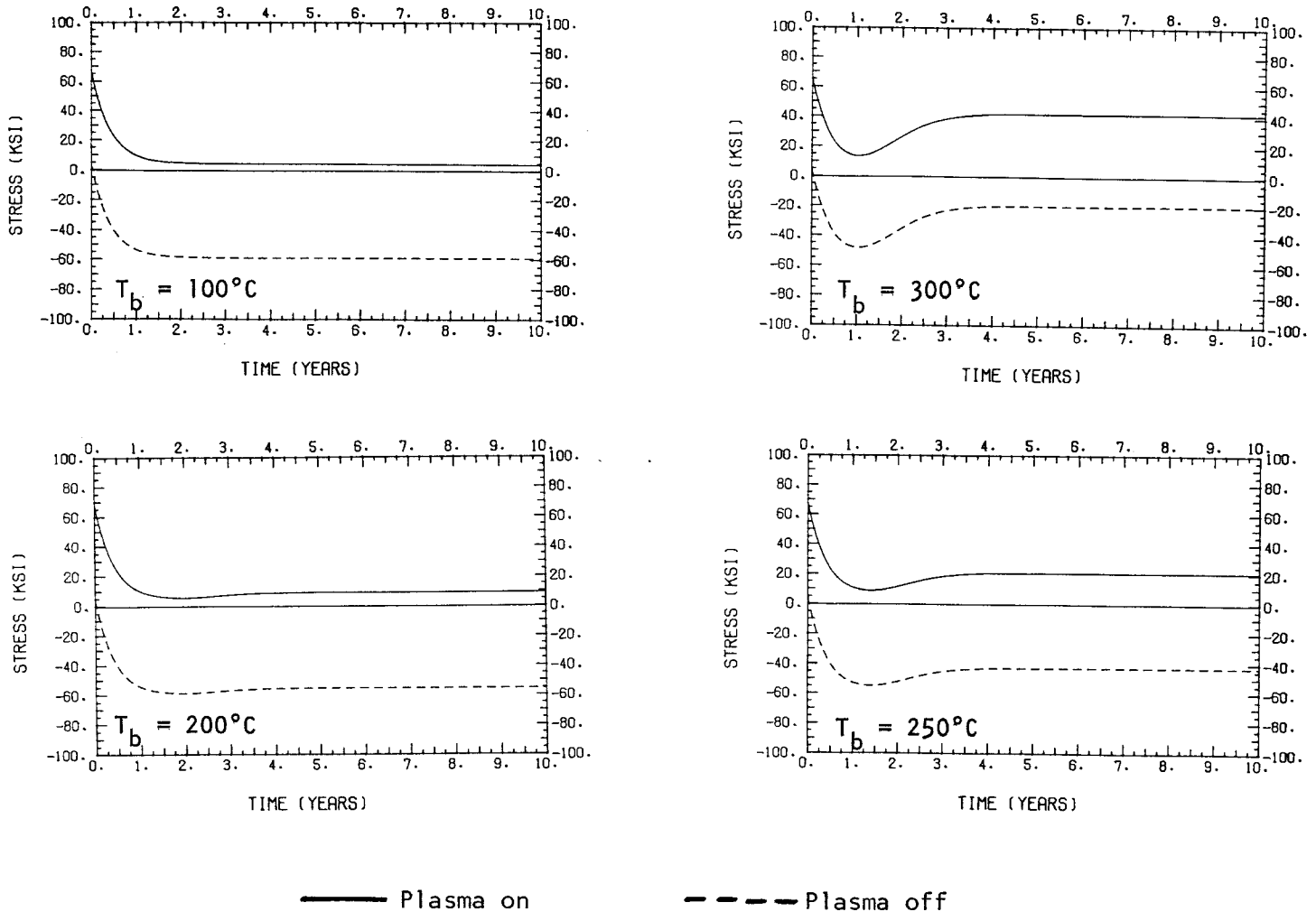

Figure 34. Stress history of plasma-on and off stresses on the coolant side for various backside wall temperatures.

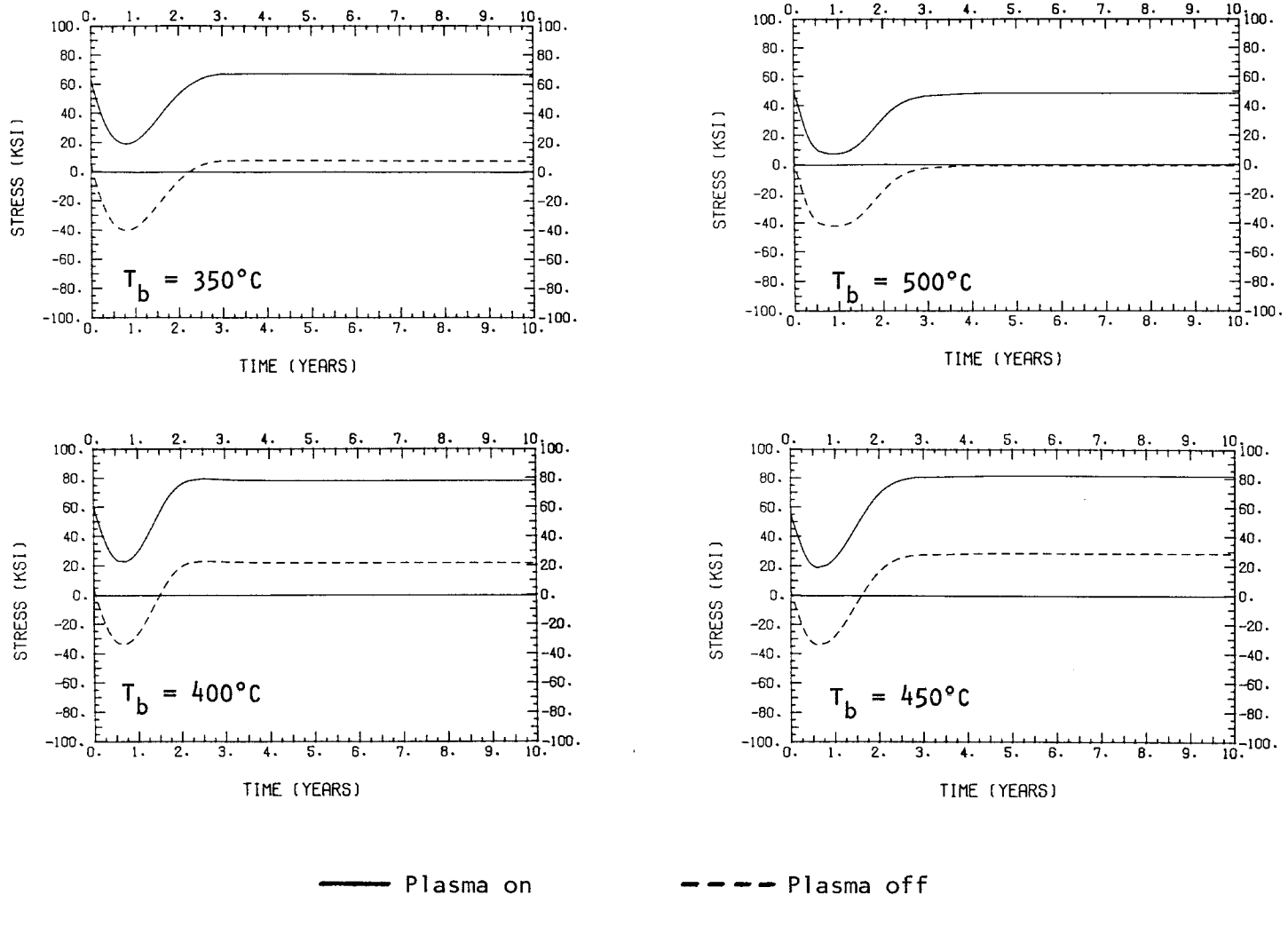

Figure 35. Stress history of plasma-on and off stresses on the coolant side for various backside wall temperatures.

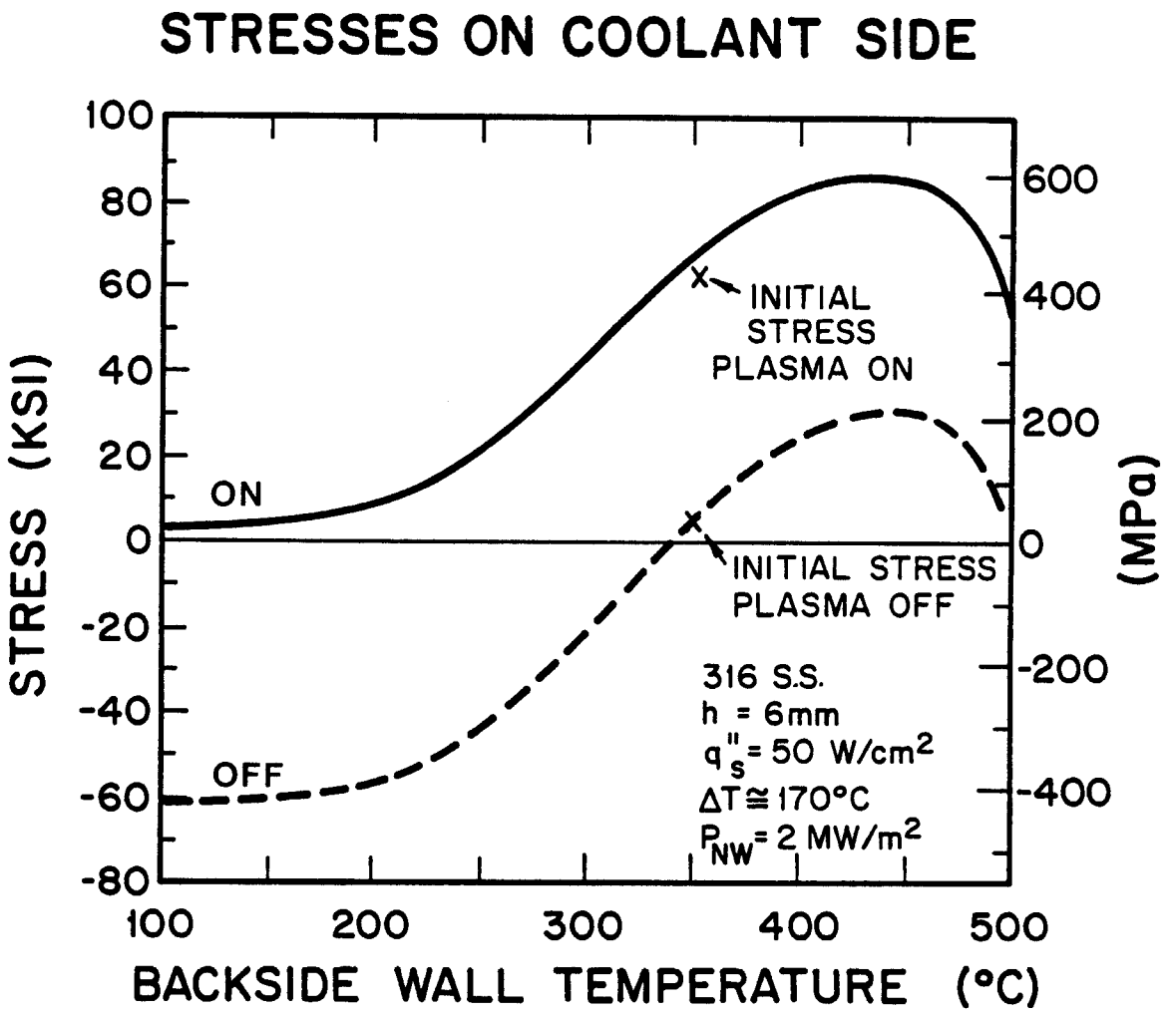

Figure 36. Steady-state stresses on the coolant side for plasma-on and off conditions plotted as a function of the backside wall temperature.

the steady-state stresses are small, or even negative. However, at higher temperatures, 350-500°C, these stresses can be quite large (e.g. 82 ksi at T_b = 450°C). As before, this is related to the temperature dependence of swelling. Again, we see that at T_b = 350°C the initial and final stresses are nearly identical, which is only a coincidence.

Qualitatively, what can we say about the effect of these different stress histories on lifetime? The answer depends on the expected design life. If the component is short-lived, e.g. less than two years, then the transient response and peak residual stress which appears upon shutdown (plasma-off) are very important. On the other hand, if the design is a long-lived component, then only the state-state stresses are of importance, and the transient behavior may be neglected.

Although this is discussed more in Chapter 8, it is instructive to plot the stress distribution through the thickness for the eight temperatures in order to identify the most likely side where cracks would grow. This is done in Figs. 37 and 38. The side with the maximum tensile mean stress will have the fastest crack growth. For example, at low average wall temperatures, the critical side is on the plasma side. However at high temperatures (T_b > 300°C) this shifts over to the coolant side. Consequently, at T_b = 250°C there is no clear preference for a critical side based on stress arguments only. Figure 39 indicates that a temperature of T_b = 270°C (average wall temperature = 360°C) is ideal because the mean stresses on either side are equal to each other, which maximizes lifetime (for 316 S.S.).

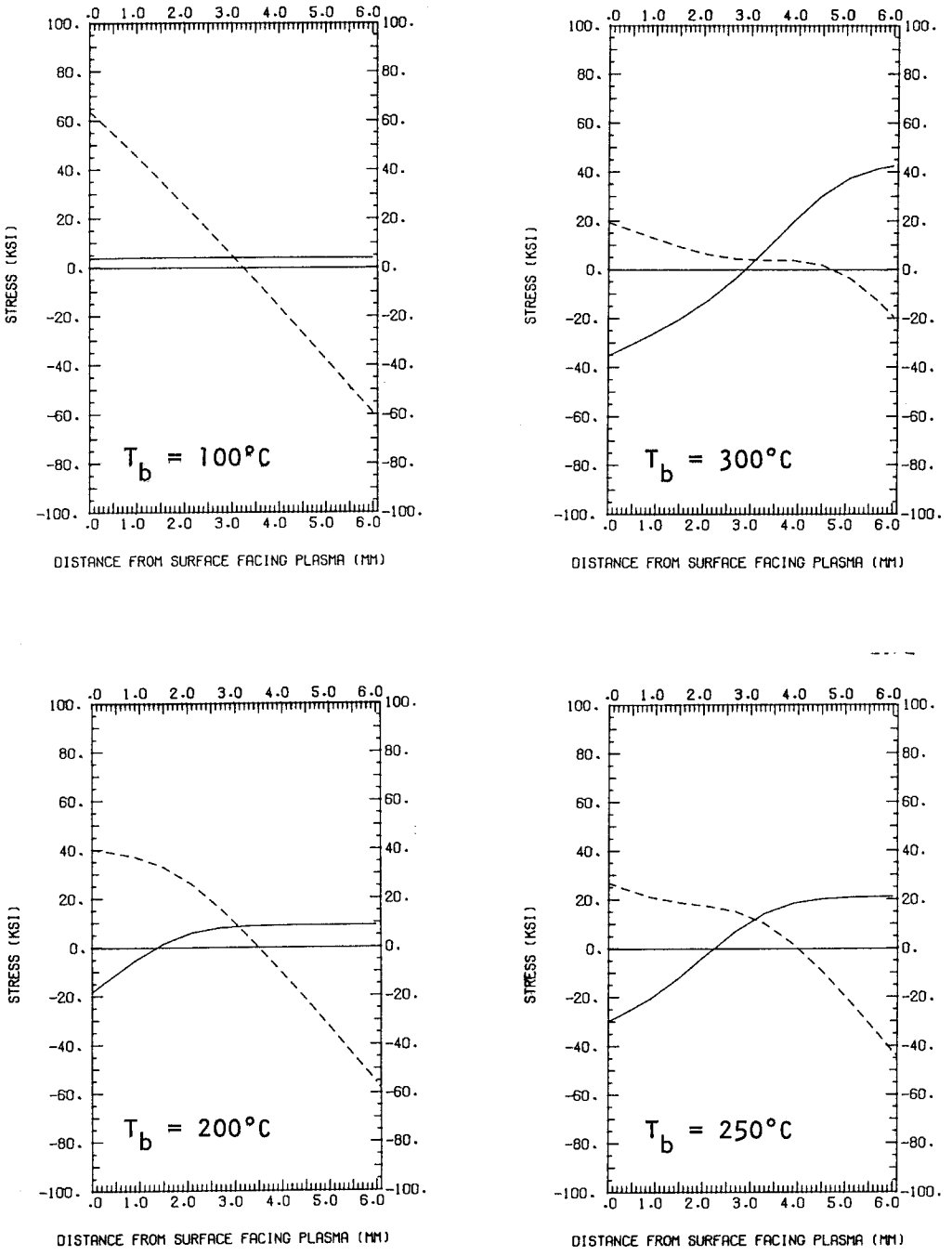

Figure 37. Steady-state stress distribution through the wall for plasma-on and off conditions for different wall thicknesses.

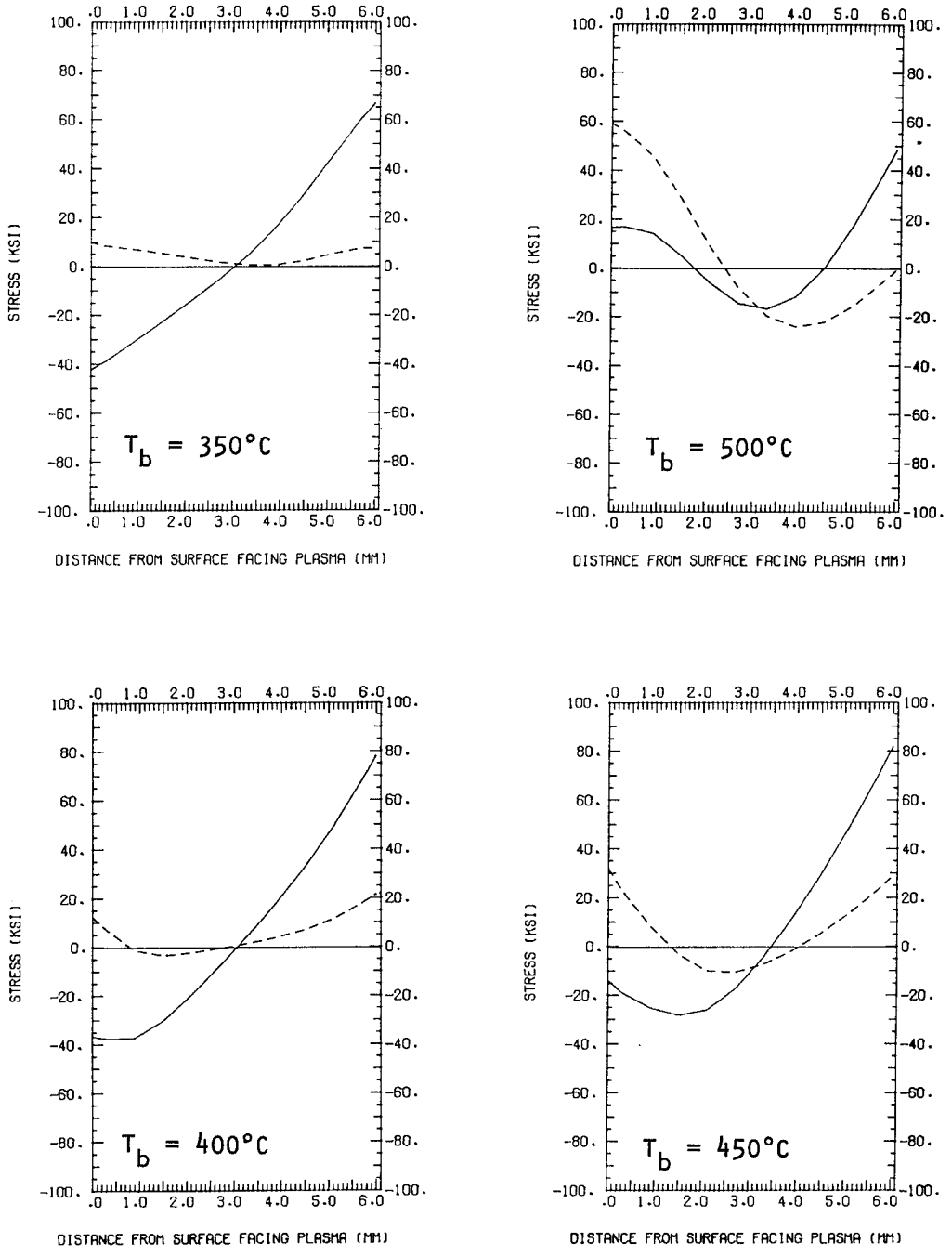

Figure 38. Steady-state stress distribution through the wall for plasma-on and off conditions for h = 6 mm and various backside wall temperatures.

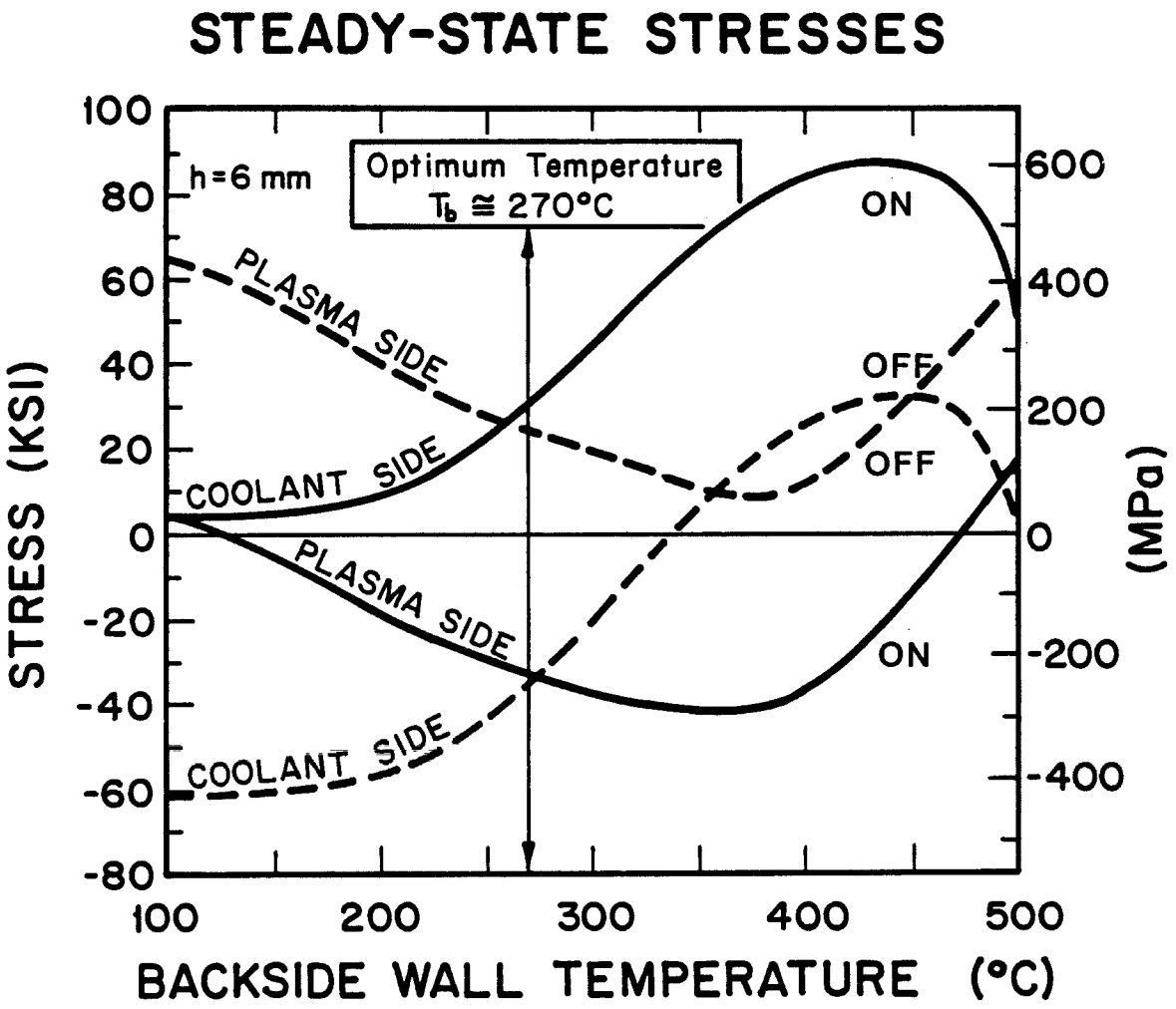

Figure 39. Comparison of steady-state stresses on either the plasma or coolant side, for plasma-on and off conditions, and for different backside wall temperatures. T_b = 270°C is the temperature at which the steady-state mean stresses on either side of the wall equal each other.

Effect of Wall Thickness

In the next series of plots we hold the back wall temperature constant at T_b = 350°C and vary the wall thickness from 2 to 10 mm. It will be shown later in Chapter 8 that changes in the thickness have a major impact on the lifetime. This is primarily due to the increase in the temperature drop across the plate, ΔT, which also causes the thermal stresses to increase in magnitude, as shown in Fig. 40 (remember that the surface heat flux is held constant at $q_s'' = 50\ w/cm^2$, hence $\Delta T/h \cong$ constant). Figures 41 to 42 show the stress histories predicted by TSTRESS for plasma-on and off conditions. We can make the following observations. As the wall thickness increases

1. the steady-state stresses increase,
2. the initial and final stresses are nearly identical,
3. the peak residual stress increases, and
4. the time to reach peak residual stress decreases from 1 year to 6 months as h increases from 2 mm to 8 mm.

Each of these points can be explained by considering the temperature drop, ΔT, across the plate. The first observation results from an increase in the swelling rate difference, $\Delta \dot{S}$, across the plate as ΔT increases. The second observation is an artifact of the particular choice for T_b, namely 350°C. Observation 3 arises from the higher initial compressive thermal stress on the plasma side which then relaxes due to irradiation creep and, hence, appears as a tensile stress upon shutdown. Finally, the last observation is related

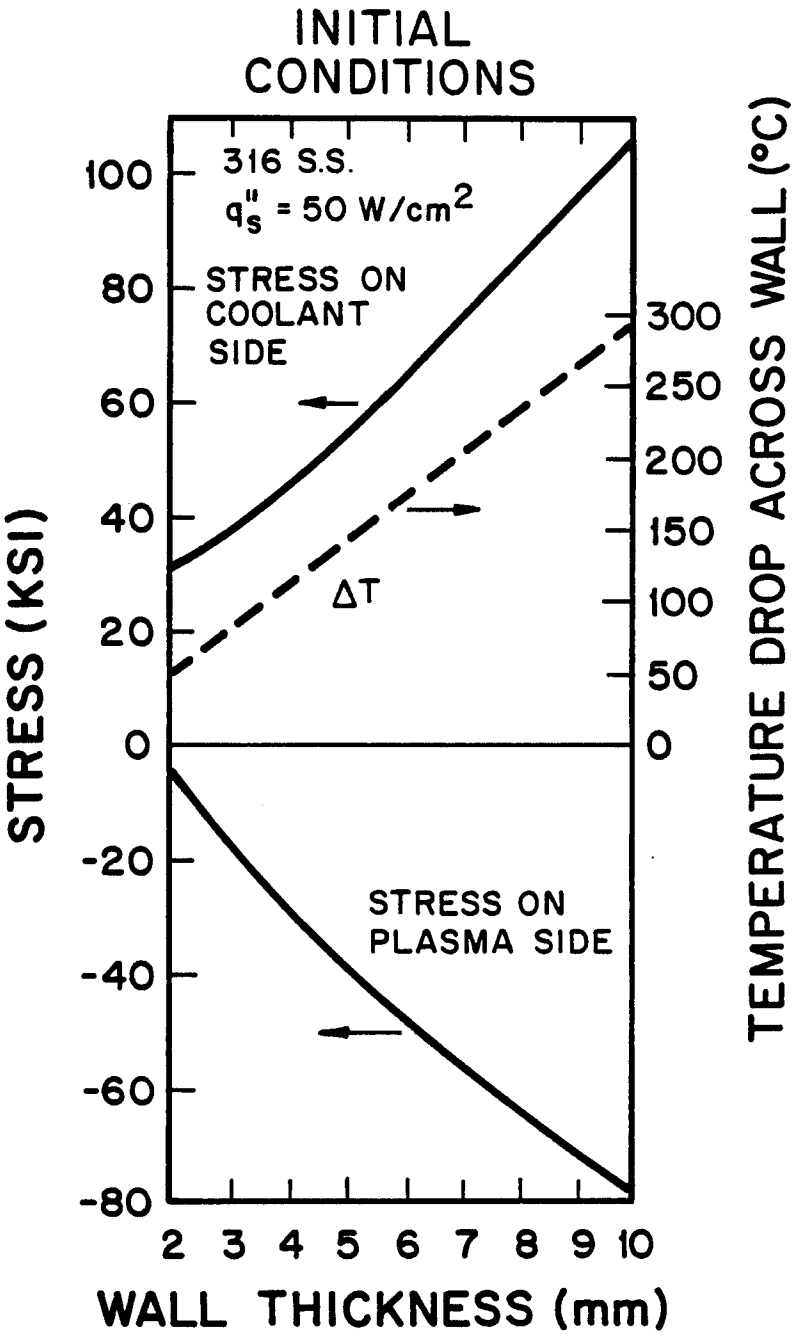

Figure 40. Initial stress and temperature on either the plasma or coolant side of the wall as a function of the wall thickness.

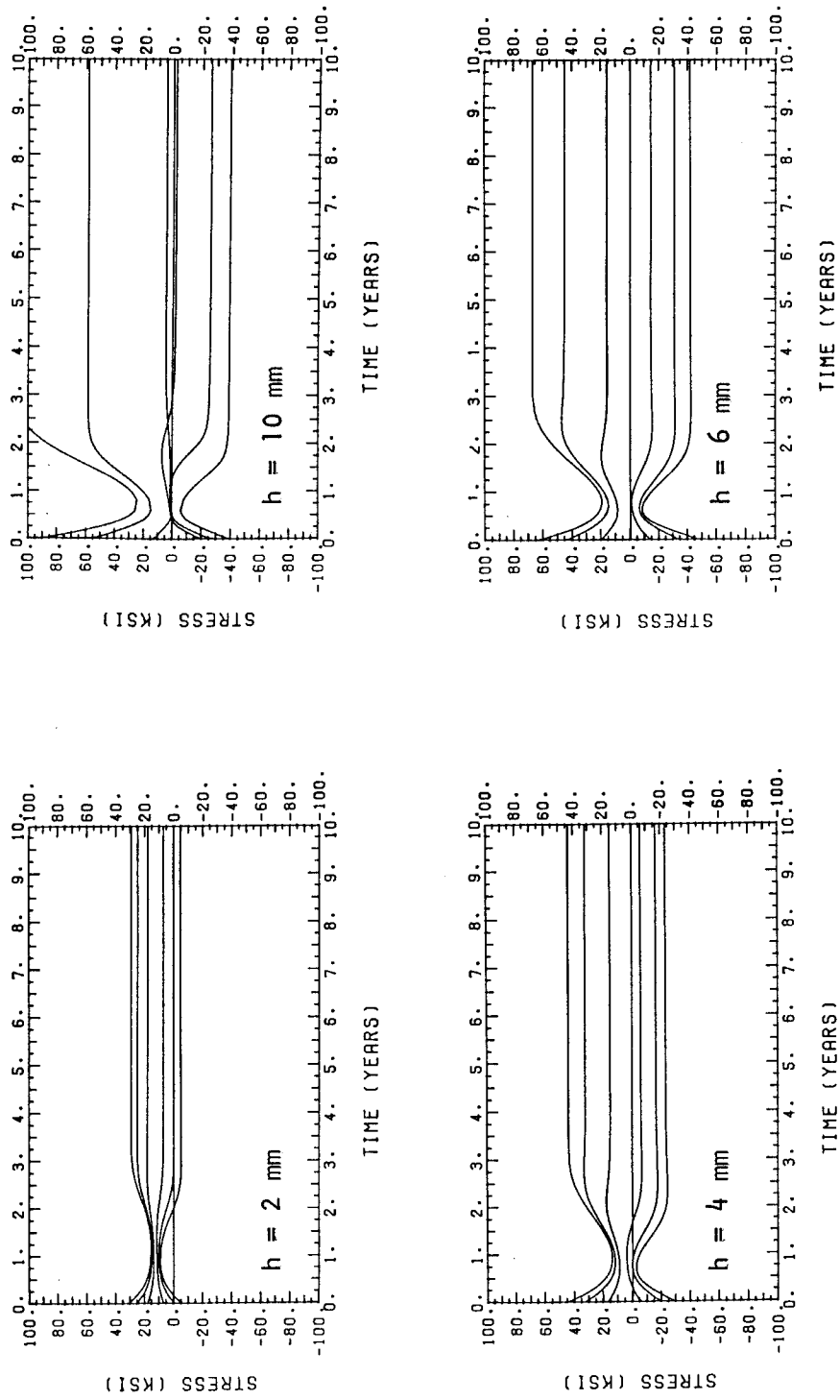

Figure 41. Stress histories for plasma-on conditions and for different wall thicknesses.

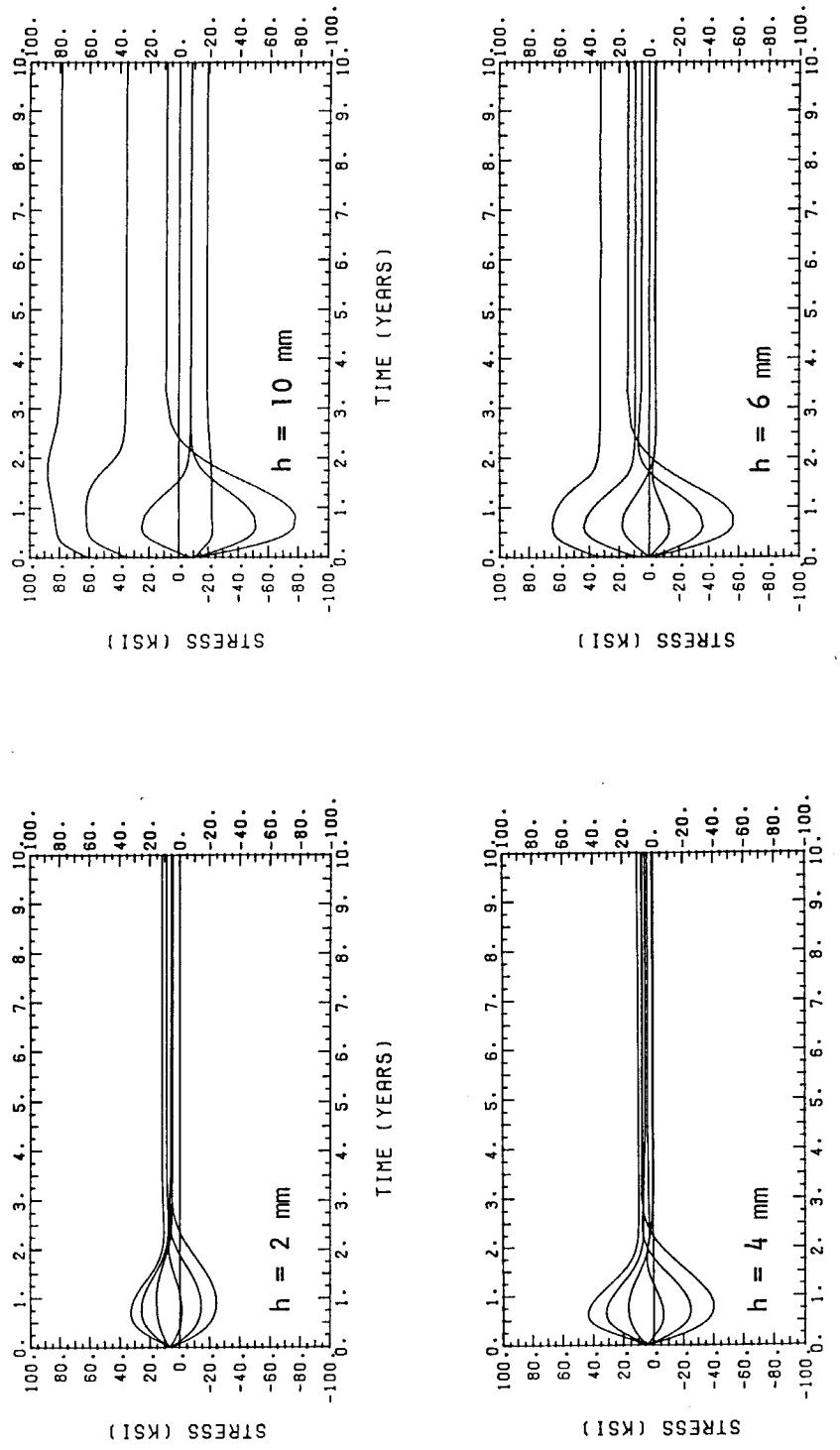

Figure 42. Stress histories for plasma-off conditions and for different wall thicknesses.

in a complex fashion to the temperature dependence of the incubation dose for swelling, the swelling rate, the creep compliance, and the elastic modulus.

For long-term applications we are more interested in the steady-state stresses than the transient response. Fig. 43 plots the final stresses for wall thicknesses of 2, 4, 6, and 10 mm. These curves are useful in that they allow us to identify the critical side that would give the shorter lifetime if a crack was present. We observe from this figure that the mean stress is always largest on the coolant side, regardless of the wall thickness. This is due to the fact that the plasma side, being hotter, swells faster than the other, thereby putting the coolant side in tension. The 10 mm thick wall is a special case, however. Here, the mean stress is positive on both sides of the wall because the peak swelling rate occurs at around 580°C, whose location lies inside the wall rather than on the surface. This induces compression in the center of the wall which must be balanced by tension on either side to preserve equilibrium.

In the next series, we continue to vary the wall thickness, but use instead a different backside wall temperature, T_b = 100°C. This temperature was chosen to represent the case of a low power, near-term fusion device such as INTOR, FED, or EBT-P. The steady-state stresses in this case are shown in Fig. 44. We can see that the tensile mean stresses appear now on the plasma side, exactly reversed from the previous figure. Since the temperatures are low, differential swelling is low and the steady-state stresses simply

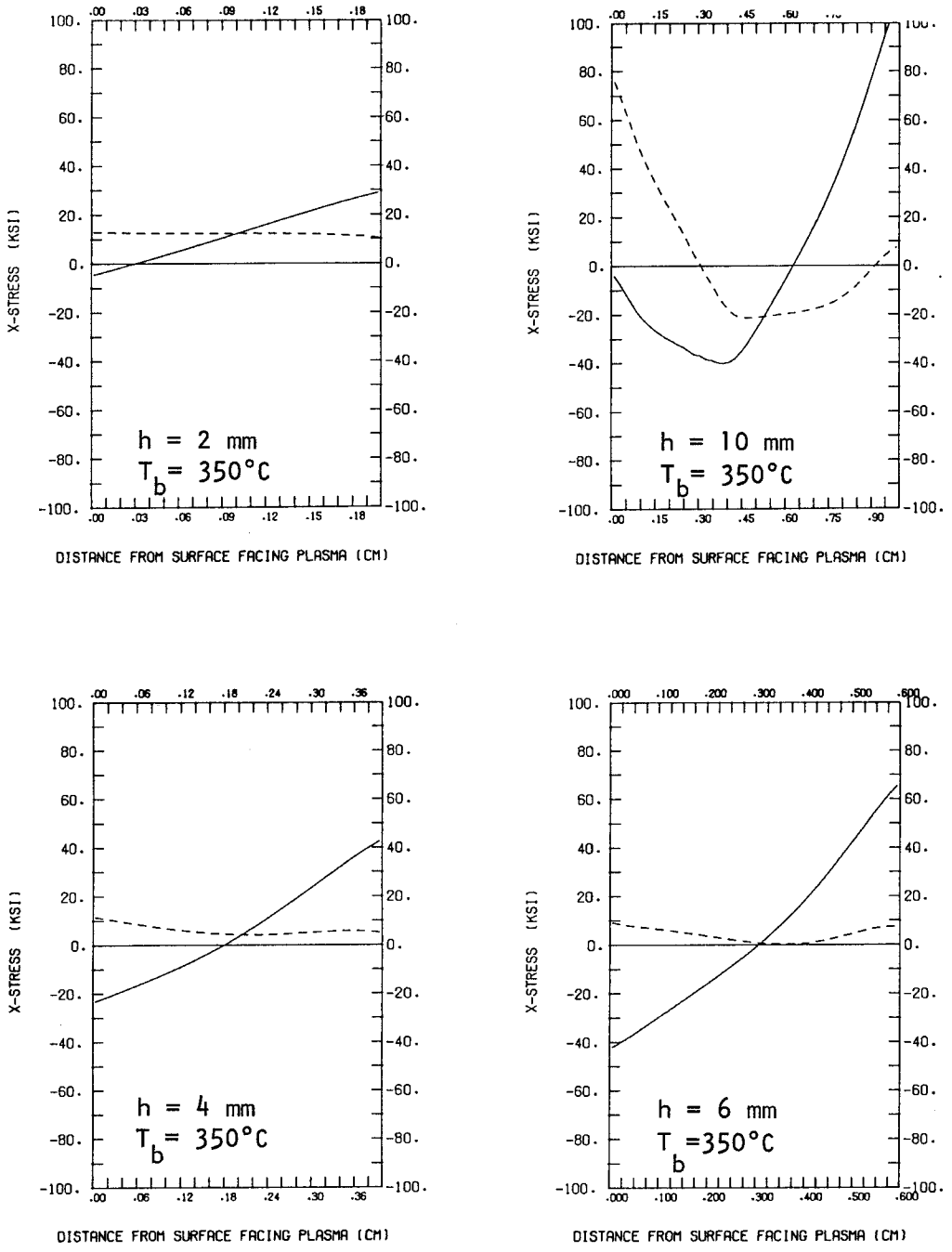

Figure 43. Steady-state stress distribution through the wall for plasma-on and off conditions for different wall thicknesses and T_b = 350°C.

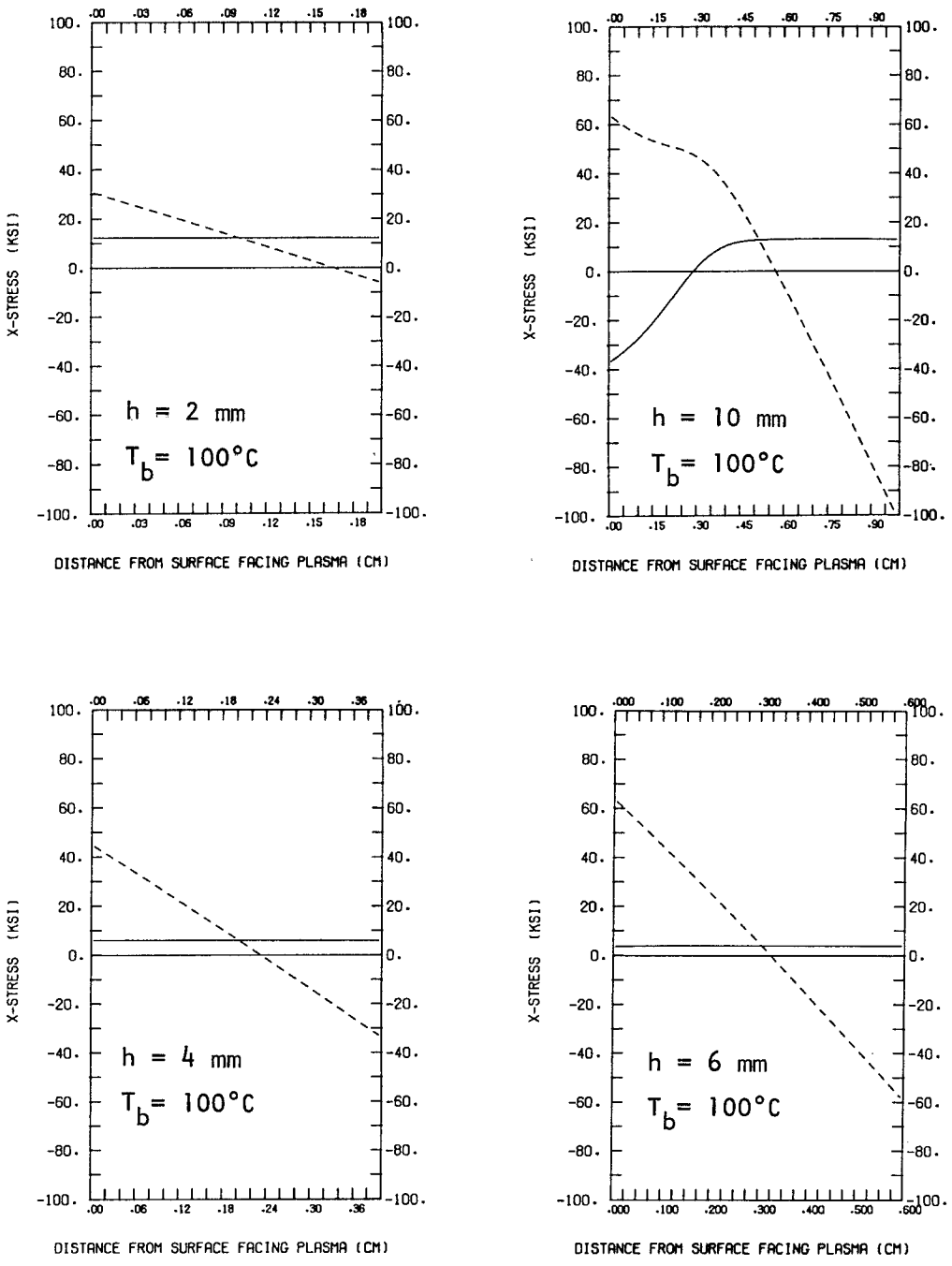

Figure 44. Steady-state stress distribution through the wall for plasma-on and off conditions for different wall thicknesses and T_b = 100°C.

equal the initial stresses reversed by irradiation creep. The stress distribution in the 10 mm thick wall, however, departs substantially from linearity. Even though T_b = 100°C, the temperature difference across the wall is sufficiently large, 340°C, to cause a substantial fraction of the wall on the plasma side to experience significant swelling, therefore creating stresses due to the swelling gradient.

In summary, it is clear that both the temperature gradient and the average wall temperature (or T_b) are major parameters that control the redistribution of first wall stresses.

Effect of Surface Erosion

Any first wall component in a fusion reactor that is exposed directly to the plasma will experience some erosion of material from the surface caused by one or more of the following processes:

1. physical sputtering from energetic particles colliding with the surface,
2. chemical sputtering such as methane and acetylene formation from hydrogen (D,T) reactions with graphite, and
3. vaporization of surface material due to locally intense heating from plasma disruptions, runaway electrons, etc.

The possibility of redeposition of lost material has been suggested but not yet confirmed [196]. Therefore, due to uncertainties in our knowledge of plasma-wall interactions, we have assumed a range of

possible surface erosion rates, e_r, from 0 to 2 mm per full power year (FPY).

Figures 45 and 46 show the history of stresses on the plasma side and on the coolant side, respectively, for e_r = 0.5, 1.0, 1.5, 2.0 mm/FPY. The overall response is characterized by four time periods. In the first period irradiation creep relaxes the initial stresses. Then, swelling begins and reverses this trend, as the stresses change back towards their initial values. Up to this point, wall erosion has had little effect.

Surface erosion begins to have a noticeable effect on the stress history in the third and fourth time periods. The third region exhibits a decrease in the cyclic thermal stress as time increases, instead of reaching a steady-state value for e_r = 0. This is caused by the reduction in the temperature drop, ΔT, across the wall as it thins down which, in turn, reduces the thermoelastic stress (for constant surface heat flux). In the fourth time period the sharp upswing in stresses dominates the behavior. This is caused by the constantly increasing membrane (hoop) stress = PR/2h as the wall thins down. Obviously, this stress must become very large in the limit as the wall thickness becomes very small.

Both processes, the reduction in $\Delta\sigma_{thermal}$ and the increase in σ_{mean} due to erosion, occur constantly throughout the entire life of the structure. However, significant effects show up only in the third and fourth time periods and the relative time which is spent in each of these periods depends on the erosion rate. For example, at

e_r = 0.5 mm/FPY the third stage is very long and the fourth does not even appear. On the other hand, at e_r = 2 mm/FPY, the second period has been compressed and cannot be observed. In all cases, the first time period appears to be unaffected by wall erosion.

Figures 47 and 48 show a similar set of plots for e_r = 0.5, 1.0, 1.5, and 2.0 mm/FPY, except that the backside wall temperature has now been changed to T_b = 100°C. Qualitatively, the overall behavior for these conditions is similar to the one illustrated by previous figures where T_b = 350°C.

Although the effect of wall erosion on lifetime is discussed in more detail in Chapter 8, we can already qualitatively assess the effect. At one extreme, if the erosion rate is large, the stress history is not really needed for a crack growth analysis because the wall thins down too fast. On the other hand, if the erosion rate is modest (less than 0.5 mm/FPY) then we would expect a longer lifetime than with no erosion because the driving force for fatigue crack growth, namely, the cyclic thermal stress, is constantly being reduced by thinning. Indeed, this is exactly what is observed.

Summary and Conclusions

Inelastic deformation of the first wall caused by irradiation creep, thermal creep, swelling, and surface erosion is expected to have major effects on the long-term redistribution of stresses through the thickness. For any thin-walled structure that can be modelled as a flat plate constrained from bending, it is possible to draw the

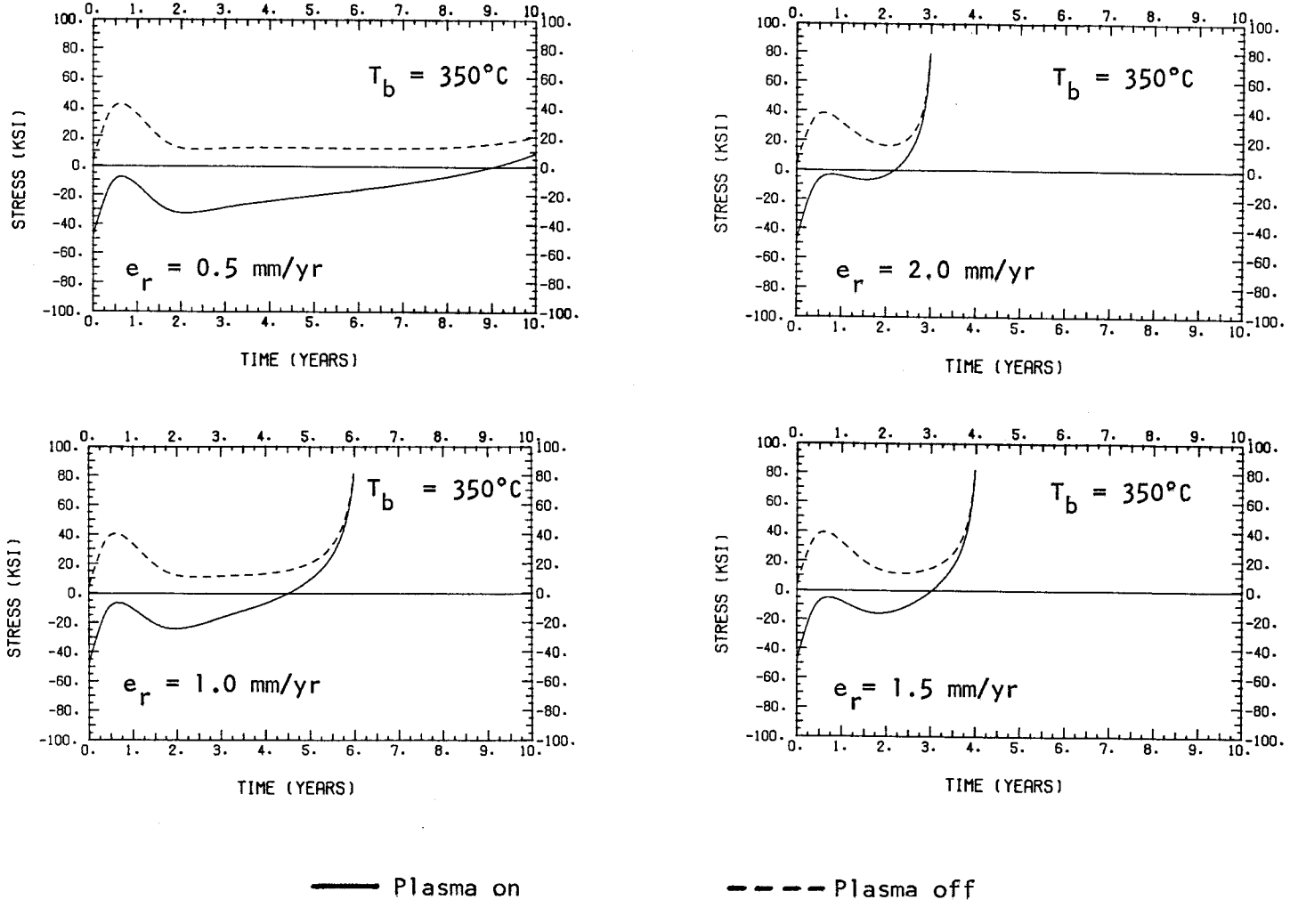

Figure 45. Effect of wall erosion on plasma-side stresses: T_b = 350°C.

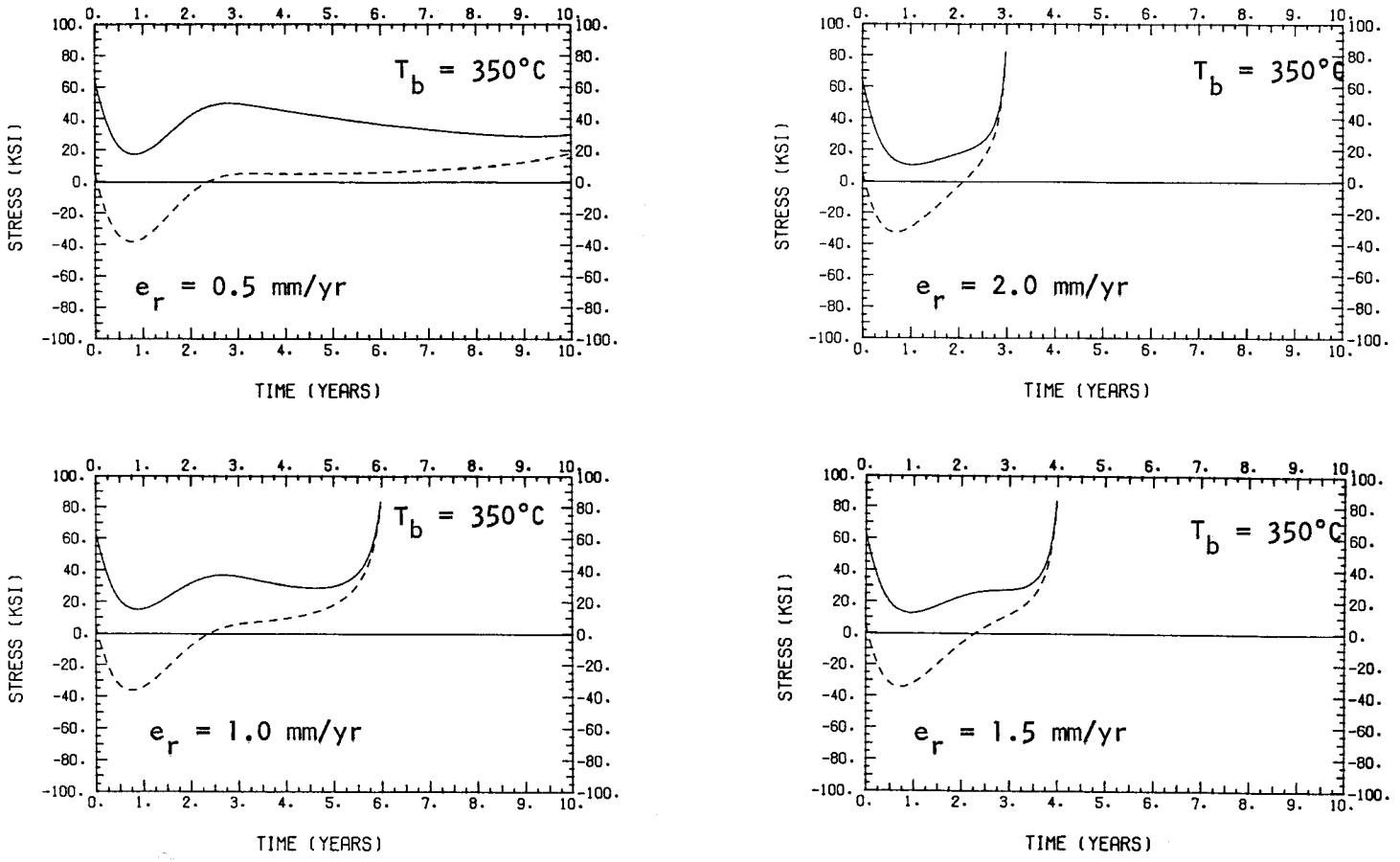

Figure 46. Effect of wall erosion on coolant-side stresses: T_b = 350°C.

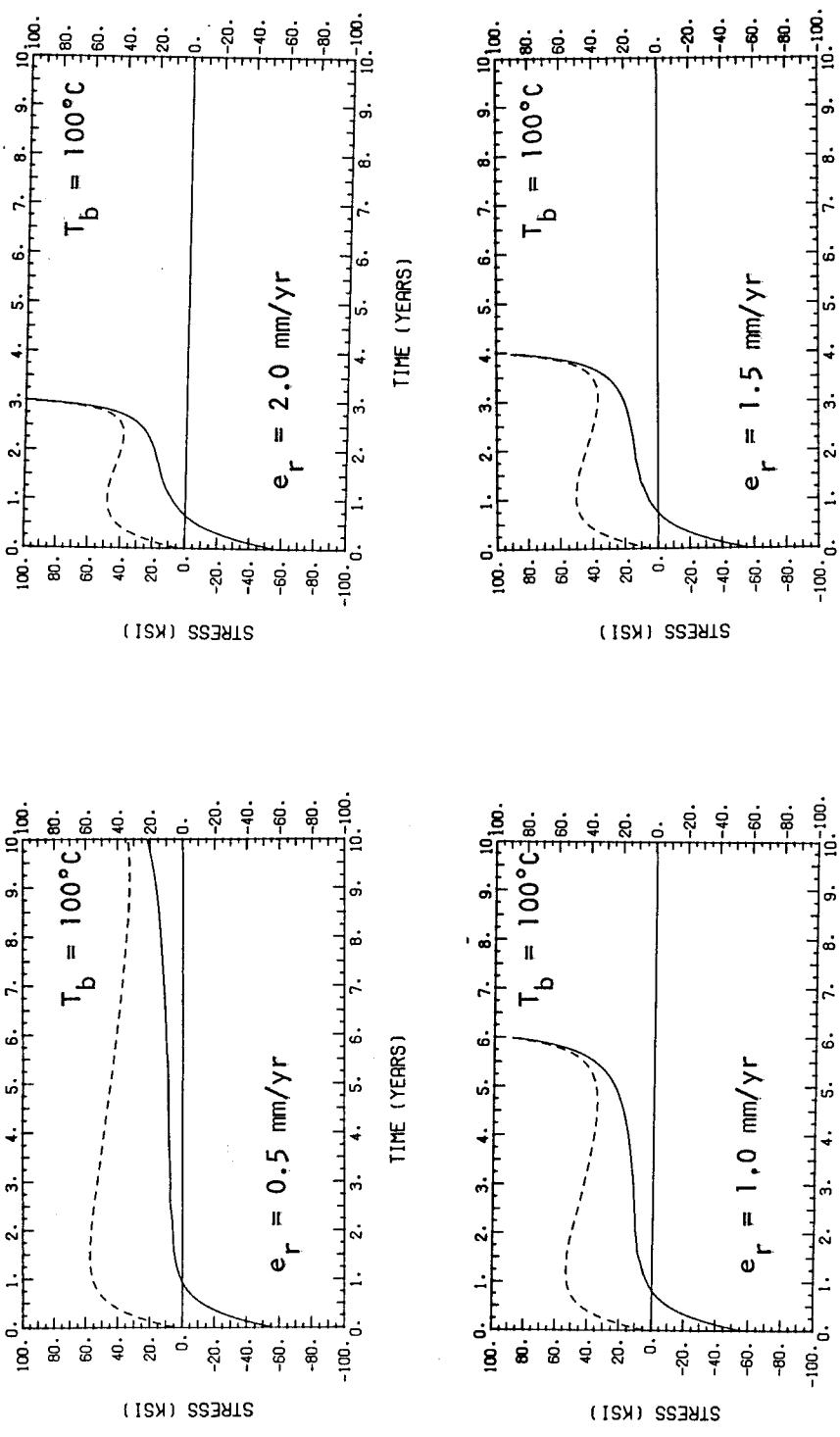

Figure 47. Effect of wall erosion on plasma-side stresses: T_b = 100°C.

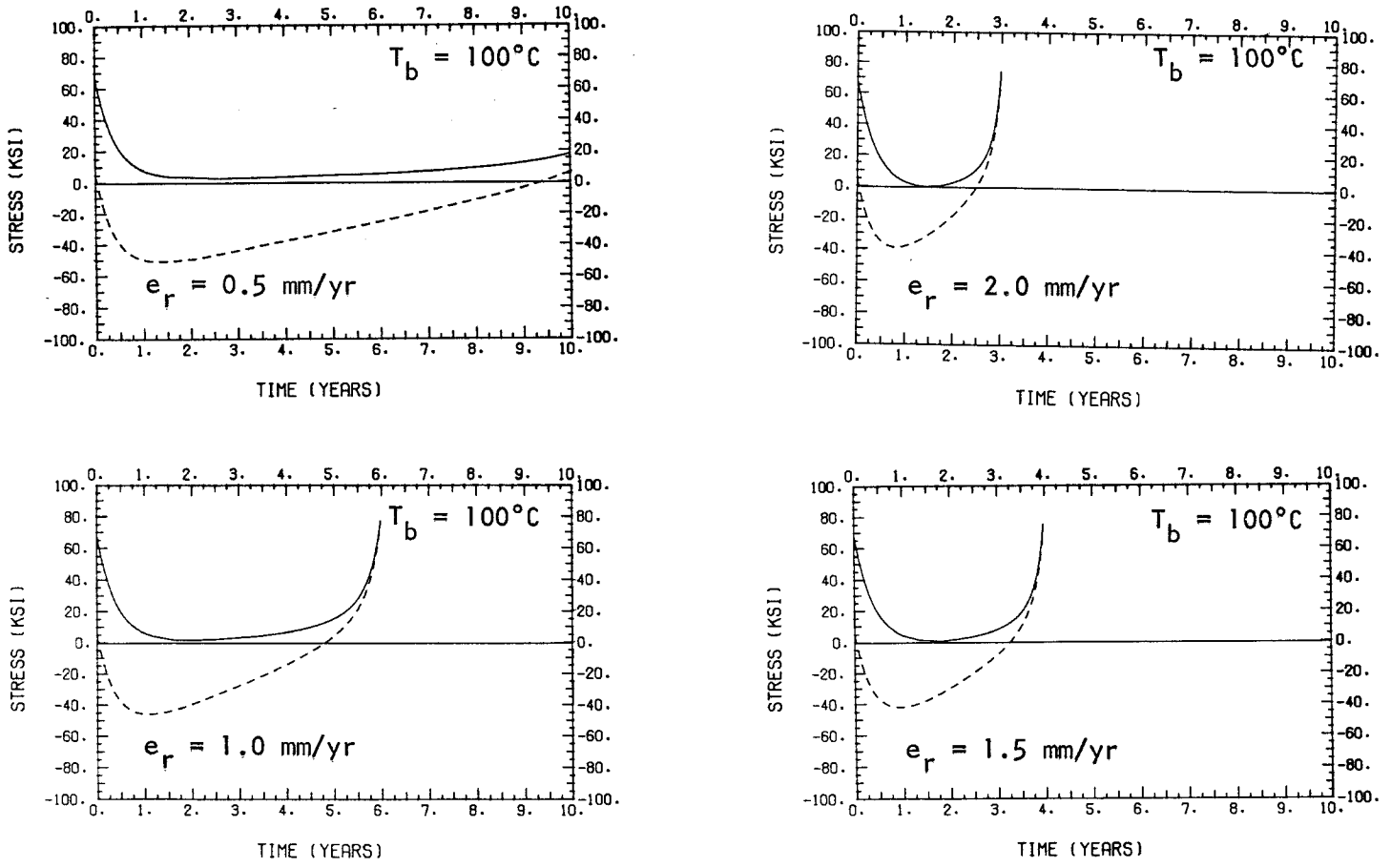

Figure 48. Effect of wall erosion on coolant-side stresses: T_b = 100°C.

following conclusions, based on calculations by the TSTRESS code.

In general, we find that when wall erosion is neglected, the long-term stress history exhibits three characteristic stages of behavior. First, irradiation creep relaxes the initial thermo-elastic stresses during the first six months of operation (5-10 dpa). Upon shutdown, these relaxed stresses reappear as tensile residual stresses on the plasma side of the wall and can be large, depending on the thermal stresses. After roughly one year (20-30 dpa) of operation the incubation dose for void swelling is reached and differential swelling through the thickness begins to redistribute the relaxed stresses. The trend during this second stage is in the direction of returning the stresses back to their initial values. Finally, in stage III an equilibrium is reached after three years (60-70 dpa) where swelling and creep exactly balance each other, resulting in a steady-state stress distribution. This saturation stress is proportional to the ratio of the differential swelling rate to the creep compliance. The cyclic thermal stresses, important to fatigue crack growth, do not change with time and are only determined by the initial conditions. On the other hand, the mean stress (which affects the R-ratio) exhibits the classic three-stage behavior and depends directly on the steady-state stresses. The average wall temperature, which is governed by the coolant temperature, also affects the steady-state distribution through the temperature dependence of swelling (unlike irradiation creep, which is insensitive to temperature).

When surface erosion is considered, a fourth stage is added to the stress history. Stages I and II are roughly unaffected. However, in stage III wall thinning reduces the ΔT and, hence, the thermal stress. Finally, in stage IV the increase in membrane (hoop) stress begins to dominate.

Future improvements to the TSTRESS code would include the capability to compute instantaneous plasticity caused by stresses that exceed the yield strength. This is needed to analyze shakedown and ratcheting phenomena, in addition to off-normal loads such as plasma disruptions, where magnetic forces and intense surface heating may occur over very short periods of time and cause locally high stresses. Also, the present stress equations in TSTRESS need to be changed by adding some new terms to account for the bending moments. While the latter task is relatively easy to accomplish, the former is more difficult because constitutive laws for high temperature plastic behaviour of metals are still being developed.

CHAPTER 6

Models For Crack Propagation

Introduction

When a cracked component is subjected to cyclic loads, a corrosive environment, or static loads together with high temperatures, then crack extension can occur due to fatigue, stress corrosion cracking, or creep cracking processes, respectively. All three of these processes will be present, to some extent, in a fusion reactor first wall component. Therefore, it is important to be able to model this behavior and predict the amount of crack growth accumulated after a given length of time. The emphasis of this chapter is on modelling slow, stable crack growth in long-lifetime components, rather than the fast, unstable ("dynamic") crack growth which is experienced in thermal shock problems.

A successful theory of crack propagation was not developed until the early 1960's when Swanson [1], and Paris and Ergodan [2] performed the definitive experiments demonstrating that fatigue crack growth rates, da/dN, correlated better with the cyclic stress intensity factor range, ΔK, than other combinations of stress, σ, and crack length, a, such as $\sigma^m a^n$. This theory provides the important connection between the stress intensity factor, as determined by linear elastic fracture mechanics (LEFM), and the crack growth rate, which is a basic materials property.

Four steps are involved in predicting crack propagation. First, the size of the initial flaw, a_o, is either measured or assumed. Then,

the stress intensity factors are calculated, depending on the applied stress and wall thickness. Next, the total crack growth rate (creep + fatigue) is computed as a function of ΔK, temperature, dpa, R-ratio, etc. Finally, the current crack size, a, is determined by integrating the total da/dN over the number of load cycles, N, namely

$$a(N) = a_o + \int_0^N \left(\frac{da}{dN}\right)_{total} dN \quad . \tag{127}$$

This chapter begins with a literature review of previous applications of fracture mechanics methods to fusion reactor first wall components. Then, equations are presented for the stress intensity factor, K_I, of a surface flaw. Next, an extensive review is given of fatigue crack growth behavior in unirradiated austenitic stainless steels, including the development of a new equation for da/dN. The effects of neutron irradiation are then discussed, along with the relatively minor effects of creep crack growth. The implications of wall thinning and crack erosion are discussed, also. Finally, the basic equation for lifetime prediction is presented, along with a summary and conclusions.

Review of Previous Work

The use of linear elastic fracture mechanics to predict stable crack growth is common among the aviation, aerospace and nuclear (fission) industries. Excellent references for this subject include the books of Liebowitz [3], Hertzberg [4], and Rolfe and Barsom [5]. Two commonly available computer codes for predicting crack propagation are CRACK and BIGIF. CRACK, a two-dimensional code written by Forman, Kavanaugh

and Stuckey in 1972 [6], was used primarily by NASA to certify the Space Shuttle Program. BIGIF, written by Besuner, Peters and Cipolla in 1978 [7], employs a sophisticated boundary integral method for three-dimensional analysis of cracked fission reactor components. The use of fracture mechanics to assess the lifetime of fusion reactor first wall components is a relatively recent phenomena, as pointed out in Chapter 2. One of the first applications was in a theory for irradiation-induced fatigue crack growth proposed by Weertman in 1974 [8]. Although this theory has never been confirmed, Weertman did identify the potential problems of crack growth in laser fusion reactors [9]. In 1976, Krakowski, Haberson and Cort [10] performed creep crack growth analysis of an edge-cracked, all-ceramic Si_3N_4 first wall. Then, in 1976, Cramer published the first of a series of lifetime predictions for tokamak first walls [11-16]. His basic methodology was to use either the 1-D SLIP or 2-D CRACK computer codes to model the fatigue crack growth of a semi-elliptical surface flaw. However, neither of these two codes incorporated bending stress intensity factors which this author has found to be important. In 1977, Kearney et al. [17] published a 1-D crack growth analysis of a helium gas cooled blanket module with 2:1 ellipsoidal head closure and a semi-circular surface flaw. No irradiation effects were considered, however. In 1978, Mattas and Smith [18] used fatigue crack growth of an edge-cracked, generic first wall element to study the lifetime parametrically.

The first use of bending stress intensity factors for a surface flaw and a drop in fracture toughness from irradiation was considered

by Prevenslick in 1978 [19]. However, he only considered the one-dimensional growth of a semi-circular flaw and included no stress history. Then, in 1979, Delaney et al [20] used the NASA CRACK code to assess the effect of electromotive forces caused by plasma disruptions on the lifetime. An interesting feature of Delaney's analysis was the assumption of an unusually small initial aspect ratio, $a_o/c_o = 0.132$. Also, in 1979, Rosenwasser et al [21] used Dalessandro's code (see ref. [17]) to re-analyze the same General Atomic blanket module, this time made out of HT-9 martensitic steel instead of Inconel 718. In 1980, Mattas et al [22] published a lifetime study of the STARFIRE tokamak power reactor first wall design. He included fatigue and creep crack growth in a model for an axially-oriented edge-crack in a long tube, with non-axisymmetric heating. Finally, the most recent application of fracture mechanics to first wall components is in the work of Adegbulugbe and Meyer in 1981 [23].

This review has shown that fracture mechanics analyses of first wall components is a new endeavor only six years old. In fact, only four researchers from the U.S.: Cramer, Delessandro, Mattas and the author are currently involved in lifetime analysis using LEFM. It is not known to what extent any foreign researchers from Russia, Japan or the European Community have progressed in this field. However, an abstract appeared recently at the Seattle meeting [24] describing an integrated lifetime code, SMILE, but no paper was published.

None of the reports reviewed here have included any wall erosion effects, effects of irradiation on fatigue crack growth rates, plasma

disruption thermal loads (which involves elastic-plastic fracture mechanics) or analyses of inertially-confined fusion reactors. More importantly, although each of these authors have considered many effects, not one of them has ever combined all of the possible effects into a single, self-consistent methodology as developed in the present thesis. In the next section, we will discuss in detail the various aspects of crack propagation and effects likely to be encountered in a future fusion device.

Flaw Characterization

The initial, pre-existent defect is assumed to be a semi-elliptical surface flaw, oriented perpendicular to the direction of maximum principal stress, as shown in Figure 49. Although it is a three-dimensional defect, its dimensions are characterized only by a depth of "a" along its minor axis and a surface length of "2c" along its major axis. The flaw is allowed to grow independently along each axis, thus changing its aspect ratio, a/c. This type of flaw would most likely be produced by a scratching or machining operation during construction or assembly of the component. Figure 50 shows different examples of how the ASME B&PV Code, Section XI [25] approximates an irregularly shaped defect with a semi-elliptical or semi-circular flaw.

What is a reasonable initial flaw size to assume? This depends completely on the capabilities of NDE (Non-Destructive Evaluation) inspection techniques. Reference [26] describes 31 different methods to probe the metal for defects. Appendix G of Section III in the ASME B&PV Code assumes a flaw size equal to 25% of the wall thickness, which

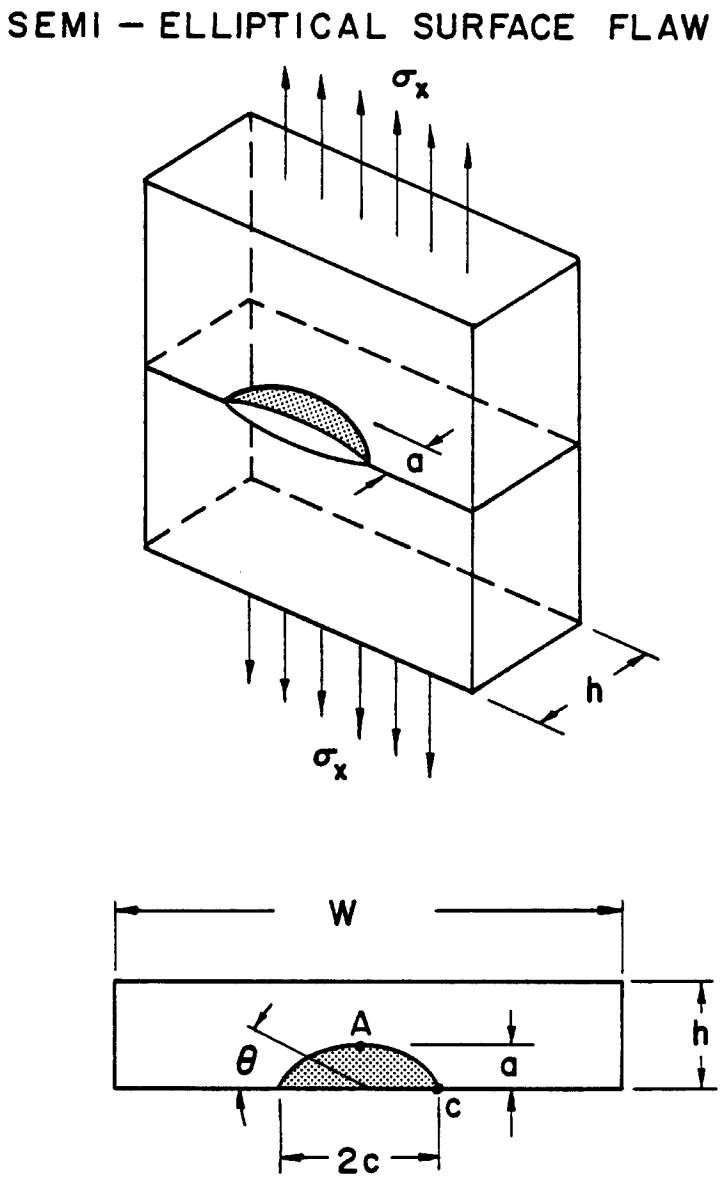

Figure 49. Definition of semi-elliptical surface flaw.

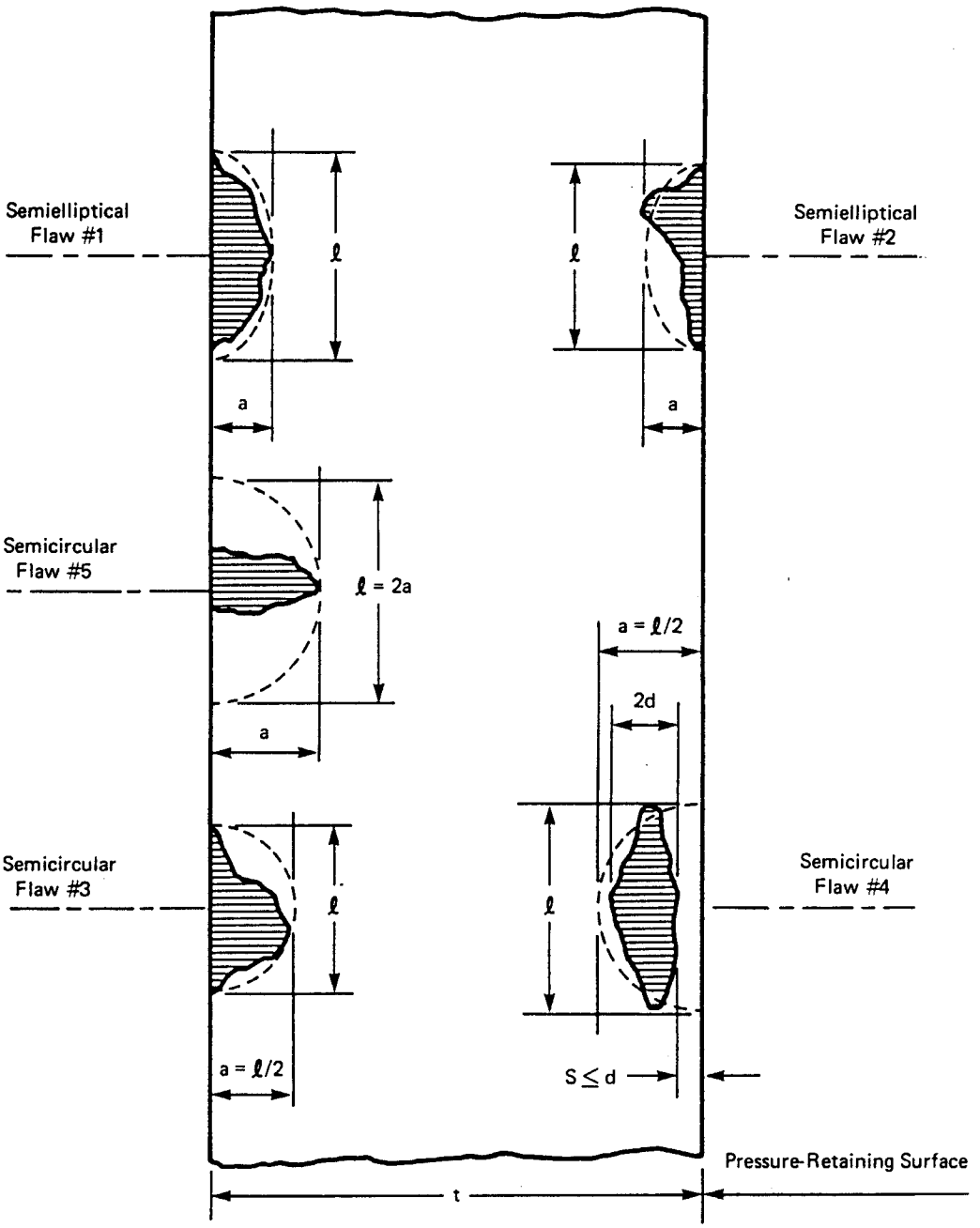

Figure 50. ASME designation of semi-elliptical flaw assumptions for surface defects [25].

translates into flaws that are 0.25 - 1.25 mm deep in typical first wall components. Alternatively, the RDT Standards for structural design of Breeder Reactor Core Components [27] recommend that the minimum crack depth be no less than 0.25 mm. Finally, Rockwell International has specified the following limits for NDE of the Space Shuttle: 0.6 mm < a_o < 1.9 mm for standard NDE or 0.25 mm < a_o < 0.6 mm for "special" NDE techniques [28].

Unfortunately, no data exists on the probability of detecting flaws below a minimum size in actual fusion reactor components. Therefore, the lifetime studies performed in Chapter 8 assume a range of sizes from 0.1 mm to 2.0 mm, with a nominal size of a_o = 1 mm. Initial flaw shapes are traditionally assumed to be semi-circular (e.g. a_o/c_o = 1).

Stress Intensity Factors

The driving force for fatigue crack growth is localized cyclic plasticity at the crack tip (or, in the case of a semi-elliptical surface flaw, plasticity around the entire crack from θ = 0 to θ = 180°). In linear elastic fracture mechanics the fundamental parameter that measures this concentration, or intensity, of stress and strain at the crack tip is defined by K_I, the stress intensity factor for type I crack opening mode (see Fig. 51). Type II and type III crack modes (K_{II} and K_{III}) are not considered in this thesis, hence, the subscript "I" in K_I will be dropped from future use.

In a typical first wall component there are two dominant sources of stress: membrane stresses caused by coolant pressure, and

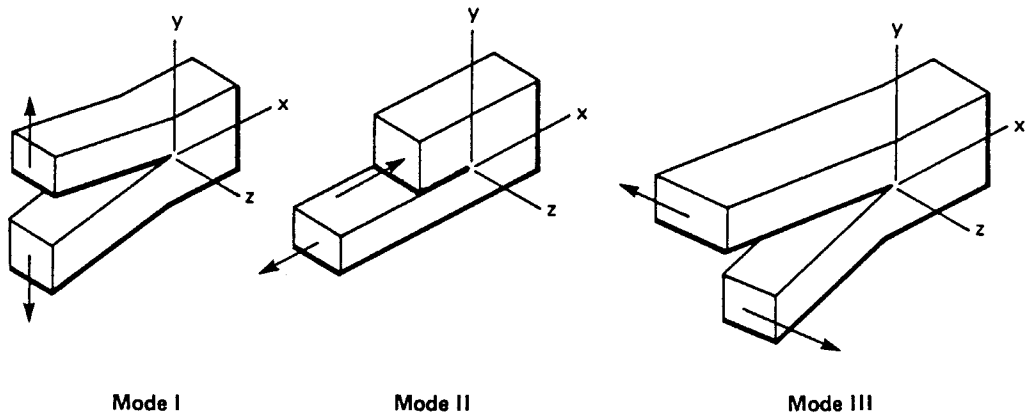

Figure 51. Crack opening modes for Mode I, II, and III stress intensity factor calculations [15].

bending stresses caused by the linear temperature gradient through the wall. Within the limits of linear elastic fracture mechanics, the stress intensity factors from each of these sources of stress can be simply superimposed. Adopting the notation used in section XI of the ASME Boiler and Pressure Vessel Code [25] we can write the total stress intensity factor, K, as

$$K = (M_m \sigma_m + M_b \sigma_b) \sqrt{\frac{\pi a}{Q}} \tag{128}$$

where a = crack depth into plate

σ_m = membrane stress

σ_b = bending stress

Q = flaw shape factor

M_m = membrane correction factor

M_b = bending correction factor.

σ_m, σ_b, and a are defined in Fig. 52. The superposition of the two load types, tension and bending, is illustrated in Fig. 53. From this it can be seen that σ_m or σ_b can be either positive or negative numbers, depending on both the particular stress distribution through the wall, and on which side of the plate the flaw is located. Note that the bending stress, σ_b, should always be measured on the same side that the crack is located (compare Fig. 53b and 53d).

It has been observed experimentally that growth patterns are different for pure tension than for pure bending loadings, as illustrated in Fig. 54. Bending causes the flaw to elongate faster along

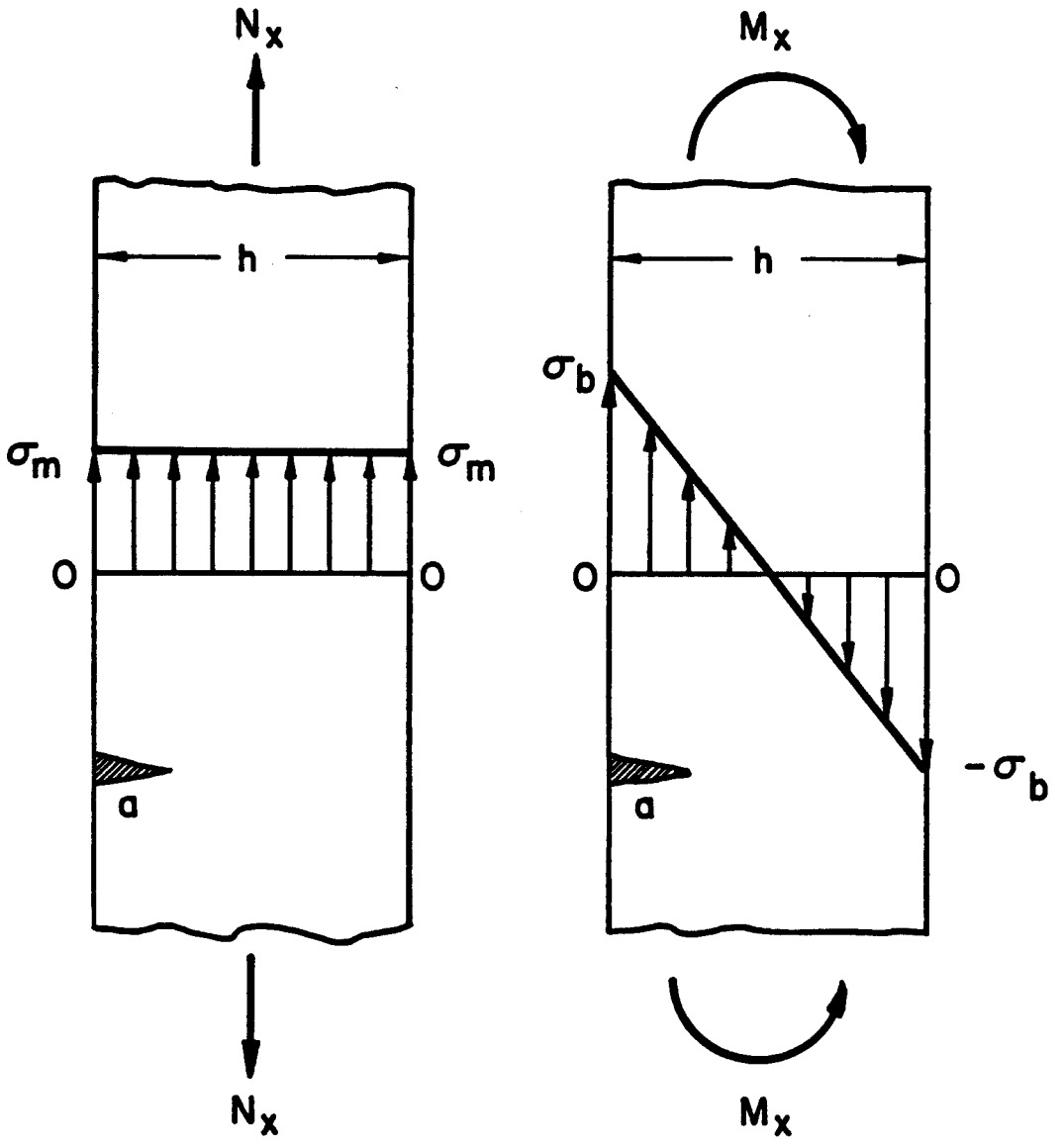

Figure 52. Definition of the membrane stress, σ_m, and the bending stress, σ_b.

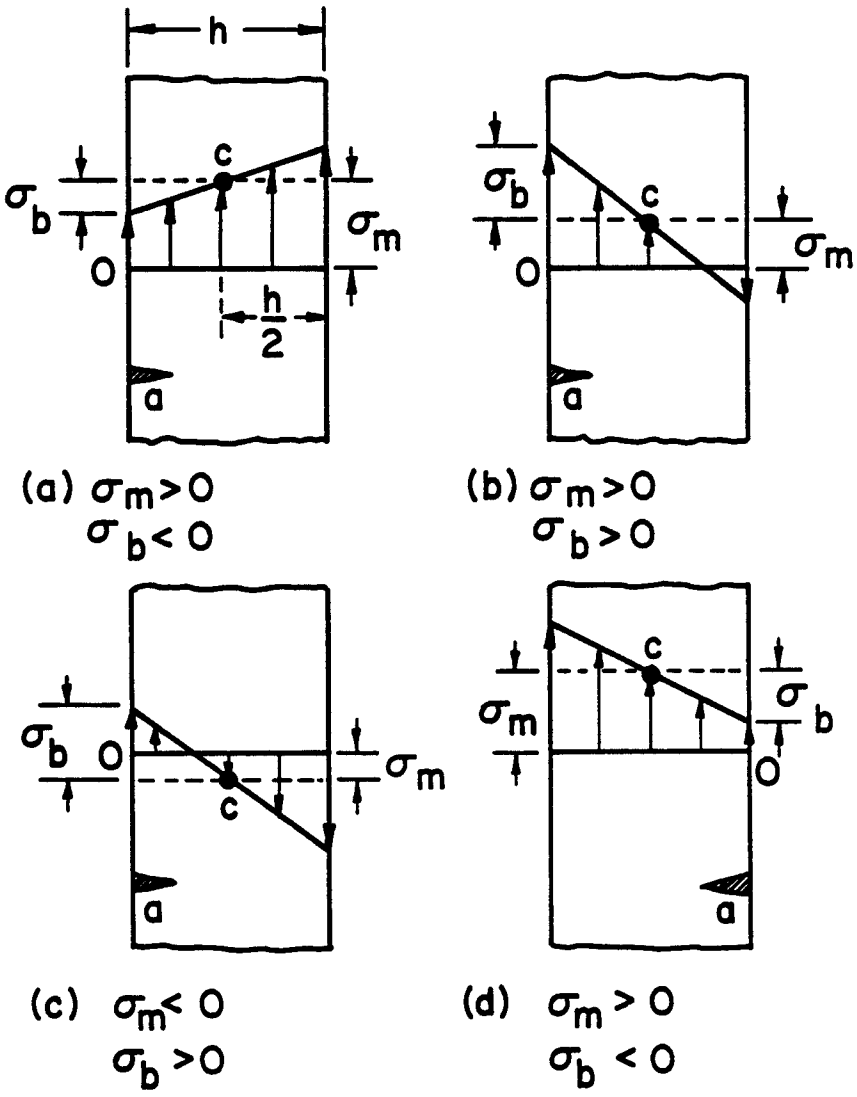

Figure 53. Method for determining σ_m and σ_b. σ_m equals the stress at the midplane and σ_b equals the difference between the stress at the surface and σ_m. σ_b is always measured on the same side that the crack is located.

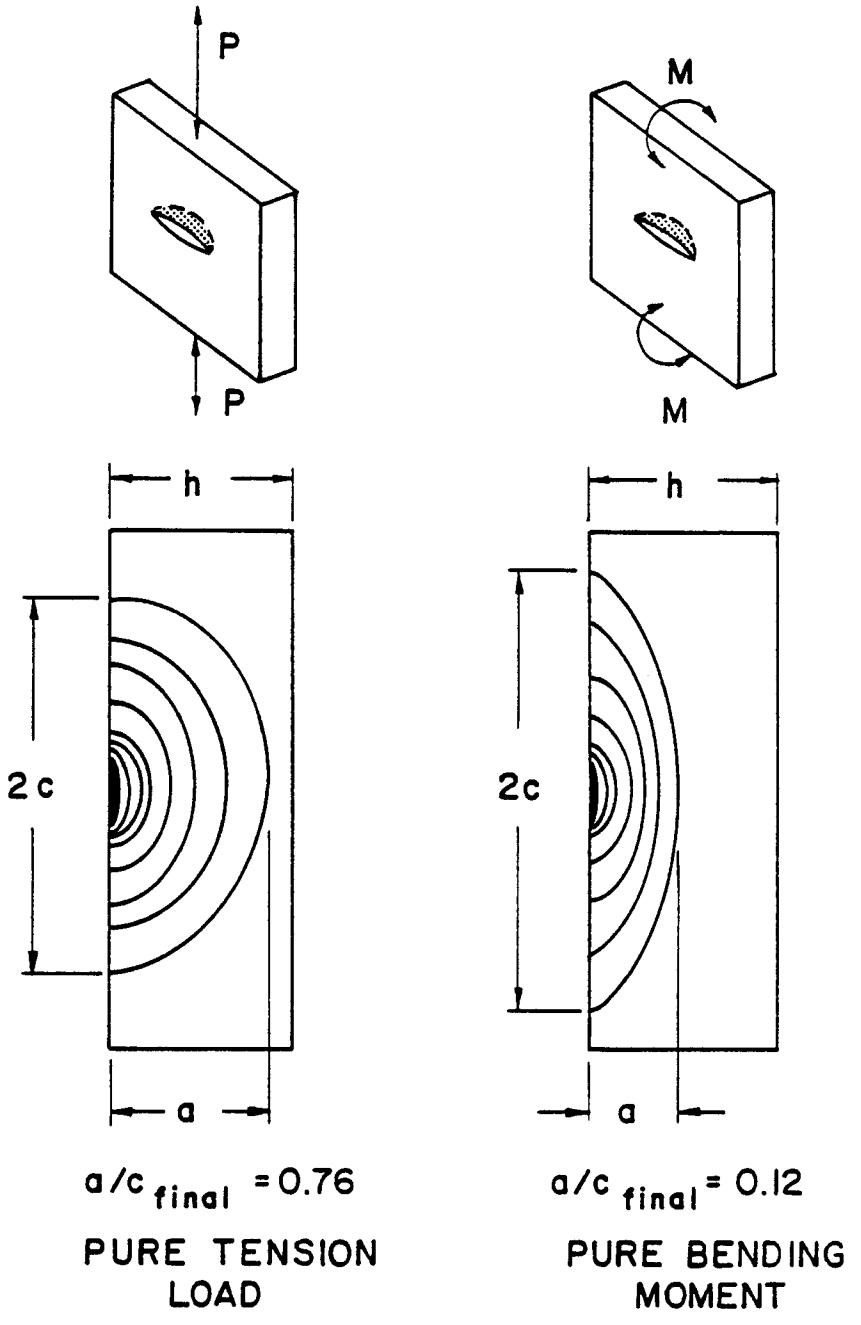

Figure 54. Crack growth pattern for either pure tension loads or pure bending moments.

the surface than it would under pure tension loads. The final aspect ratio in this case is predicted by the WISECRACK code to be $(a/c)_f$ = 0.76 for pure tension and $(a/c)_f$ = 0.12 for pure bending loads. Since most high heat flux components sustain a linear temperature gradient through the wall and, hence, a linear stress gradient (bending), we can reasonably expect all surface flaws to grow into long, thin cracks. It is, therefore, incorrect to assume that an initially semi-circular flaw (a/c = 1) will keep its same shape for the entire life, as has been assumed in previous lifetime studies.

Over a period of many years while the reactor is running, inelastic deformation caused by irradiation creep and swelling will modify the initially linear stress distribution through the wall. However, the equations given by Newman and Raju [29] for the stress intensity factor only apply to a linear stress gradient. Therefore, we use a method recommended by the ASME Boiler and Pressure Vessel Code [25] to linearize these nonlinear stresses over the crack depth. Figure 55 illustrates this approach. First, a straight line is drawn between points A and B, where point B is determined by the crack depth a. Line $\overline{AB}$ therefore represents an equivalent linear stress distribution from which the two stresses, σ_m and σ_b, are easily calculated by using the drawings in Fig. 53.

This particular method of linearization is derived from the assumption that only those stresses which act upon the face of the crack are important in determining the stress intensity factor. For moderately nonlinear gradients (e.g. long burn-time plasmas), Bloom

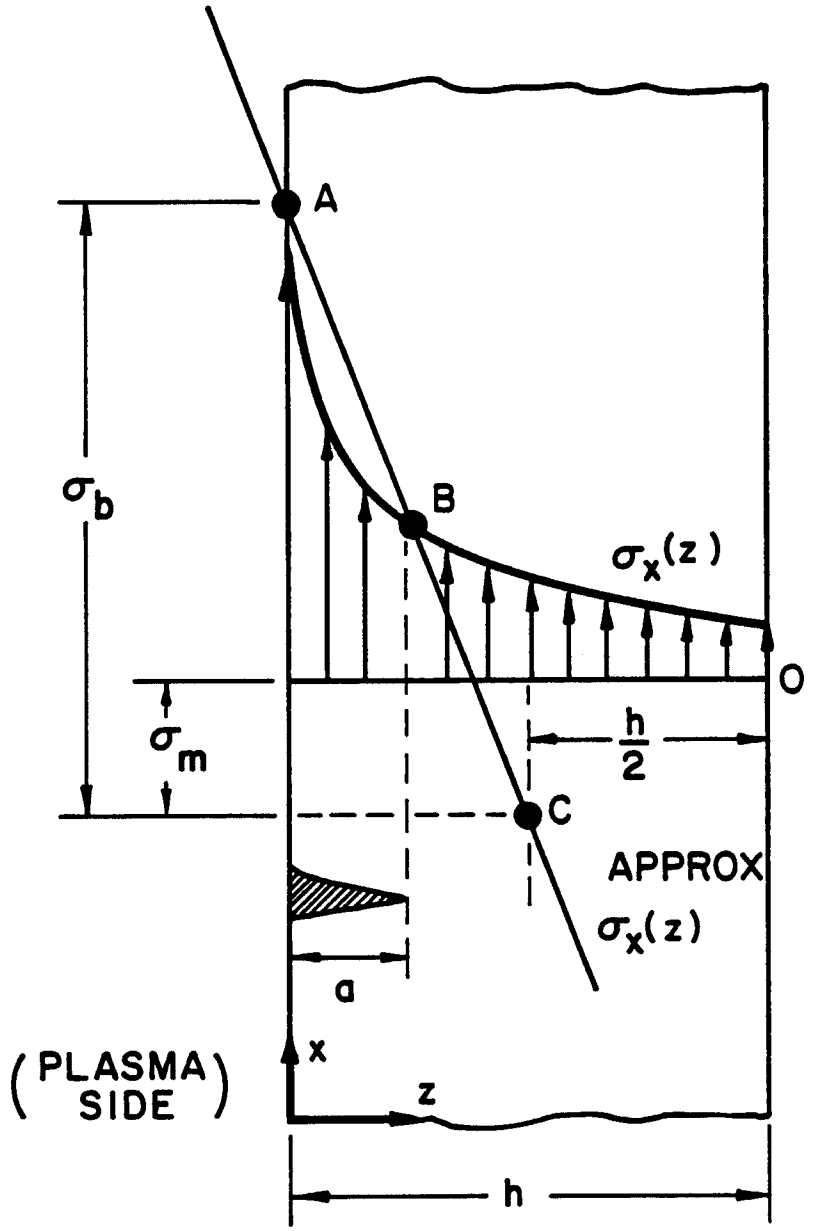

Figure 55. Technique for linearization over-the-crack of the non-linear stress distribution, $\sigma_x(z)$, through the thickness.

and VanderSluys [35] have shown that this method agrees very well with more accurate polynomial or finite element methods. However, it is not as accurate for the steep stress gradients that are produced from either ICF microexplosions or plasma disruption heat pulses. This remains an area of possible improvement.

Returning to Eq. (126), the flaw shape factor, Q, is equal to ϕ^2, where ϕ is the complete elliptic integral of the second kind

$$\Phi = \int_0^{\pi/2} [1 - (\frac{c^2 - a^2}{c^2} \sin^2\theta)]^{1/2} \, d\theta \, . \tag{129}$$

A convenient approximation is commonly used for ϕ^2, namely

$$Q = 1.0 + 1.464 \, (\frac{a}{c})^{1.65} \tag{130}$$

for $a/c \leq 1.0$. In the limit as $c \to \infty$, the surface flaw becomes an edge crack, for which $Q = 1$.

The expressions used in the WISECRACK code for M_m and M_b are those developed by Newman and Raju [29]. They used a 3-D hybrid finite element method to compute accurate correction factors that depend on the crack depth (a), aspect ratio (a/c), plate width (W), angular location (θ), and load type (tension or bending) for the following ranges: $0 \leq a/c \leq 1$, $0 \leq a/h \leq 1$, $c/W \leq 0.5$, and $0 \leq \theta \leq \pi$. The membrane correction factor, M_m, is given by

$$M_m = [M_1 + M_2(\frac{a}{h})^2 + M_3(\frac{a}{h})^4] \, f_\theta f_w g \tag{131}$$

where

$$M_1 = 1.13 - 0.09\left(\frac{a}{c}\right) \tag{132}$$

$$M_2 = -0.54 + \frac{0.89}{0.2 + a/c} \tag{133}$$

$$M_3 = 0.5 - \frac{1}{0.65 + a/c} + 14\left(1 - \frac{a}{c}\right)^{24} \tag{134}$$

$$g = 1 + \left[0.1 + 0.35\left(\frac{a}{h}\right)^2\right](1 - \sin\theta)^2 \tag{135}$$

$$f = \left[\left(\frac{a}{c}\right)^2 \cos^2\theta + \sin^2\theta\right]^{0.25} \tag{136}$$

$$f_w = \left[\sec\left(\frac{\pi c}{2W}\sqrt{\frac{a}{h}}\right)\right]^{0.5} \tag{137}$$

The bending correction factor, M_b, is given by

$$M_b = H \cdot M_m \tag{138}$$

where

$$H = H_1 + (H_2 - H_1)\sin^p\theta \tag{139}$$

$$p = 0.2 + \frac{a}{c} + 0.6\left(\frac{a}{h}\right) \tag{140}$$

$$H_1 = 1 - 0.34\left(\frac{a}{h}\right) - 0.11\left(\frac{a}{c}\right)\left(\frac{a}{h}\right) \tag{141}$$

$$H_2 = 1 + G_1\left(\frac{a}{h}\right) + G_2\left(\frac{a}{h}\right)^2 \tag{142}$$

$$G_1 = -1.22 - 0.12\left(\frac{a}{c}\right) \tag{143}$$

$$G_2 = 0.55 - 1.05\left(\frac{a}{c}\right)^{0.75} + 0.47\left(\frac{a}{c}\right)^{1.5} \quad . \tag{144}$$

Going back to Eq. 126, it can be rewritten in a more transparent form as either

$$K = \left(\frac{M_m}{\sqrt{Q}}\ \sigma_m + \frac{M_b}{\sqrt{Q}}\ \sigma_b\right)\ \sqrt{\pi a} \tag{145}$$

or

$$K = \left(F_m \sigma_m + F_b \sigma_b\right)\ \sqrt{\pi a} \tag{146}$$

where we have defined the magnification factors F_m and F_b as

$$F_m = \frac{M_m}{\sqrt{Q}} \tag{147}$$

and

$$F_b = \frac{M_b}{\sqrt{Q}} \quad . \tag{148}$$

For comparison, the stress intensity factor for a through-thickness crack of length 2a subjected to a uniform tensile stress, σ, is given by (see Ref. [5])

$$K = \sigma\sqrt{\pi a} \quad . \tag{149}$$

By comparing this to Eq. (146) we see that the magnification factors F_m and F_b are essentially a measure of the enhancement in stress in-

tensity for a semi-elliptical surface flaw over that for a through-crack of the same surface length (width). The dependence of F_m and F_b upon the aspect ratio, a/c, and the dimensionless depth, a/h, is shown in Figs. 56, 57, 58 and 59. Note that while a limiting value of a/c = 0 represents an edge crack, a value of a/h = 0 describes a surface flaw in a semi-infinite body (half-space). A general observation from these curves is that pure tension loads cause higher stress intensities than pure bending loads, for the same value of $\sigma_m = \sigma_b$. Also, when the stress field is predominently bending, K is higher at the surface than at the tip of the crack (for $a/h \gtrsim 0.1$). This implies that fracture will usually originate at the surface in high heat flux components, rather than from within.

Models for Fatigue Crack Growth

The rate of fatigue crack growth, da/dN, can be defined as the amount of crack extension caused by cyclic stresses within a single load cycle. It has been found experimentally to correlate very well with the stress intensity factor range, ΔK, where

$$\Delta K = K_{max} - K_{min} \quad . \tag{150}$$

For most metals, the relationship between da/dN and ΔK exhibits three different regimes of behavior, as shown schematically in Fig. 60.

During stage I, the so-called threshold regime, da/dN becomes vanishingly small as ΔK approaches ΔK_o, the threshold stress intensity

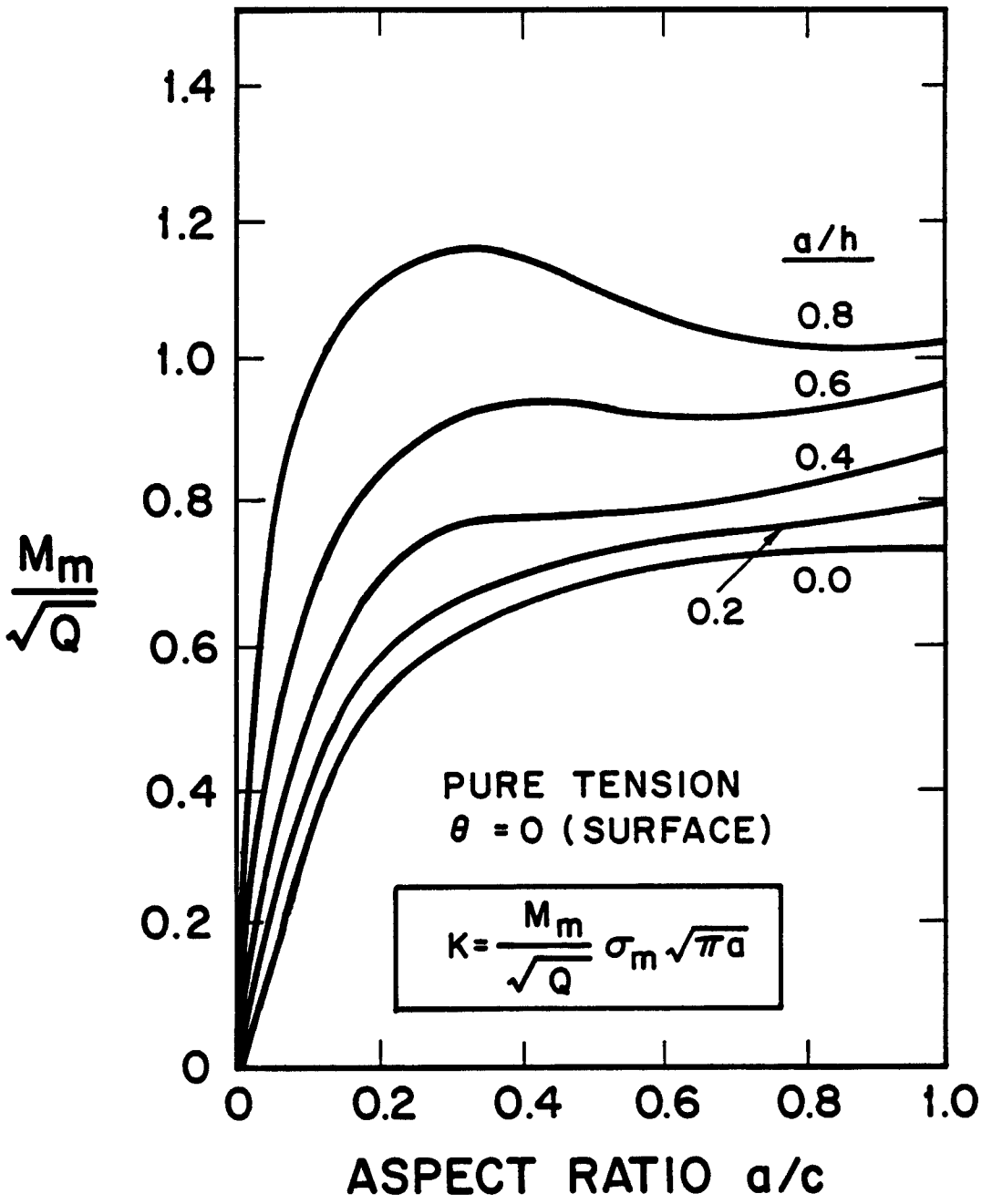

Figure 56. Variation of the magnification factor, F_m, with aspect ratio and crack depth for pure tension loads and $\theta = 0$ [29].

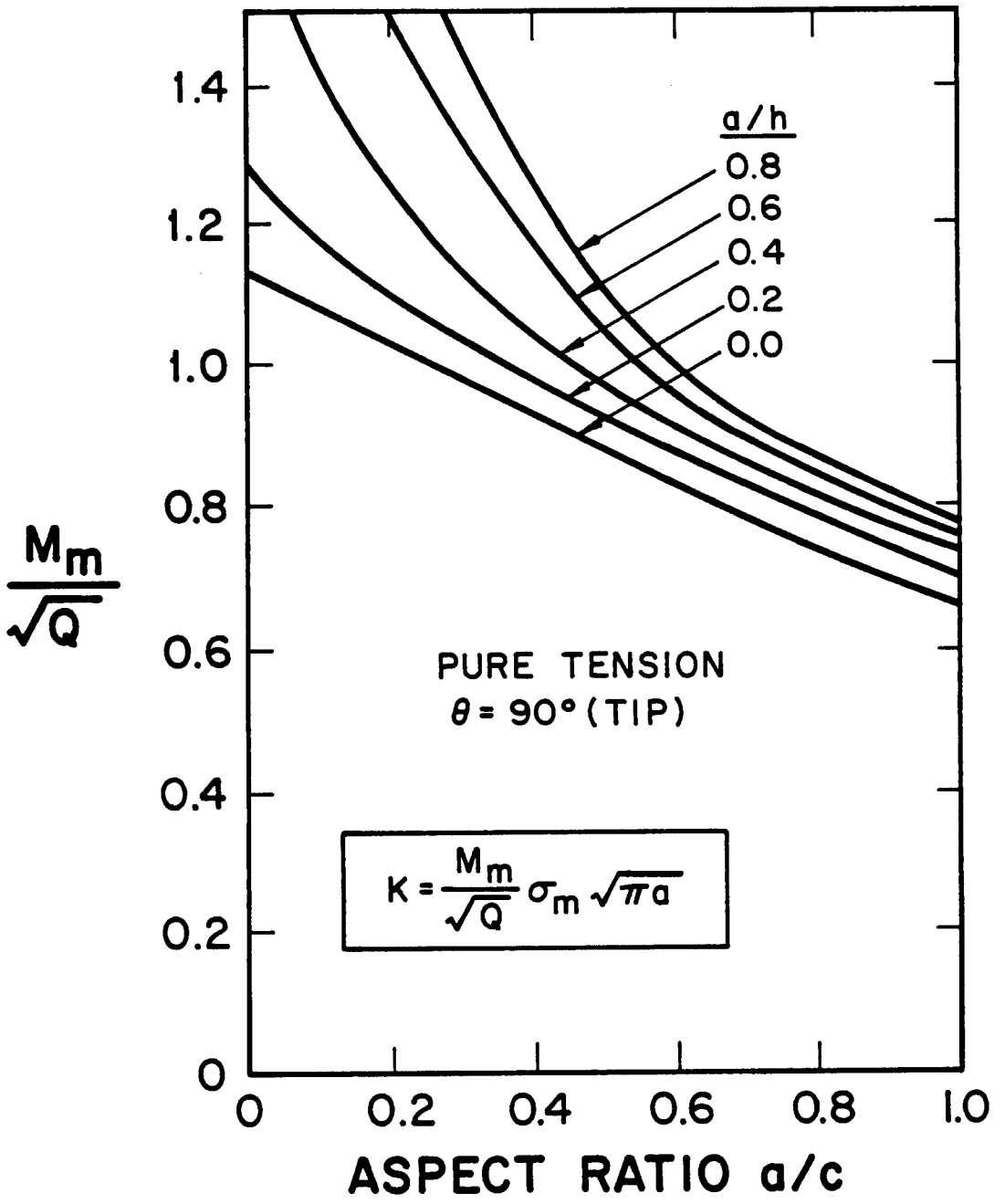

Figure 57. Variation of the magnification factor, F_m, with aspect ratio and crack depth for pure tension loads and $\theta = 90°$ [29].

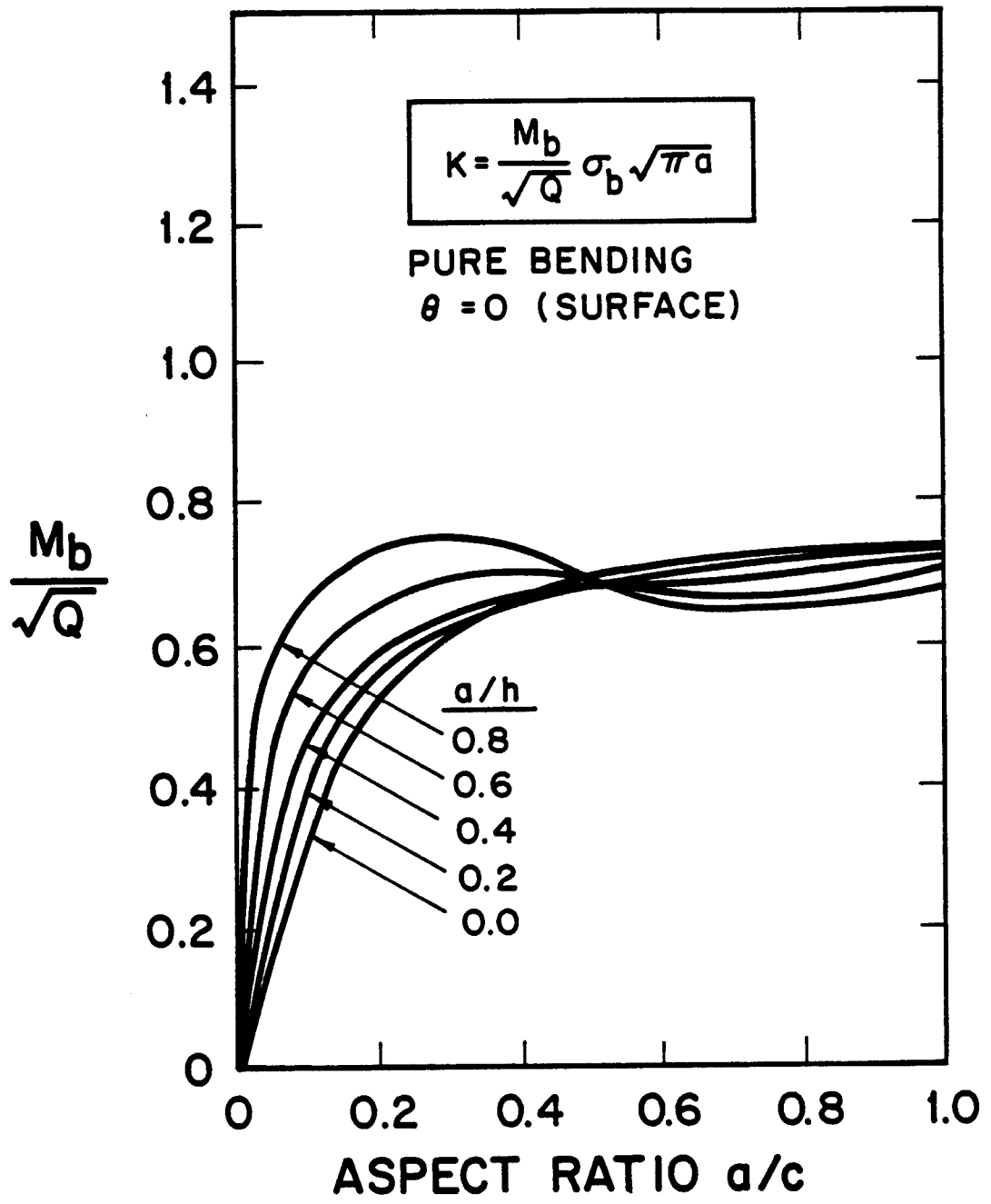

Figure 58. Variation of the magnification factor, F_b, with aspect ratio and crack depth for pure bending moments and $\theta = 0$ [29].

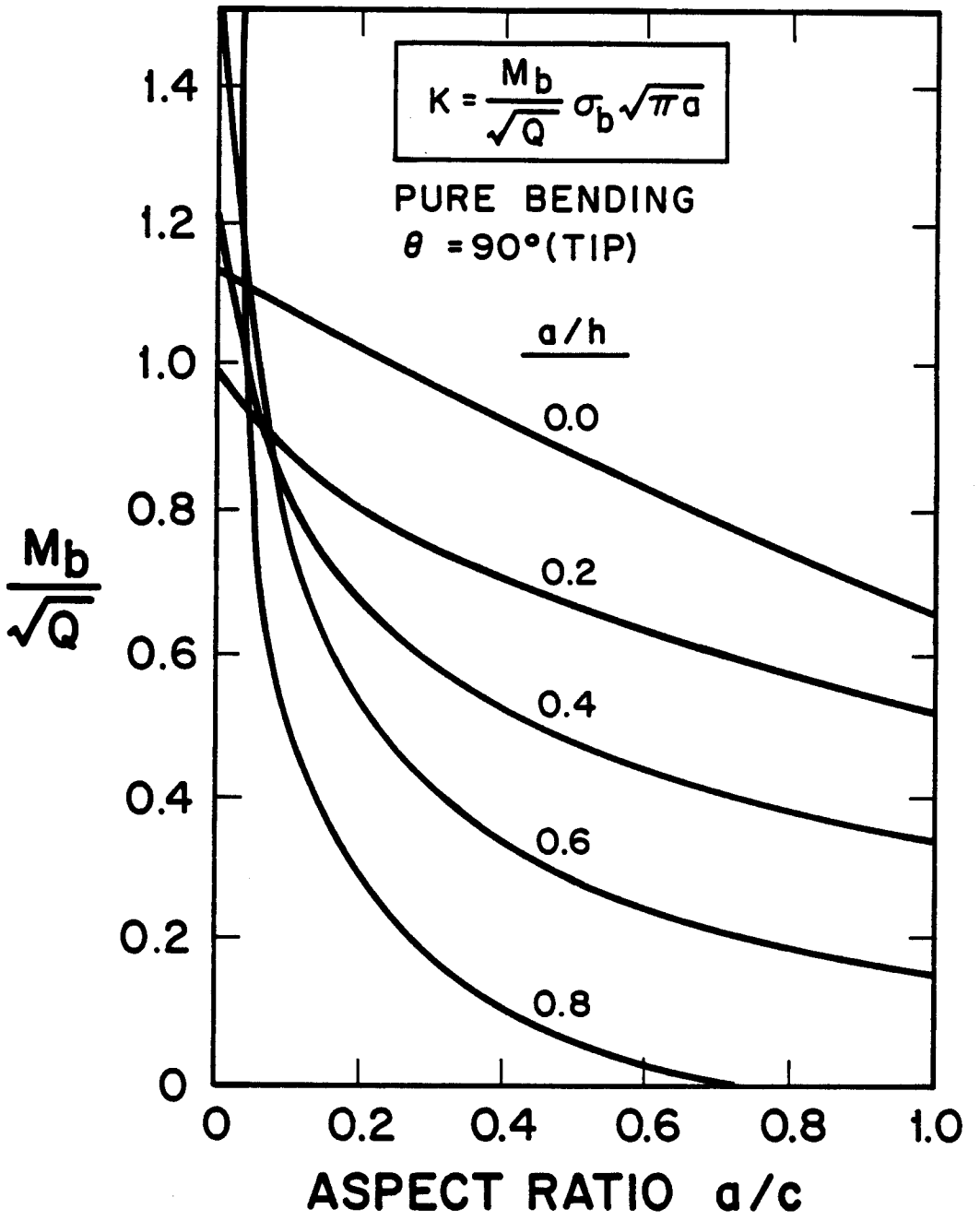

Figure 59. Variation of the magnification factor, F_b, with aspect ratio and crack depth for pure bending moments and $\theta = 90°$ [29].

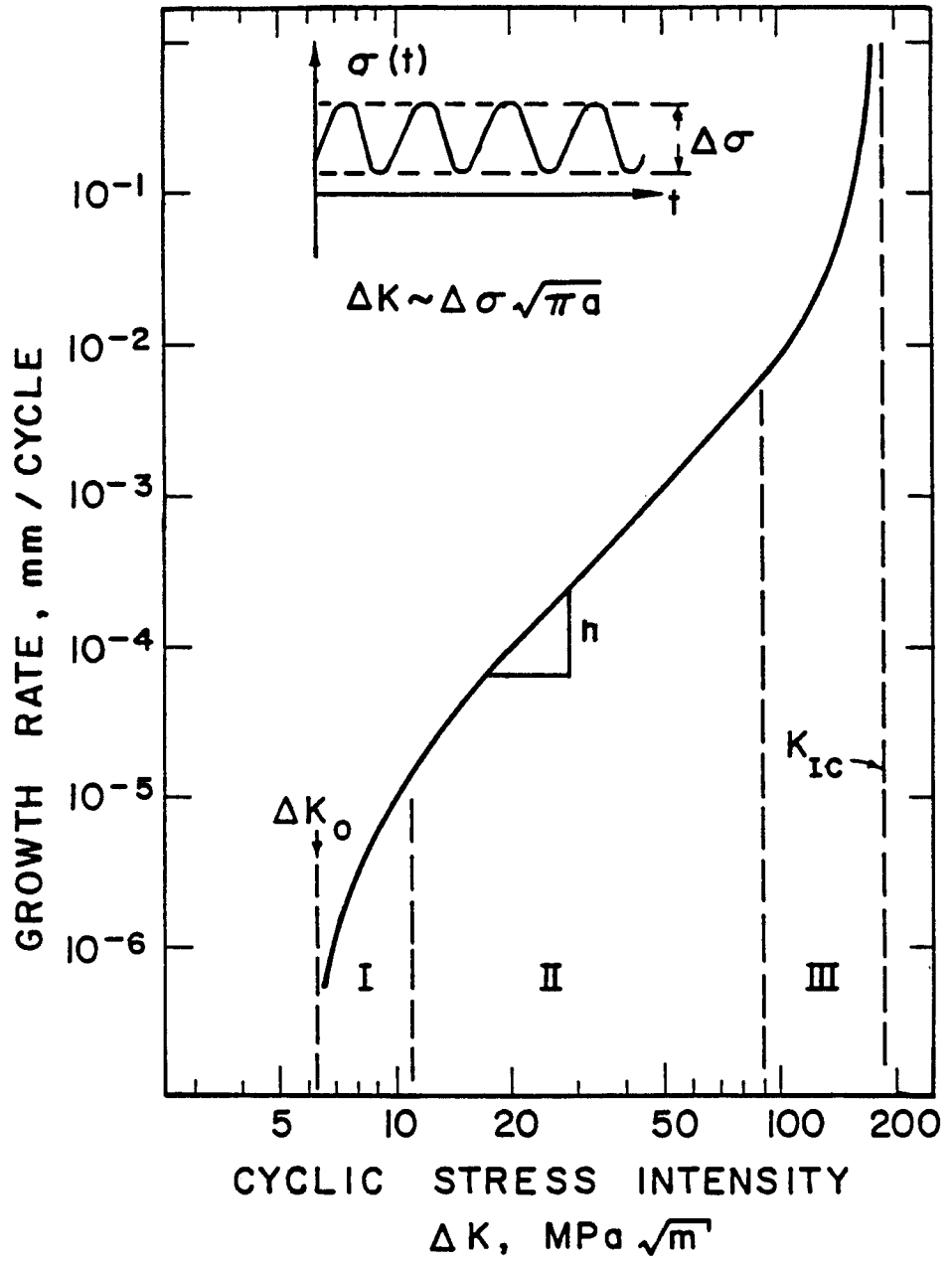

Figure 60. Schematic of three stages of fatigue crack growth behavior. Stage I is the threshold regime. Stage II is the linear, stable growth regime, and Stage III is the unstable, fast growth/fracture regime.

factor. In stage II, stable crack growth is observed over the range of ΔK from 10 MPa $\sqrt{m}$ to 100 MPa $\sqrt{m}$, for steels. Here, the data can be successfully fit to a power law equation proposed by Paris in 1963 [30]:

$$\frac{da}{dN} = C(\Delta K)^n \quad . \tag{151}$$

Finally, in stage III, unstable crack growth occurs when ΔK approaches K_{Ic}, the plane strain fracture toughness. Fast fracture occurs when $K_{max} \geq K_{Ic}$. ΔK_o and K_{Ic} are traditionally considered to be basic materials properties, however, neutron irradiation is expected to degrade both of these properties. Figure 61 presents the actual da/dN data base for 304 stainless steel, compiled by James [31]. Figure 62 shows the design curves for both 304 and 316 S.S. as given by the Nuclear Systems Materials Handbook (NSMH) [32]. Neither of these data sets show the stage I or stage III regimes, however. Note that a scatter factor of four is present in the data.

Temperature Effects on FCG

The effects of temperature on fatigue crack growth (FCG) rates for stainless steels can be significant. Increases in da/dN of two to eight times has been observed by raising the temperature from 25°C to 593°C in an air environment (see James [31]). Because the effect persists even in a vacuum, as seen in Fig. 63, its cause cannot be solely attributed to an environmental interaction, such as oxidation at the crack tip. Instead, it appears to be related to the amount of

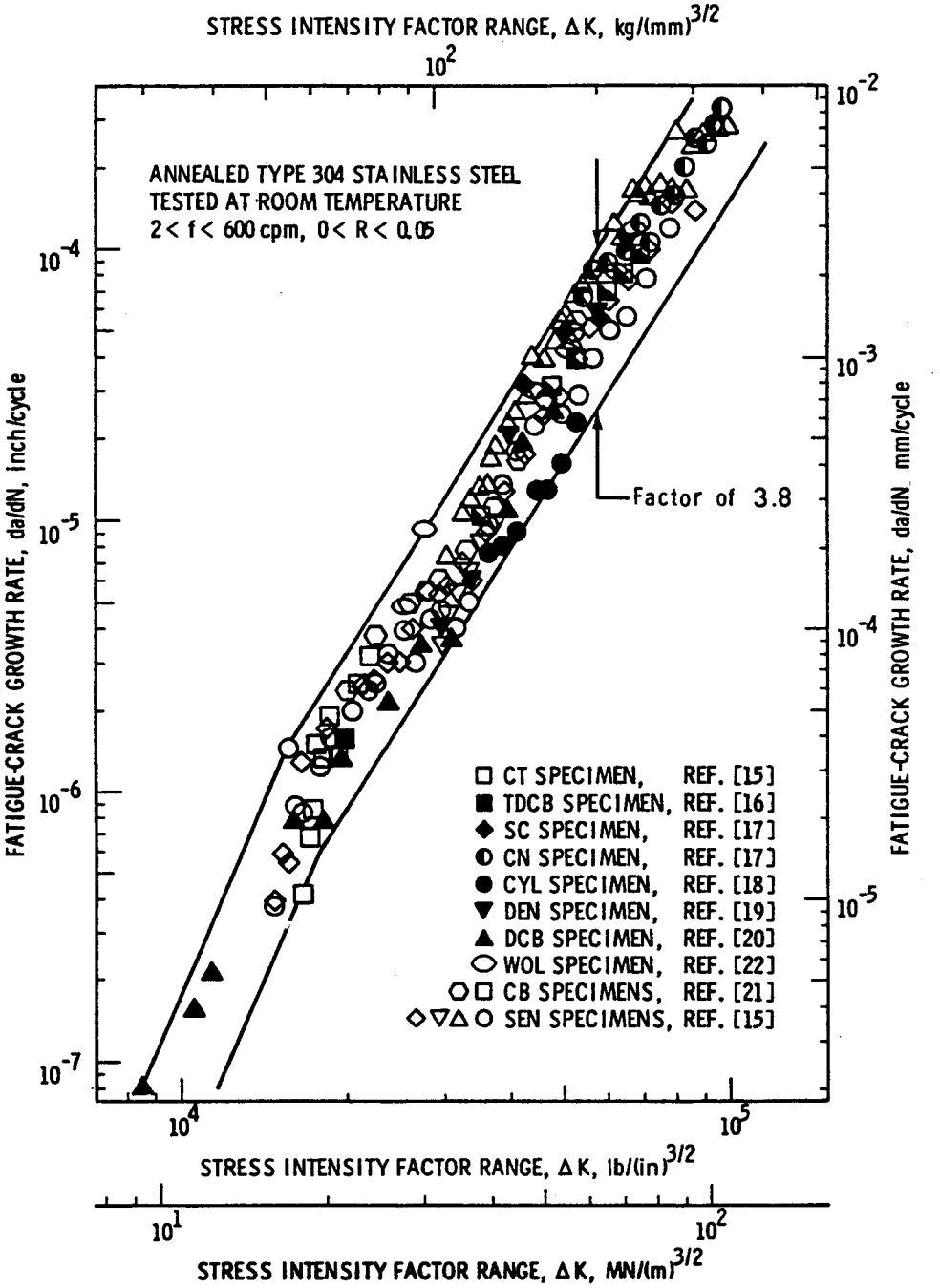

Figure 61. Fatigue crack growth behavior of 304 stainless steel at room temperature as determined from 10 different specimen designs [31].

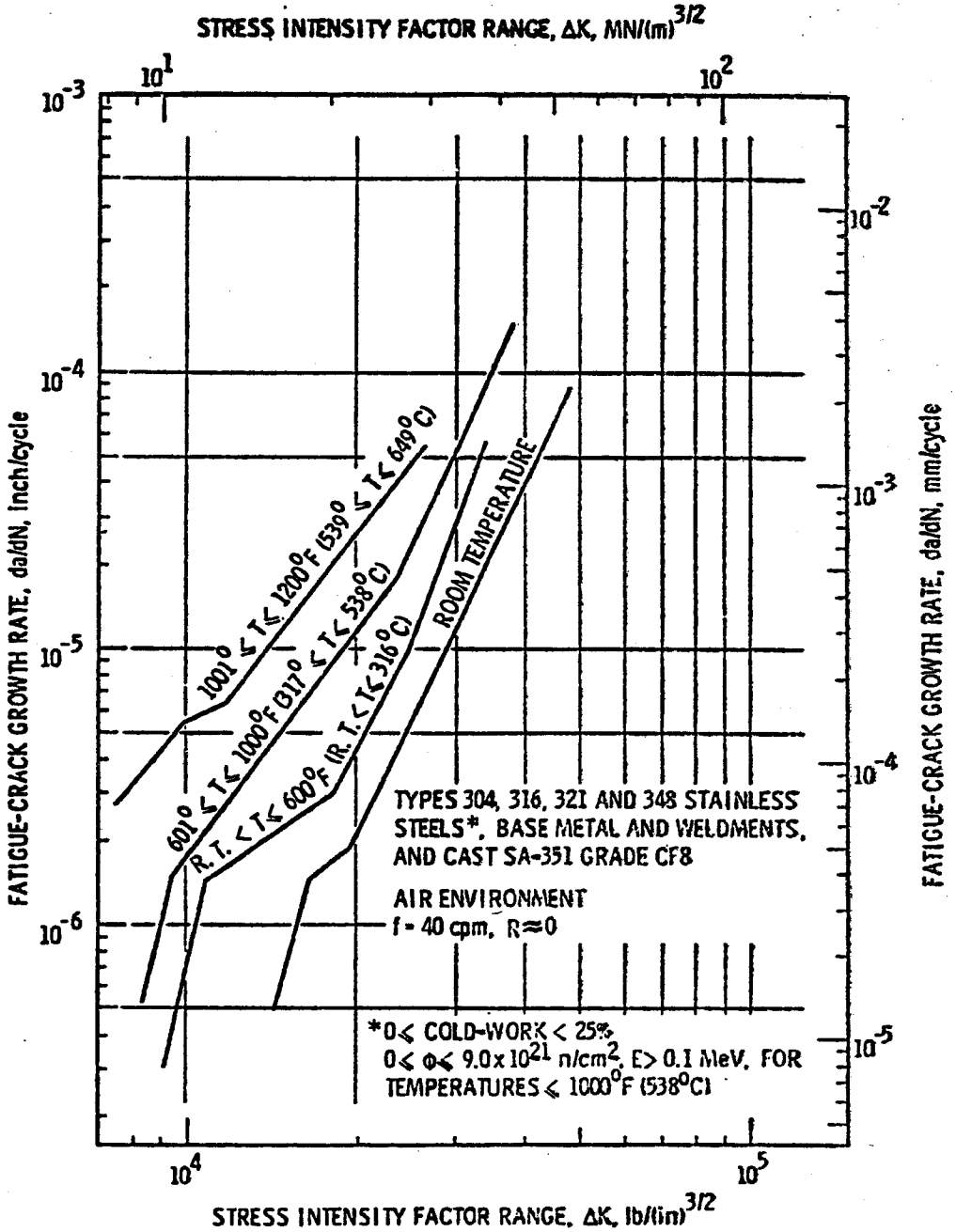

Figure 62. Design fatigue crack growth curves for austenitic stainless steels at various temperatures taken from the Nuclear Systems Materials Handbook [32].

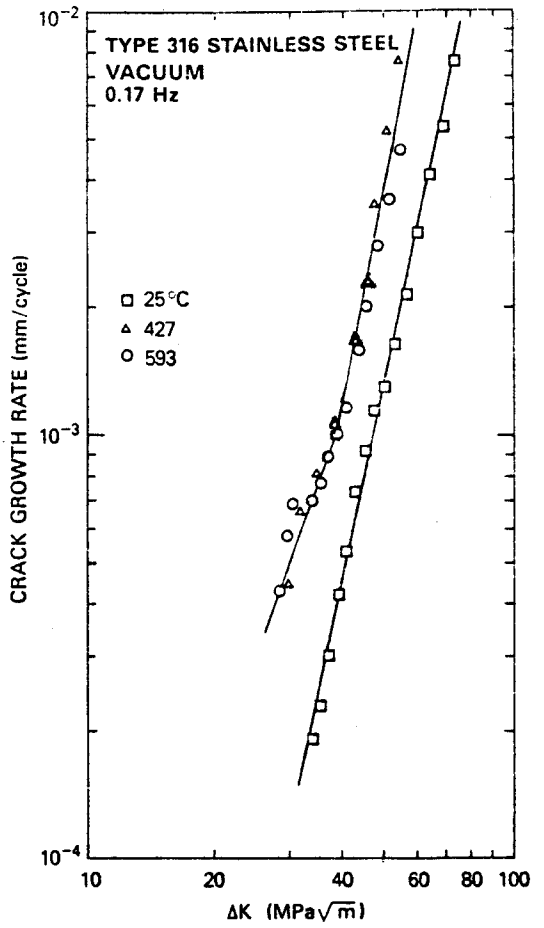

Figure 63. Fatigue crack growth rates for 316 stainless steel in vacuum for different temperatures [36].

cyclic strain at the crack tip. Since this is dependent on the elastic modulus, E, it was proposed by Pearson [33] in 1966 that da/dN for many different metals could be plotted on a single master curve by normalizing ΔK as $\Delta K/E$. As shown by Speidel [34] in Fig. 64, Pearson's idea works surprisingly well.

Sadanada and Shahinian [36] recognized that since the elastic modulus decreases with increasing temperature, then the temperature effect could be predicted by the modulus correction $\Delta K/E$. Their results, shown in Figure 65, show excellent agreement with this concept.

The WISECRACK computer code, described in Chapter 7, uses this concept by replacing ΔK each place it appears in the da/dN equations with $f \cdot \Delta K$, where f is defined as

$$f = \frac{E(T_o)}{E(T)} \tag{152}$$

and T_o is room temperature (25°C). However, since the temperature is a function of both space and time, we must choose the appropriate value of T to compute f. This is accomplished by first selecting the temperature corresponding to the specific angular location along the crack front, θ, (see Fig. 49). Secondly, we assume that the temperature must be chosen at the particular moment in time when the crack opening is the greatest, i.e. at K_{max}.

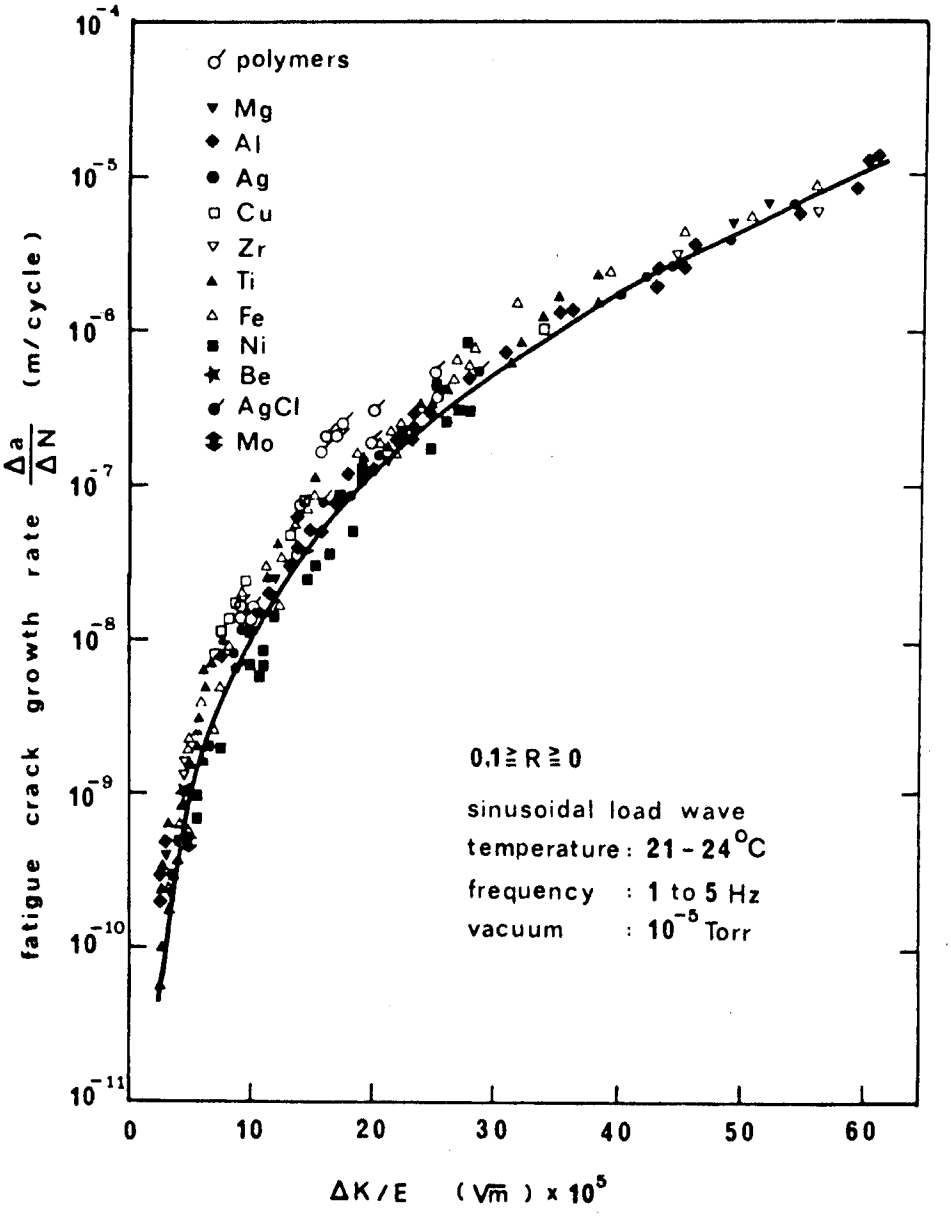

Figure 64. Normalization of fatigue crack growth rates with Young's Modulus for 11 different metals [34].

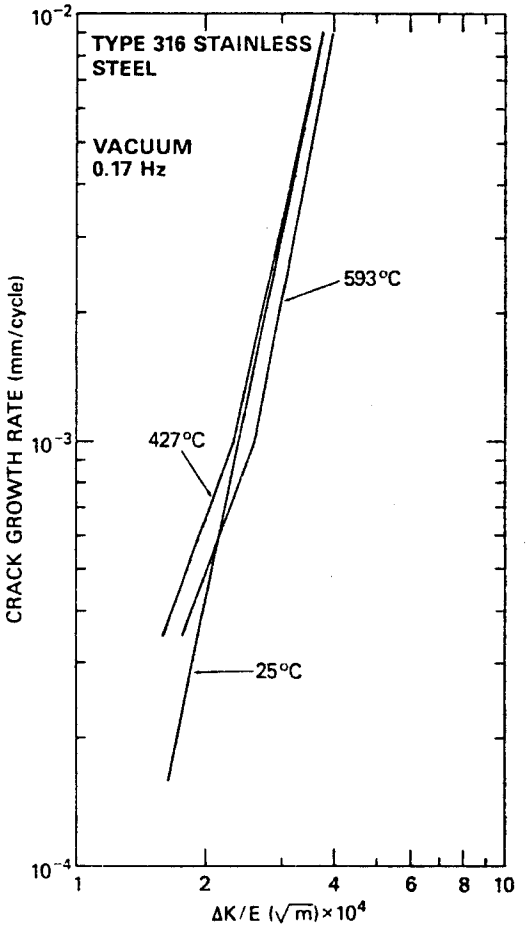

Figure 65. Normalization of fatigue crack growth rate of 316 stainless steel in vacuum to Young's Modulus at various temperatures [36].

R-Ratio Effect on FCG

In addition to the temperature effect, increasing the mean (or average) stress level, $\frac{1}{2}(\sigma_{max} + \sigma_{min})$, is also found to accelerate crack growth, as shown in Fig. 66. To model this effect we can define a mean stress intensity factor, K_{mean}, which is directly proportional to the mean stress, and is given by

$$K_{mean} = \frac{1}{2}(K_{max} + K_{min}) \quad . \tag{153}$$

This is related to the so-called R-ratio by

$$K_{mean} = \frac{1}{2}\Delta K \left[\frac{1 + R}{1 - R}\right] \tag{154}$$

where

$$R = \frac{K_{min}}{K_{max}} \quad . \tag{155}$$

From Eg. (153) we observe that for constant ΔK, increasing values of K_{mean} also correspond to larger values of R. A traditional method of correlating the R-ratio effect is to use the Walker correction [38] with the Paris equation, namely

$$\frac{da}{dN} = C[K_{max}(1-R)^m]^n \quad . \tag{156}$$

where $m = 0.3 - 0.7$.

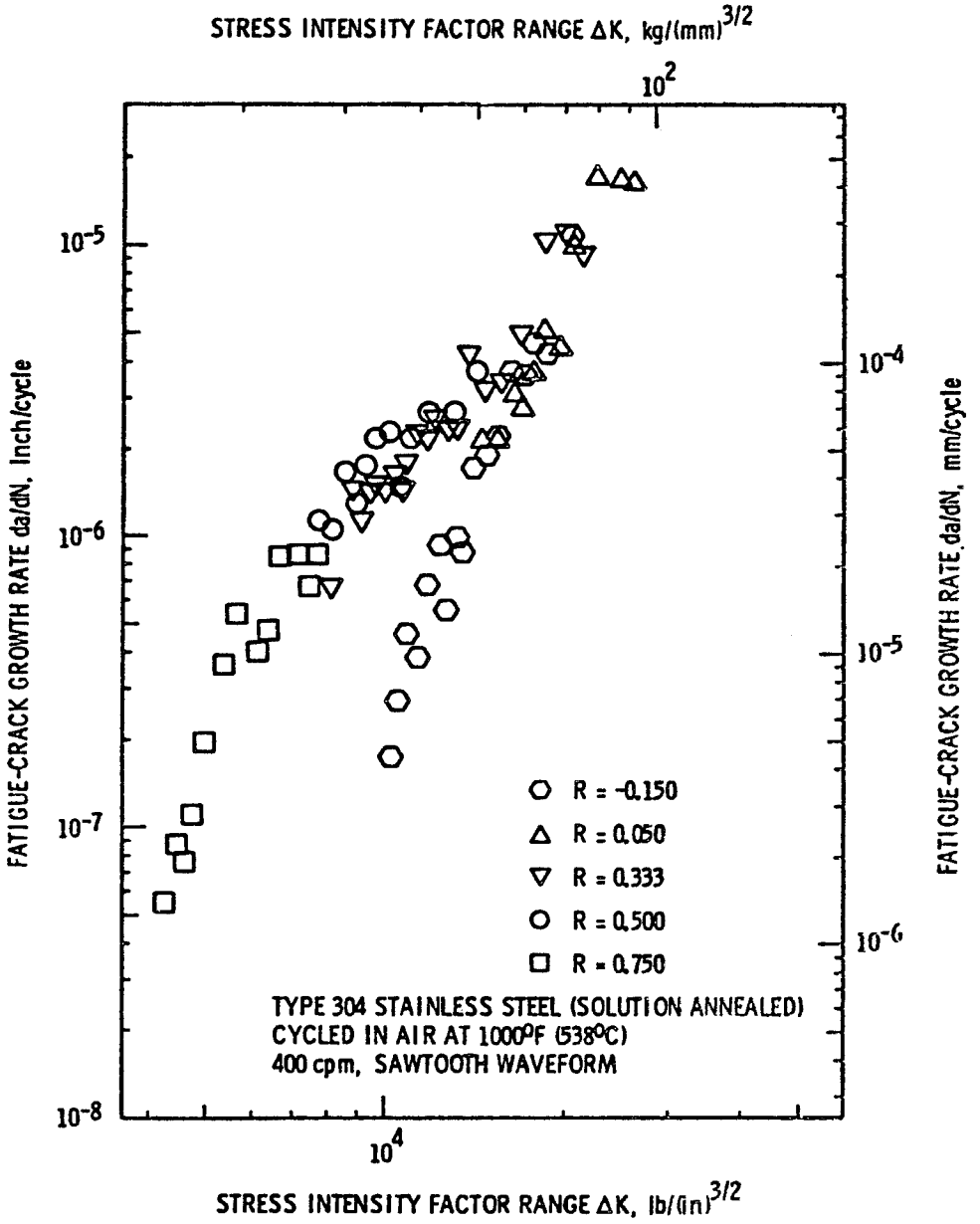

Figure 66. Effect of R-ratio on fatigue crack growth rates in 304 stainless steel at 538°C in air [31].

Threshold Effect on FCG

In the stage I regime of fatigue crack growth (see Fig. 60), da/dN decreases and eventually becomes vanishingly small as ΔK approaches ΔK_o, the threshold stress intensity factor for non-propagating cracks. Figure 67 illustrates this effect for 304 S.S., tested at R = -1 and T = 77°K and 293°K by Tschegg and Stanzel [39]. The rates measured in this Figure are three orders of magnitude lower than traditional da/dN data and indicate a threshold $\Delta K_o \cong 6$ MPa$\sqrt{m}$. In many respects, ΔK_o is analogous to $\Delta\sigma_e$, the endurance limit for smooth speciman fatigue testing where cyclic stresses less than $\Delta\sigma_e$ permit an infinite number of cycles-to-failure, N_f.

Although a conservative engineer can simply extrapolate the Paris equation into the threshold regime, therefore giving higher da/dN values, it is economically beneficial to seek a better understanding of the actual behavior in stage I. Moreover, when 10^9 to 10^{10} cycles can be accumulated in an inertially-confined fusion reactor first wall, it may be essential to know da/dN vs. ΔK at 10^{-12} - 10^{-14} m/cycle. Fortunately, threshold behavior has been studied for roughly 20 years and an adequate set of data exists for steels.

Three excellent reviews of threshold behavior have been published including: Lucas and Ritchie in 1981 [40], Ritchie in 1979 [41] and Weiss and Lal in 1973 [42]. Not included in these reviews are recently published papers by Tschegg and Stanzl [39, 43, 44], Muherjee and Vanderglas [45] and Stewart [46]. The review by Ritchie [41] includes references to threshold data of ferritic martensitic and austenitic steels,

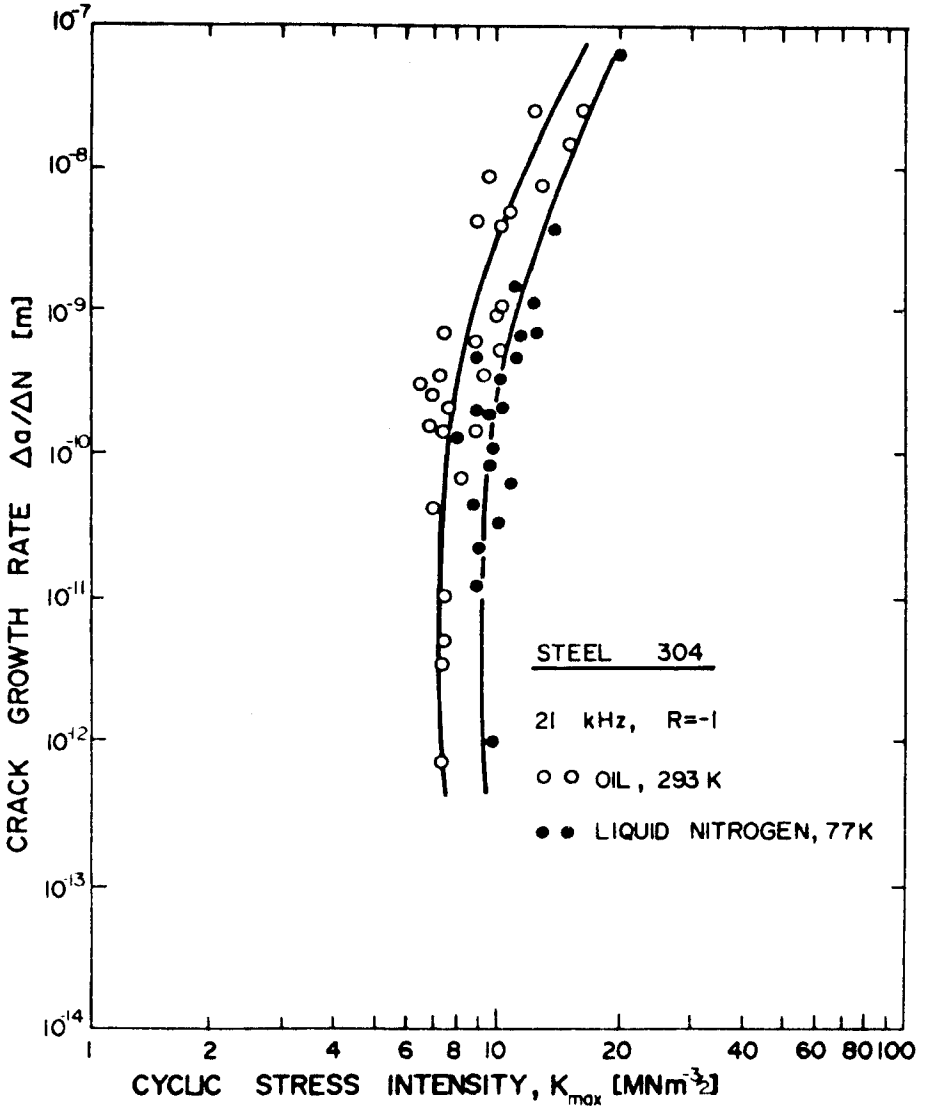

Figure 67. Fatigue crack growth rates in the threshold regime for 304 stainless steel [39].

titanium, titanium alloys, copper alloy, aluminum alloys and nickel alloys. Ritchie also discusses the sensitivity of da/dN in this regime to the following variables: mean stress (R-ratio), temperature, environment, monotonic and cyclic strengths, crack size, cyclic frequency, prior stress history, grain size and grain-boundary composition. Apparently, no data exists regarding radiation effects on ΔK_o.

With regard to environmental effects on ΔK_o, it appears that higher thresholds are measured in inert environments, such as vacuum, helium, and liquid sodium. Surprisingly, low temperature (260°C) steam has also been found to increase threshold values in 403 S.S. as shown in Fig. 68 from Tu and Seth [124]. This is contrary to the observed effect in stage II, where steam enhances da/dN. Tu and Seth explain that the beneficial effects of steam in stage I is due to crack branching: "It is concluded that the higher ΔK_{th} value in steam than in air is attributed to the presence of small branched cracks. The crack branching may be due to an embrittlement process caused by steam. Crack branching is a much more efficient process in reducing the crack tip stress intensity factor range than crack blunting in the high frequency corrosion fatigue test in steam." It is clear that much more data is needed on environmental effects in this regime of ultra-low crack growth rates.

Three different but equally successful methods have been proposed to correlate the da/dN data in both stage I and II. In 1971, Klesnil and Lukas [47] suggested the following modification to the Paris equation:

$$\frac{da}{dN} = C(\Delta K^n - \Delta K_o^n) \quad . \tag{157}$$

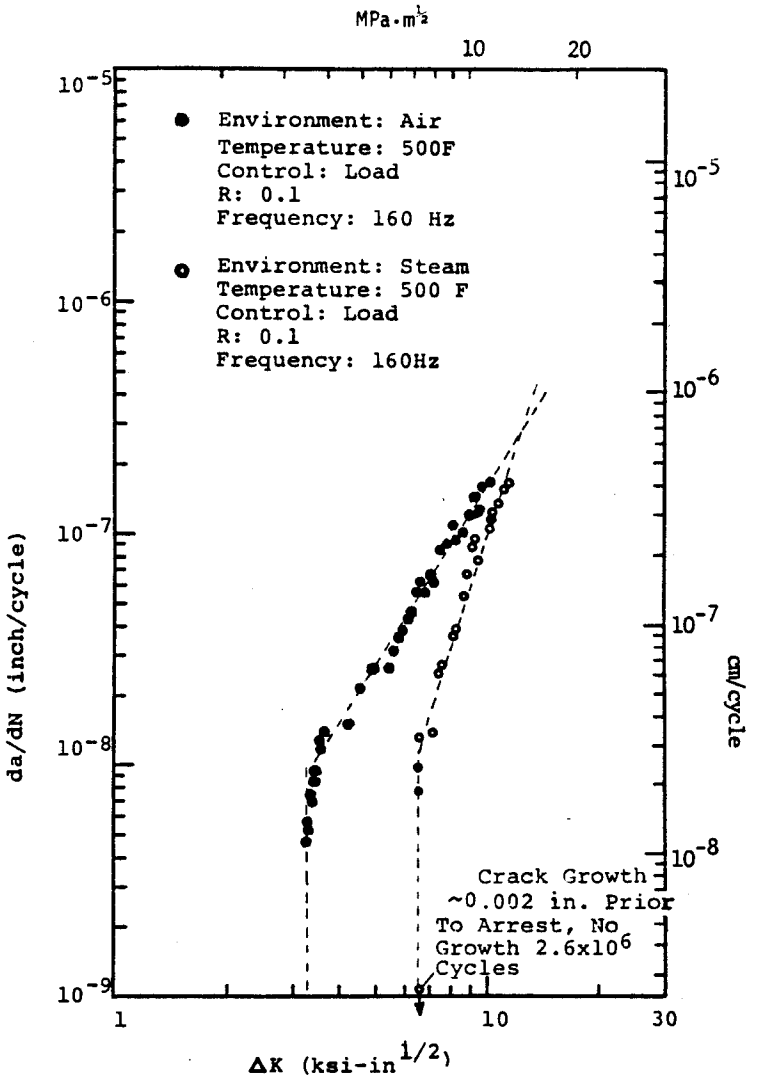

Figure 68. Effect of an air or steam environment on threshold fatigue crack growth in a stainless steel at 260°C [124].

Then, in 1972, Donahue et al [49] found good agreement with the following:

$$\frac{da}{dN} = \frac{4A}{\pi\sigma_y E} [\Delta K^2 - \Delta K_o^2] \quad (158)$$

Finally, in 1974, Speidel [34] proposed a somewhat different form:

$$\frac{da}{dN} = C(\Delta K - \Delta K_o)^n \quad (159)$$

Stanzl and Tschegg [43] have applied Eq. 158 to threshold data for mild steel, copper, and 304 S.S. with very good success over four orders of magnitude for da/dN.

Up to this point, we have assumed that the R-ratio is zero. However, it was shown earlier that an increase in the R-ratio (mean stress level) caused increased fatigue crack growth rates in stages II and III. This effect is enhanced in the threshold regime, as shown in Figure 69.

As the R-ratio increases, ΔK_o decreases in a roughly linear fashion. Barsom [50] first suggested, in 1974, that the data could be correlated by

$$\Delta K_o = \Delta K_{oo} (1 - bR) \quad (160)$$

where ΔK_{oo} is the threshold ΔK at R = 0 and b is a constant ranging from 1.05 to 0.31 for steels [51]. Figure 70 presents a recent compilation of threshold data at various R-ratios for 304 and 316 stainless steel by Lucas and Ritchie [40].

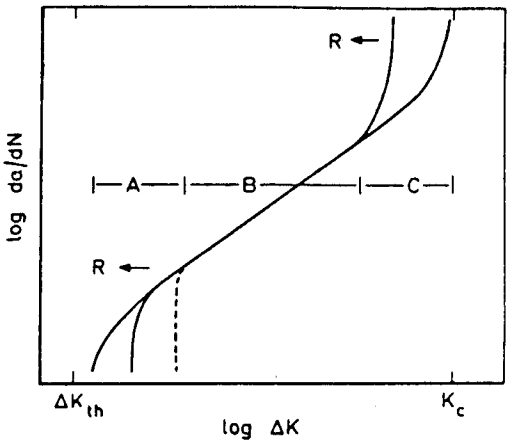

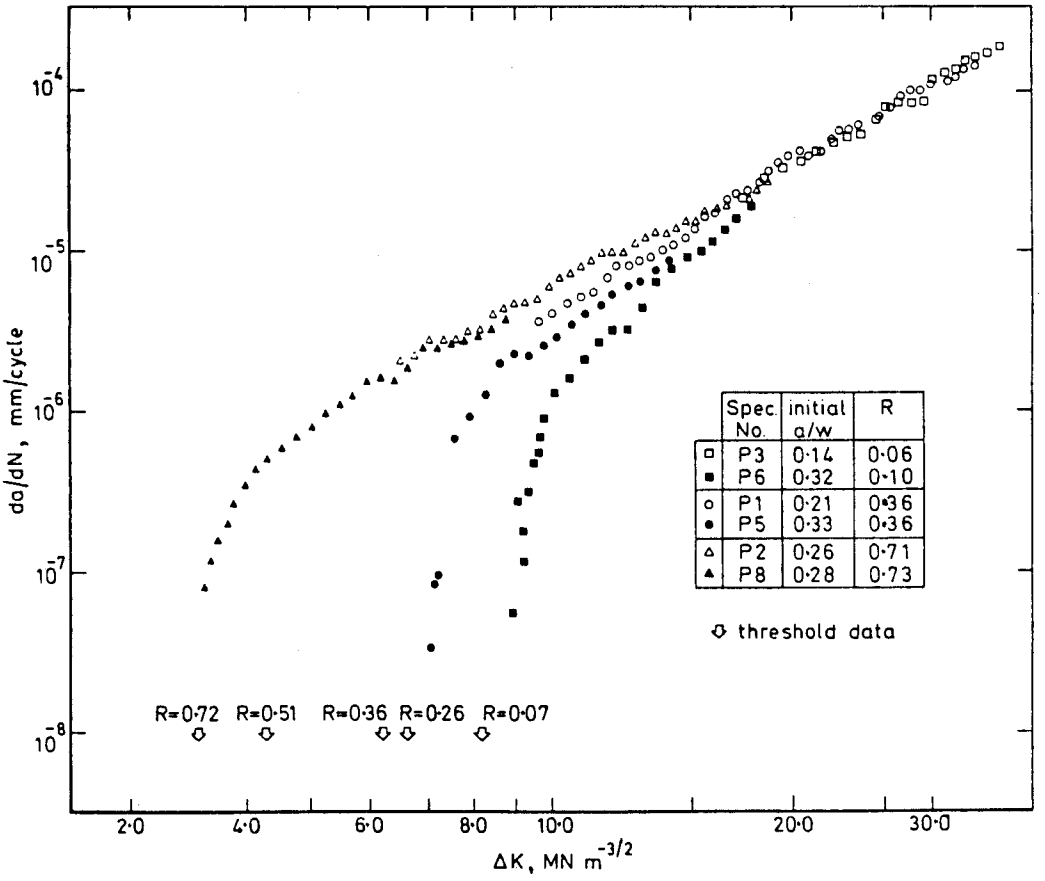

Figure 69. Effect of R-ratio on the threshold fatigue crack growth rates for a pearlitic steel tested at room temperature [202].

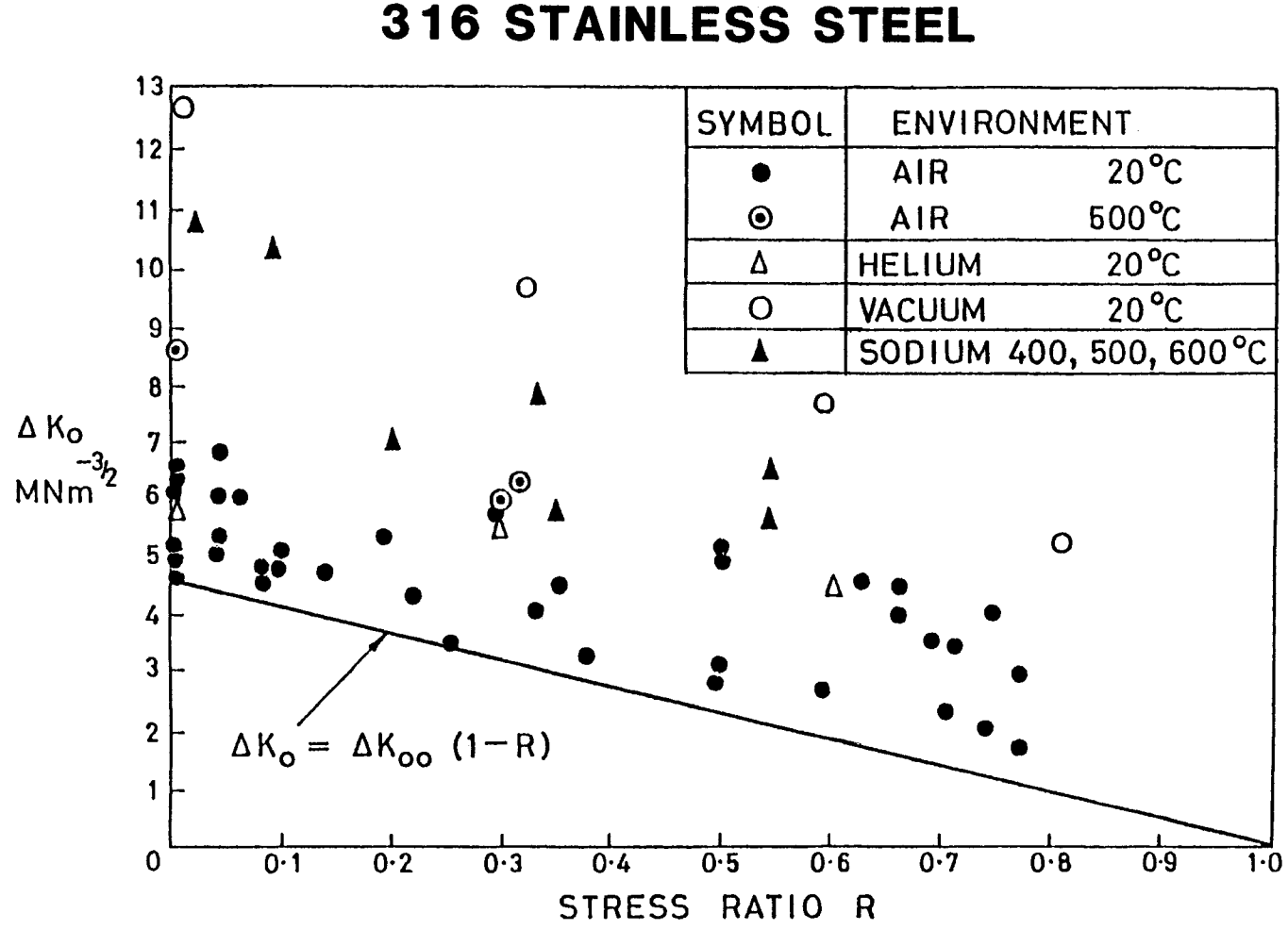

Figure 70. Effect of R-ratio on threshold stress intensity factor for 316 stainless steel [40].

As with the other steels, the general trend of decreasing ΔK_o with increasing R-ratio is also obeyed. For negative R-ratios the sensitivity appears to be less. A nominal fit to the data, using Eq. (160), gives the following:

$$\Delta K_o = 5.4\ (1 - 0.9R) \text{ for } R > 0 \tag{161}$$

and

$$\Delta K_o = 5.4\ (1 - 0.2R) \text{ for } R < 0\ . \tag{162}$$

The data in Fig. 70 also indicate that higher temperatures and "inert" environments such as helium, liquid sodium, or vacuum result in higher thresholds, at the same R-ratio. Although this is beneficial, other factors may degrade the threshold, especially radiation damage and hydrogen effects. Therefore, a conservative, lower-bound envelope for stainless steel threshold data in air would be

$$\Delta K_o = 4.5\ (1 - R) \text{ for } R > 0 \tag{163}$$

and

$$\Delta K_o = 4.5\ (1 - 0.33R) \text{ for } R < 0. \tag{164}$$

The effect of yield strength on ΔK_o will be discussed in a later section.

Short Crack Correction

Most of the data for da/dN is usually obtained from "large" cracks, e.g. $a_o > 1$ mm. However, when "short" cracks are used, $a_o <$ 0.5 mm, they are observed experimentally to grow faster than long

cracks at the same ΔK and R-ratio. Unfortunately, for the thin-walled high heat flux components in a fusion device, this is within the range of flaw sizes of interest. Pearson [52], in 1975, was the first to report this effect. He found significant increases in da/dN for short cracks in Al alloys. Also, the data shown in Fig. 71, from Topper and El-Haddad [53], demonstrate that this enhancement is only significant in the stage I threshold regime. Then, in 1976, Kitagawa et al [54, 55] reported that the threshold ΔK_o was smaller for cracks less than 0.3 mm than for large cracks where ΔK_o = constant.

Two possible effects may explain this behavior; both being related to the breakdown of continuum mechanics for these small flaws. First, Talug and Reifsnider [56] demonstrated that the crack tip stresses are increased, when compared to the classical Westergaard solution, as the tip approaches the free surface. This would increase ΔK, and hence, da/dN. The second explanation of an enhanced ΔK is related to the reduced flaw resistance of the surface grains, as compared to interior grains, due to their lack of constraint by the surrounding grains.

El Haddad and co-workers [57,58] have developed a simple scheme for empirically correlating the increase in da/dN with small crack sizes. They recommend replacing the actual crack length, a , by an effective length, $a + \ell_o$, whenever this term appears in equations for K. Consequently, Eq. (128) would then become

$$K = (M_m\sigma_m + M_b\sigma_b)\sqrt{\frac{\pi(a + \ell_o)}{Q}} \quad . \tag{165}$$

As $a >> \ell_o$, we see the effect of the correction becomes negligible.

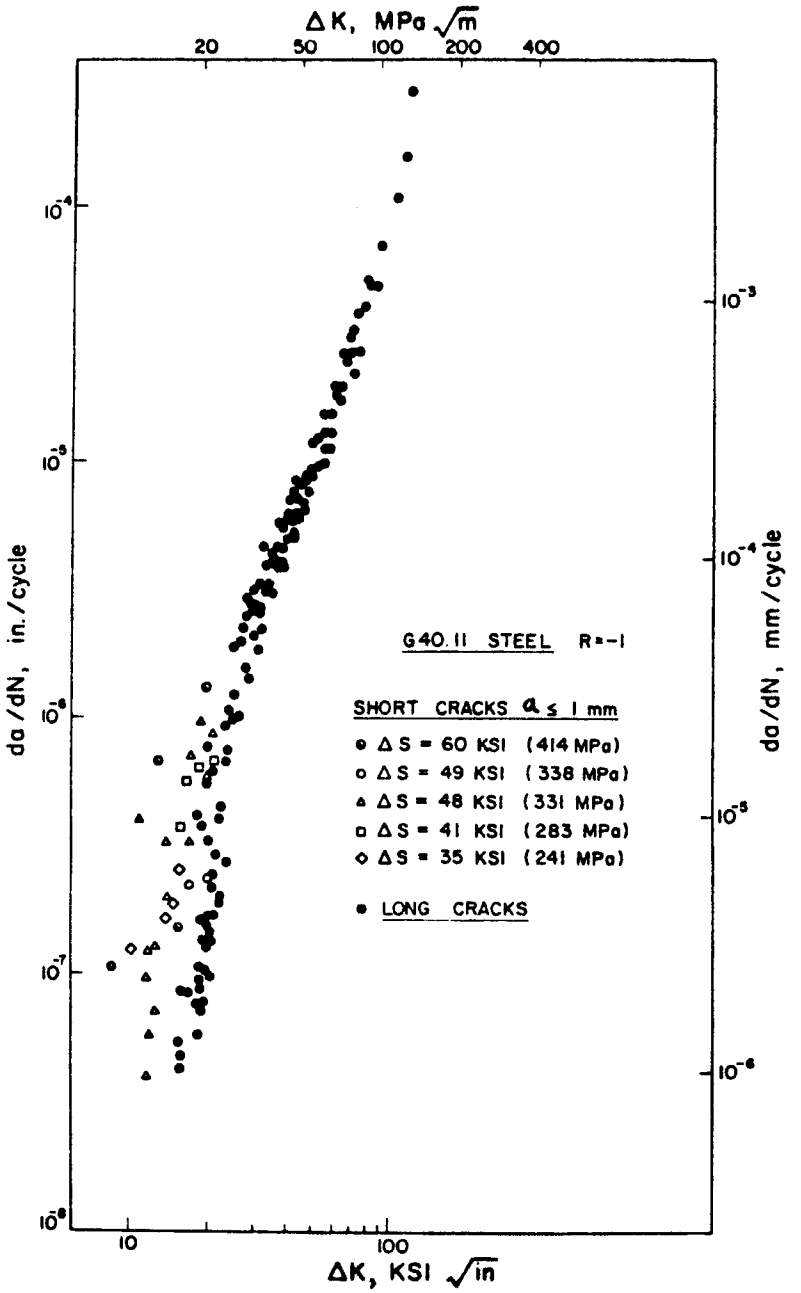

Figure 71. Comparison of fatigue crack growth rates for short and long cracks [53].

The reasoning behind this short crack correction factor, ℓ_o, is related to the threshold stress intensity factor. If we use the ΔK correction for a through-crack in a plate, we obtain

$$\Delta K = \Delta\sigma\sqrt{\pi(a + \ell_o)} \quad . \tag{166}$$

Now, at the threshold, we can write

$$\Delta K_o = \Delta\sigma_o \sqrt{\pi(a + \ell_o)} \tag{167}$$

where $\Delta\sigma_o$ is the cyclic stress range for specimans with non-propagating cracks. Solving this equation for $\Delta\sigma_o$ gives

$$\Delta\sigma_o = \frac{\Delta K_o}{\sqrt{\pi(a + \ell_o)}} \quad . \tag{168}$$

Figure 72 plots this equation using the data from Fig. 71. The proper limiting behavior is predicted as $a \to 0$. According to a recent review article by Hudak [59], the use of Eq. (168) has been successful in correlating stage I behavior for both long and short cracks.

To determine ℓ_o, we must consider the limit as the actual crack depth, a, goes to zero from Eq. (168):

$$\lim_{a \to o} [\Delta\sigma_o] = \frac{\Delta K_o}{\sqrt{\pi \ell_o}} \quad . \tag{169}$$

For smooth, uncracked fatigue specimens the left-hand side of Eq. (169) can now be interpreted as a definition of the traditional endurance

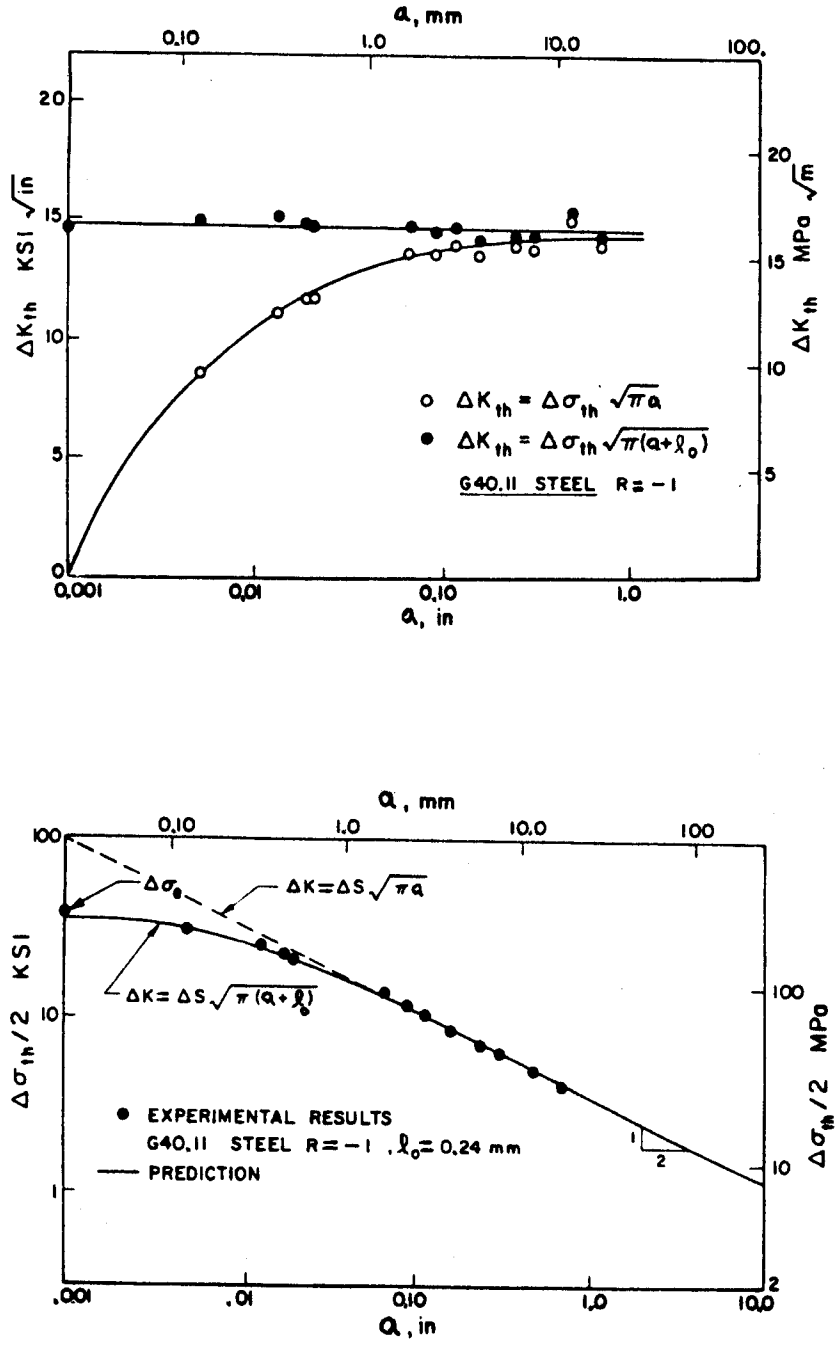

Figure 72. Behavior of the threshold stress and threshold stress intensity factor for short cracks. The short crack correction is seen to correlate all of the data [58].

limit, $\Delta\sigma_e$, below which fatigue failure never occurs. Equating these two concepts then gives us a theoretical relationship between the endurance limit and the threshold stress intensity factor:

$$\Delta\sigma_e = \frac{\Delta K_o}{\sqrt{\pi \ell_o}} \quad . \tag{170}$$

Conversely, if both $\Delta\sigma_e$ and ΔK_o are known, it would allow us to calculate ℓ_o as

$$\ell_o = \frac{1}{\pi} \left[\frac{\Delta K_o}{\Delta\sigma_e}\right]^2 \quad . \tag{171}$$

Using ΔK_o = 5.4 MPa $\sqrt{m}$ and $\Delta\sigma_e$ = 380 MPa (55 ksi) for 316 SS, we find that ℓ_o = 0.064 mm.

Environmental Effects on FCG

It is well known that the type of environment can significantly affect fatigue crack growth, especially at low ΔK, low cyclic frequencies and elevated temperatures. The phenomenon is often referred to as corrosion-fatigue or fatigue-environment interactions. In general, we can define an "aggressive" environment as one that enhances da/dN when compared to room temperature data in air (all other variables being equal). Conversely, an "inert" environment refers to lower crack growth rates than in room temperature air. In a fusion reactor, aggressive environments include hydrogen (tritium), liquid lithium, and possibly water or steam. Inert environments would include liquid sodium, helium, and vacuum. For a bare unprotected component

that is subjected to energetic particle fluxes, it is not clear how one might catagorize this environment (refer to the section in this chapter on wall thinning and crack erosion). The purpose of this section is to qualitatively discuss the wide range of environmental effects on stainless steel at elevated temperatures.

The effect of air on elevated temperature fatigue crack propagation is important to review because previous investigators have used high temperature air data for their lifetime assessments (see Ref. [12] for example). Figure 73 compares the effects of air vs. vacuum on da/dN for temperatures of 25, 427 and 593°C. It can be seen that a high ΔK ($\Delta K > 30$ MPa$\sqrt{m}$), there is little difference between air and vacuum because the rates are too fast. But at lower ΔK ($\Delta K < 30$ MPa$\sqrt{m}$), air becomes an increasingly "aggressive" environment as the rates are slower and the interaction time is greater. This trend persists even when the air data is normalized by the elastic modulus, $\Delta K/E$, according to results from Shahinian, et al [37]. This demonstrates that a significant environmental interaction is occurring for low ΔK's.

According to Smith et al [60] and Ericsson [61], oxygen in the air promotes oxidation at the crack tip surfaces at elevated temperatures. Figure 74 from Smith's paper confirms this explanation by showing an increase of two orders of magnitude in da/dN for 316 SS at 500°C when the oxygen pressure was increased from 10^{-3} torr to 1 torr. We conclude from this that it will be very important to control the impurity level (appm) of oxygen in the coolant streams to minimize oxidation-assisted fatigue cracking.

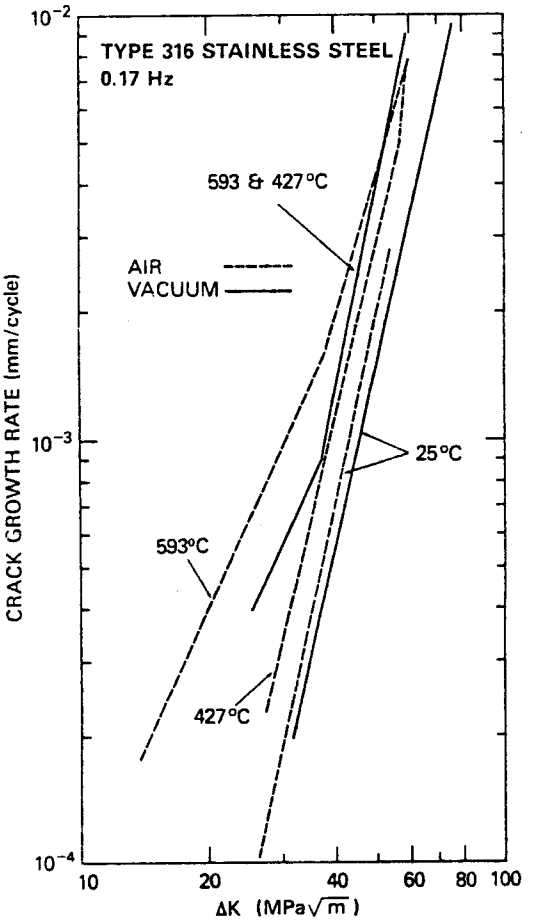

Figure 73. Effects of air and vacuum environments on fatigue crack growth rates for 316 stainless steel at various temperatures [36].

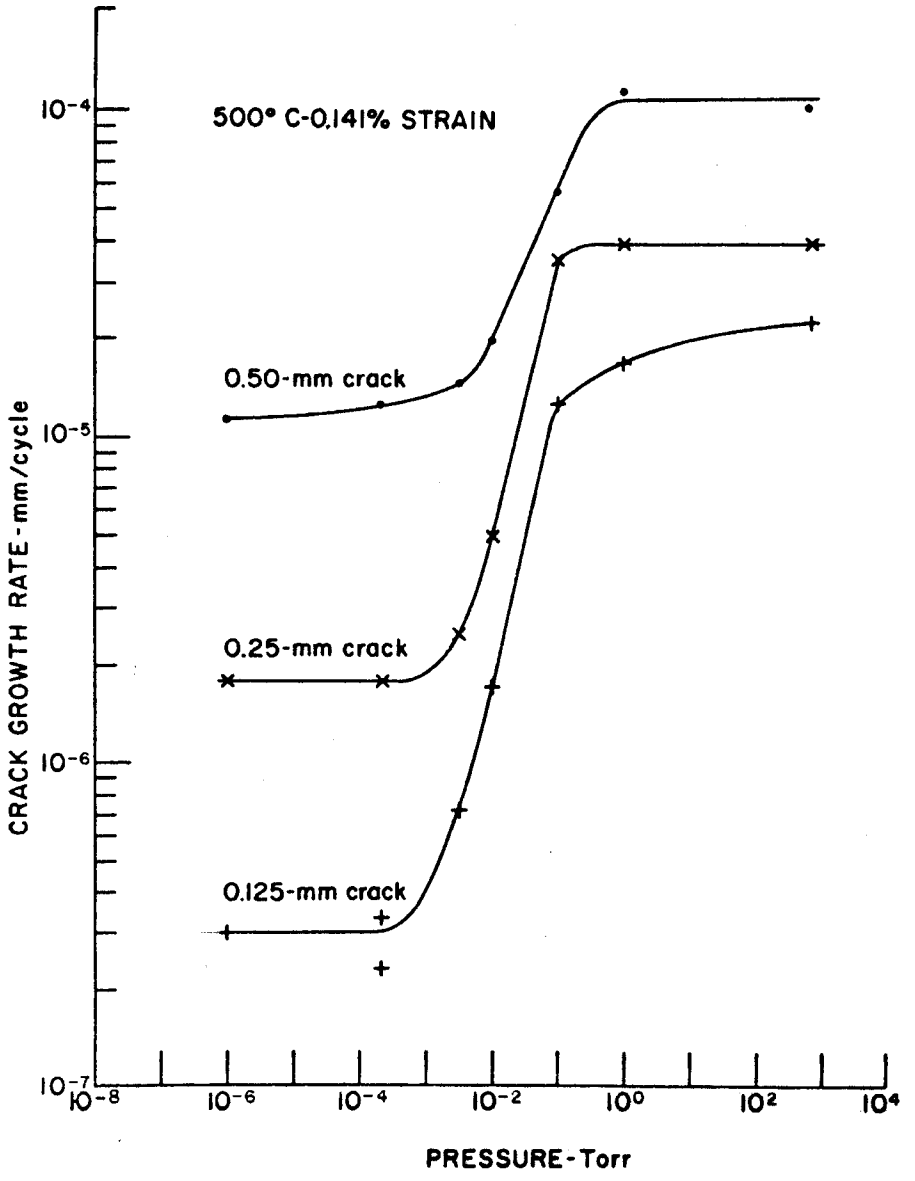

Figure 74. Effect of oxygen pressure on fatigue crack growth rate of 316 stainless steel at 500°C [60].

Hydrogen will be present throughout the first wall components, in the form of tritium at concentrations of 0.1 - 1 appm [77]. This is known to cause hydrogen embrittlement and stress corrosion cracking in ferritic steels and other metals (see Ref. [82]). However, in the austenitic stainless steels, no serious effects appear to exist. Fatigue crack growth rates measured by Habashi et al [175] in 316L S.S. indicate only a slight increase in da/dN when charged with internal hydrogen. Bamford [73] also tested 304 and 316 SS in a hydrogen sulfide environment at 300°C and concluded..."In general, austenitics are less influenced by hydrogen than ferritics due to the greater solubility of hydrogen in austenite, the slower diffusion kinetics, and a difference in the specific surface energies which may be associated with such events such as cleavage and slip step emergence, which are probably responsible for the lack of any environmental enhancement." This conclusion, however, needs to be verified with more experimental measurements.

The influence of inert gases such as nitrogen, argon, and helium on fatigue crack growth rates, as compared to vacuum data, has been studied by many investigators [62-66] and reviewed by James [31]. Their results, shown in Fig. 75, indicate no environmental effect of these gases, apparently due to the lack of oxygen in the system. For the very same reason, liquid sodium behaves also as an inert environment, as reported by James [31].

In contrast to this, the behavior is liquid lithium is apparently quite different, although only preliminary test results have been

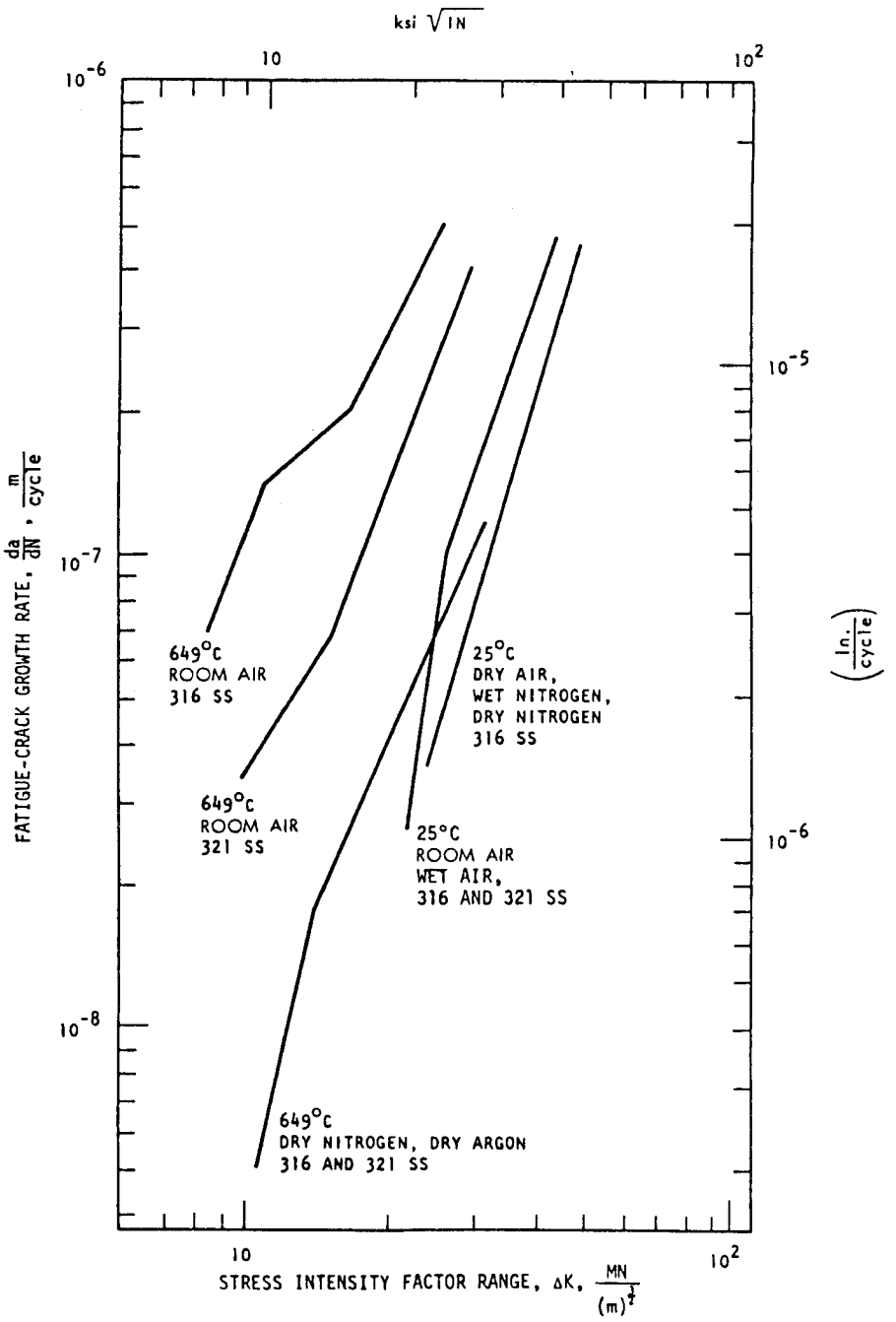

Figure 75. Effect of air, nitrogen and argon gases on fatigue crack growth rate of 316 and 321 stainless steel at various temperatures [62].

published. In recent papers by Hammon et al [69,70] and Spencer [71], fatigue crack growth rates of 304 SS in lithium at 200 and 700°C were measured to be four to ten times faster than in argon gas at $\Delta K = 20$ MPa$\sqrt{m}$, as shown in Fig. 76. According to Hammon and Spencer, the enhancement of da/dN is attributed to preferential grain boundary attack at the crack tip. Lithium therefore, is classified as an aggressive environment, which reduces its attractiveness as a first wall coolant. Obviously, liquid sodium would be preferred for this reason.

The effects of water or steam appear to be highly dependent on temperature, according to James [31]. In stage II, the effects of a pressurized water reactor environment, 2000 psi and 300°C on 304 and 316 SS are negligible (see Bamford [72,73]). However, Matsuda et al [74] have shown that 500°C steam can increase fatigue crack growth rates in stage II from one to three orders of magnitude over room temperature air data or, equivalently, by factors of 30-60 times more than in air at the same temperature (see Fig. 77). Consequently, high temperature steam appears to be the most severe of all the environments for stage II crack growth.

In summary, even when the temperature effect has been accounted for by the modulus connection (i.e. $\Delta K/E$), we find that environmental effects can have a tremendous impact on fatigue crack growth rates. When compared to vacuum data for stainless steels, at the same temperature, R-ratio, and ΔK, the following inert environments cause essentially no change da/dN: helium, argon, nitrogen, hydrogen, sodium, steam below 300°C and air at room temperature. Aggressive environments,

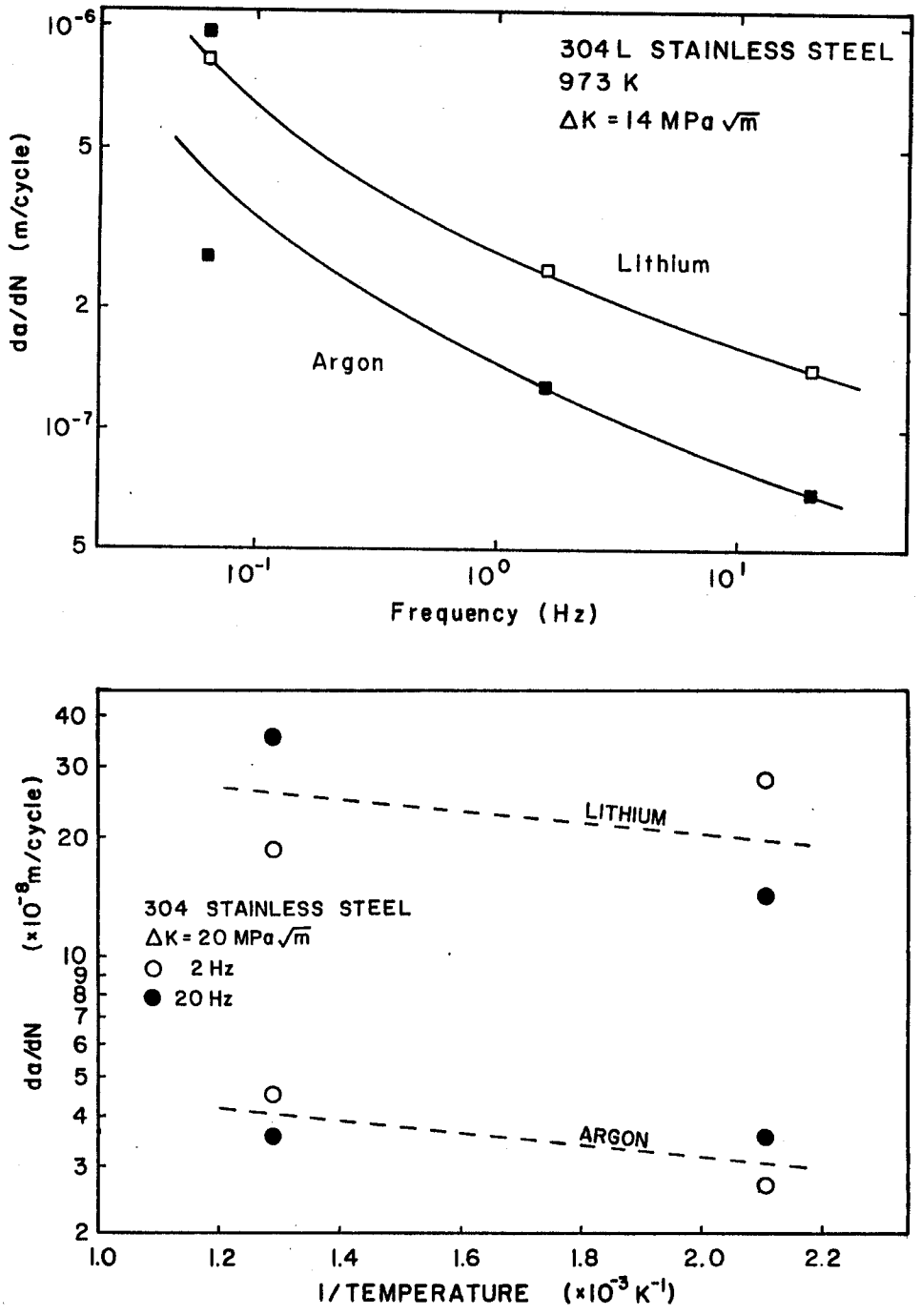

Figure 76. Effect of liquid lithium environment on fatigue crack growth rates of 304L stainless steel at various temperatures and loading frequencies [69].

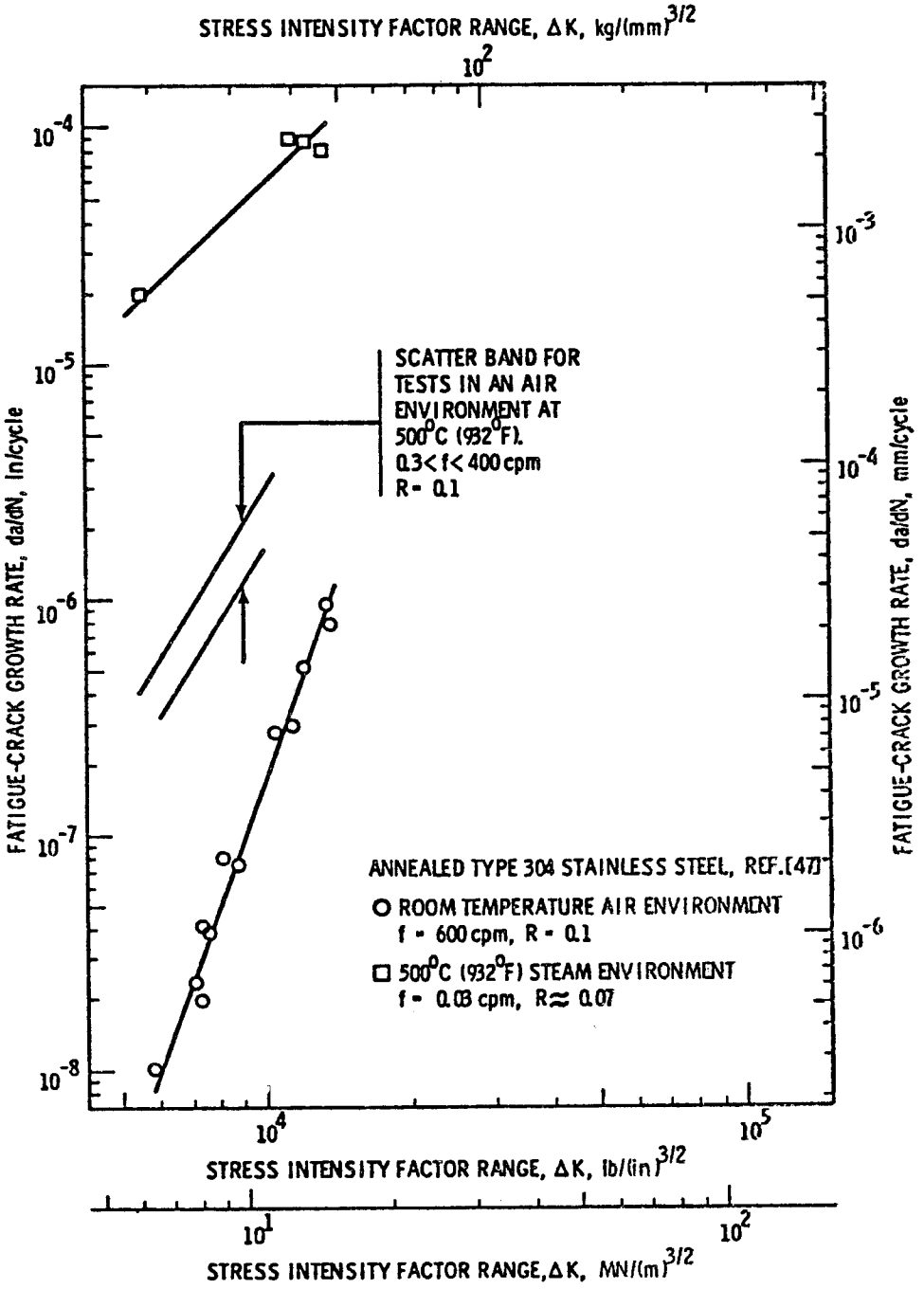

Figure 77. Effect of high temperature steam environment on fatigue crack growth rates for 304 stainless steel [31].

those which enhance da/dN only up to one order of magnitude, include: steam at around 400°C, air at high temperatures and low ΔK, and liquid lithium. The most severe environment appears to be steam at 500°C, which enhances da/dN by one to three orders of magnitude.

The data set used in the computer code WISECRACK is based on room temperature air data, which models only inert environments. Since the results presented later on in Chapter 8 assume a helium-cooled first wall, we would then expect these lifetimes to be drastically reduced (up to ten times) if steam or liquid lithium were used instead as a coolant.

da/dN Equations Used in WISECRACK

One of the objectives of this research was to find an equation for the fatigue crack growth rate of austenitic stainless steels that could model the complete range of behaviors, including stage I, II and III (see Fig. 60). Over forty different equations were found in the literature for da/dN, including thirty-one listed in a paper by Hoeppner and Krupp [76]. Of these, the modified Forman equation, proposed by Speidel [34] in 1973, was chosen to be used in the computer code WISECRACK. It can be written as

$$\frac{da}{dN} = \frac{C\lambda^m[f\Delta K - \Delta K_o]^n}{K_{Ic} - \lambda f\Delta K} \qquad (172)$$

where $\lambda = 1/(1-R)$

$R = K_{min}/K_{max}$

$f = E(T_o)/E(T)$ (continued next page)

T_o = room temperature (25°C).

This equation models the effects of threshold ΔK, temperature, mean stress, and embrittlement.

Historically, the modified Forman equation has evolved from four previous equations, shown in Fig. 78. In 1963, Paris [30] proposed his power law equation for the stage II regime:

$$\frac{da}{dN} = C\ (\Delta K)^n \quad . \tag{173}$$

Then, in 1971, Donahue [49], modelled the threshold effect by forcing da/dN to approach zero as ΔK approached the threshold value, ΔK_o:

$$\frac{da}{dN} = C\ (\Delta K^2 - \Delta K_o^2) \tag{174}$$

Next, in 1972, Forman [78] developed a model that included the plain strain fracture toughness, K_{Ic}, in such a manner that da/dN approaches infinity as K_{max} approaches K_{Ic}:

$$\frac{da}{dN} = \frac{C\ (\Delta K)^n}{(1-R)K_{Ic} - \Delta K} \quad . \tag{175}$$

Also in 1972, Nordberg [77] proposed a modification of the Forman equation to reduce the sensitivity of da/dN to mean stress effects:

$$\frac{da}{dN} = \frac{C\,\lambda^m\,\Delta K^n}{K_{Ic} - \lambda\Delta K} \tag{176}$$

where $\lambda = 1/(1-R)$.

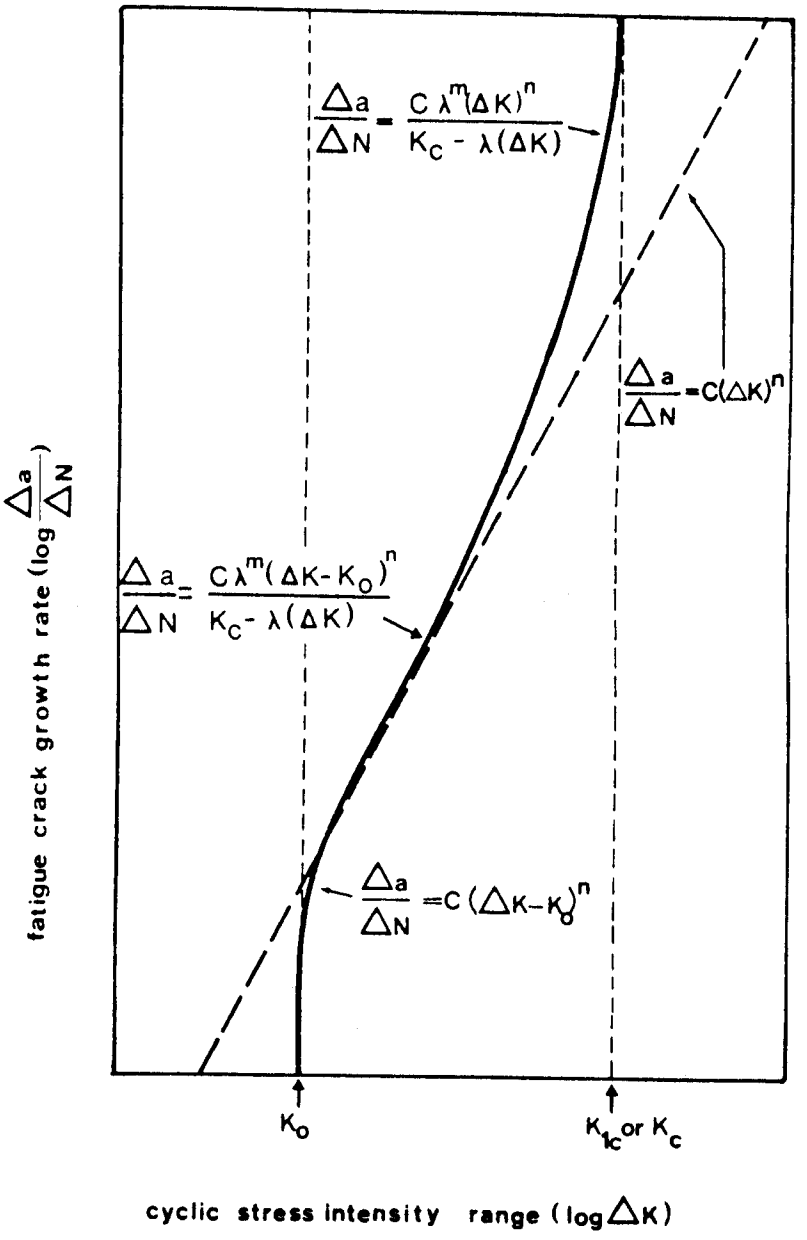

Figure 78. Evolution of fatigue crack growth rate equations [34].

One year later, Speidel linked all three regimes of crack growth by combining Eq. (174) with Eq. (176) to yield:

$$\frac{da}{dN} = \frac{C\,\lambda^m(\Delta K - \Delta K_o)^n}{K_{Ic} - \lambda\Delta K} \quad . \tag{177}$$

Two additional modifications have been made by the author. To model the temperature effect, ΔK is replaced with $\Delta K \cdot E(T_o)/E(T)$, as discussed on page 169. Second, ΔK_o was allowed to be a function of the R-ratio:

$$\Delta K_o(R) = \Delta K_{oo}(1 - bR) \tag{178}$$

where ΔK_{oo} is the threshold value at R = 0 and b is a constant, ranging from zero to one (see page 178). The constant "C" in Eq. (177) depends on the environment.

There is one confusing aspect in the literature about the use of ΔK and R that should be mentioned. Many times, when plotted for negative R-ratios, the ΔK values are computed from only the tension portion of the load cycle (see, for example, Sullivan and Croocker [79] and Croocker [80]). This approach is correct to a first approximation when based on the argument that the crack surfaces are closed under compression and, hence, would not contribute to any growth. However, when the Forman equation (or its variations) is used, it predicts the correct results when the complete, full range of ΔK is used. WISECRACK follows the latter method. Of course, when both

K_{max} and K_{min} are negative, then da/dN is always assumed to be zero. The reader, therefore, should be careful when interpreting original da/dN data when $R < 0$, and ascertain whether ΔK is the full range or only the tensile portion of the load cycle.

To give the user some flexibility, WISECRACK allows a choice between two different equations for da/dN: the traditional Paris equation and the more accurate, modified Forman equation. The Paris equation, which models only stage II accurately, is given by

$$\frac{da}{dN} = C(f\Delta K_{eff})^n \quad . \tag{179}$$

In order to correlate da/dN with the R-ratio, this equation uses the Walker correction [38]:

$$\Delta K_{eff} = K_{max}(1 - R)^m \quad . \tag{180}$$

Table 8 lists the constants for austenitic stainless steels which are used in WISECRACK for the da/dN equations.

Table 8. Fatigue Crack Growth Data for Stainless Steels

Paris Eq. (179)

$C = 3.94 \times 10^{-13}$ m/cycle

$n = 3.66$

$m = 0.5$

Modified Forman Eq. (177)

$C = 3.122 \times 10^{-9}$ m/cycle

$n = 2.95$

$K_{Ic} = 150$ MPa $\sqrt{m}$

$$m = \begin{cases} 1-0.31R - 1.23R^2 & R > 1 \\ 1.88 & R < 0 \end{cases}$$

$$\Delta K_o = \begin{cases} 5.4(1 - 0.9R) & R > 0 \\ 5.4(1 - 0.2R) & R < 0 \end{cases}$$

Figure 79 shows both equations plotted for R = 0 and T = 25°C. As expected, the Paris equation overpredicts da/dN in the threshold regime ($\Delta K < 10$ MPa $\sqrt{m}$). Figure 80 shows the effect of temperature as predicted by the modified Forman equation. Finally, Figure 81 shows the predicted effects of the R-ratio. Note that the exponent "m" in Table 8 for Eq. (177) was chosen to be a function of R. This was done in order to more closely match the actual data, which indicates a saturation of the R-ratio effect for $R \geq 0.5$ (see Sasaki et al [81]). The effect of a decreasing fracture toughness, K_{Ic}, will be discussed in a later section on irradiation effects.

Other Effects on Fatigue Crack Growth

The effect of the stress state (biaxial vs. uniaxial) on mode I crack growth is known to be small (see Ref. [68, 48]). This is physically reasonable because tensile stresses in the plane of the crack have no

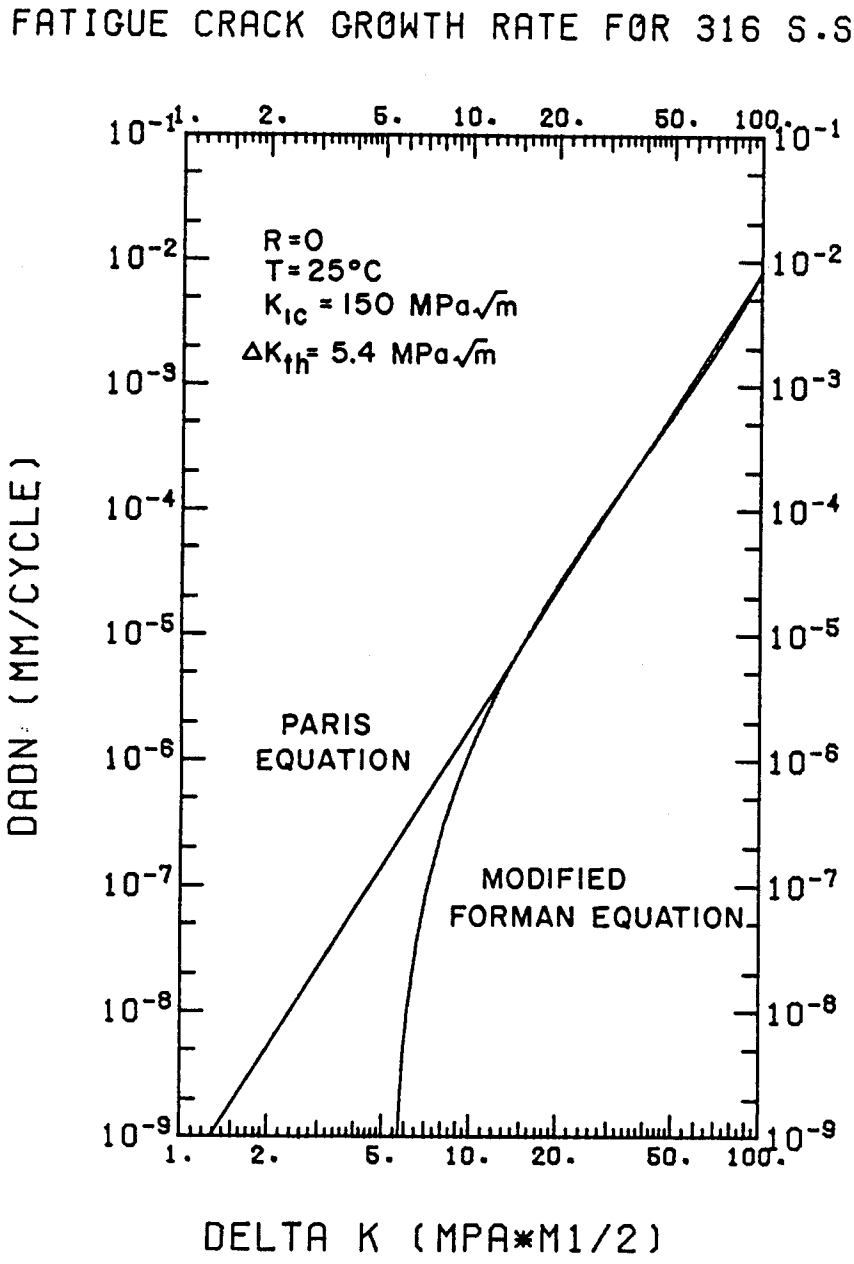

Figure 79. Fatigue crack growth rate equations used in WISECRACK for 316 stainless steel.

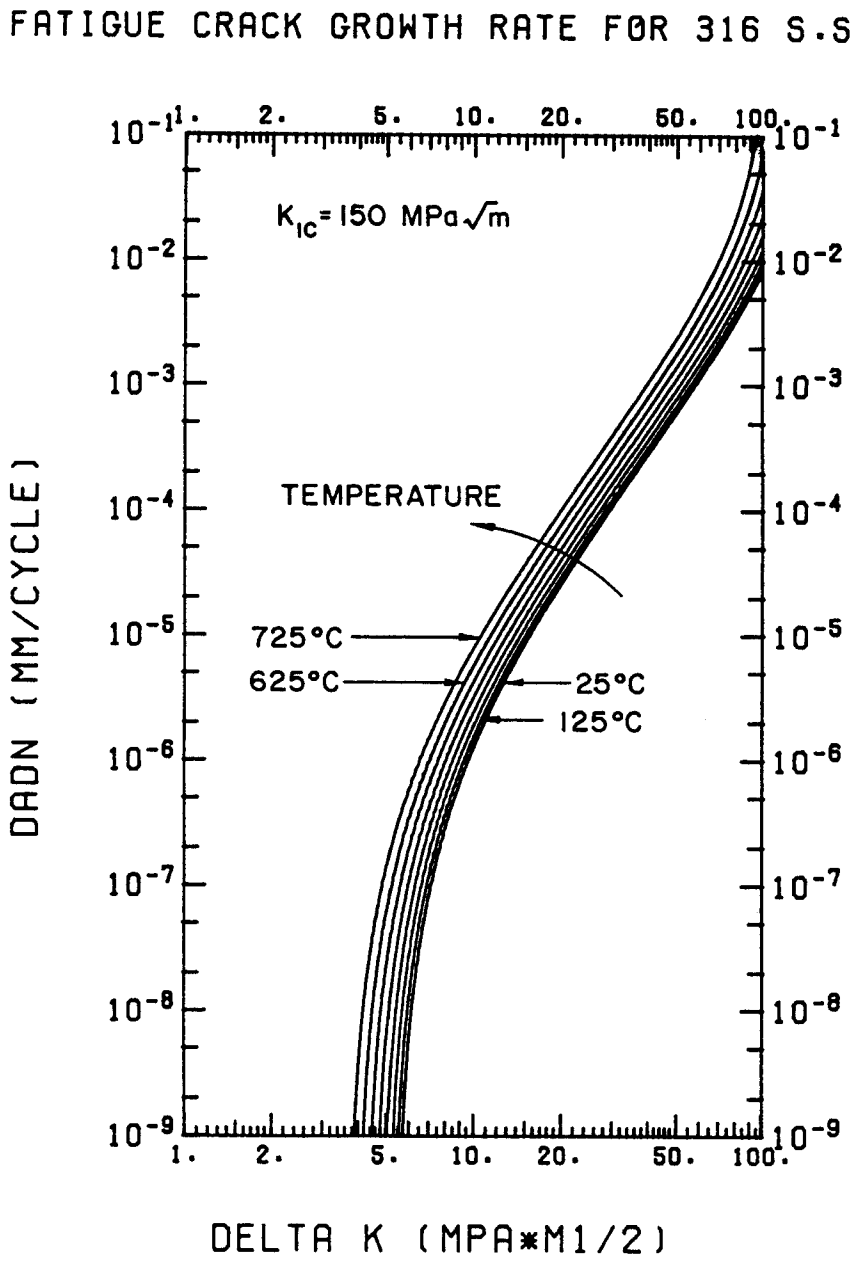

Figure 80. Effect of temperature on fatigue crack growth in 316 stainless steel.

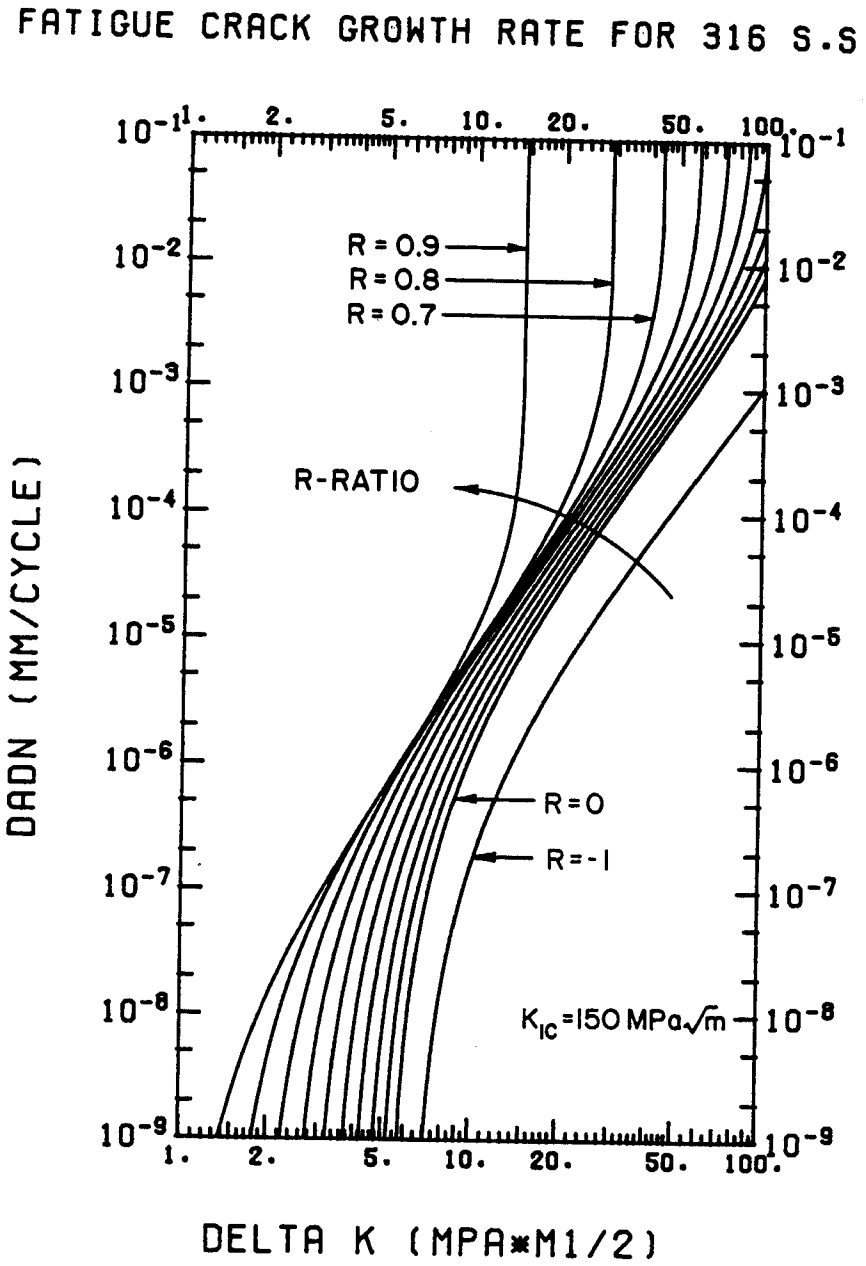

Figure 81. Effect of R-ratio on fatigue crack growth in 316 stainless steel.

tendency to open up the crack.

Tensile overloads in the cyclic stress history can cause temporary retardation of the crack growth rates as the crack grows through a larger plastic zone. Conversely, compressive overloads can cause crack acceleration. Overloads are not expected during normal reactor operations, but plasma disruptions may cause an overload-type stress spectrum. However, since disruptions are not included in this thesis, then this particular phenomenon will be neglected.

In the study of fracture mechanics, it is well known that there is a thickness effect in measurements of fracture toughness caused by a transition from a state of plane stress in thin speciments to one of plane strain conditions in thick specimens. The effect on fatigue crack growth rates is not as large, however. Shahinian [67] has measured crack propagation in 316 S.S. at temperatures of 24, 427 and 593°C and found that the rates were not affected by specimen thicknesses within the range of 7.6 mm to 25.4 mm. Because typical first walls are 1 to 5 mm thick, the thickness effect is not expected to be of much concern.

Radiation Effects on Crack Propagation

The preceeding sections of this chapter have shown that crack propagation in unirradiated 304 and 316 stainless steel is very well characterized over a wide range of conditions, with the possible exception of environmental effects in the threshold regime. However, this is not the case for our understanding of the effects of 14 MeV neutron irradiation on crack growth, primarily due to a lack of data

at sufficiently high damage levels (>30 dpa). This is unfortunate, because the analysis done in this section indicates a potentially severe degradation of crack growth resistance.

The effects of EBR-II irradiations of 304, 316 and 308 stainless steel specimans have been reported by James [81] and Michel et al [83-86]. At 427°C in air, the highest damage level, 25 dpa, produced no measurable effect on fatigue crack growth rates in 304 SS. However, at 593°C in air, irradiation to 8.7 dpa produced roughly one order of magnitude increase in da/dN for both zero and one-minute hold times, as shown in Fig. 82. No explanation was given for this dramatic effect. However, the difference between the irradiation temperature, 400-500°C, and the test temperature 593°C, may have an impact on the evolution of both the microstructure and the partioning of helium bubbles between the matrix and grain boundaries. This situation may be analogous to the difference in creep rupture behavior for specimans tested in-situ and out-of-reactor, the latter having shorter lifetimes (see Bloom and Wolfer [123]).

Until more data is obtained, theoretical models must be used to qualitatively assess the radiation effects. We know experimentally that neutron irradiation will induce severe embrittlement and loss of ductility (see Bloom [88], and Strassland and Bloom [89]). Above 550°C, the primary mechanism is helium embrittlement at grain boundaries. However, below 550°C, radiation hardening is the dominant source of embrittlement. This hardening is characterized by an increase in both

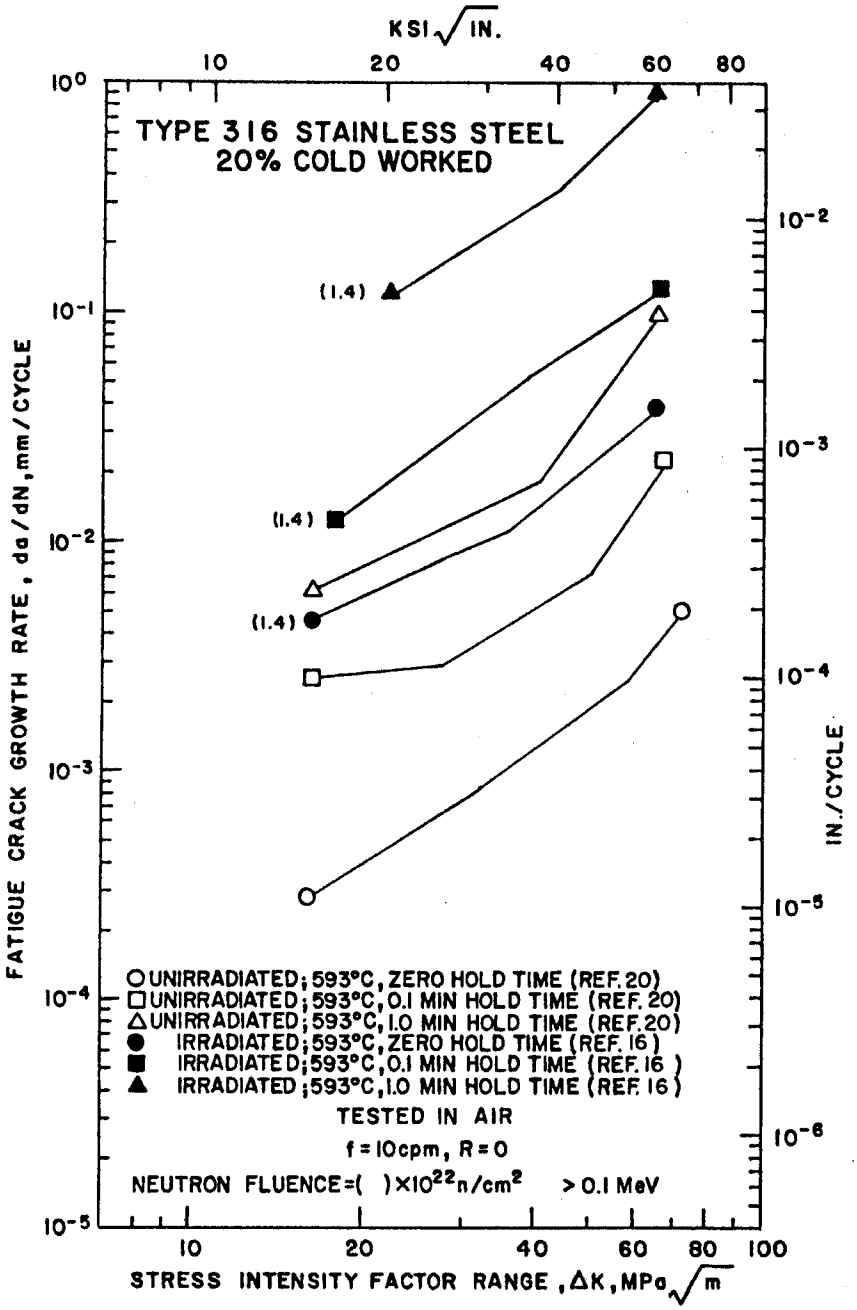

Figure 82. Effect of neutron irradiation on fatigue crack growth rate of 20% CW 316 stainless steel, with and without hold-times, tested in air at 593°C [86].

the yield strength, σ_Y, and the ultimate strength, σ_u, but a decrease in the difference, $\sigma_{ult} - \sigma_Y$, with increasing dpa. The ability of the metal to plastically deform and work harder therefore decreases as the difference, $\sigma_{ult} - \sigma_Y$, decreases.

Wolfer [105], Odette and Frey [106], and Cramer [107] have surveyed existing models relating mechanical properties to K_{Ic}. Odette and Frey used the Hahn and Rosenfeld model, $K_{Ic} \cong n\sqrt{2E\,\sigma_y\varepsilon_f/3}$, where n is the work hardening exponent and ε_f is the fracture strain to predict the embrittlement of 316 SS, as shown in Fig. 83. Very low values of K_{Ic} are predicted after 30 dpa for temperatures below 550°C, according to this model.

Unfortunately, these models are based upon the concept of homogeneous plastic deformation at the crack tip. In reality, irradiated specimens often exhibit flow localization and subsequent channel fracture at temperatures where swelling occurs (300-600°C). Homogeneous models are not expected to apply in this regime. Recognizing this, Wolfer and Jones [90], combined a channel fracture model with Simmon's [91] correlations for ε_f, σ_Y, to predict the drop in K_{Ic} with increasing fluence, as shown in Fig. 84. The minimum toughness they predict is 30 MPa$\sqrt{m}$, which is not as severe as might be expected from very low ductilities of $\leq$ 0.1%. From this analysis, it is clear that radiation hardening will reduce K_{Ic}, possibly as much as 30 MPa$\sqrt{m}$. However, definitive experiments are needed to confirm these predictions.

The next step is to investigate the effect a reduction in fracture toughness might have on fatigue crack growth rates. Referring to

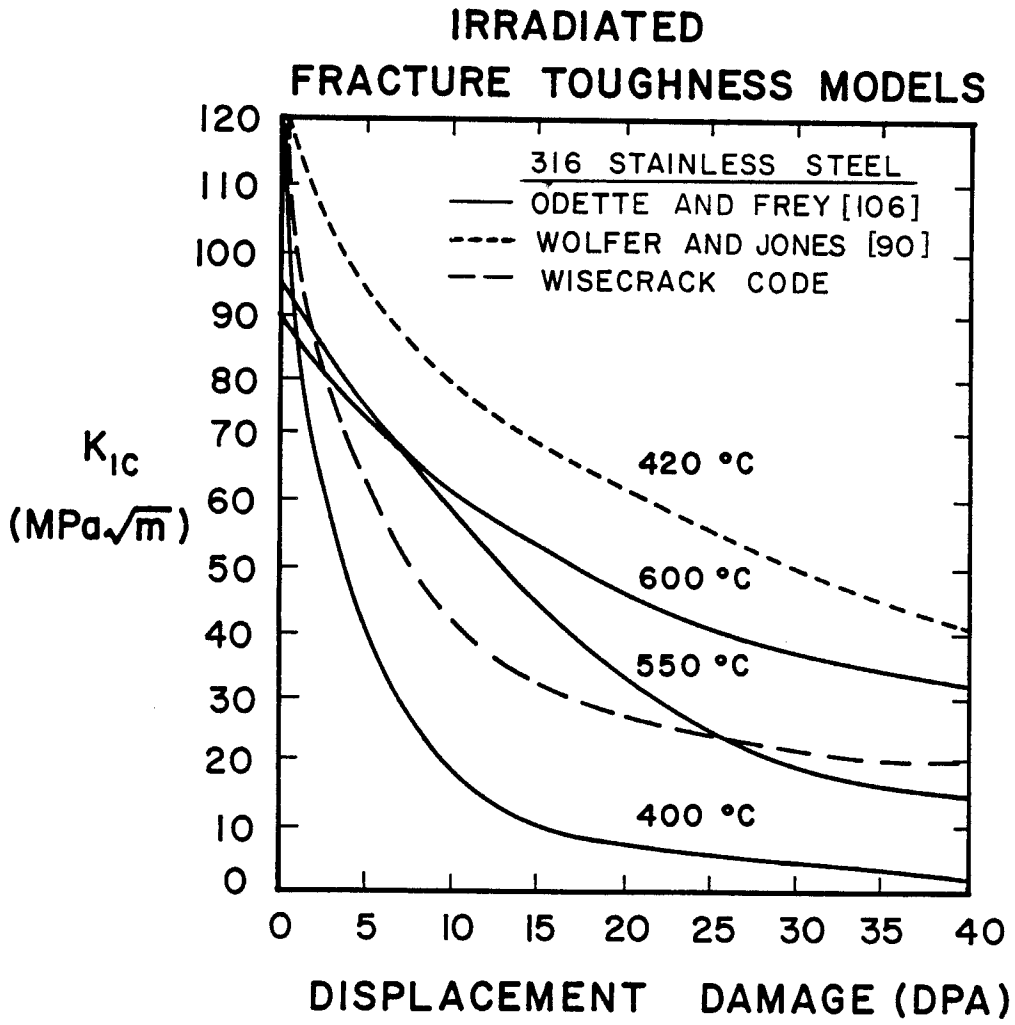

Figure 83. Models for the effect of displacement damage (dpa) on the fracture toughness.

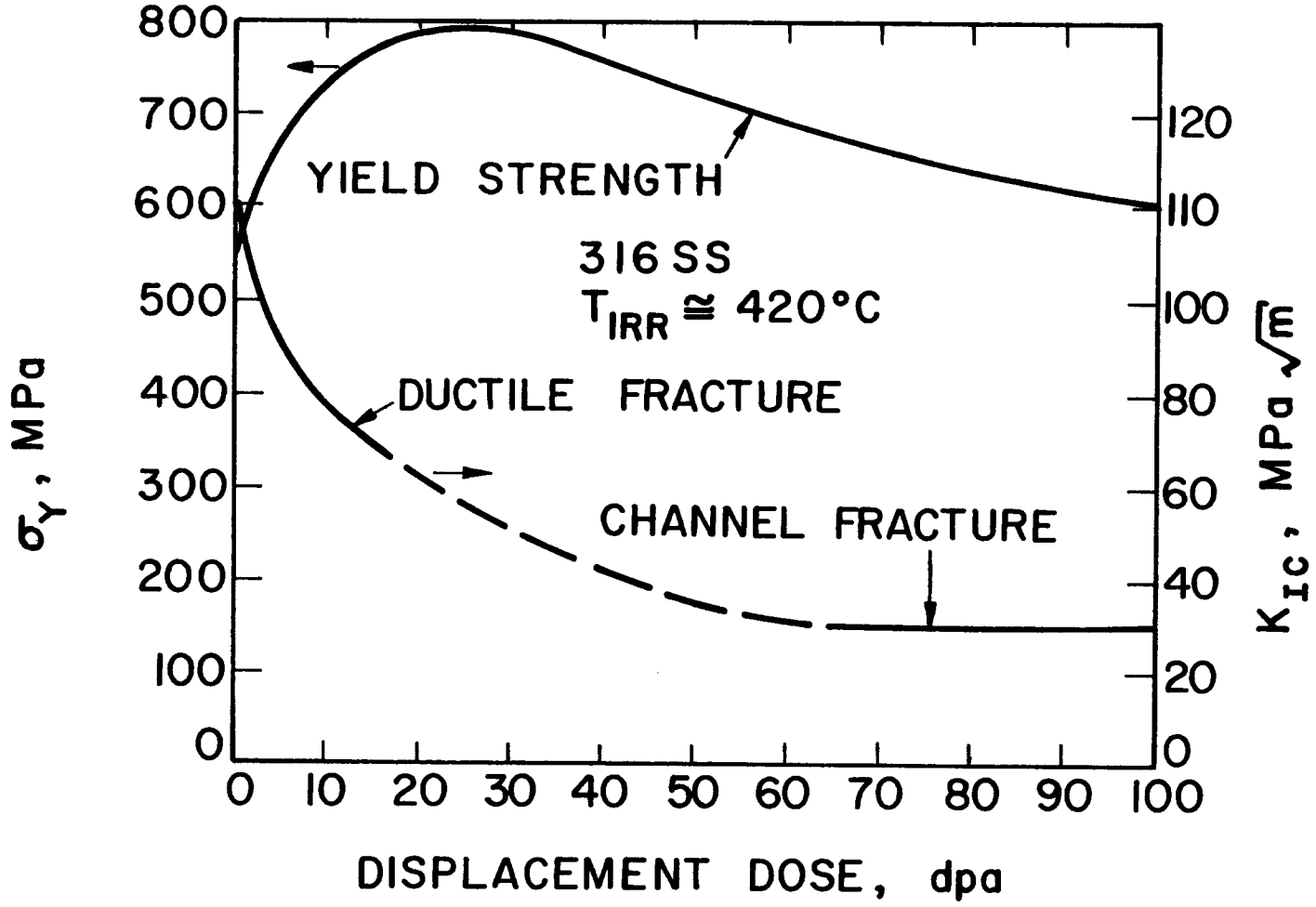

Figure 84. Models for the effect of displacement damage (dpa) on yield strength and fracture toughness of 316 stainless steel irradiated at 420°C [90].

Fig. 60, we can expect that as K_{Ic} decreases, the stage III regime of unstable crack growth will move to lower values of ΔK because ΔK can never be greater than K_{Ic}. When K_{Ic} drops low enough, then it appears plausible that the slope, n, of the stage II regime will increase, hence increasing da/dN, as illustrated in Fig. 85. These curves were generated by inserting the following correlation for K_{Ic}, as a function of dpa, into the modified Forman equation:

$$K_{Ic} = 115 \exp(-0.25\ F) + 35 \exp(-0.0134\ F) \quad MPa\sqrt{m} \qquad (181)$$

where

F = displacement damage in dpa.

This equation was fitted by the author to the model by Odette and Frey for T ≈ 500°C, as shown in Fig. 83. Equation (181), which is used in WISECRACK, is a more severe estimate of K_{Ic} than that of Wolfer and Jones [90].

The predictions in Fig. 85 are qualitatively identical to experimental results on metallurgically embrittled steel. Results from Speidel [92], and Ritchie [93], shown in Figures 86 and 87, respectively, for two different temper-embrittled steels show a marked upturn in da/dN when K_{Ic} drops from the level of K_{Ic} > 50 $MPa\sqrt{m}$ down to levels around 30-40 $MPa\sqrt{m}$. The data in Figure 87 also indicate a decrease in the threshold ΔK_o with decreasing K_{Ic}, Figure 88 cross-plots this data to further illustrate this effect. The reduction in ΔK_o is more pronounced for lower R-ratios than for higher R-ratios.

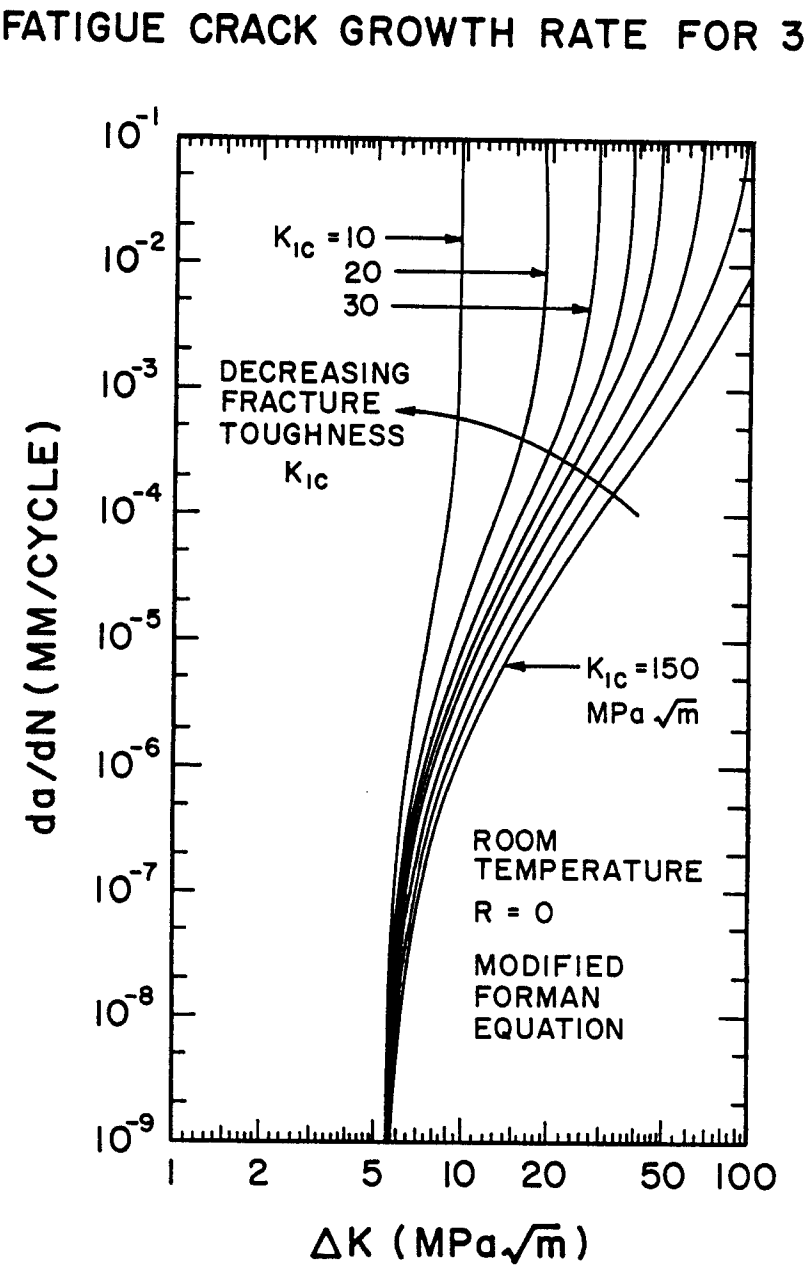

Figure 85. WISECRACK predictions of the effect of decreasing fracture toughness on fatigue crack growth rates in 316 stainless steel at room temperature and R = 0.

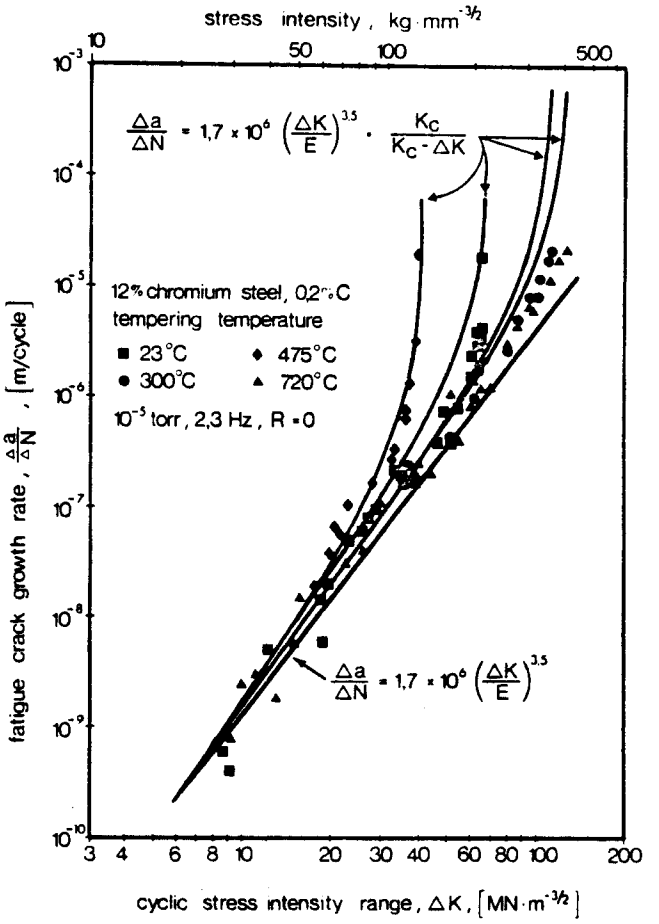

Figure 86. Effect of reduction in fracture toughness on fatigue crack growth rates in a 12% chromium steel [92].

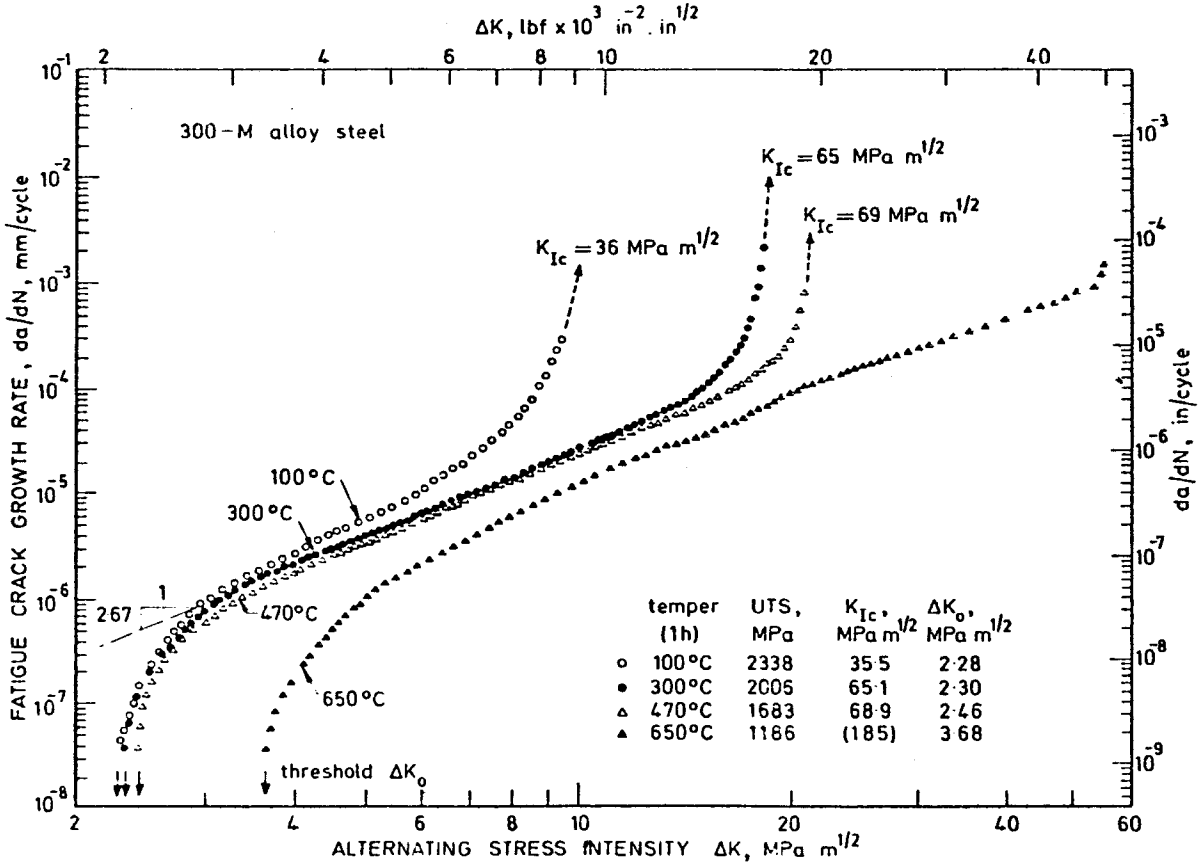

Figure 87. Effect of temper embrittlement and reduction in fracture toughness on fatigue crack growth rates in a 300-M alloy steel [93].

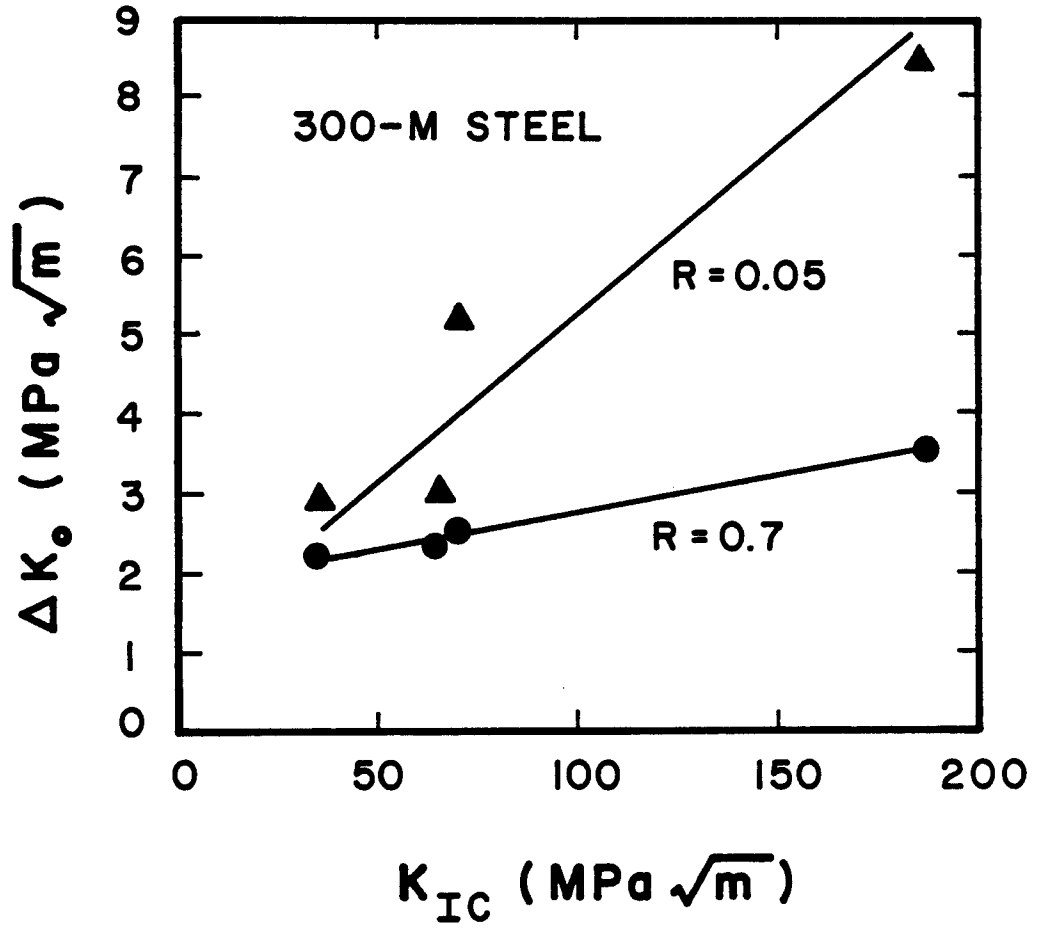

Figure 88. Effect of fracture toughness on the threshold stress intensity factor for a 300-M alloy steel [93].

In the same paper by Ritchie [93], it is shown that a higher yield strength correlates with a lower ΔK_o according to measurements by eight different investigators (see Fig. 89). Those results also tend to support an expected similar behavior in a neutron environment. However, because no data exist to either confirm or deny this, WISECRACK does not include any irradiation effects on ΔK_o at the present time.

Returning to the effect of embrittlement on stages II and III, we find that the measurements made by Stonesifer [94] on da/dN for a medium-strength pressure vessel steel, A533-B, also indicate a dramatic upturn in the slope of the stage II regime when tested below the DBTT (ductile-to-brittle transition temperature), where the toughness drops from 85 $MPa\sqrt{m}$ at 300°K to 30 $MPa\sqrt{m}$ at 77°K. The increased sensitivity to ΔK in stage II of embrittled steels as measured by the slope has been correlated with K_{Ic} by Ritchie and Knott [97] and Tanaka [96], as shown in Fig. 90. In each case, a large increase in the Paris exponent, n, is realized when K_{Ic} drops below 40-70 $MPa\sqrt{m}$. This "knee" in the curves lies exactly in the same range of uncertainty in K_{Ic} which is currently projected for neutron embrittlement, namely 30-60 $MPa\sqrt{m}$.

From these consideration, it is reasonably certain that severe embrittlement will enhance fatigue crack growth rates. The question that remains is: how strong is the effect? Figure 91 illustrates two possible behaviors which are programmed into the WISECRACK code. Assuming an irradiated toughness of 30 $MPa\sqrt{m}$, da/dN from the modified

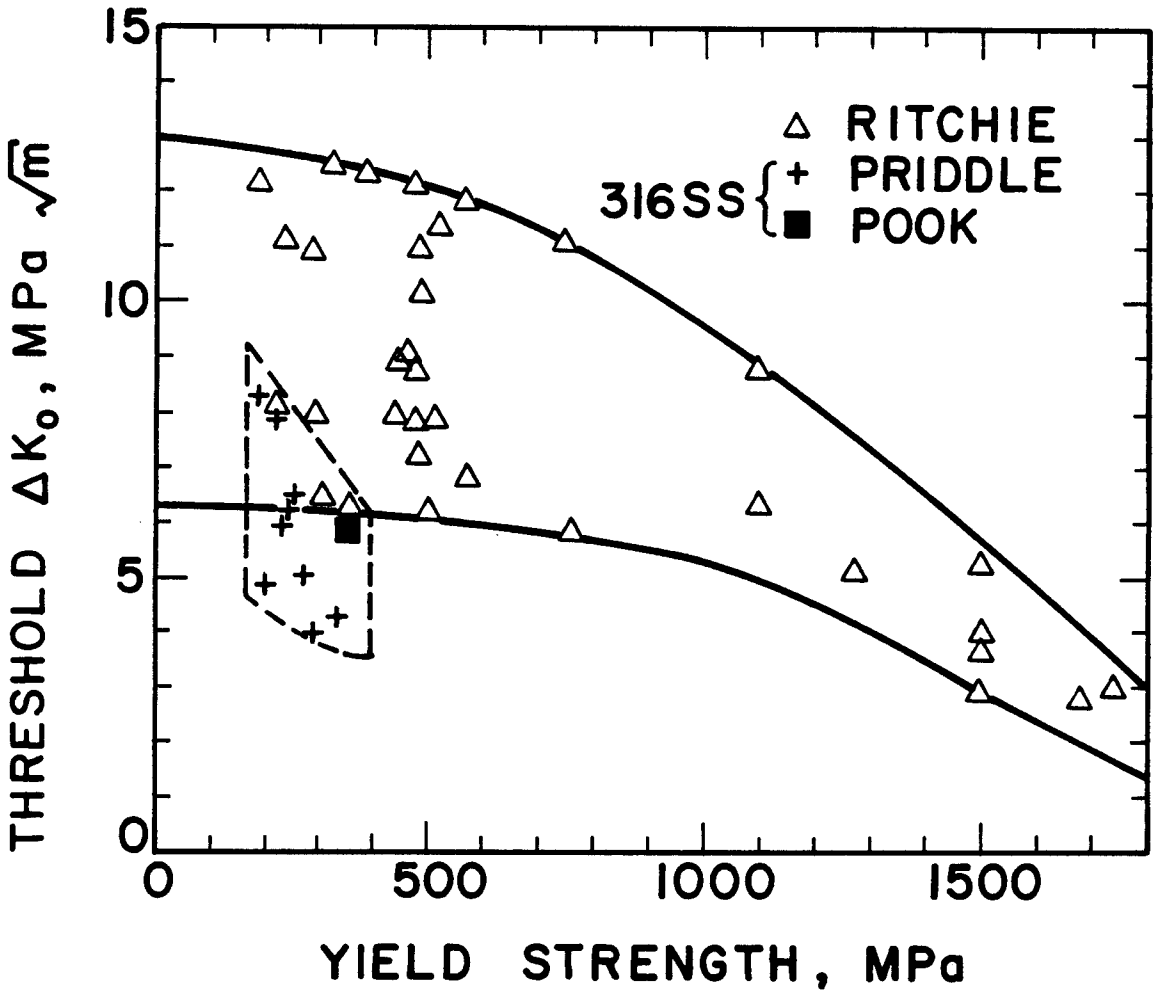

Figure 89. Trend for the variation of the threshold stress intensity factor in steels at R = 0 [90].

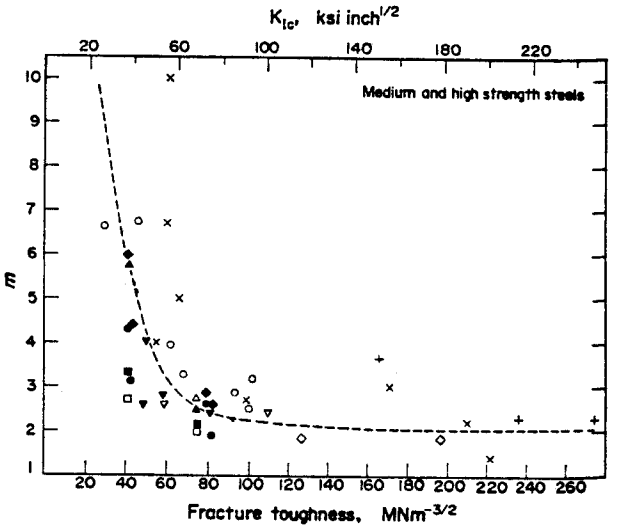

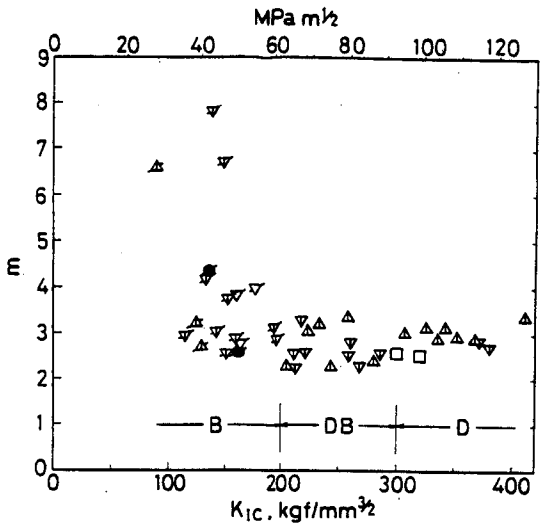

Figure 90. Variation of the Paris exponent n (or m) with fracture toughness for a variety of medium and high strength steel [96,97].

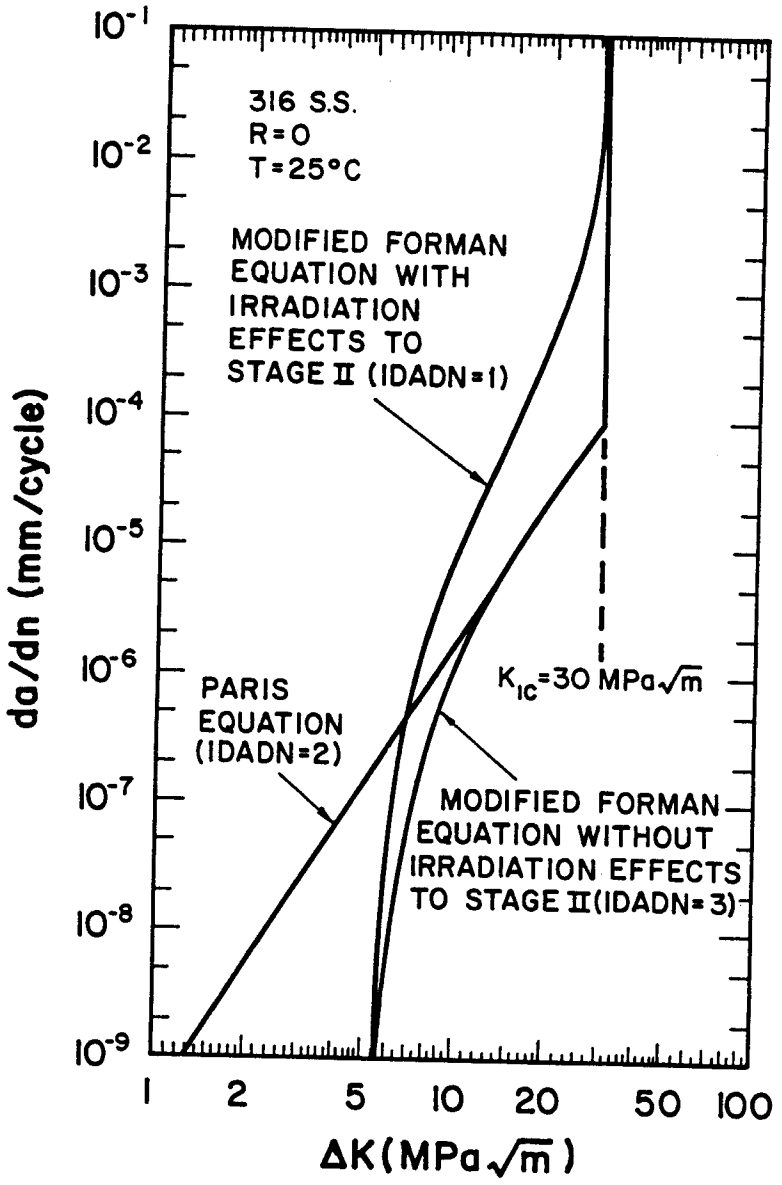

Figure 91. Three different model assumptions used in WISECRACK for the effects of neutron irradiation on fatigue crack growth in 316 stainless steel.

Forman equation with irradiation effects is significantly higher than the same equation without any effects to stage II (both have the same limit as $K \rightarrow K_{Ic}$). The latter curve, marked by "IDADN=3", is generated by holding K_{Ic} in the denominator of Eq. (55) equal to its unirradiated value. A third possibility shown in the figure is the Paris equation without any irradiation effects, marked by "IDADN=Z".

It appears that the modified Forman equation with irradiation effects may overpredict the enhancement effect as shown in Fig. 86. The data in this Figure indicate that the upturn in da/dN, as ΔK approaches K_{Ic}, occurs at a higher value of ΔK than the Forman equation would predict. Unpublished results from HEDL confirm this trend as well. We conclude that high fluence data (50-100 dpa) is needed at 400-500°C in 316 SS where $\Delta K \approx 20$ MPa$\sqrt{m}$ and $K_{Ic} = 30$ MPa$\sqrt{m}$ to more fully understand this effect. If, indeed, the upturn in stage II is not as pronounced as the modified Forman equation predicts, then the following modification may be warranted

$$\frac{da}{dN} = \frac{C \lambda^m [f\Delta K - \Delta K_o]^n}{K_{Ic}^{\ell} - (f\Delta k)^{\ell}} \qquad (182)$$

where ℓ is a constant greater than one. This new equation still displays the correct limiting behavior as $K_{max} \rightarrow K_{Ic}$, but now provides a fourth adjustable constant to allow a better match for the stage II behavior. This modification is only a suggestion and has not been included in the WISECRACK code.

Models for Creep Crack Growth

Time-dependent cracking, or creep crack growth can be defined as the continuous extension of a crack in a specimen held at elevated temperature under static loads. The physical process of creep cracking involves the nucleation of microcracks at grain boundary junctions ahead of the main crack due to grain boundary sliding and vacancy diffusion followed subsequently by a linking-up of these microcracks with the main crack. Only one researcher in the fusion community has written about this subject, namely T.V. Prevenslick [98], and he concluded that below 450°C the effect was negligible. The purpose, then, of this section is to review the literature which led to this conclusion and then present a new model for creep crack growth.

Jones [31], Shahinian [99] and Sadananda [36] have measured low-temperature (e.g. below 600°C) creep crack growth rates, da/dt, in 304 and 316 stainless steels for both air and vacuum environments, as shown in Fig. 92. Their data can be correlated with a Paris equation, modified by an Arrhenius expression for the temperature dependence:

$$\frac{da}{dt} = D_o e^{-Q/RT} (K_{max})^p \quad . \tag{183}$$

The activation energy, Q, has been measured by Kawasaki and Horiguchi [16] and Yokobori et al [17] and lies within the range of 35-90 Kcal/mole depending on the stress level. The data in Figure 92 show a very strong sensitivity to the maximum stress intensity factor, K_{max}, with exponents, p, ranging from 8-15. All of the data currently available

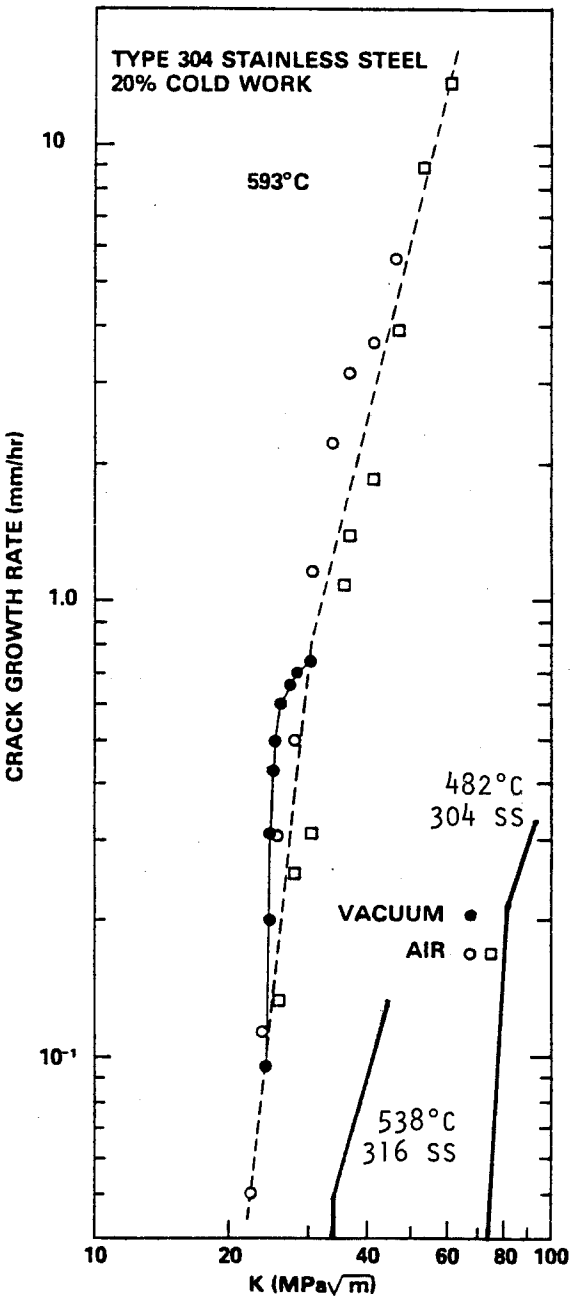

Figure 92. Effect of environment and temperature on creep crack growth rates for 316 stainless steel [36].

for 304 and 316 SS are listed in Table 10.

The majority of researchers have concentrated on high temperature creep crack growth (600-800°C). However, at these high temperatures the use of linear elastic fracture mechanics becomes somewhat questionable. This is due to large creep deformation at the crack tip which relaxes the $r^{-1/2}$ stress distribution and, hence, invalidates the stress intensity factor solutions. In this regime the data correlates best with the time-dependent J-integral, $\dot{J}$ or C*, according to recent reviews by Sadananda and Shahinian [174, 175]. Unfortunately, $\dot{J}$ or C* is very difficult to calculate for a surface flaw.

Therefore, the constants p and D_o in Eq. (183) were fit by the author to data taken by James [31] at 538°C, where the ΔK correlation is assumed to be valid. These constants are listed in Table 9. This equation should not be used for temperatures above 650°C.

Table 9. Creep Crack Growth Rate Data for 316 SS

p	= 15
D_o	= 1.39×10^{-16} m/sec
Q	= 391,000 J/mole
R	= 8.31
K_{max}	[MPa $\sqrt{m}$]
da/dt	[m/sec]

Table 10. Stainless Steel Creep Crack Growth Rate Data

Reference	Metal	Temperature	Environment	Correlation	Range in K	Test Geometry
[36]	SA 316	593 (°C)	Air	K	50-150 (Mpa$\sqrt{m}$)	CT
	SA 316	593	Vacuum	K	40-70	CT
	20% CW 316	593	Air	K	30-70	CT
	20% CW 316	593	Vacuum	K	40-60	CT
	20% CW 304	593	Air	K	20-70	CT
	20% CW 304	593	Vacuum	K	20-30	CT
[109]	304	650	Helium	K, σ_n	5-11	PTC
	304	700	Helium	K, σ_n	7-14	PTC
	304	750	Helium	K, σ_n	6-11	PTC
	304	800	Helium	K, σ_n	5-8	PTC
	304	750	Helium	K, σ_n	5-9	DEN PTC, CN
[110]	316	600,650	Air	$\dot{J}$, σ_n	-	CNC
	304	650	Air, Vacuum	$\dot{J}$, σ_n	-	CNP,CNC
[99]	CW 304	427	Air	K	67	CT
	CW 304	482	Air	K	70-150	CT
	CW 304	593	Air	K	20-60	CT
	CW 316	593	Air	K	30-70	CT
[111]	SA 308	593	Air	K	40-70	CT
	SMA 308	593	Air	K	40-120	CT
[112]	Review Paper - No Data					
[100]	304	600	Air	K, σ_n	25-40	DEN
	304	650	Air	K, σ_n	20-50	DEN
	304	700	Air	K, σ_n	25-35	DEN
	304	650	Air	K	25-40	NRB

Table 10 continued.

Reference	Metal	Temperature	Environment	Correlation	Range in K	Test Geometry
[113]	316	538	No da/dt data; only failure times and lengths, etc. are reported.			CT
	316	488				CT
	316	513				CT
[114]	304	650	Air	$K, \sigma_n, \dot{J}$	7-20	DEN,CN
[115]	316	600, 700 740, 800 850	Air	σ_n	-	DEN
[116]	304	650	Air	K, σ_n	9-17	DEN, NRB
[117]	CW 316	593	Air	K	20-60	SEN
[118]	316	740	Air	K, σ_n	8-20	SEN,NCH
[119]	CW 316	650	--- inferred da/dt ---		(1-6)	
[120]	CW 316	538	Air	K	30-40	CN,CT
[100]	304	600-700	Air	K, σ_n	20-40	DEN,NRB
[101,102 103]	304	600-700	Vacuum	K, σ_n	7-13	DEN

Note: $K = K_{max}$ and $\sigma_n = \sigma_{net}$

Specimen types:
- CT = compact tension
- PCT = part-through crack
- DEN = double-edged notch
- SEN = single-edged notch
- CN = center notched
- NRB = notched round bar
- NCH = notched center hole
- CNC = center notched cylinder
- CNP = center notched plate

Creep-Fatigue Crack Growth

Future tokamak reactors will operate with plasma burn times, t_{burn}, of anywhere from 100 seconds to hours. A simple model, therefore, is proposed to account for simultaneous creep and fatique crack growth phenomena. It consists of linearly superimposing the two rates while assuming no creep-fatigue interaction between them:

$$\left(\frac{da}{dN}\right)_{total} = \frac{da}{dN} + \frac{da}{dt} \times t_{burn} \quad . \tag{184}$$

(total) (fatigue) (creep)

This model has also been used by McGowan and Liu [121] and Wei and Landes [122] to predict time-dependent effects.

Because the data for creep crack growth is sparse for temperatures below 600°C and $\Delta K \leq 20$ MPa$\sqrt{m}$ and non-existent for irradiation, R-ratio, threshold or environmental effects, it would be useful to know in what regimes of ΔK and temperature will creep cracking make a significant contribution to the total da/dN. This has been accomplished as shown in Fig. 93, by plotting the locus of points where $\frac{da}{dN} = \frac{da}{dt} \times t_{burn}$, for 316 SS and burn times of 10,100 and 1000 minutes. The region below the curves are combinations of ΔK and temperature for which fatigue crack growth dominates. Points within the boxed region represent typical operating condition for tokamak first wall components. Only at the high temperature, high ΔK corner of the box does creep crack growth appear to be significant. The opposite will be true, of course, for steady-state machines such

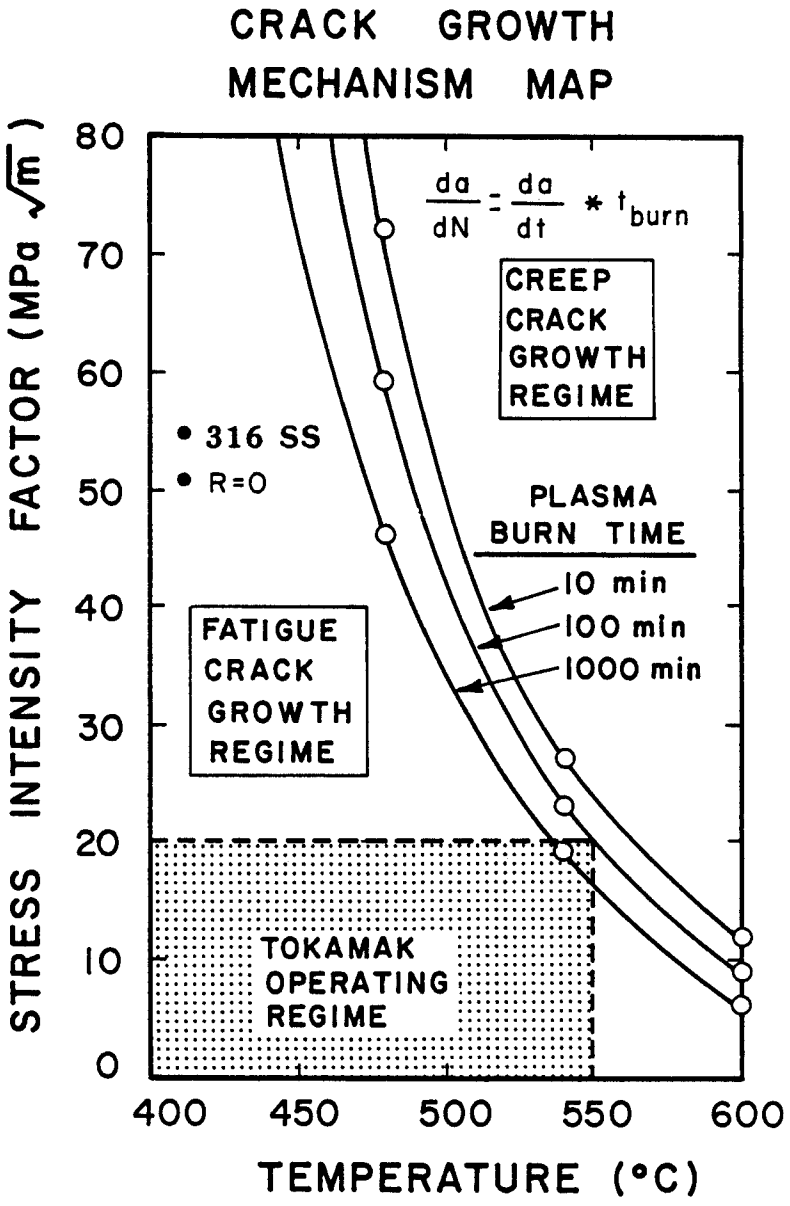

Figure 93. Crack growth mechanism map for 316 stainless steel at R = 0. The solid lines represent the locus of points where fatigue and creep crack growth contribute an equal amount to the total crack growth rate. For most tokamak reactors, crack growth is dominated by fatigue processes.

mirror machines, stellarators, or steady-state tokamaks (e.g. STARFIRE).

The total crack growth model represented by Eq. (184) assumes no creep-fatigue interaction to exist. While this is probably correct for "low" temperatures, e.g. less than 500°C, it appears that an interaction does exist for higher temperatures, i.e. greater than 500°C. Sadanada and Shahinian [31] have shown that for 20% CW 316 SS at 593°C in a vacuum the total crack growth rate for a one-minute hold-time test was greater than the sum of the corresponding static (e.g. creep) and zero-hold time (e.g. fatigue) tests. A possible explanation of this may be due to re-sharpening of the crack tip after each fatigue cycle, which previously had been blunted during the hold-time period by creep deformation.

Surprisingly, the opposite behavior has been observed by the same investigators [201] on Alloy 718 at 650°C. As shown in Fig. 94, with a one-minute hold time at K_{min} for R = 0.5, da/dN was observed to decrease with increasing ΔK with eventual crack arrest. They explained this by postulating that the stress intensity factor, K_{min}, during the hold-time was below the threshold for creep crack growth, ΔK_{thc}; therefore, no creep crack growth would occur, only crack tip blunting, and, ultimately, crack arrest. In this sense, long plasma burn times in a fusion reactor may be beneficial rather than harmful to crack propagation.

Another potentially beneficial effect which may occur during hold times is crack tip branching due to corrosion processes. This has been observed by Hammon et al [70] for 304L SS in liquid lithium

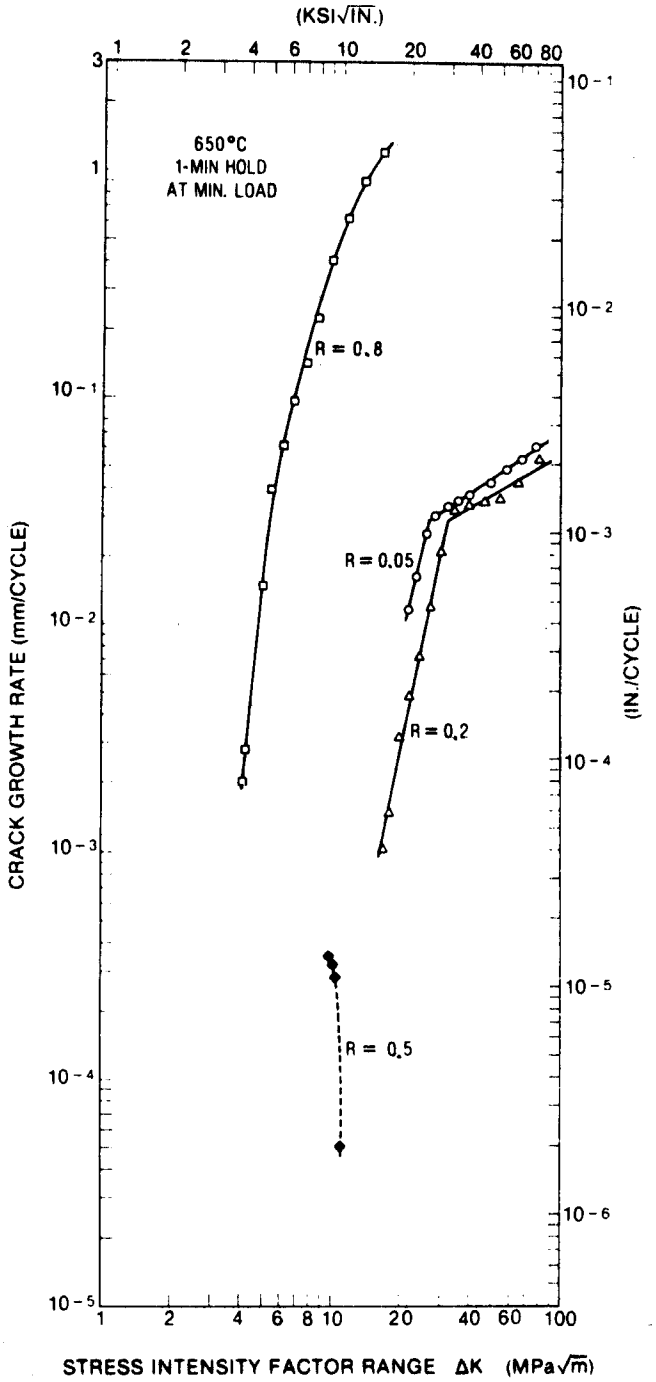

Figure 94. Effect of a one-minute hold-time at K_{min} and 650°C in alloy 718 for various R-ratios. Note the decreasing da/dN with increasing ΔK at R = 0.5 [201].

at 700°C under static loads. These two contrary effects illustrate the competing processes of damage accumulation from cavity or microcrack nucleation and growth, which are assisted by grain boundary sliding and diffusion, and the healing processes of stress relaxation process from creep deformation and crack tip blunting or crack branching due to grain boundary attack.

Wall Thinning and Crack Erosion

Physical sputtering, chemical sputtering, and vaporization of material from plasma disruptions are three mechanisms that can erode the surface of unprotected first wall components. Total erosion rates as large as 1-2 mm/yr have been calculated for INTOR conditions [125]. Because these rates are large, WISECRACK and TSTRESS both model the effects of surface erosion.

Surface erosion causes wall thinning, which affects the long-term stress history. As the wall thins down, the temperature difference across the wall decreases, thus lowering the cyclic thermal stress, $\Delta\sigma_{th}$. Since $da/dN \sim (\Delta\sigma_{th})^4$, even a small amount of erosion will extend the lifetime. However, too much erosion then causes the coolant pressure stress to increase, thereby enhancing the R-ratio (mean stress) and, hence, accelerating da/dN. Usually, the first effect dominates over the second. TSTRESS computes this complicated stress history and passes it on to WISECRACK.

If the crack is located on the plasma side of the wall, then surface erosion is assumed to reduce both of its dimensions, a and c, by an amount equal to Δa and Δc, respectively. For a given number of

cycles, N, we can write

$$\Delta a = e_r \cdot \Delta N \cdot t_{pulse} \tag{185}$$

and

$$\Delta c = c\left[1 - \sqrt{1 - \left(\frac{\Delta a}{a}\right)^2}\right] \tag{186}$$

where: e_r = erosion rate

t_{pulse} = period of one pulse.

WISECRACK assumes that if the rate of crack erosion in the a-direction,

$$\frac{\Delta a}{\Delta N} = e_r t_{pulse} \tag{187}$$

is greater than the total crack growth rate, $(da/dN)_{total}$, then the flaw will begin to shrink in size and eventually be obliterated. Although this seems plausible, no experimental data have been found to either confirm or refute this assumption. In existing tokamak machines, severe surface events such as arc tracks from runaway electrons have left pits or flaws on the surface rather than removing them. Further work is needed in this area.

There is a third synergistic effect caused by surface erosion that should be described. Wall thinning will indirectly change the stress intensity factor solutions by increasing the dimensionless depth ratio, a/h. This ratio is used in Eqs. (131,135,137,

140-142) to compute the membrane and bending correction factors, M_m and M_b. Therefore, since $\frac{da}{dN} \sim (\Delta\sigma)^4$, small changes in a/h due to wall thinning may have a significant effect on da/dN indirectly through M_m and M_b.

Method of Lifetime Prediction

The basic approach to predicting crack propagation consists of integrating the crack growth rates over the life of the component. For two-dimensional flaw growth this can be written as:

$$a_f = a_o + \int_o^{N_f} \left(\frac{da}{dN}\right)_{total} dN \tag{188}$$

and

$$c_f = c_o + \int_o^{N_f} \left(\frac{dc}{dN}\right)_{total} dN \tag{189}$$

where:

a_o = initial flaw depth

$2c_o$ = initial flaw surface length

a_f = flaw depth at failure

$2c_f$ = flaw length at failure

N = number of load cycles

N_f = cycles to failure.

Because the flaw changes shape, a closed form solution to these equations is not possible. Therefore we solve these equations numerically by choosing a small increment in cycles, ΔN, and then computing an approximate increment in growth as:

$$\Delta a \cong \left(\frac{da}{dN}\right)_{total} \times \Delta N \tag{190}$$

and

$$\Delta c \cong \left(\frac{dc}{dN}\right)_{total} \times \Delta N \quad . \tag{191}$$

The new crack size is obtained by adding these increments to the current dimensions:

$$a_{new} = a_{old} + \Delta a \tag{192}$$

$$c_{new} = c_{old} + \Delta c \quad . \tag{193}$$

The number of cycles is then updated by adding ΔN to the old value of N. Any degree of accuracy can be obtained with this method by choosing a sufficiently small step size ΔN. Chapter 7 describes this algorithm in more detail.

The end-of-life is defined by one of two possible failure modes. One possible mode is when $a_f \geq h$ and coolant therefore leaks through the wall. Typically, this mode is dominant when either the toughness is high ($K_{Ic} > 100$ MPa$\sqrt{m}$) or when the wall erosion rates are high ($e_r > 1$ mm/yr). The other failure mode is catastrophic fracture, which occurs when $K_{max} \geq K_{Ic}$. For embrittled steels, it is this latter mode that controls the lifetime. Obviously, one would prefer the leak-through failure mode over catastrophic fracture because of the safety and clean-up problems of spilling coolant into the vacuum chamber.

Summary and Conclusions

Linear elastic fracture mechanics is used in this chapter to model the growth of a semi-elliptical surface flaw in austenitic stainless steel first wall components operating at elevated temperatures in a neutron environment. The driving force for crack growth is measured by the stress intensity factor at the crack tip and can be determined very accurately during normal operating conditions in magnetically-confined devices. Next, a fatigue crack growth rate equation was developed that includes the effects of temperature, mean stress (R-ratio), threshold ΔK_o, short crack correction, aggressive environments, and embrittlement. The effects of neutron irradiation were predicted by modeling the impact of a reduction in fracture toughness on da/dN. Toughness levels of 30-60 MPa$\sqrt{m}$ for irradiated steels are expected to result in increased growth rates during stage II. Also, the contribution of creep crack growth in 304 and 316 SS was studied and determined to be small for temperatures below 550°C.

Three important conclusions can be made. First, there is a very good understanding of the linear elastic fracture mechanics analysis of a surface flaw as it applies to a first wall component. Some more research needs to be done on K-solutions for highly non-linear stress gradients, however. Secondly, there is a good understanding of the modelling of crack propagation in austenitic stainless steel outside of a fusion environment. However, we are just beginning to be able to model da/dN in a fusion environment because

effects of lithium enhanced corrosion-fatigue, creep-fatigue interactions, hydrogen and neutron embrittlement, surface erosion, void/crack-tip interactions, crack tip blunting or branching all need to be assessed before an accurate lifetime calculation can be made. Unfortunately, all of these uncertainties must be superimposed on a scatter factor of four, typically inherent in the basic data for fatigue crack growth rates. Nevertheless, the models that were presented in this chapter, along with their implementation into the WISECRACK code, represent a substantial improvement over existing methods of fracture mechanics that are currently in use within the fusion community.

CHAPTER 7

WISECRACK - A Computer Code for Crack Growth Analysis

Introduction

The purpose of WISECRACK (Wisconsin semi-elliptical crack growth code) is to predict the lifetime of first walls, limiters, neutral beam dumps, divertor collector plates, or other high heat flux components used in fusion reactors. The component is modeled as a flat plate containing a small, pre-existant semi-elliptical surface flaw oriented perpendicular to the direction of maximum principal stress and is subjected to membrane loads, cyclic temperature gradients, irradiation creep and swelling, embrittlement, and surface erosion as caused by sputtering. The crack grows along both its major and minor axes due to the combined action of cyclic stresses (fatigue crack growth) and constant stresses at high temperatures (creep crack growth). Failure results when the crack either penetrates through the wall, therefore causing coolant to leak into the plasma chamber, or when the maximum stress intensity factor exceeds the material's fracture toughness and causes catastrophic fracture. Figure 95 illustrates a typical flaw growth pattern expected for a tokamak first wall component. In this example, WISECRACK predicted leak-through failure (leak-before-break) after 621,000 cycles of normal operation [182]. A detailed description of the code and user's instructions are given in Reference [183]

Because of the unique environment in a fusion reactor, it was

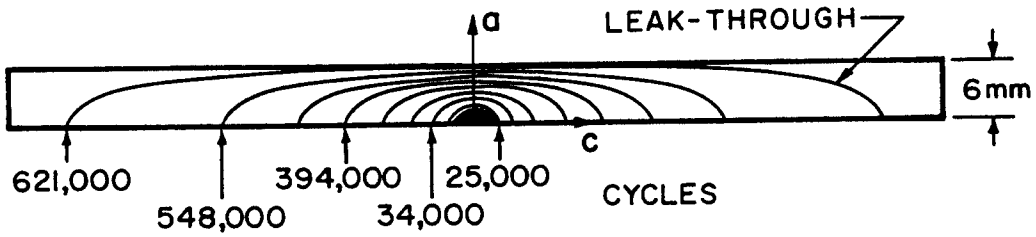

Figure 95. Typical two-dimensional flaw growth pattern for tokamak reactor first wall predicted by WISECRACK.

necessary to devise a special lifetime code that would include the effects of radiation damage and surface erosion. Table 11 highlights the important features of WISECRACK which make it an ideal choice for fusion applications. While other codes have been used within the fusion community (e.g. NASA CRACK [67]), WISECRACK has three special features which distinguish it from existing codes:

1. Linearization of non-linear stress distributions.
2. Recently published, state-of-the-art stress intensity factor solutions for tension and bending loads.
3. Wall thinning and crack erosion.

Method of Solution

The two coupled growth equations solved by WISECRACK are:

$$a(N) = a_o + \int_o^N \left(\frac{da}{dN}\right)_{total} dN \tag{195}$$

and

$$c(N) = c_o + \int_o^N \left(\frac{dc}{dN}\right)_{total} dN \tag{196}$$

where a_o and c_o are the crack's initial dimensions at N = 0. The numerical solution involves approximating the integrals with sums therefore

$$a(N + \Delta N) \cong a(N) + \left.\frac{da}{dN}\right|_N \Delta N. \tag{198}$$

Table 11. Highlights of WISECRACK Code

- Linear elastic fracture mechanics.
- Semi-elliptical surface flaw in a flat plate.
- Two-dimensional shape change growth model.
- Time-dependent stress cycle (variable R-ratio).
- Fatigue and creep crack growth rates linearly superimposed.
- Leak-through and catastrophic fracture failure modes.
- Bending stress intensity factor solutions.
- Linearization over-the-crack of nonlinear stress gradients through the wall.
- Fatigue crack growth model includes temperature effect, R-ratio effect, threshold ΔK, and embrittlement.
- Short crack correction factor for $a_o < 1$ mm.
- Wall thinning and crack erosion included.
- Neutron-induced reduction in fracture toughness.
- Fourth-order Runge-Kutta numerical integration method with automatic step size selection.
- Two different models for fatigue crack growth rate.
- Option for one-dimensional crack growth.

and

$$c(N + \Delta N) \cong c(N) + \left.\frac{dc}{dN}\right|_N \Delta N. \tag{198}$$

The smaller ΔN is, the more accurate the approximation becomes. The actual numerical algorithum that WISECRACK employs is a 4th order, Runge-Kutta multistep procedure, as shown schematically in Fig. 96. With this more accurate method, we replace Eqs. (197) and (198) by

$$a(N + \Delta N) \cong a(N) + \Delta a \tag{199}$$

$$c(N + \Delta N) \cong c(N) + \Delta c \tag{200}$$

where

$$\Delta a = \frac{1}{6}\left[\Delta a_1 + \frac{1}{2}\ \Delta a_2 + \frac{1}{2}\ \Delta a_3 + \Delta a_4\right] \tag{201}$$

$$\Delta c = \frac{1}{6}\left[\Delta c_1 + \frac{1}{2}\ \Delta c_2 + \frac{1}{2}\ \Delta c_3 + \Delta c_4\right] . \tag{202}$$

It should be noted that the two governing equations for da/dN_{total} and dc/dN_{total} are coupled by a common dependence on the flaw shape factor, Q, the membrane correction factor, M_m, and on the bending correction factor, M_b, via the aspect ratio, a/c. The coupling with Q is not very significant, but the M_m and M_b coupling can be very strong is some cases.

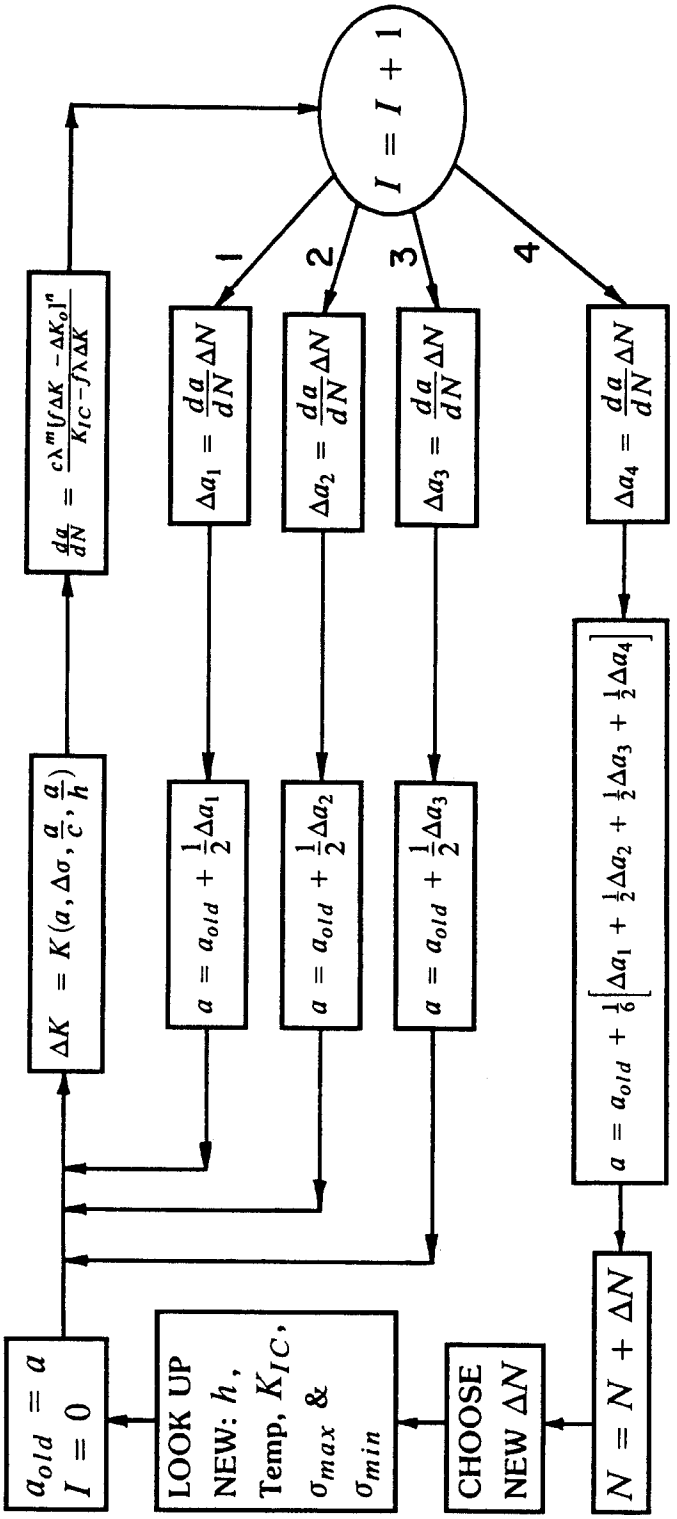

Figure 96. Method of solution used in WISECRACK.

Step Size Control

In order to minimize computing times, WISECRACK automatically calculates the increment in cycles, ΔN, at the beginning of each program iteration. The chosen value of ΔN must then satisfy four separate adjustable criteria which allow the largest possible ΔN, without sacrificing accuracy. ΔN is chosen to be the smaller of the following two numbers,

$$\Delta N = \text{minimum} \left\{ \begin{array}{c} \varepsilon \dfrac{a}{da/dN} \\ \\ \varepsilon \dfrac{c}{dc/dN} \end{array} \right\} \quad . \tag{203}$$

These numbers are chosen so that $\Delta a \leq \varepsilon a$ and $\Delta c \leq \varepsilon c$, where ε is defined as the maximum allowed fractional change in crack size. The default value of ε is 1%.

The first of four limiting criteria prevents ΔN from exceeding a specified maximum, therefore

$$\Delta N \leq \Delta N_{max} \cdot \tag{204}$$

The second rule prevents ΔN from growing faster than an allowed rate. If ΔN_{old} is the current value of ΔN, then

$$\Delta N \leq \Delta N_{old} \cdot T_g \tag{205}$$

where T_g typically equals 1.5.

The third criterion is related to the long-term stress history as computed by TSTRESS. These stresses are stored in an array at specific points in time: t_1, t_2, $t_3 \ldots t_n$. Since these stresses should not change significantly within the ΔN cycles, ΔN may not exceed the ratio

$$\Delta N \leq \frac{t_{n+1} - t_n}{t_{pulse}} \quad . \tag{206}$$

This insures that the stress history will be followed accurately.

Finally, the fourth criterion simply prevents ΔN from taking on any fractional values, hence

$$\Delta N \geq 1 \quad . \tag{207}$$

The user can control the accuracy and/or efficiency of the calculation by setting his/her own values for ε, ΔN_{max}, and T_g.

Crack Shape Changes

It has been observed experimentally that surface flaws will change shape as they grow in size [184-192]. Figures 97 and 98 show WISECRACK predictions for the change in aspect ratio as a function of depth through the plate for pure tension or pure bending stresses, respectively. The data in Figure 99 from Nair [189] and Pierce and Shannon [192] compare well to the WISECRACK predictions. The assumption commonly made among first wall analysts that a semi-circular flaw (a/c = 1.0) will keep its shape throughout its life during tension

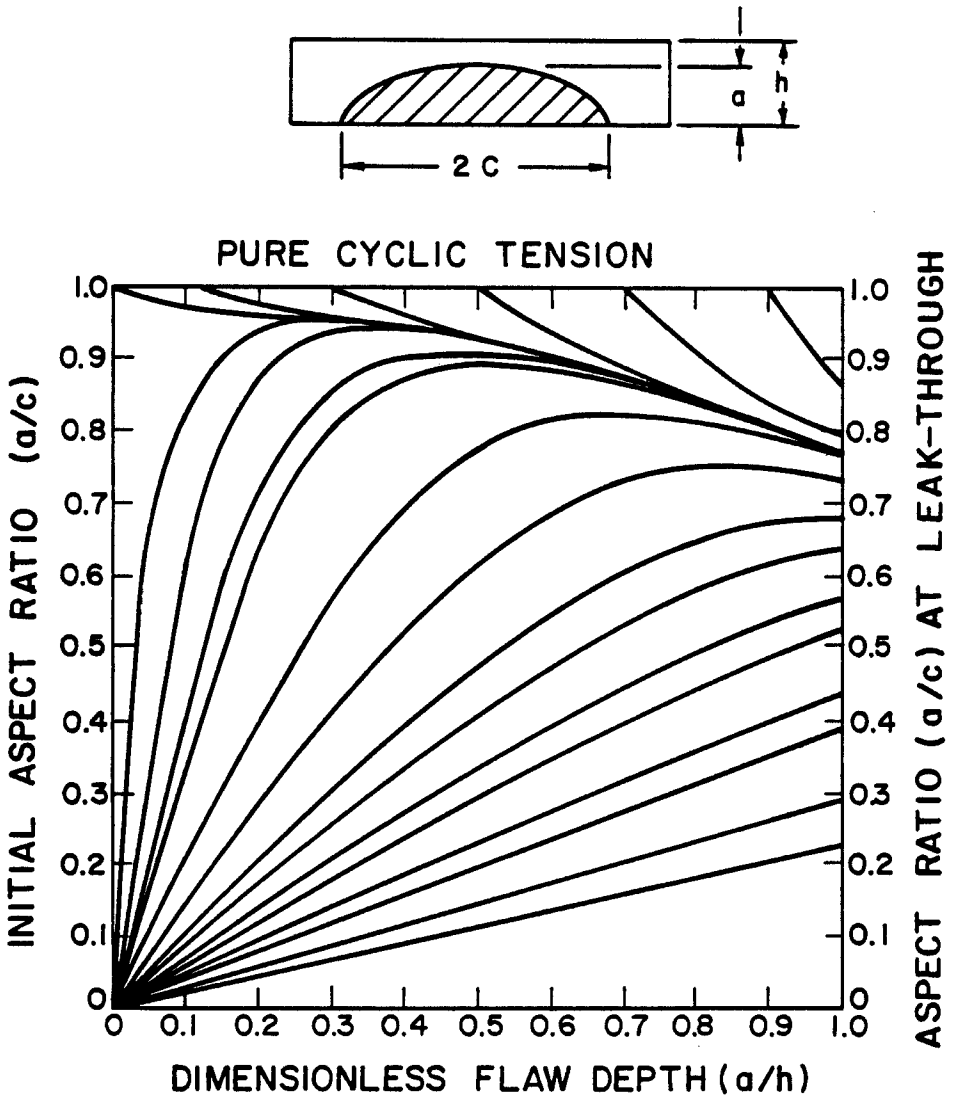

Figure 97. Flaw shape changes for pure cyclic tension loads from WISECRACK predictions.

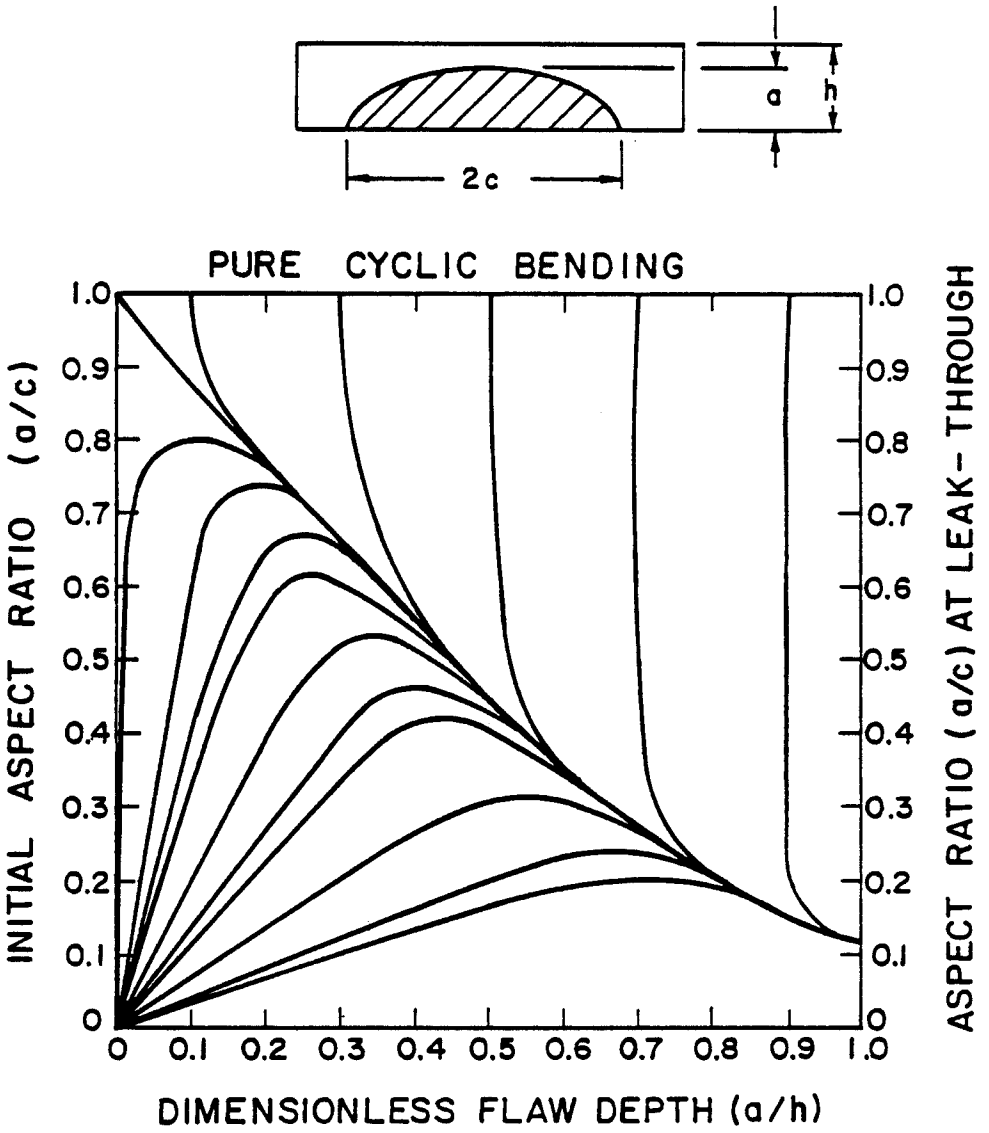

Figure 98. Flaw shape changes for pure bending moments from WISECRACK predictions.

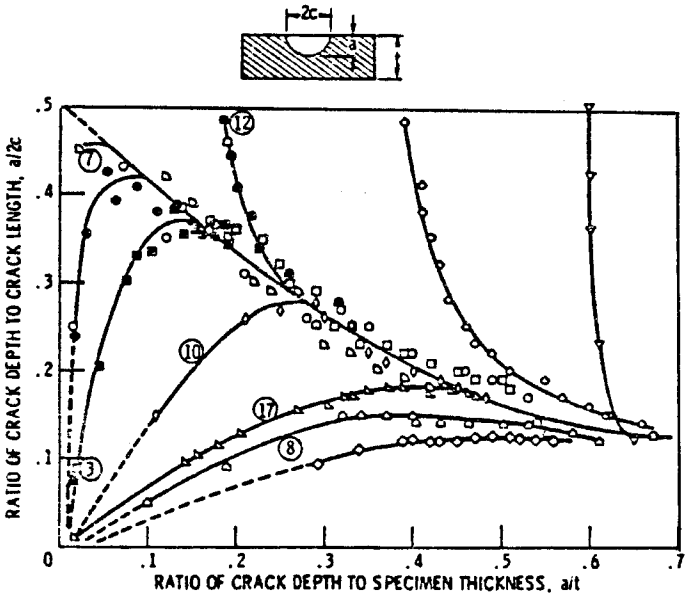

(a) pure bending moments

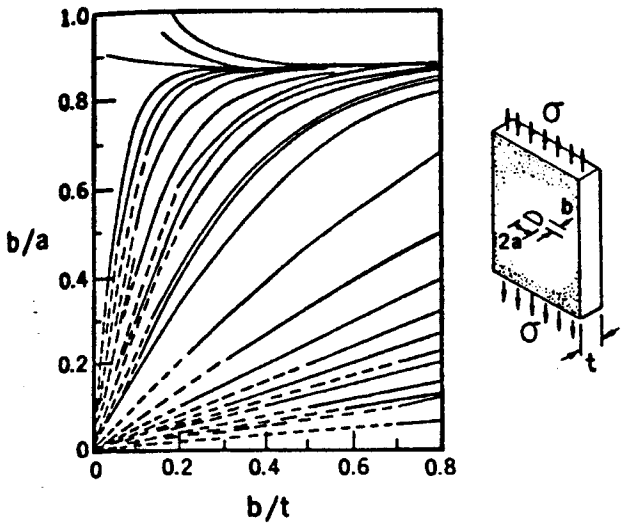

(b) pure tension loads

Figure 99. Flaw shape changes for (a) pure bending and (b) pure tension [189,192].

loads is reasonably accurate, according to Fig. 97. However, when subjected to pure bending, the flaw quickly changes its shape by elongating faster along the surface than through the depth. With a final aspect ratio of a/c = 0.12, it is obvious that the previous assumption of a final a/c = 1.0 is clearly incorrect. As will be demonstrated later on in Chapter 8, this one-dimensional flaw growth assumption can lead to quite erroneous lifetime predictions.

Comparison of WISECRACK Predictions with Experimental Results

The verification of WISECRACK was accomplished by comparing the code's predictions to both experimental results and other codes' predictions. The primary source of data comes from a symposium held in October, 1977 entitled: "Part-Through Crack Fatigue Life Prediction" [193]. Extensive experimental data were presented in this symposium on fatigue crack growth of a semi-elliptical surface flaw loaded in pure cyclic, constant amplitude tension loads. A major task that was set up for this symposium was a set of round-robin verification tests which were given to six different independent investigators, including:

1.	J.B. Chang	Rockwell International
2.	R.G. Forman	NASA
3.	G. Hales & W.S. Johnson	General Dynamics
4.	C.M. Hudson	NASA - Langley
5.	D.E. Peterson	Rockwell International
6.	J.L. Rudd	Air Force Flight Dynamics Lab.

Each of these six investigators were given the same initial conditions and were asked to predict with their codes the number of cycles to either break-through or catastrophic fracture. To insure objectivity, the experimental number of cycles-to-failure were not given to them. Typical results of Chang's predictions are shown in Figure 100. These plots show the classic crack growth curve, where the largest percentage of life is consumed while propagating only a small distance through the specimen. As the crack grows, it accelerates until it finally becomes unstable as the stress intensity factor approaches the fracture toughness, K_c.

The combined predictions of all six investigators for ten different aluminum alloy specimens gave an averaged prediction ratio of 1.007 (prediction ratio is defined as: predicted life / experimental life). This important result indicates that the state-of-the-art methods for life prediction are very accurate when averaged over many specimens (at least for cyclic, pure tension loads). The results also showed, however, that individual specimen lifetimes could differ from the predicted value by as much as a factor of two.

The WISECRACK code was then used to predict lifetimes for two different load conditions, 14 ksi and 32 ksi, which covered 8 out of the 10 specimens included in the round-robin study. The approach taken for these problems was to use the same constitutive laws for crack growth as were used by each of the four different investigators. The actual WISECRACK predictions are compared to the other four in

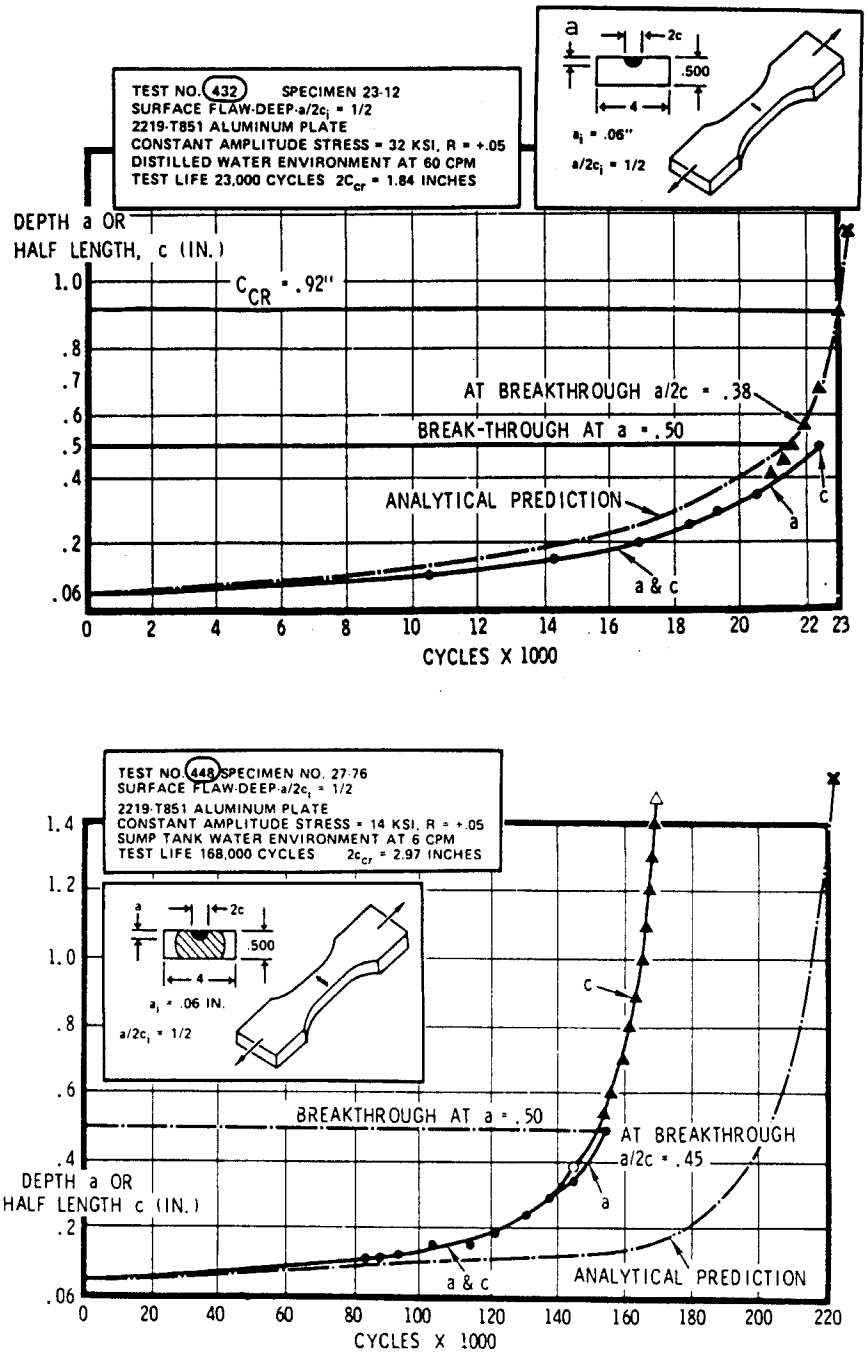

Figure 100. Crack growth under pure tension loads at 14 and 32 ksi [193].

Figure 101. The notation "Chang-1,2,3" refers to three different lines through the data that were fit by Chang, as shown in Fig. 102.

From Figure 101, it can be seen that the WISECRACK predictions are as accurate as any of the others considering the inherent scatter in the data. The average of all the predictions is very close to the experimental average and the scatter among investigators compares well to the real scatter in data.

Another series of verifications were then conducted on a second data set. Using the materials' data as provided by Engle [193], lifetimes were predicted by WISECRACK for constant amplitude cyclic tension tests with various R-ratio and initial flaw sizes ranging from: $0.28 < a/c < 1.0$, $0.25 < a/h < 0.85$, $R = 0.1$ or 0.5. Figure 103 summarizes the results, where the ratio of predicted lifetime/experimental lifetime is plotted for two different investigators (Engle and Watson) for a total of 34 specimens and three different metals. The scatter in predictions is significant, as much as 1.5 times larger or 0.6 times smaller than the experimental value. However, each "test number" refers to only one specimen for a given load condition, so that the effect of scatter in material properties is not accurately represented here. Nevertheless, the overall prediction ratios of both the WISECRACK code and Engle's code averaged out to be quite good, as summarized in Table 12.

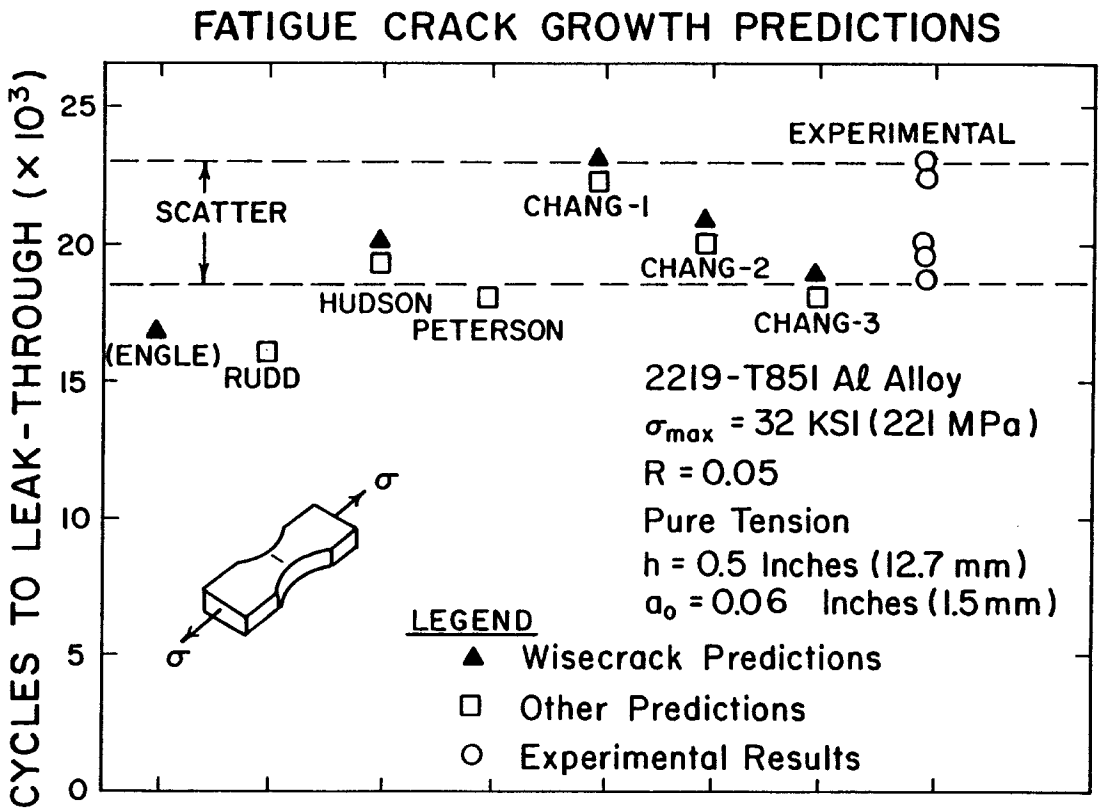

Figure 101. Comparison of WISECRACK predictions to experimental results and other investigators predictions for pure tension loads [193].

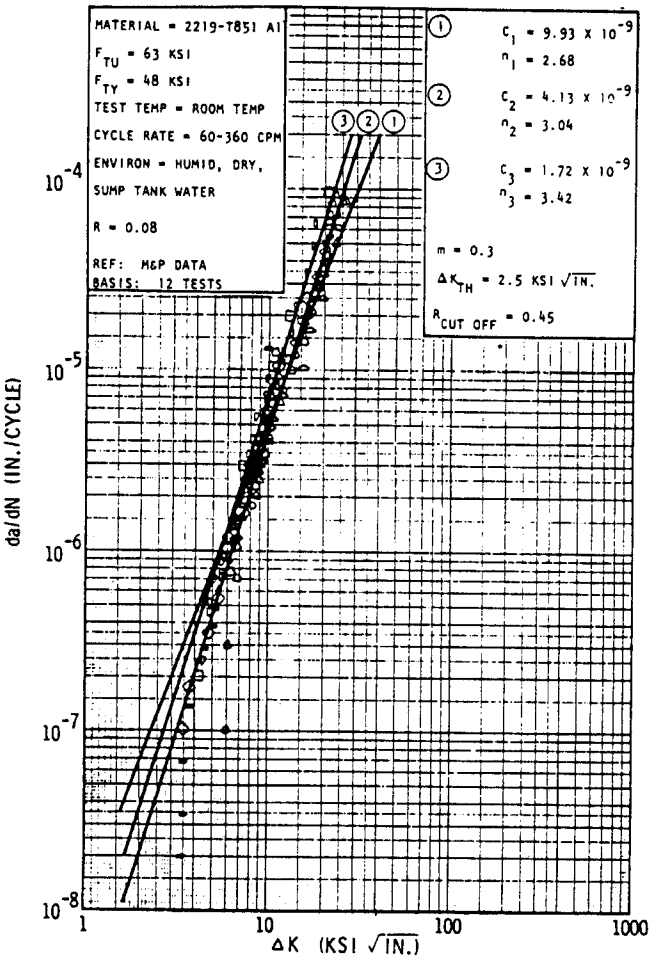

Figure 102. Fatigue crack growth rate data for 2219-T851 aluminum alloy used in verification tests for WISECRACK [193].

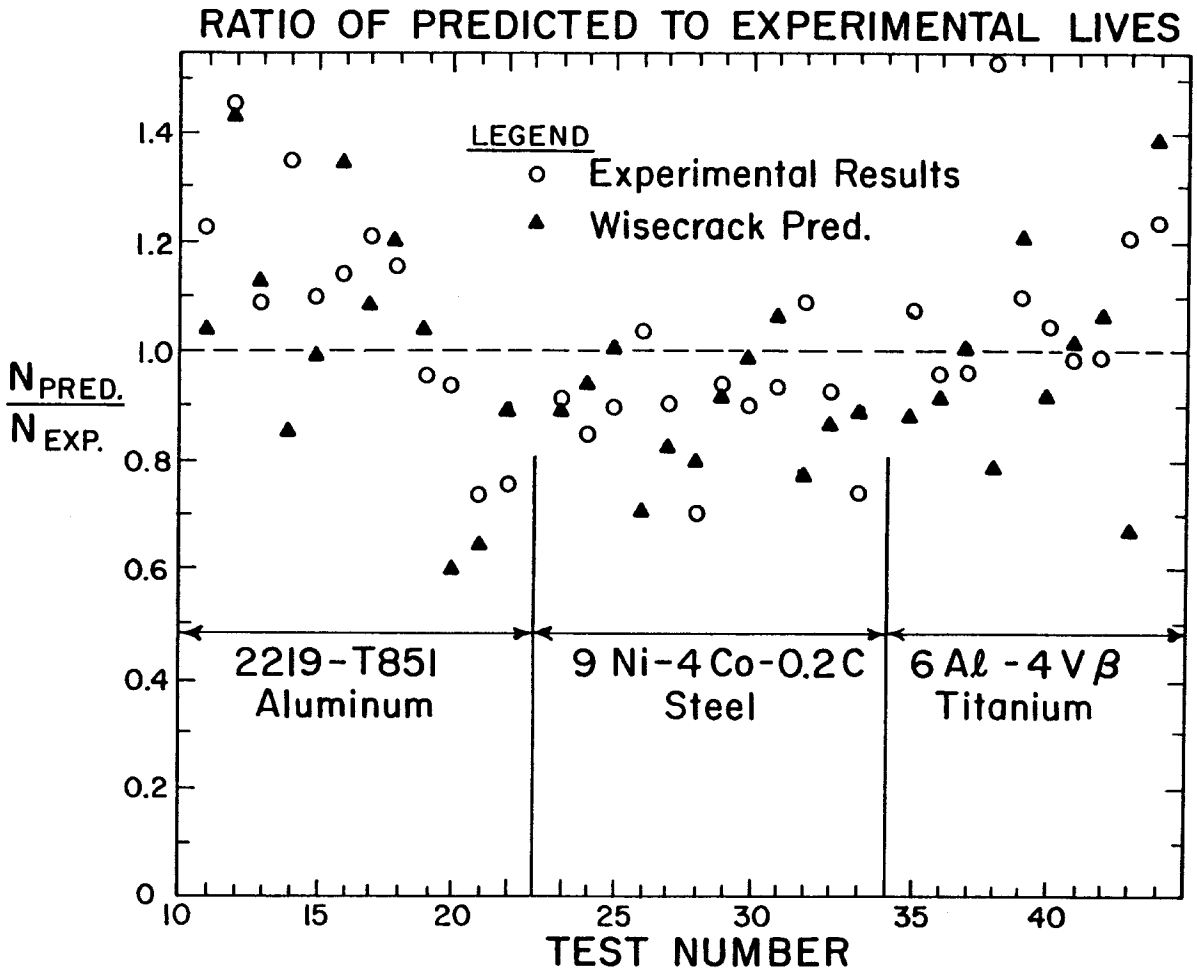

Figure 103. Ratio of predicted to experimental lives for three different metals all tested in pure tension loads [193].

Table 12. Accuracy of WISECRACK Code

	Average Prediction Ratio	Standard Deviation
WISECRACK	0.96	± 0.18
Engle Code	1.03	± 0.17

Note: 34 specimens

All three sets of sample problems described so far have been examples of pure tension loadings, and the majority of experimental data fits into this category. However, some experiments have also been performed for pure alternating bending loads. The following is a set of predictions that were performed to verify the accuracy of the WISECRACK code under a linear stress gradient.

Probably the best source of experimental tests of part-through cracks is A.F. Grandt's PhD thesis entitled "A Fracture Mechanics Analysis of Surface Cracks in Bending" (1971) [194]. He determined crack growth data for seven tests on polymethylmethacrylate (PMMA), a transparent elastic polymer. Grandt first measured the fatigue crack growth constitutive law for PMMA, as shown in Figure 104. WISECRACK then used this data and the same initial flaw sizes to simulate the seven bending tests from Grandt's thesis. Results are pre-

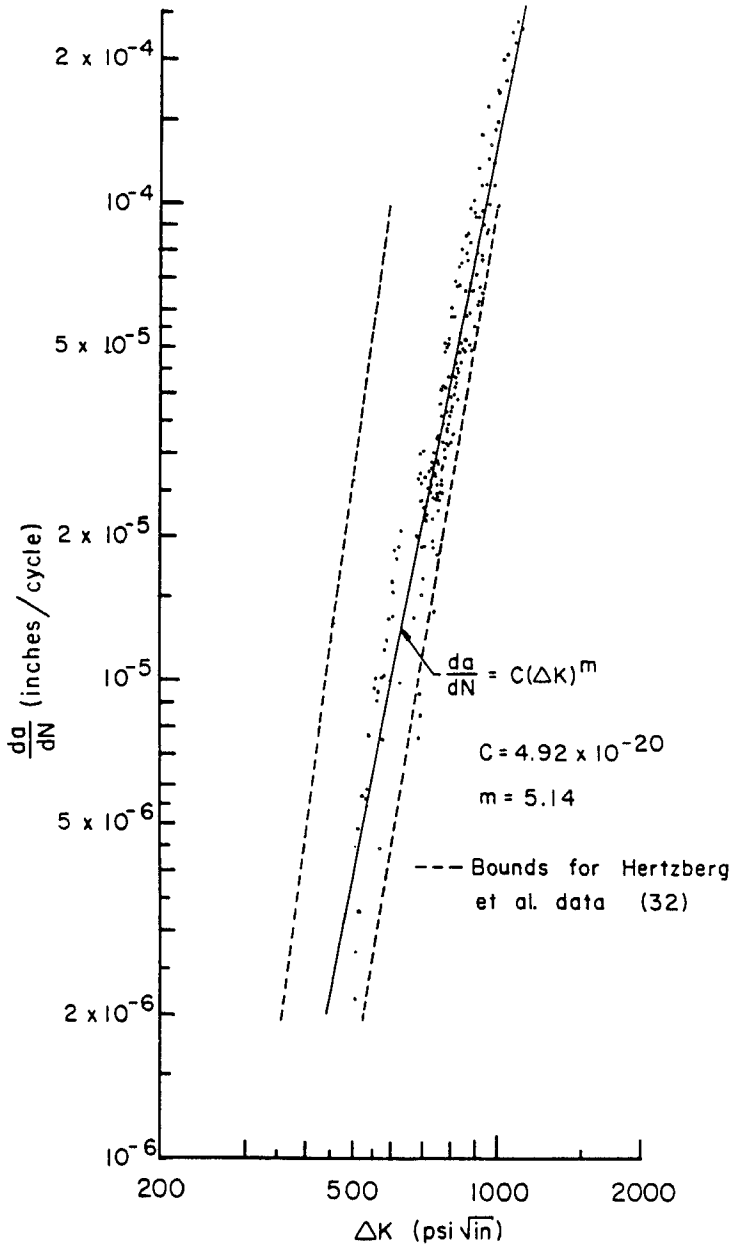

Figure 104. Fatigue crack growth rate data for polymethylmethacrylate bending tests [194].

sented in Table 13. Figure 106 shows actual test data from specimen #7.

From Table 14 we can see that the average WISECRACK prediction ratio for lifetimes is 0.81 with a standard deviation of ±0.15. This is considered to be in good agreement with the data, and is conservative as well. The measure of scatter (±0.15) is also very comparable to the scatter in predictions for pure tension tests (±0.18, ±0.17). Table 13 shows that WISECRACK predicted the final crack dimensions, a_f and $2c_f$, more accurately than it did for the cycles-to-failure, N_f (lifetime). The scatter in size predictions is a factor of 2 smaller as well. Nevertheless, these particular verification tests for pure bending are considered to be successful.

In only one paper have the results of a combined tension and bending test been reported. Nagai et al [195] loaded a 9% Ni steel plate with a linear stress gradient of 290 MPa on the cracked side and 170 MPa on the other side. Table 15 summarizes the predictions and results for the following conditions: a_o = 3.1 mm, h = 12 mm, $2c_o$ = 6.2 mm and R = 0.

Table 13. Bending Test Results vs. WISECRACK Predictions

TEST NUMBER	a_{final} (inch)		$2c_{final}$ (inch)		cycles to failure*	
	results	prediction	results	prediction	results	prediction
7	0.36	0.356	1.61	1.64	7002	6109
200	0.37	0.320	1.44	1.32	5886	4017
201	0.33	0.300	1.33	1.17	1767	1577
211	0.30	0.274	1.21	0.99	8131	8177
212	0.32	0.286	1.21	1.07	10764	7292
220	0.29	0.235	1.00	0.75	7890	4862
221	0.34	0.326	1.44	1.40	9224	8389

*brittle fracture

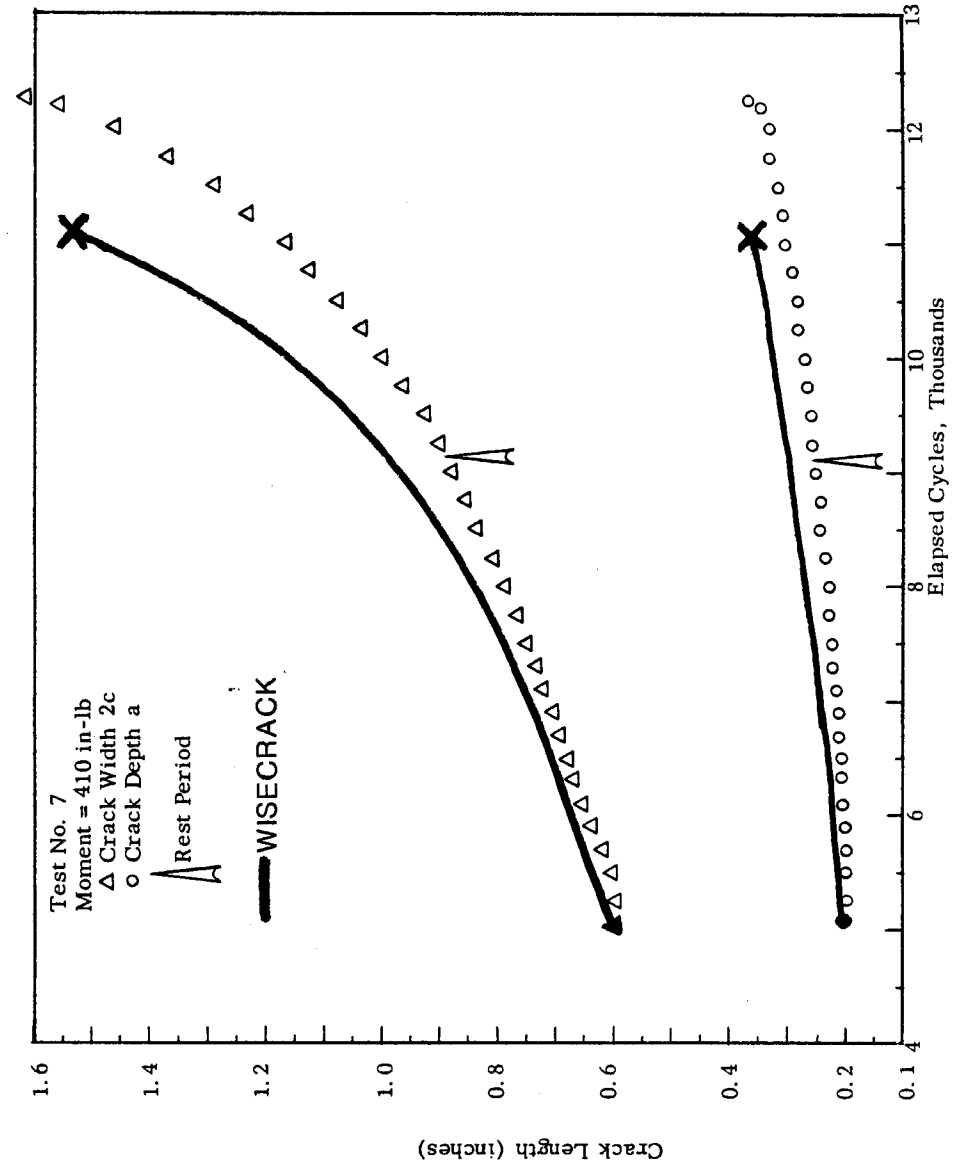

Figure 106. Comparison of WISECRACK predictions to experimental results for pure bending crack growth in PMMA [194].

Table 14. Prediction Ratios for Bending Tests

TEST NUMBER	DEPTH a_{pred}/a_{exp}	HALF-LENGTH c_{pred}/c_{exp}	CYCLES N_{pred}/N_{exp}
7	0.99	1.02	0.87
200	0.86	0.91	0.68
201	0.91	0.88	0.89
211	0.91	0.82	1.01
212	0.89	0.89	0.68
220	0.81	0.75	0.62
221	0.96	0.98	0.91
mean	0.90	0.89	0.81
standard deviation	± 0.06	± 0.09	± 0.15

Table 15. Combined Tension and Bending Loads

	Nagai prediction	WISECRACK	experimental
cycles	76,000	89,000	85,000
a_f (mm)	-	12.0	12.0
$2c_f$ (mm)	29.4	35.6	28.6

Again, it can be seen that the WISECRACK predictions are in good agreement with the experimental results.

Finally, it would be desirable to verify the accuracy of WISECRACK in predicting creep crack growth of a part-through crack in a plate loaded in static tension at elevated temperatures. Unfortunately, no experimental results appear to have been published. Nevertheless, we conclude that if the initial flaw size is known, then WISECRACK will accurately predict the entire growth pattern and, hence, the lifetime, within the inherent scatter in the data.

Applications: Tokamak Reactor First Walls

In the preceeding section we compared the accuracy of the WISECRACK predictions to experimental results and found excellent agreement, considering the scatter inherent in the da/dN data. In this section, we apply the WISECRACK code to a specific first wall design for a tokamak power reactor. This design is the same cylindrical blanket module referred to previously in Chapter 5 as the "reference design" (see Figure 1). The reference design parameters are listed in Table 7. We assume a hypothetical surface flaw located on either side of the wall, with the following dimensions: a_o = 1 mm and a_o/c_o = 1.0 (semi-circular). This flaw size is within the range of detection for "standard" nondestructive evaluation (NDE) techniques, and is four times larger than the smallest flaw detectable by "special" NDE, according to the Space Shuttle criteria [28]. Therefore, the assumed size, a_o = 1 mm, is somewhat larger than what could be detected; a

more realistic choice might have been a_o = 0.3 - 0.5 mm. Because of the uncertainty in the detectable crack size, the sensitivity of lifetime to the choice of the initial a_o was studied, and it is discussed in Chapter 8. Choosing a_o = 1 mm as the reference parameter allows us to compute a "worst case" lifetime, while the actual lifetime is probably longer, if indeed the special NDE techniques can detect with confidence cracks as small as 0.25 mm deep.

Figure 107 shows the results of WISECRACK predictions of crack growth through the thickness for three different cases which were chosen to illustrate the wide range of possible behaviors. The first example is for the reference parameters, and the curve is labelled "Irradiation only". Here, failure occurred after two years due to catastrophic fracture associated with neutron induced embrittlement of K_{Ic} = 30 MPa$\sqrt{m}$.

The second example, marked "No irradiation," illustrates the case where all of the reference parameters are held the same, while assuming that the mechanical properties remain unaffected by neutron irradiation, by assuming that the neutron flux, ϕ, is equal to zero. This case gives the longest lifetime, with failure occurring by coolant leak-through. The shift in failure mode from the previous example is due to the much higher unirradiated fracture toughness, $K_{Ic} \cong$ 150 MPa$\sqrt{m}$, which allows a "leak-before-break" design for these thin walls ($h \lesssim$ 10 mm). Also, by comparing the two cases, with and without irradiation, we can see that the former starts out with a slower crack growth rate, da/dN. This is caused by irradiation creep,

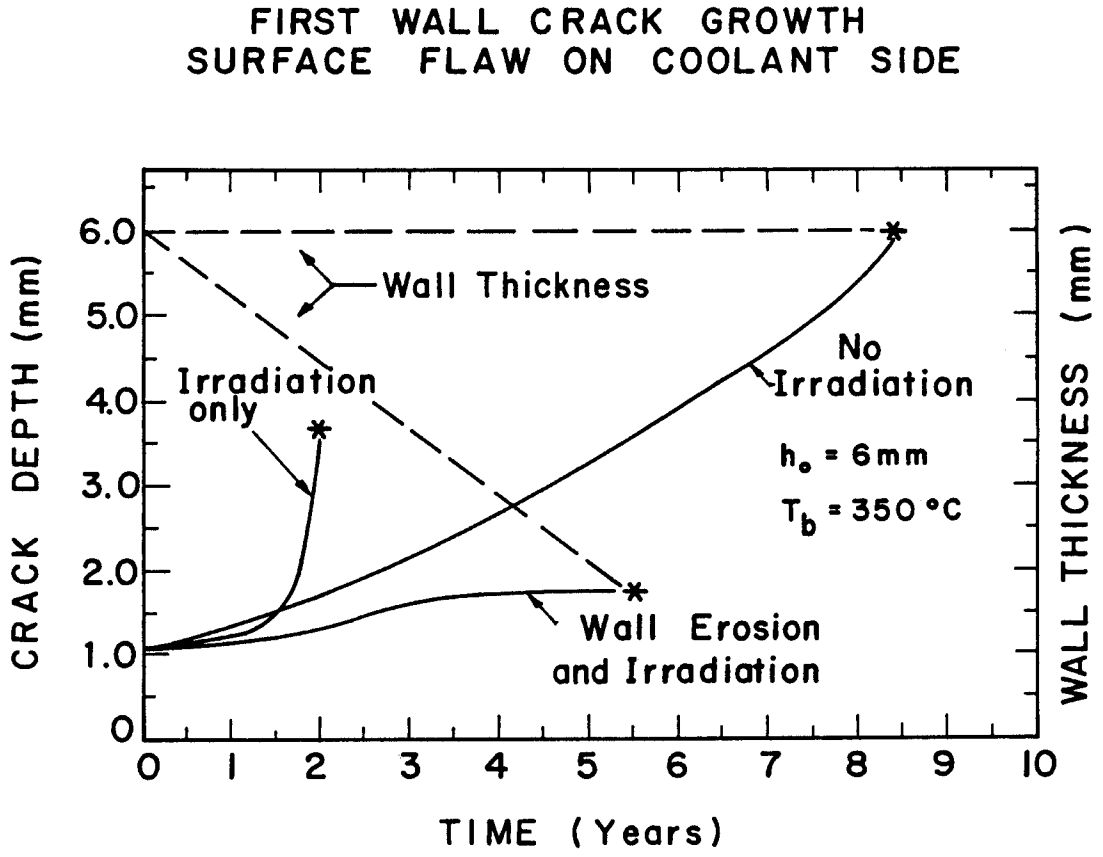

Figure 107. WISECRACK predictions of crack growth for the reference design for various conditions.

which reduces the mean stress level (and hence the R-ratio) towards zero during the first year of operation (see Fig. 24). However, after one year the stresses on the coolant side begin to increase due to swelling. This, coupled with the predicted increase is the slope, n, of stage II fatigue crack growth which accompanies the drop in K_{Ic} to 30 MPa$\sqrt{m}$, combine to increase da/dN over the unirradiated case, after just one year.

The third example plotted in Fig. 107 is with irradiation and with a wall erosion rate of 0.82 mm/FPY. The crack growth is very small throughout the 5.5 year lifetime. This behavior is controlled by the stress history, which is shown in Fig. 108. The dominant effect which reduces the fatigue crack growth rate is the reduction in the cyclic thermal stresses, $\Delta\sigma_{thermal}$, caused by a reduction in the temperature gradient across the wall as the wall thins down. Therefore, we see that a moderate amount of wall erosion will actually slow down the rate of crack growth for cracks on the coolant side.

For cracks located on the plasma side, the effects of surface erosion on crack propagation can be somewhat different. Fig. 109 shows WISECRACK predictions of crack growth for the reference design with a wall erosion rate of 1 mm/FPY. Here we can see that the original surface flaw is eroded away and eventually is obliterated after 1.3 years of operation. Now, let us take this same example and change only the backside wall temperature, T_b, from 350°C to 100°C. The impact on crack propagation is to increase the growth rates due to the higher mean stresses caused by less swelling at the

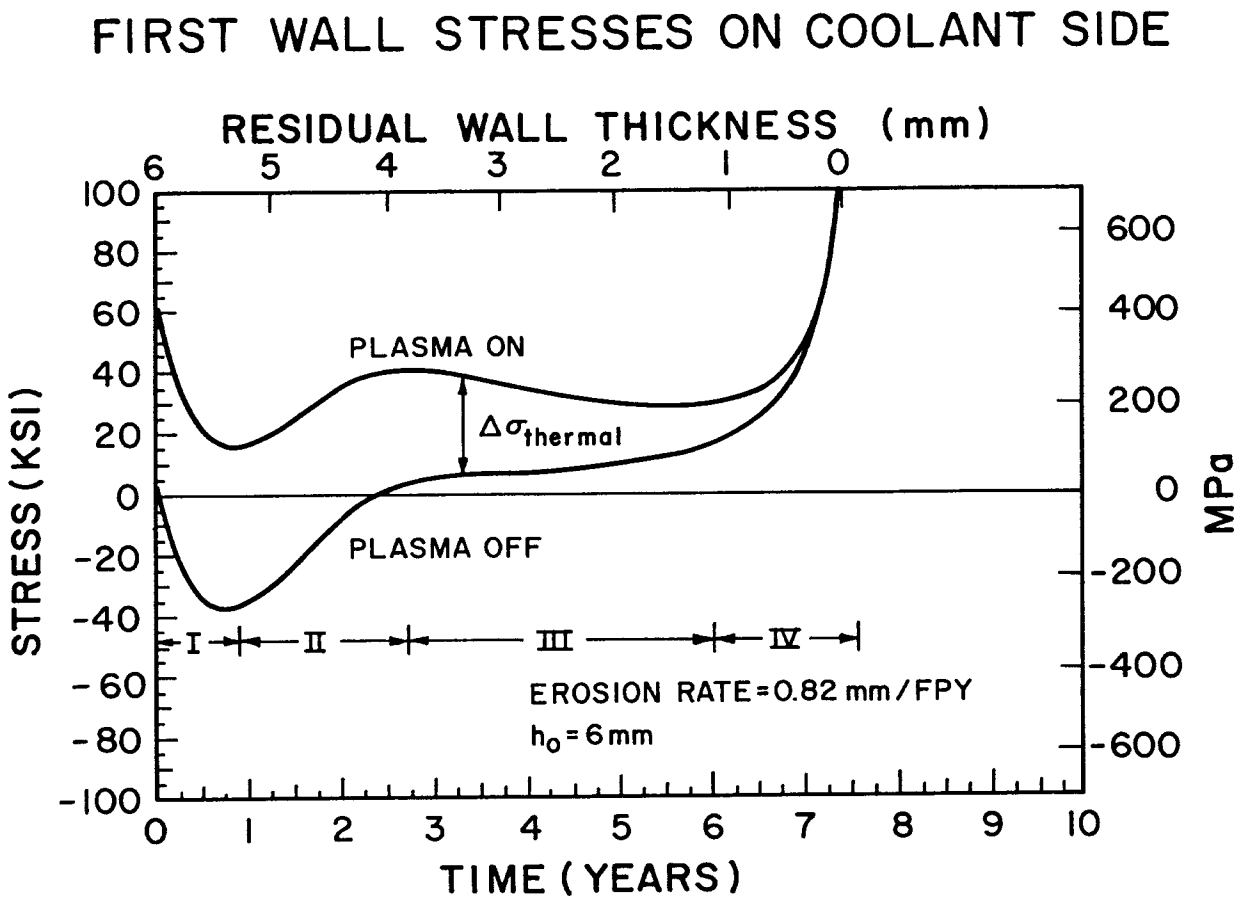

Figure 108. Effect of wall erosion on stress history of coolant side stresses, e_r = 0.82 mm/FPY.

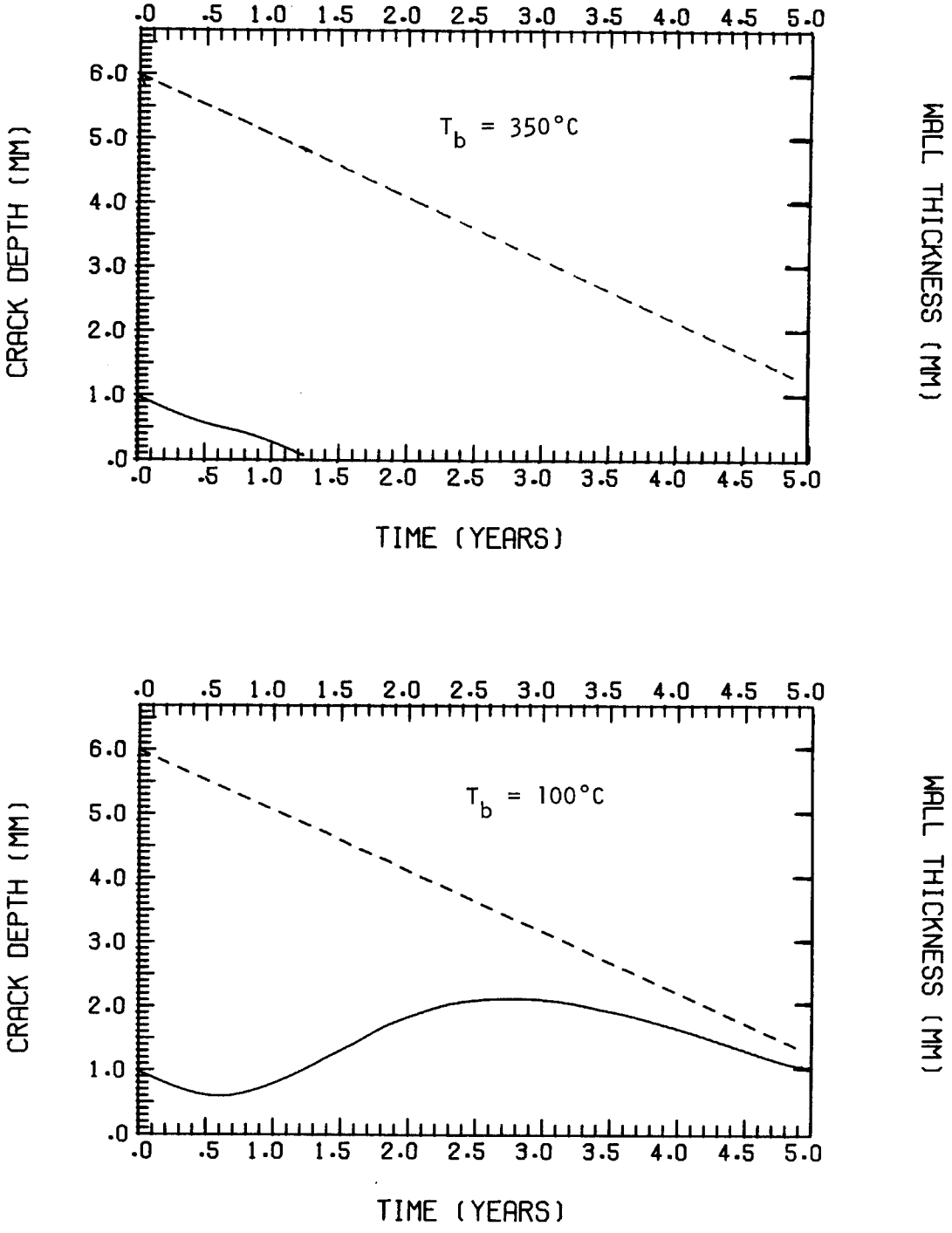

Figure 109. Effect of wall erosion on crack growth of flaws on plasma side for two different backside wall temperatures, 100°C and 350°C for e_r = 1 mm/FPY.

lower temperature, as can be seen by comparing the stress histories for these two temperatures in Figs. 45 and 47. The resulting crack growth, as shown in Fig. 109, becomes much more complex, and illustrates the "competition" between crack growth and crack erosion processes. Chapter 8 will discuss in more detail the overall implications of surface erosion on the lifetime.

Summary and Conclusions

This chapter presented a newly developed computer code called WISECRACK for 2-D crack growth analysis of first wall components. The basic algorithm used in the code involves a 4th-order Runge-Kutta method for integrating the two coupled growth rates $(da/dN)_{total}$ and $(dc/dN)_{total}$ over time. Crack shape changes are computed by the code and were seen to agree very well with experimental observations. A comparison of WISECRACK with experimental results of surface flaw growth produced excellent agreement between the two, considering the scatter inherent in the data. Finally, examples of the application of WISECRACK to a specific first wall design were discussed.

In conclusion, the development of this code represents a significant improvement over existing methods and codes for predicting crack growth. Especially notable is the capability of WISECRACK to model both irradiation effects and surface wall erosion, in a non-linear stress field. Neutron irradiation affects crack growth in two ways: it changes the long-term stress history and it enhances the crack growth rates due to severe embrittlement. Wall erosion,

on the other hand, was found to be beneficial to crack growth by either reducing the driving force (cyclic thermal stresses) for FCG, or by actually eroding the crack away from the surface. The effect of the nearly linear stress distribution through the wall was found to transform an initially semi-circular surface flaw into a long, thin crack with a small aspect ratio, a/c. For these flaw shapes, fracture was usually predicted to occur at the surface, where the stress intensity factor is a maximum.

Future improvements in WISECRACK would include more work on the stress intensity factor solutions to allow for steep, non-linear stress gradients such as would be encountered in ICF reactors or during plasma disruptions. The linear elastic fracture mechanics approach should be extended to include elastic-plastic behavior, when the fracture toughness is still at high values before embrittlement. The effects of overloads and crack retardation could be modelled as well. Most importantly, though, is the need for better data on the effects of high dpa neutron irradiation and aggressive environments (such as lithium and steam) on stage I and II fatigue crack growth rates. Nevertheless, by coupling with the TSTRESS code, WISECRACK is a very useful and versatile tool for studying the impact of fusion environments on crack propagation in first wall components.

CHAPTER 8

Applications: Tokamak First Wall Lifetime Analysis

Introduction

In this chapter, the two coupled computer codes, TSTRESS and WISECRACK, are used to parametrically study the effects of changes in certain variables and assumptions on the lifetime, as illustrated in Fig. 110. The primary motivation for doing this is to explore the sensitivity of the predictions to the wide range of uncertainties in our knowledge of the effects of plasma-wall interactions and radiation damage to materials. We are also interested in studying what specific combination of design variables and operating conditions would result in the longest life. Finally, these codes are used to investigate how sensitive the predictions are to changes in the fracture mechanics assumptions.

These parametric analyses are performed on a specific first wall design, the same one used previously in chapters five and seven. By using a single design, this allows us to compare the predictions with each other on an equal basis, thus identifying the relative benefits of one set of parameters over the other. In this way, the TSTRESS/WISECRACK combination represents a powerful tool for researching lifetime phenomena, even though a single prediction is subject to a certain degree of uncertainty.

The cylindrical blanket module shown in Fig. 111 is used for

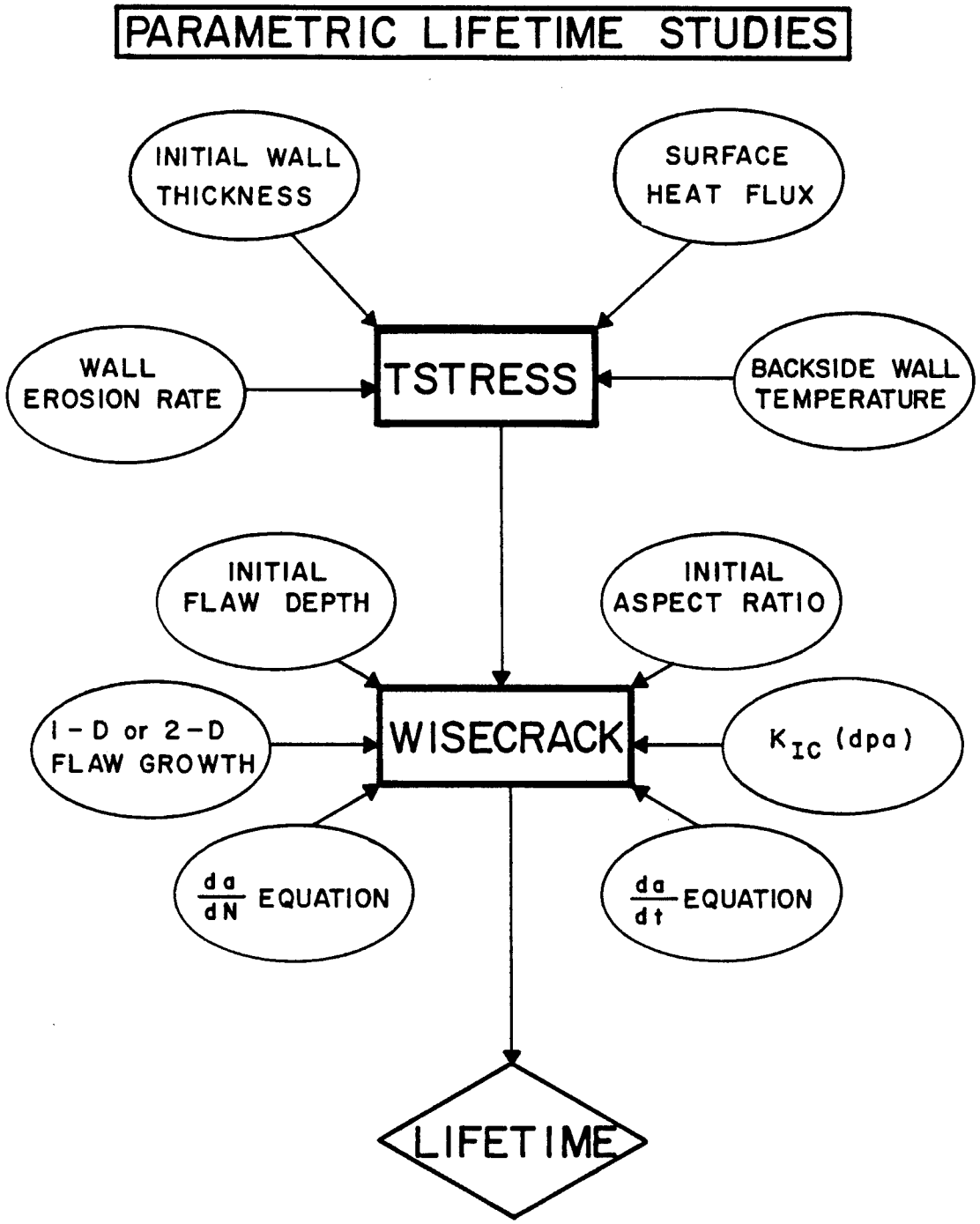

Figure 110. Schematic of parametric lifetime studies.

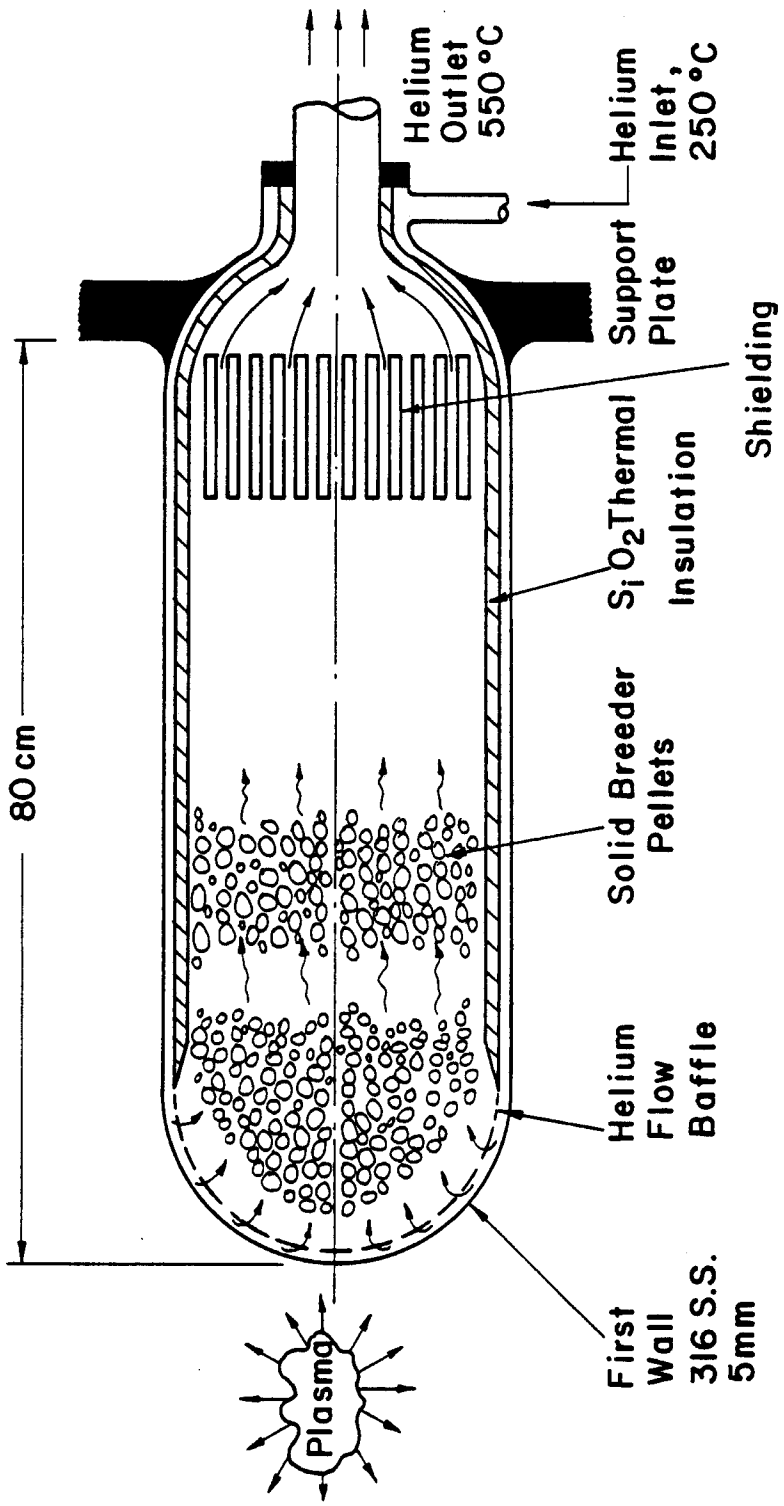

Figure 111. Reference design cylindrical blanket module with hemi-spherical end cap.

this study because it possesses six of the most important characteristics common to all first wall designs in magnetically-confined reactors. These features are:

1. thin-walled metallic structure ($h << R_o$)
2. actively-cooled design
3. thermal stresses dominant over pressure-induced membrane stress
4. structure is strongly constrained from bending, but relatively free to expand
5. stress distribution through the thickness is approximately independent of global variations in loads throughout the structure
6. critical location exists where temperature gradient through the wall is largest.

Since the tip of the cylindrical blanket module sustains the highest surface heat flux, we assume that this is the critical region in which the analysis should be made. Table 7 lists the reference parameters which are representative of a medium-sized tokamak power reactor. In principle, however, any other device, such as a mirror machine, EBT, etc., could have been chosen as well.

Reference Design Lifetime Analysis

In this section, we will discuss in detail the lifetime assessment of the reference design. The coupled TSTRESS/WISECRACK codes predict two lifetimes, depending on which side the flaw is located, namely: (1) a lifetime exceeding thirty years for a flaw on the

plasma side and (2) catastrophic fracture after two years for a coolant side flaw. Figure 112 shows the crack growth as a function of time, a(t), for these two cases. Similarly, Fig. 113 shows the behavior of both the maximum stress intensity factor, $K_{max}(t)$, and the fracture toughness, $K_{Ic}(t)$, as a function of time. In order to explain these curves, however, it will be necessary to also refer to the stress history for these two locations, as shown in Figs. 114 and 115.

Consider, first, the flaw on the plasma side of the wall. Very little crack extension is predicted during the thirty year life simply because the mean stresses on that side are compressive during most of the time, hence, retarding fatigue crack growth. Of more significance, however, is the behavior of K_{max} over the thirty years. We observe from Fig. 113 that K_{max} rapidly increases, reaches a maximum value of 12 $MPa\sqrt{m}$ at t = 0.8 years, and then drops back down to a lower level. Since minimal crack growth has occurred, this behavior reflects the history of stress on the plasma side during the plasma-off period. The peak value of K_{max} corresponds, therefore, to the occurrence of the peak residual stress. This behavior is typical for flaws on the plasma side. Although it did not happen in this example, it is possible for the peak value of K_{max} to exceed the fracture toughness if K_{Ic} drops to a sufficiently low value in a short amount of time (e.g. less than two years). Since crack growth does not enter into this scenario, then the conclusion is also valid for very

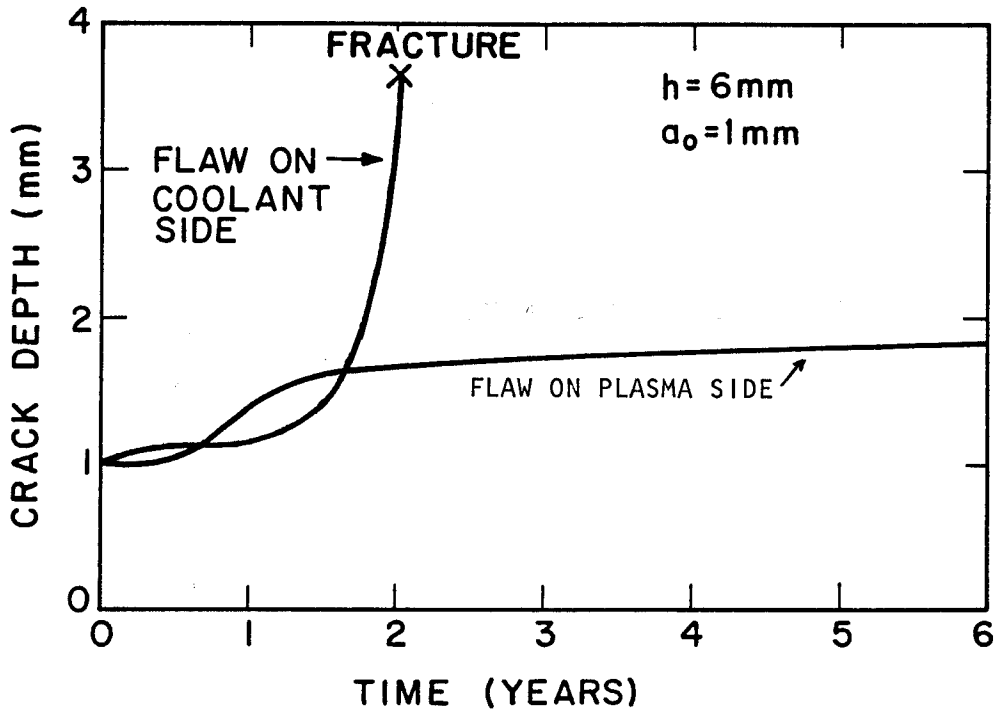

Figure 112. Predicted crack growth for reference design with flaw on either side of wall.

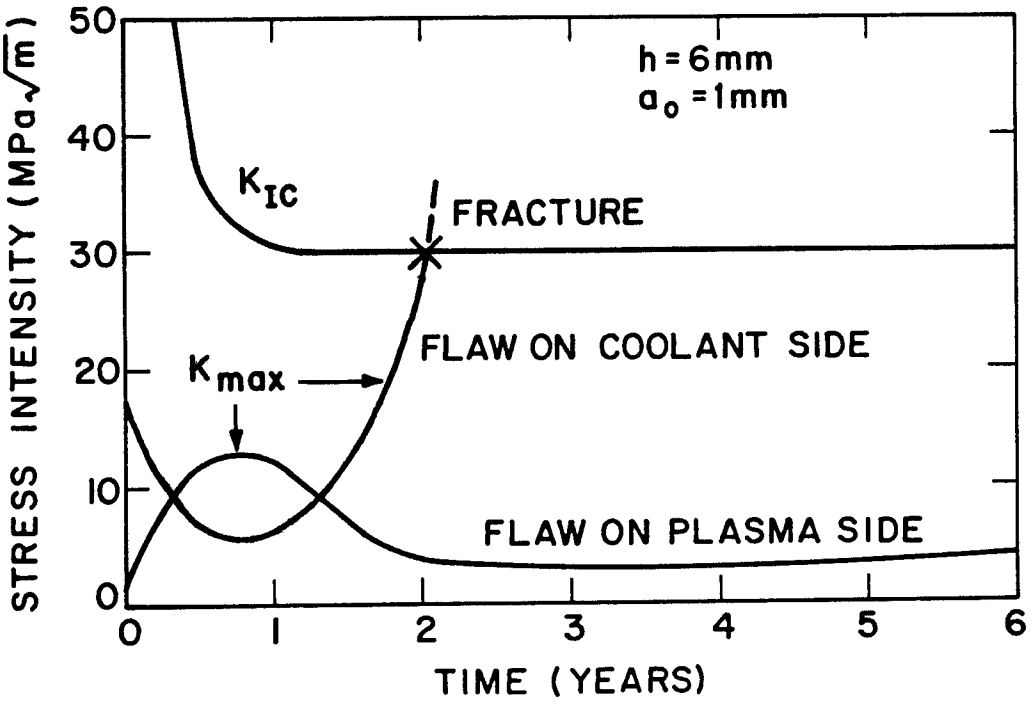

Figure 113. Evolution of the fracture toughness and maximum stress intensity factor for flaws on either side of the wall for the reference design parameters.

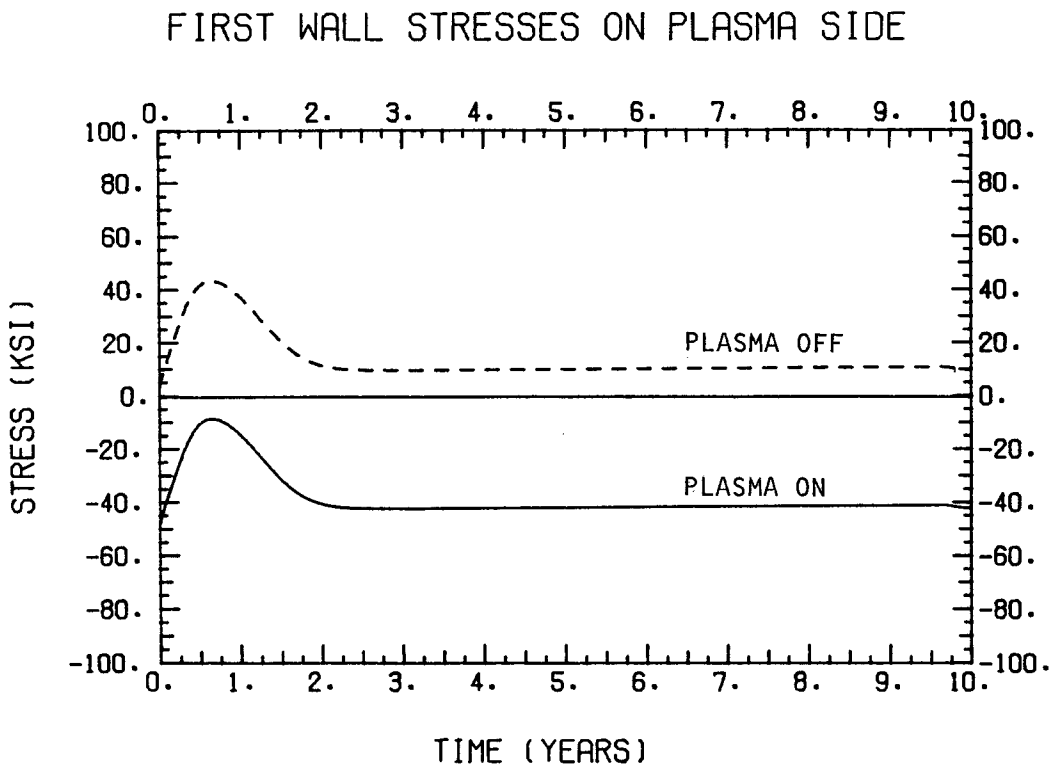

Figure 114. Stress history of plasma-side stresses for reference design.

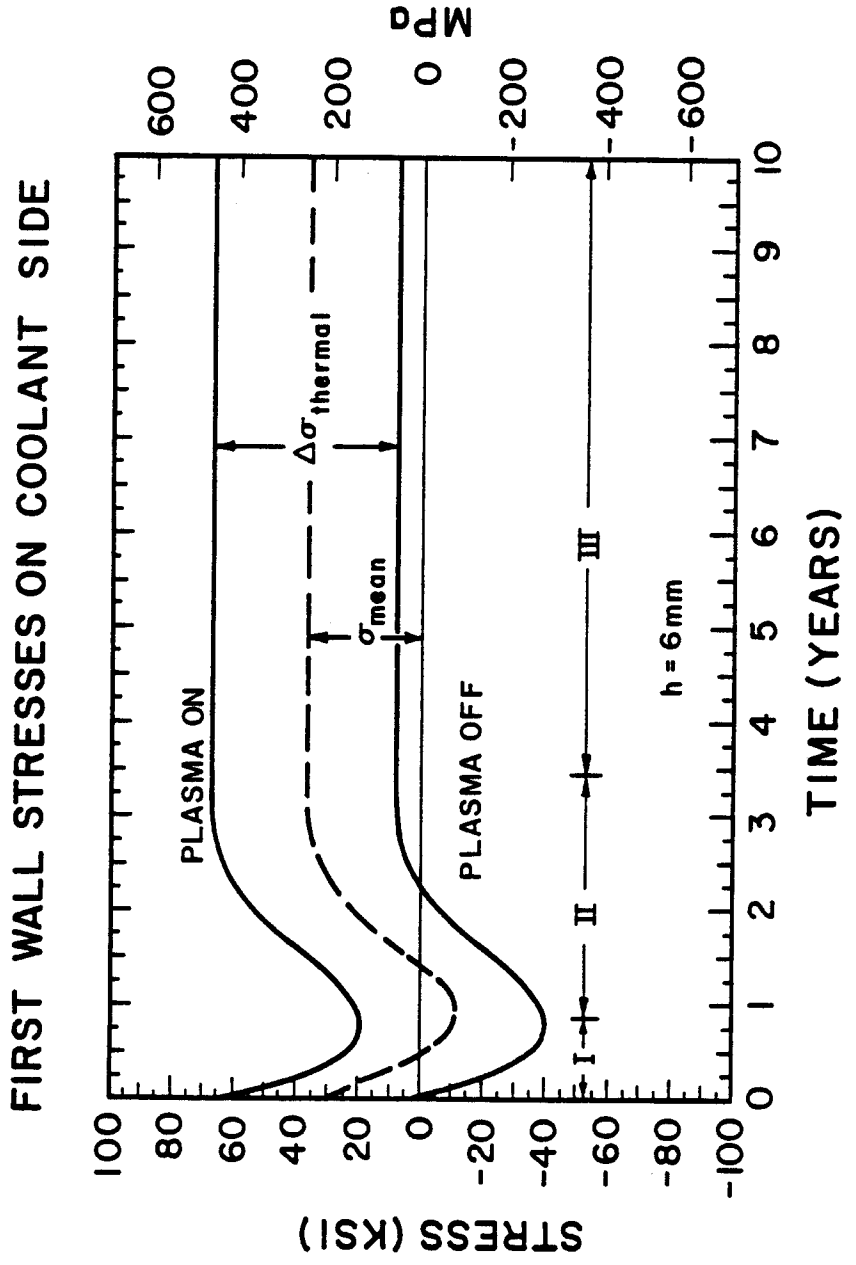

Figure 115. Stress history of coolant-side stresses for reference design.

long-pulse devices, such as mirror machines or steady-state tokamaks. However, if K_{Ic} drops more slowly, on the order of 3-4 years (60-100 dpa), then the "window" for catastrophic fracture will have closed because K_{max} will have dropped back to a lower level in a shorter period of time, and catastrophic fracture will have been avoided.

The situation is very different for a flaw on the coolant side. Here, we find a much shorter lifetime, only two years, and failure is from catastrophic fracture. Again, the mean stress is found to play an important role. In Fig. 115 we see that during the first year the mean stress relaxes due to creep, which slows down crack growth significantly. However, when swelling turns on, the stresses reverse their trend and increase back to an average tensile level, which has the effect of increasing ΔK and, hence, da/dN. Occurring at the same time is the reduction in K_{Ic}, which is expected to accelerate da/dN (see Fig. 85). Both of these effects when combined result in rapid crack growth, eventually causing fracture in 1.5 to 2.0 years (see Fig. 112). Therefore, a strong synergism is seen to exist between embrittlement and the effects of swelling and creep on mean stresses.

Parametric Study of Selected Design Options

In this section, we shall study the effects on lifetime by changing the following design variables: the wall thickness, the backside wall temperature, the surface heat flux, and the wall

erosion rate. The range of variation for each variable is shown in Table 16. Either one or two variables at a time are changed, while all others are held constant. The reader will remember that the impact of these variations on the stress history has already been presented and discussed in Chapter 5 (with the exception of changes in the surface heat flux). Now, we wish to combine those effects with a failure analysis while assuming that the fracture mechanics parameters remain unchanged. This requires running TSTRESS and WISECRACK in the coupled mode. In this way, we will be able to study some of the complex synergisms that exist between the structural response and the damage processes.

Table 16. TSTRESS Variables

Variable	Reference Value	Range of Variation
wall thickness	6 mm	2-10 mm
backside wall temperature	350°C	100-500°C
surface heat flux	50 W/cm^2	0-50 W/cm^2
erosion rate	0 mm/FPY	0-2 mm/FPY

Effect of Wall Thickness

The effect on lifetime of changing only the wall thickness is shown in Fig. 116. The first observation from this figure is that the lifetime is very sensitive to wall thickness, decreasing

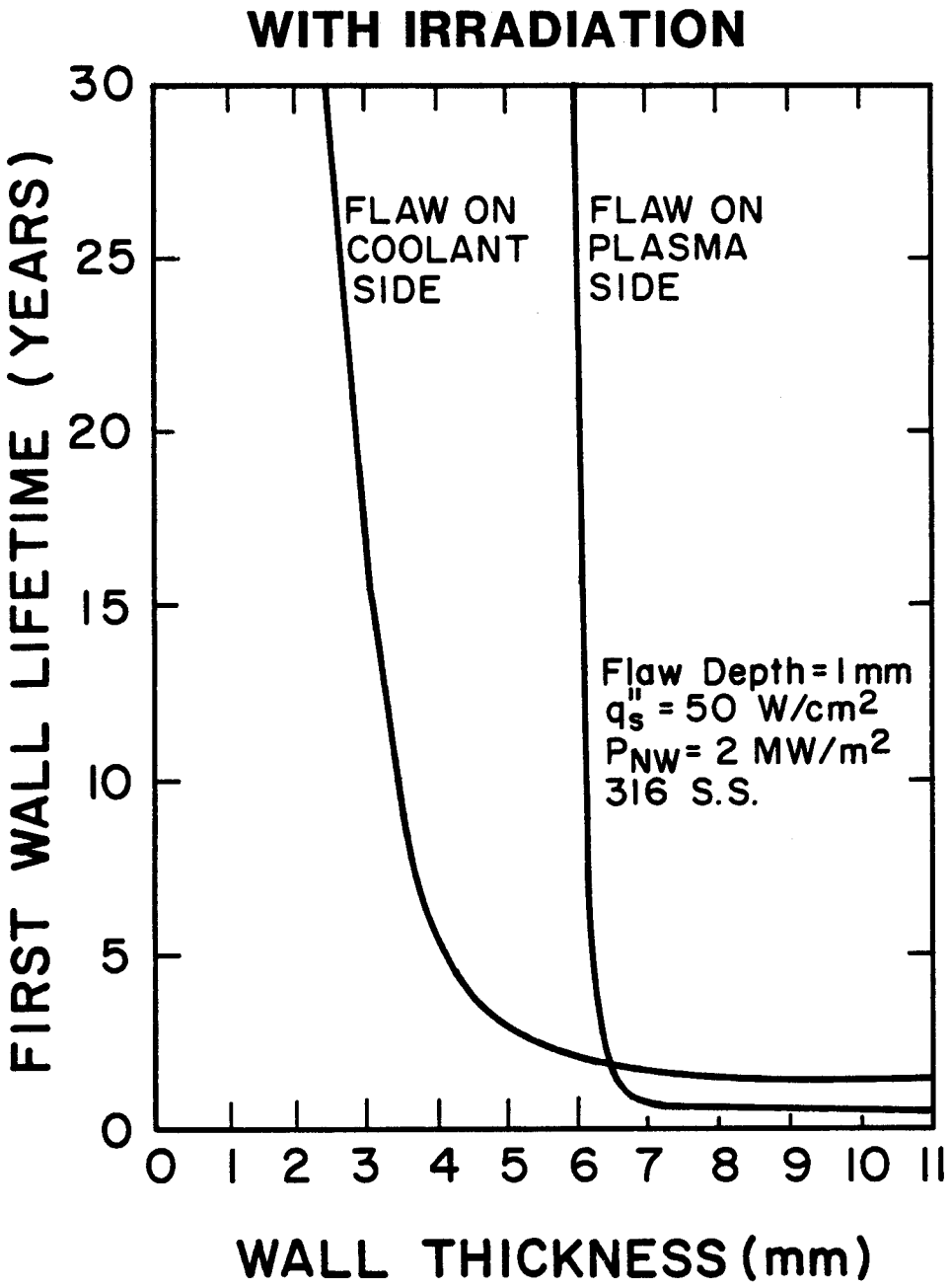

Figure 116. Effect of wall thickness on first wall lifetime.

rapidly with increasing thickness until about 7 mm, where the life becomes insensitive to thickness. Consider first the flaw on the coolant side. As the wall thickness increases, so do the cyclic thermal stresses, $\Delta\sigma$. This, in turn, increases ΔK in proportion to $\Delta\sigma$. Since $da/dN \sim (\Delta\sigma)^4$, according to the Paris equation, then the lifetime, N_f, can be easily shown to vary as $N_f \sim a_o^{-1} (\Delta\sigma)^{-4}$ (this is derived in the Appendix). The general shape of the curve in Fig. 116 is seen to follow this equation. In fact, this appears to be a very general result, namely that the fatigue crack growth lifetime varies in inverse proportion to the cyclic stresses at the surface of the wall raised to roughly the fourth power. Of course, it is somewhat more complicated than this, as we shall see, but this insight can be applied as a general rule-of-thumb in many cases. Fig. 117, taken from Ref. [17], compares favorably with Fig. 116 when one considers that the surface heat flux is proportional to the neutron wall loading and, in turn, is proportional to the cyclic thermal stress.

The sensitivity to thickness for the flaw on the plasma side is quite different and does not follow the above general rule-of-thumb. Instead, the lifetime follows an almost step-like behavior, being long for $h < 6.5$ mm and very short for $h > 6.5$ mm. The explanation for this is related to the "window" for catastrophic fracture discussed in the previous section. This window exists for a critical period of time during the first two years of operation where the residual stresses on the plasma side are increasing

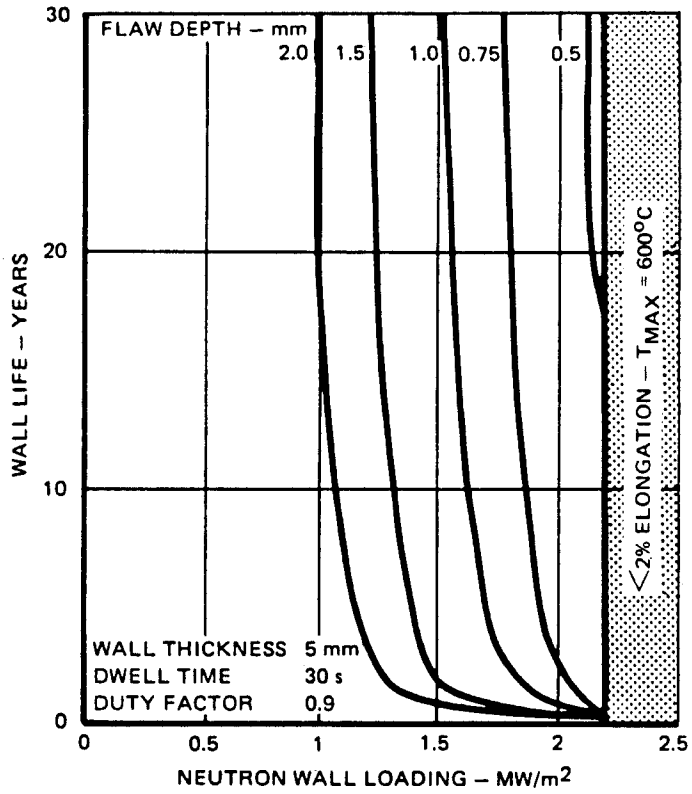

Figure 117. Effect of neutron wall loading on first wall lifetime for different flaw depths [17].

during the plasma-off period due to creep relaxation. The peak residual stress results in a peak maximum stress intensity factor, K_{max}. If the wall is thicker than 6.5 mm, then the initial thermal stress is large, causing a large peak residual stress, which in turn, causes K_{max} to exceed the irradiated fracture toughness of 30 MPa$\sqrt{m}$ in less than two years. On the other hand, if h < 6.5 mm, K_{max} never exceeds K_{Ic} and the critical period of time is passed by, thus permitting no crack growth (on this side) due to compressive mean stresses after two years. Clearly, one would want to design a wall thinner than 6.5 mm (for this example) in order to close that "window" and avoid this particular mode of failure. To prevent any crack growth from occuring, the wall thicknesses should be chosen in the range of 2-3 mm because the cyclic thermal stresses are low, resulting in low stress intensity ranges of ΔK = 5-9 MPa$\sqrt{m}$. These values of ΔK lie in the threshold regime for crack growth where da/dN drops to extremely low values. We conclude that within certain limits the thinner the wall is, the longer its life will be. However, a wall that is too thin will have unacceptably large tensile membrane stresses. Also, this conclusion is only applicable to walls that sustain minimal or zero surface erosion.

Effect of Coolant Temperature

In this section, we discuss the effect on lifetime achieved by varying the backside wall temperature, T_b, from 100°C to 500°C. The results, shown in Fig. 118, can be interpreted in two different ways. We can see that each life curve, for flaws on either side of the wall, is very sensitive to the temperature. Since the cyclic thermal stresses remain basically constant over time, we conclude that the effect is due to the temperature dependence of the mean stress (R-ratio) distribution through the wall, which was discussed extensively in Chapter 5. Simply stated, tensile mean stresses cause shorter lifes by accelerating fatigue crack growth, while compressive mean stresses cause longer lifes by retarding FCG. A comparison between Fig. 32 and Fig. 36 readily demonstrates this trend. However, when the shorter of the two lifetimes is chosen, then we find that the composite lifetime, as shown by the cross-hatched region in Fig. 118, is somewhat insensitive to the backside wall temperature. The maximum lifetime occurs at $T_b \cong 300°C$. This observation, however, is most likely to be sensitive to small changes in the swelling correlation. Nevertheless, we can conclude that some moderate amount of swelling is highly desirable, because the extreme cases of either low or high swelling, ($T_b = 100°C$ or $T_b = 400°C$) both give shorter lifetimes.

Now, let us consider what happens when both the wall thickness and the backside wall temperature are changed together. The results shown in Fig. 119, indicate only a small effect of varying T_b from

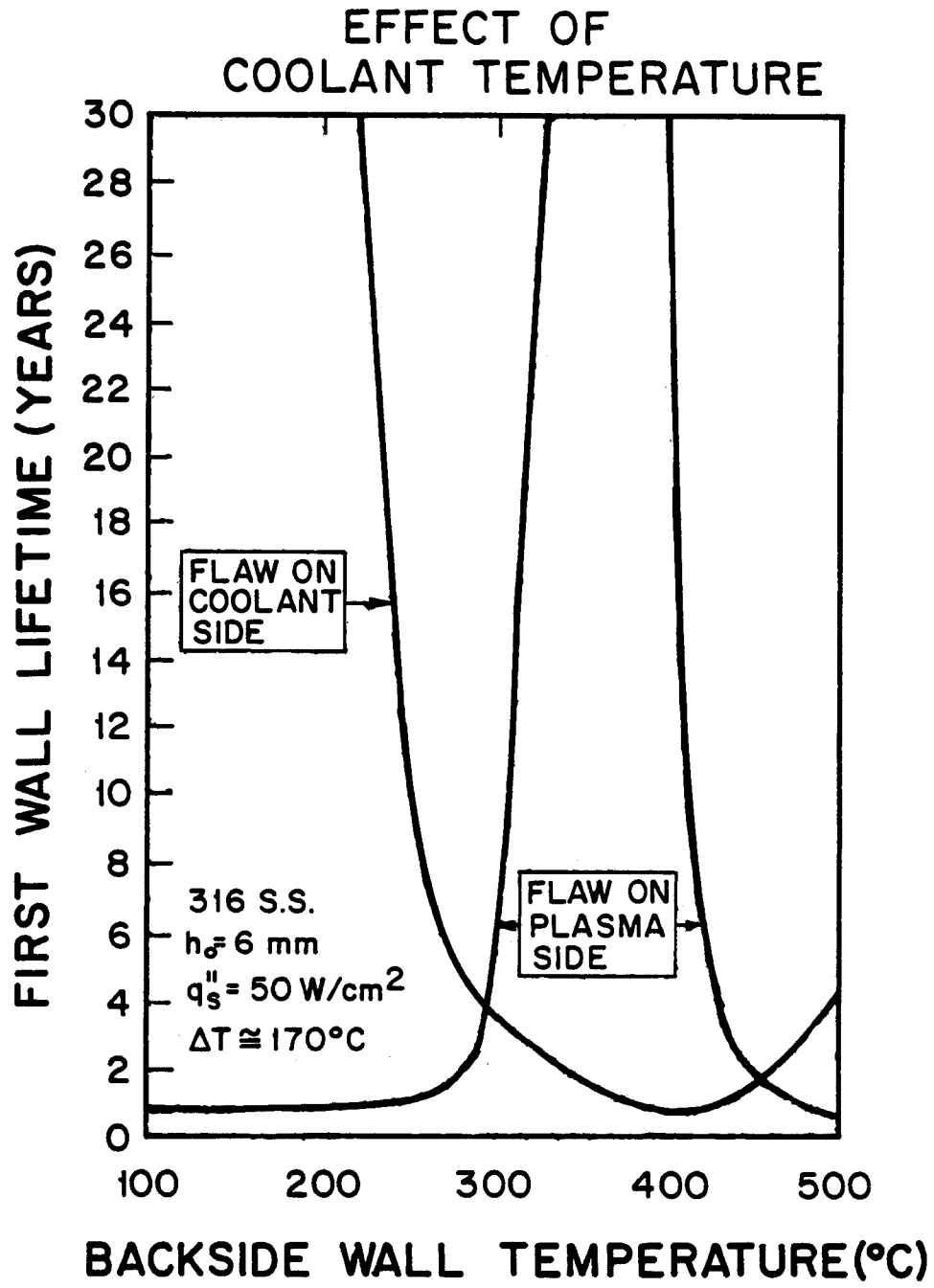

Figure 118. Effect of backside (or coolant) temperature on first wall life-time.

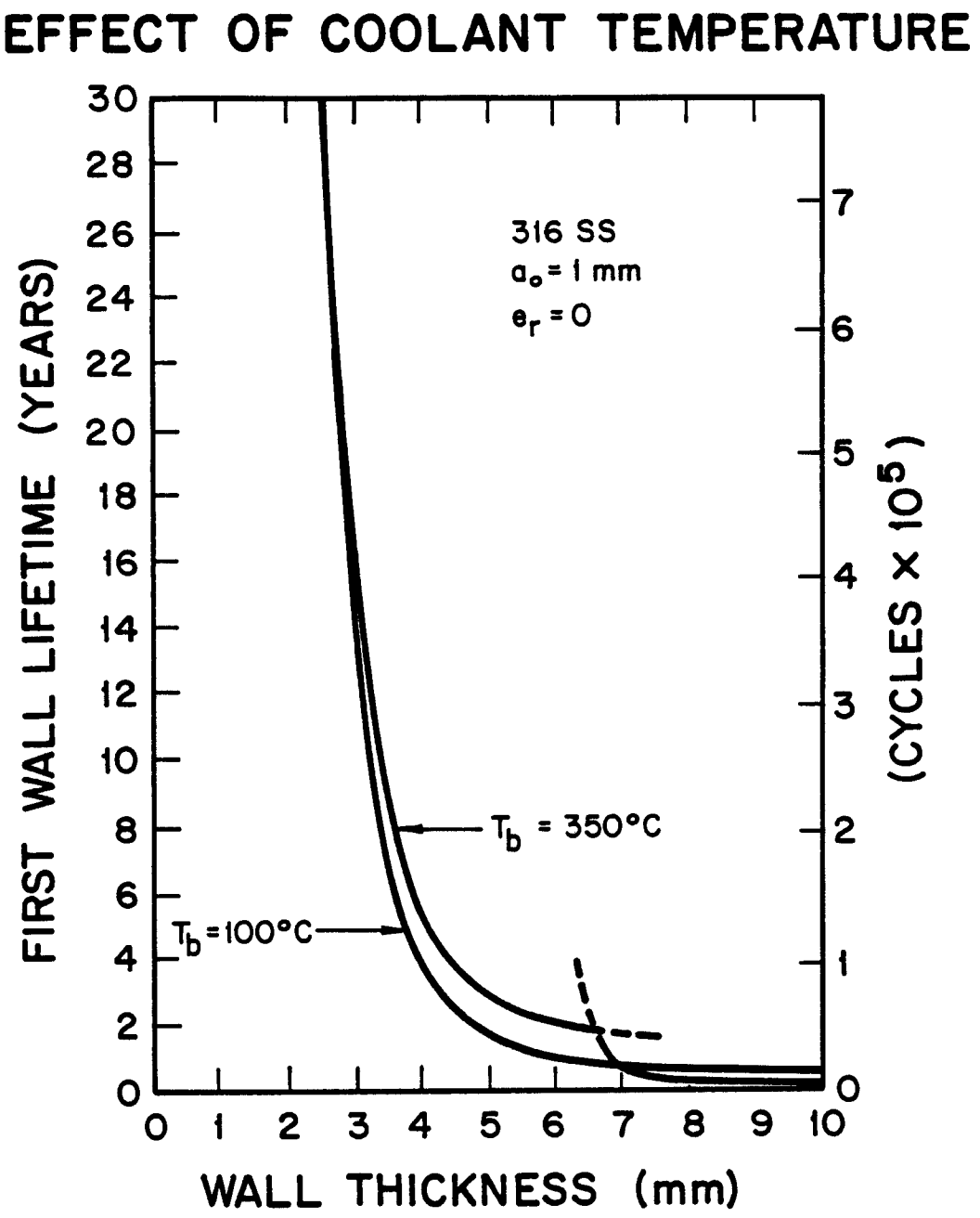

Figure 119. Effect of wall thickness on first wall lifetime for two different backside temperatures, T_b = 100°C and 350°C.

100°C to 350°C. Nevertheless, we conclude that over a wide range of stresses, i.e. wall thicknesses, a very low temperature wall is not as desirable as a moderately hot wall. This contradicts a common belief among designers who believe that no swelling is the best solution to a long wall-life. Our analysis indicates that the optimum average wall temperature for long-lived components is one which results in equal steady-state mean stresses on both sides of the wall. One method of finding this optimum is to pick the right value of $\Delta\dot{S}/\psi_{irr}$ (see Eq. 115) so as to make $\sigma_x(z,\infty) = \sigma_x(z,0)/2$ (see Fig. 37, $T_b = 250°C$).

Effect of Surface Heat Flux

In Fig. 120, we plot the lifetime as a function of the surface heat flux, q_s'', for various values of the wall thickness. It is assumed, however, that the neutron wall loading remains constant at 2 MW/m^2. Therefore, the variation in q_s'' is related to the efficiency of a divertor or limiter device which removes that component of q_s'' which is due to energetic particles. In this figure, the lifetime increases dramatically with decreasing heat flux, which is caused by the simultaneous reduction in cyclic thermal stresses. Consequently, for a constant wall thickness even a modest reduction in the heat flux can cause substantial gains in the lifetime.

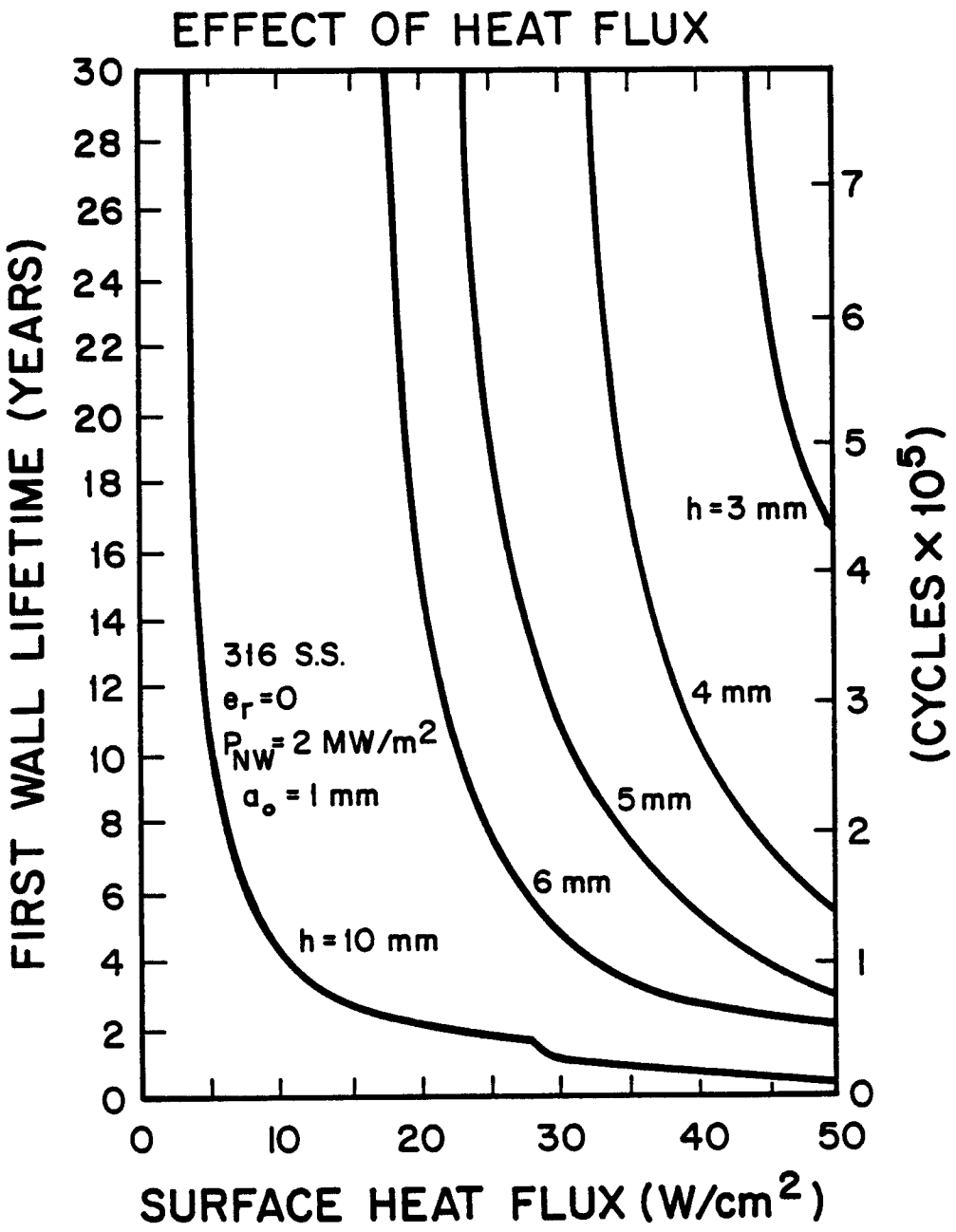

Figure 120. Effect of surface heat flux on first wall lifetime for constant neutron wall loading of 2 MW/m^2.

Effect of Wall Erosion

The effect of varying the rate of surface erosion on the plasma side, e_r, from 0 to 2 mm/FPY (full power year) is shown in Fig. 121, for different initial wall thicknesses, h_o. We observe that as e_r increases, so does the lifetime. This is caused by the continuous decrease in thermal stresses as the wall thins down (see Figures 45 and 46).

The increase in lifetime is eventually limited to a maximum value. When this point is reached, the reduced cyclic stresses are so small that minimal fatigue crack growth occurs and the lifetime is simply determined by overall thinning. In this regime, the lifetime is inversely proportional to the erosion rate. Figure 122 illustrates these two competing processes in more detail.

Both of these figures are for a flaw located on the coolant side. However, for a flaw on the plasma side all of the cases that were considered resulted in the flaw being obliterated after a short period of time simply because it was not growing fast enough. When this happens the life is only limited by overall thinning. If, on the other hand, the backside wall temperature is lower, then crack growth can occur in spite of the erosion, as was shown in the previous chapter (see Fig. 109).

Figure 123 demonstrates that for a specific erosion rate, it is possible to choose an initial wall thickness which will allow the maximum life to be achieved.

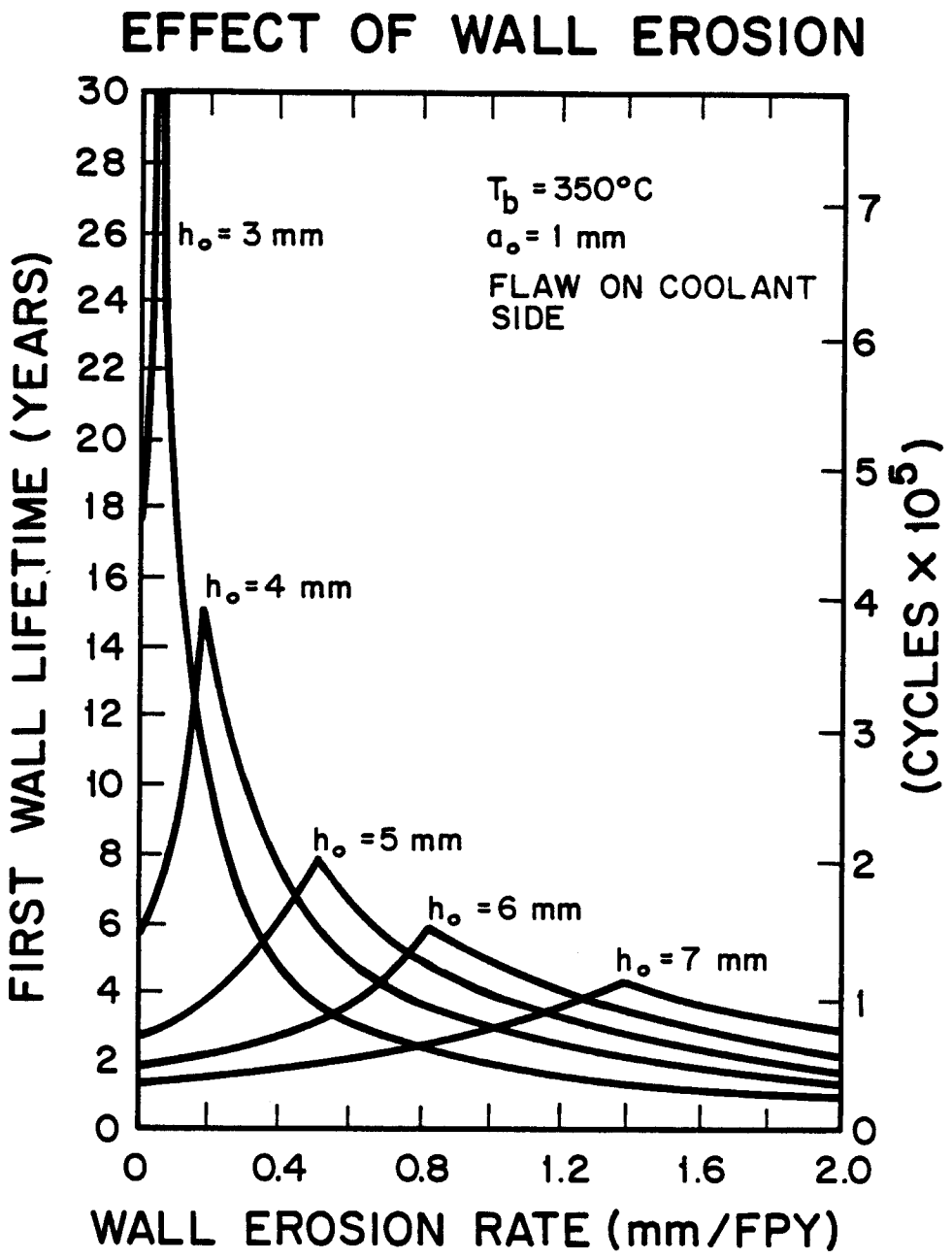

Figure 121. Effect of wall erosion on first wall lifetime for various initial wall thicknesses.

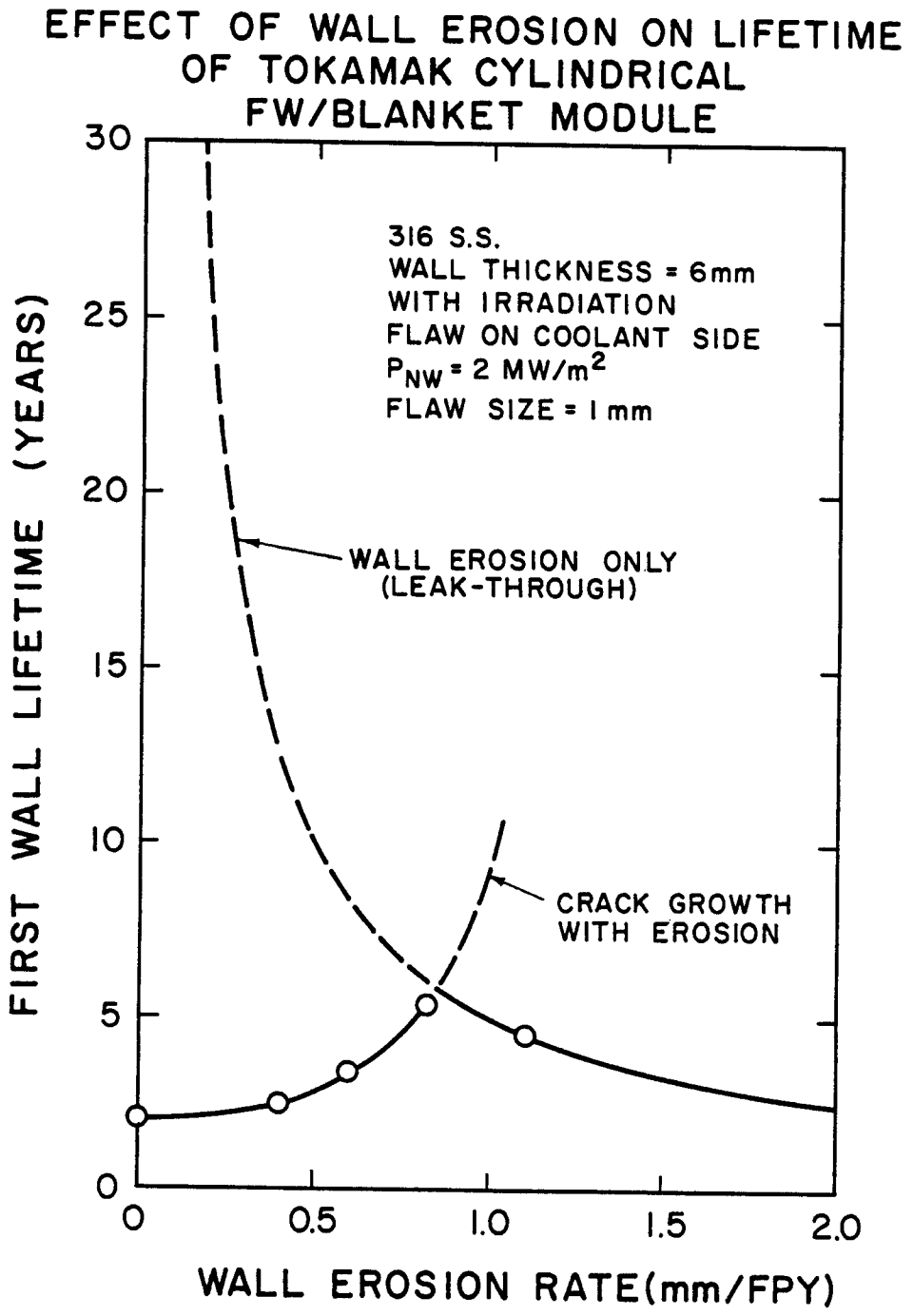

Figure 122. Effect of wall erosion on first wall lifetime for h = 6 mm.

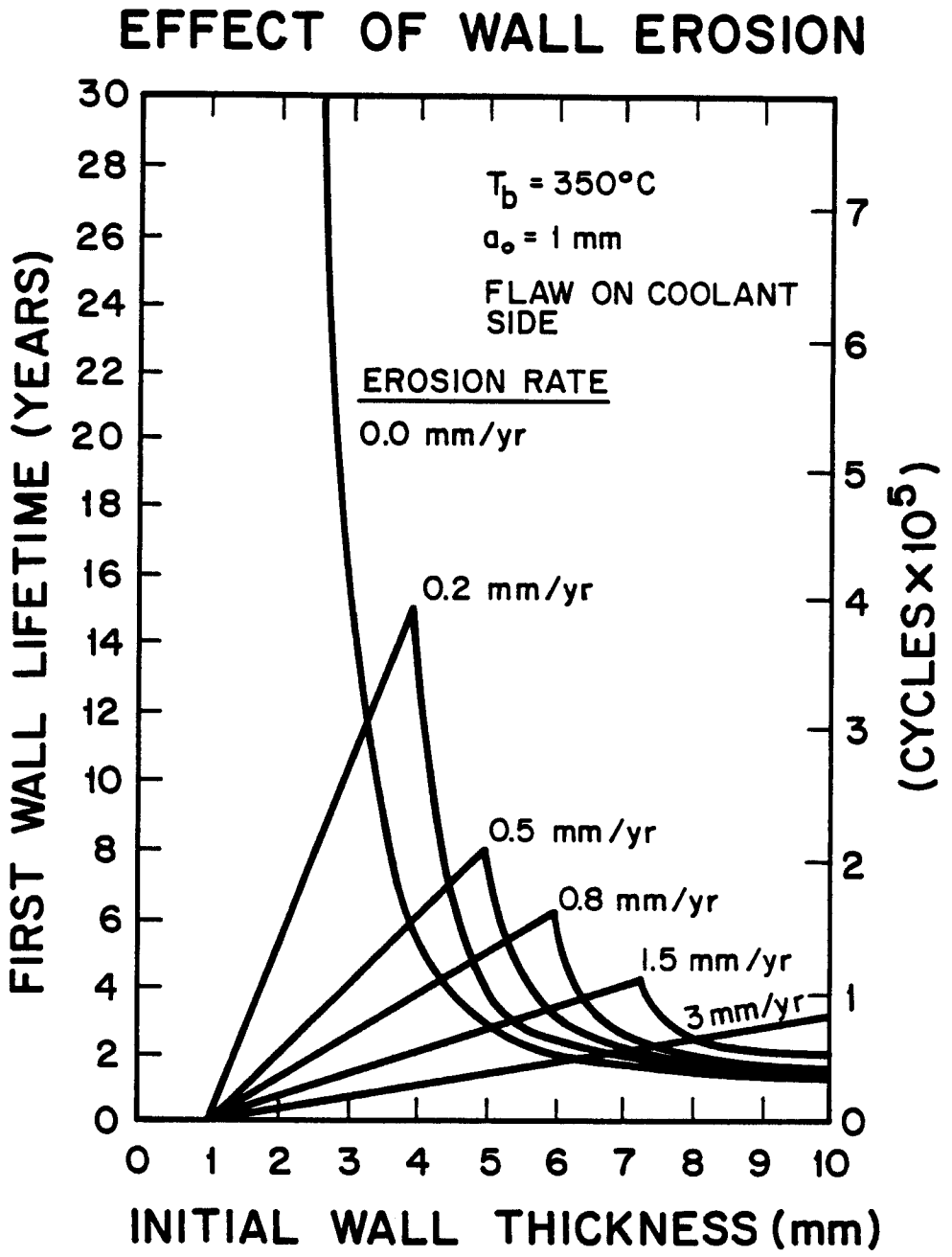

Figure 123. Effect of wall thickness on first wall lifetime for various erosion rates.

Sensitivity to Fracture Mechanics Assumptions

In this section, we investigate the sensitivity of the life-time predictions to the assumptions used in the fracture mechanics analysis. These assumptions fall into three separate catagories: (1) uncontrollable variables, which include the initial flaw depth, flaw aspect ratio, and scatter in fatigue crack growth rate data; (2) unknown effects, such as the amount of embrittlement and its possible effect on da/dN; and (3) different methods of analysis, including 2-D or 1-D flaw growth assumptions and various choices of the da/dN equation. Table 17 summarizes these assumptions and their possible range of variation.

Table 17. WISECRACK Variables

Variable	Reference Value	Possible Range
initial flaw depth	1 mm	0-2 mm
initial aspect ratio	1.0	0.2-1.4
irradiated fracture toughness	30 Mpa$\sqrt{m}$	10-150 MPa$\sqrt{m}$
scatter factor on da/dN	1.0	0.5-2.0
da/dN equation	modified Forman	Paris Eq. or modified Forman
flaw shape changes	2-D	1-D or 2-D

Effect of Initial Flaw Depth

The initial flaw depth is an important variable to study because the entire methodology developed for this project is based on the postulated existence of a surface flaw of a certain size that has escaped detection by non-destructive evaluation (NDE) techniques. Figure 124 shows the effect of varying a_o from 0 to 2 mm, for different wall thicknesses. The results are not surprising. A smaller flaw has a lower cyclic stress intensity factor, ΔK, associated with it and, hence, a lower fatigue crack growth rate, which gives a longer life. According to the Appendix, the fatigue life is approximately inversely proportional to the initial flaw depth and this is exactly what we observe in Fig. 124. A slight deviation from this trend is seen for $h = 6$ mm when $a_o <$ 0.2 mm. This is caused by the short crack correction factor, $\ell_o =$ 0.06 mm, which when added to a_o, produces an effective ΔK that is larger and hence, flattens out the curve by shortening the lifetime. Nevertheless, it is a small effect for cracks larger than 0.5 mm.

Two important conclusions can be drawn from this analysis. First, for thin walls of 3-4 mm thick, the lifetime increases dramatically with decreasing a_o. Therefore, there is a great incentive for improving NDE techniques for reliable detection of flaws in the range of 0.5 mm deep. Secondly, for walls thicker than 5 mm, their short lifetimes are relatively insensitive to changes in a_o, unless a_o is smaller than 0.3 mm. The reason for the

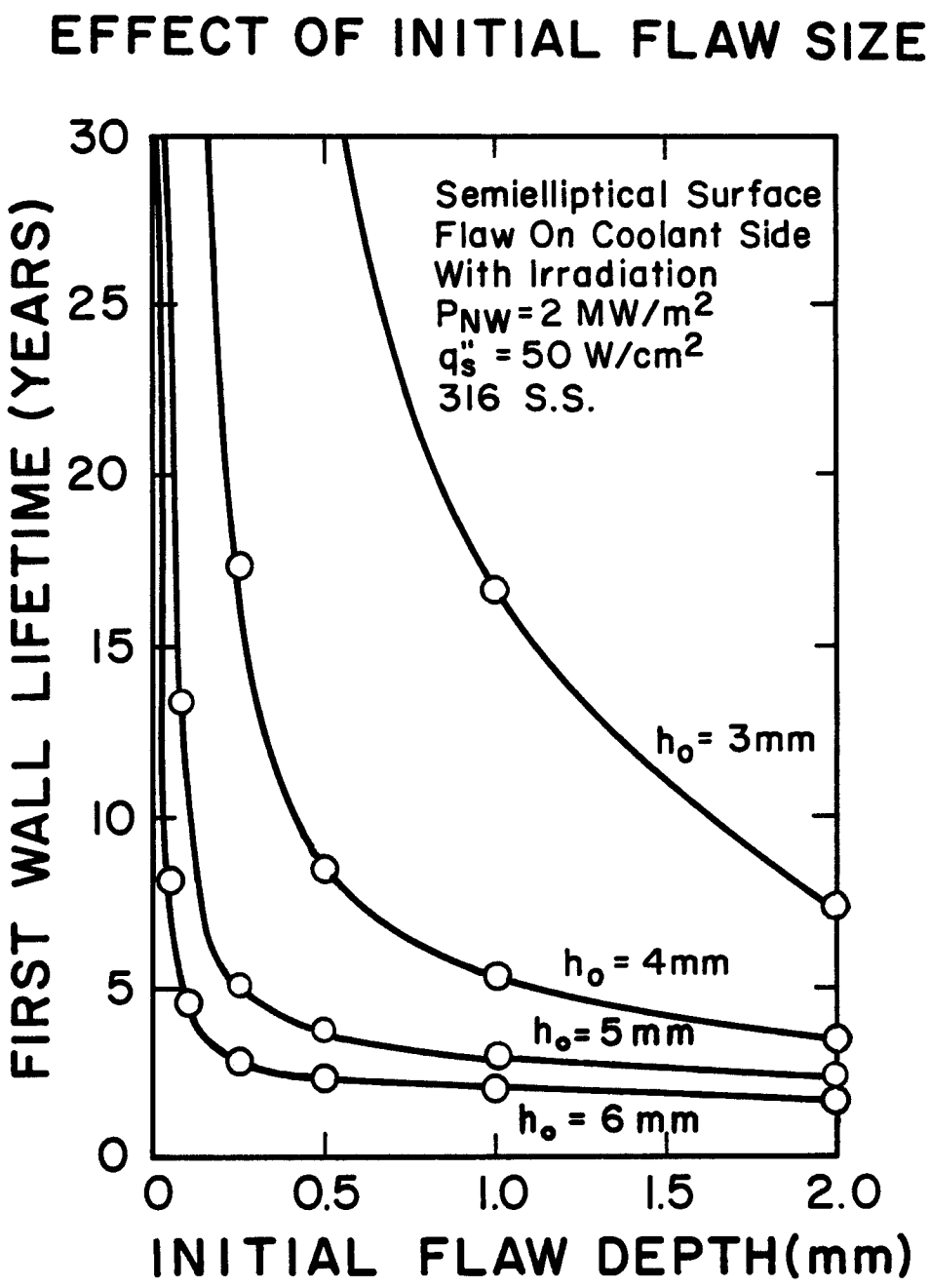

Figure 124. Effect of initial flaw depth on first wall lifetime for various wall thicknesses.

shift in behavior at h ≅ 5 mm is due to the fact that the initial ΔK for thin walls was located in the threshold regime (stage I) for fatigue crack growth, while the thicker walls had a ΔK in stage II where the slope "n" is not as steep as in stage I, thus reducing the sensitivity to the flaw size. Since the reliable detection of these small flaws is uncertain, this result implies that first wall designs thicker than 5 mm are probably unacceptable. However, it should be emphasized that this particular conclusion is dependent on other design parameters, especially q_s'' = 50 W/cm^2 and the choice of 316 S.S. Nevertheless, the trends are expected to be the same for any thin-walled design.

Effect of Initial Aspect Ratio

The aspect ratio of a crack, a/c describes its shape; a/c = 1.0 is a semi-circular flaw and small values of a/c describe long, thin scratches. While most first wall designers assume a semi-circular flaw, which might be caused by dents, pits or surface inclusions, it is just as probable that small aspect ratio flaws could be created from machining operations or scratching during fabrication and assembly of the components. Because of this uncertainty in being able to specify a/c, WISECRACK was used to investigate the sensitivity of the lifetime predictions to this parameter.

The results, shown in Fig. 125, indicate that the lifetime can be significantly reduced by starting with a long, thin flaw rather than a semi-circular one (as is usually the case). For

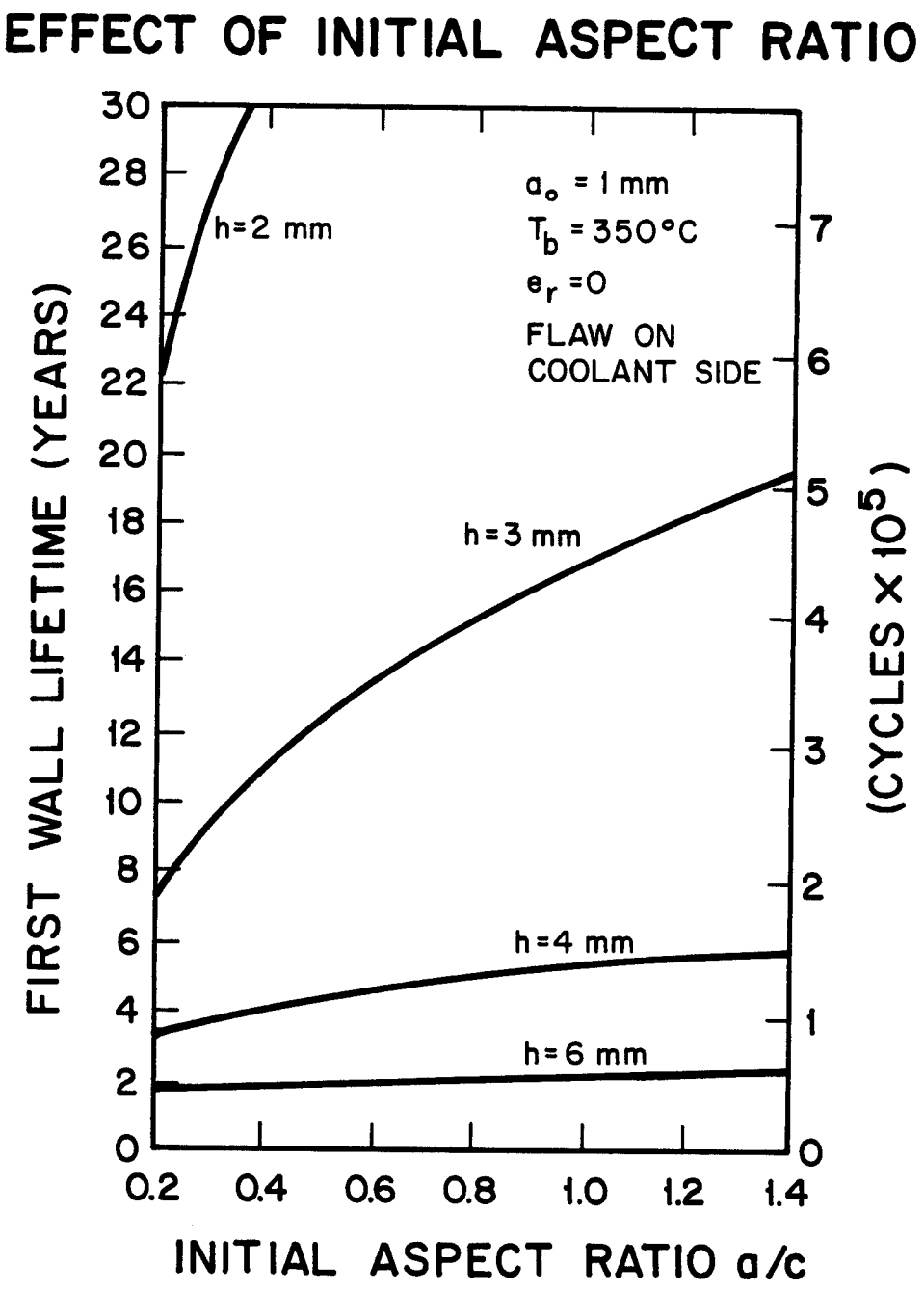

Figure 125. Effect of initial aspect ratio on first wall lifetime for various wall thicknesses.

thin walls, e.g. h < 4 mm, the large reduction is life as a_o/c_o decreases can be explained as follows. Since the flaws are subjected to a predominantly bending state of stress, we know that semi-circular flaws will always grow faster along the surface (where the stress is the highest) than through the thickness (see Fig. 95). Consequently, a flaw with $a_o/c_o = 1.0$ will eventually change shapes in the direction of making $a/c \cong 0.1$, which is the asymptotic aspect ratio at leak-through. Therefore, we argue that a flaw which starts out originally with a smaller aspect ratio, e.g. $a_o/c_o = 0.2$, will already have used up some of its life because it is starting with the same shape that it would have grown into eventually if it had started originally as a semi-circular flaw.

The behavior for thick walls, h > 5 mm, displays the same general trend as before, except with a vastly reduced sensitivity to a_o/c_o. In fact, the lifetime is virtually unaffected by a_o/c_o. In this case, the thermal stresses are much higher than before and cause large residual stresses during plasma refueling or reactor shutdown due to irradiation creep. Failure occurs on the plasma side when the tensile residual stress combines with the presence of a flaw to produce fracture if K_{Ic}, is a low value (due to embrittlement). The time at which fracture occurs depends on three factors: the rate of stress relaxation, K_{Ic} K_{max}. Since $K_{max} = [F_m \sigma_m + F_b \sigma_b] \sqrt{\pi a}$, where F_m and F_b are plotted in Figs. 56 to 59, we observe that F_b^{max} is not a strong

function of a/c for this example (a/h = 0.167, $\sigma_m \ll \sigma_b$). Therefore, the lifetime should not depend very much on the initial aspect ratio, as is the case in Fig. 125.

Effect of Flaw Shape Changes

In the literature review of previous lifetime studies, we found that it is common among investigators to assume that the flaw does not change its shape but, rather, grows in a self-similar fashion. In this case, i.e. 1-D flaw growth, a flaw with $a_o/c_o = 1.0$ would remain semi-circular throughout its entire life. Since we know that surface flaws do change their shapes, especially in bending stress fields, then a 1-D analysis is clearly incorrect. We wanted to know how much of an error this represented. Therefore, WISECRACK was run in both the 1-D and 2-D shape change mode in order to study this effect.

Fig. 126 shows the results. We can see that the two-dimensional calculations predict much shorter lifetimes than the 1-D model. This somewhat unfortunate result can be explained by considering how the stress intensity factor changes with aspect ratio. By comparing Figs. 58 and 59, we observe that ΔK at the surface of the wall ($\theta = 0°$) is always larger than ΔK at the tip of the crack. Consequently, da/dN is smaller than dc/dN. This implies that a 1-D model, which only uses da/dN, will predict slower crack growth and hence, a longer lifetime than a 2-D model.

The difference between the two different models is not as

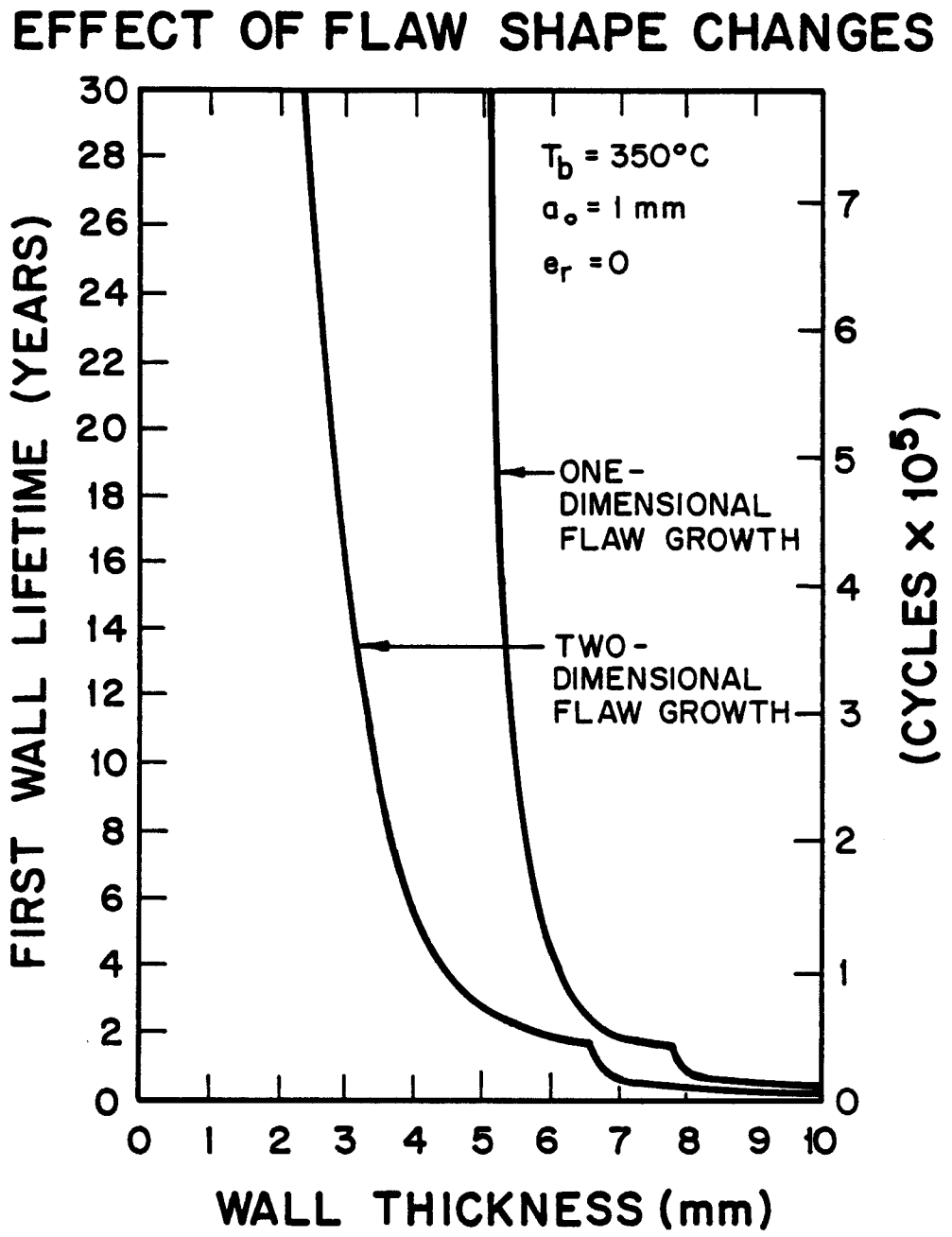

Figure 126. Effect of wall thickness on first wall lifetime for either a one-dimensional or a two-dimensional flaw growth model.

great for the thicker walls, which is due to the fact that only minimal crack extension occurs before fracture and any effects of shape changes would be negligible. Nevertheless, the important conclusion from this analysis is that the more realistic 2-D flaw growth model predicts shorter lifetimes than a comparable 1-D model. In some cases, the reduction can be as large as one order of magnitude.

Effect of Scatter in da/dN

The fatigue crack growth rate typically exhibits a scatter of roughly 2 in the data. Figure 61 shows the scatter in da/dN for 304 S.S. to be a factor of 3.8 ($\approx$4) difference between the upper and lower bounds. One method of using this factor to account for the data scatter is to divide the predicted lifetime by either 2 or 4 (see Cramer [12-14]). Although this is a conservative approach, an alternative is to apply the scatter factor directly to the fatigue data and then compute the lifetime. Figure 127 shows WISE-CRACK predictions using the second approach. We observe only a small effect of scatter for thick walls, $h > 5$ mm, because only small amounts of crack growth have occurred. For thinner walls, we find that we can simply multiply or divide the nominal lifetime by a factor of 2 to reproduce the results, as suggested by Equation (A12) in the Appendix. In conclusion, it is important to realize that there is a fundamental uncertainty in any lifetime prediction based on fatigue crack growth because of the scatter inherent in the data for da/dN. The error can be as much as 100%,

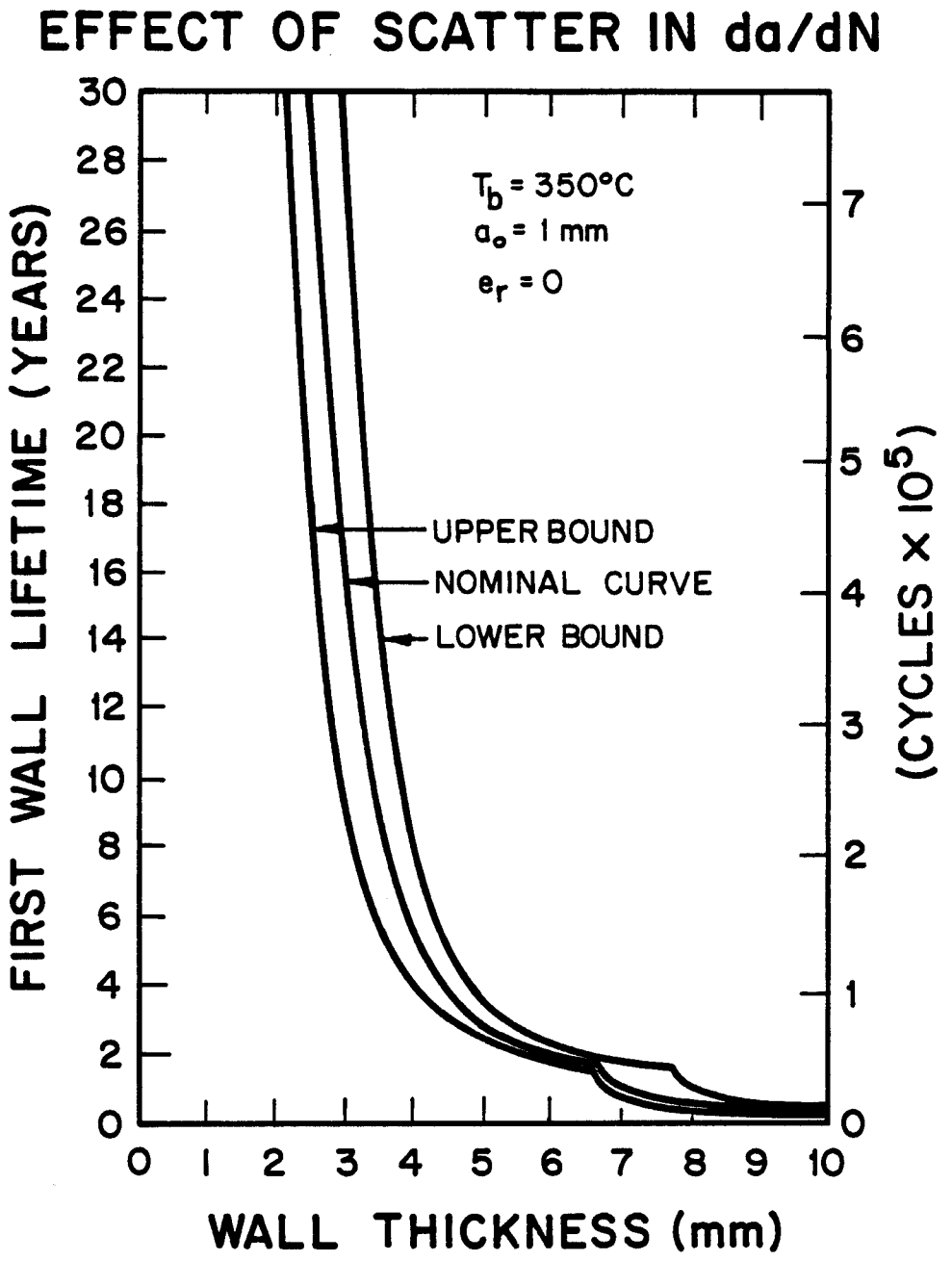

Figure 127. Effect of wall thickness on first wall lifetime for upper, nominal, and lower bound curves on fatigue crack growth rate data.

but probably can be reduced through strict metallurgical quality control.

Effect of Neutron Irradiation

All of the results shown so far have included the effects of radiation damage from 14 MeV neutrons. However, the effects of radiation damage on the fracture toughness and fatigue crack growth rate are not well known at the high dpa levels expected in a first wall of a power reactor. Therefore, it is important to understand how sensitive our predictions are to the various assumptions that have been made.

Figure 128 shows the variation in lifetime with wall thickness when all of the radiation effects have been turned off in both TSTRESS and WISECRACK. As before, thin walls have much longer life. Also, the flaw on the coolant side always gives the shorter life because the mean stresses on this side are tensile for the entire time. All of the failures in this figure were of the leak-through mode because the fracture toughness in the unirradiated state is sufficiently large (150 MPa$\sqrt{m}$) to prevent catastrophic fracture for even a through-crack (see Fig. 132).

Figure 129 compares the two cases with and without irradiation. Clearly, radiation damage causes a significant reduction in life. The major reason for this, as we shall see shortly, is due to embrittlement and changes in the da/dN curve.

Figure 130 illustrates the sensitivity of lifetime to the effects of radiation on da/dN. The curve marked "A" is the

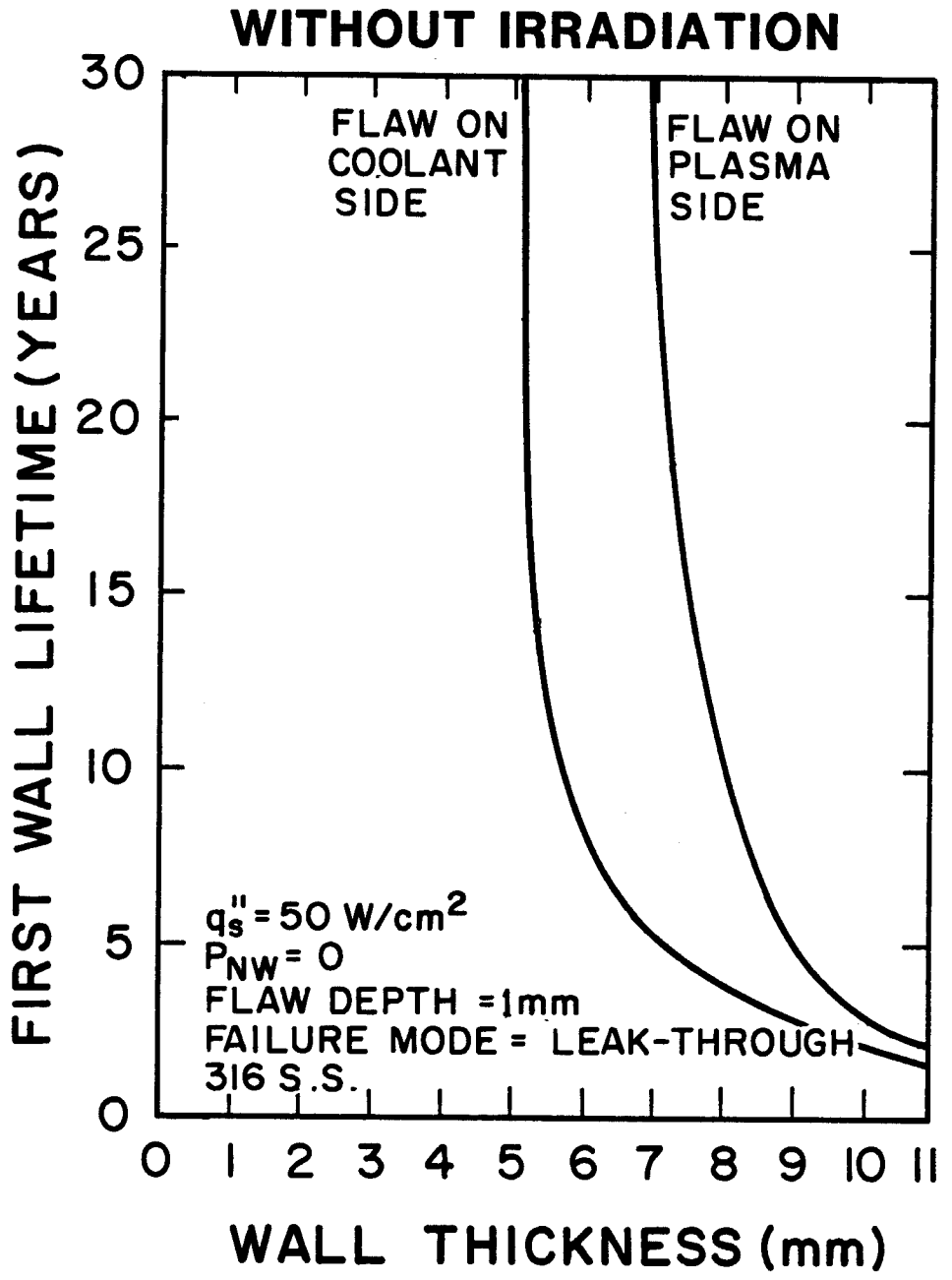

Figure 128. Effect of wall thickness on first wall lifetime without any irradiation effects.

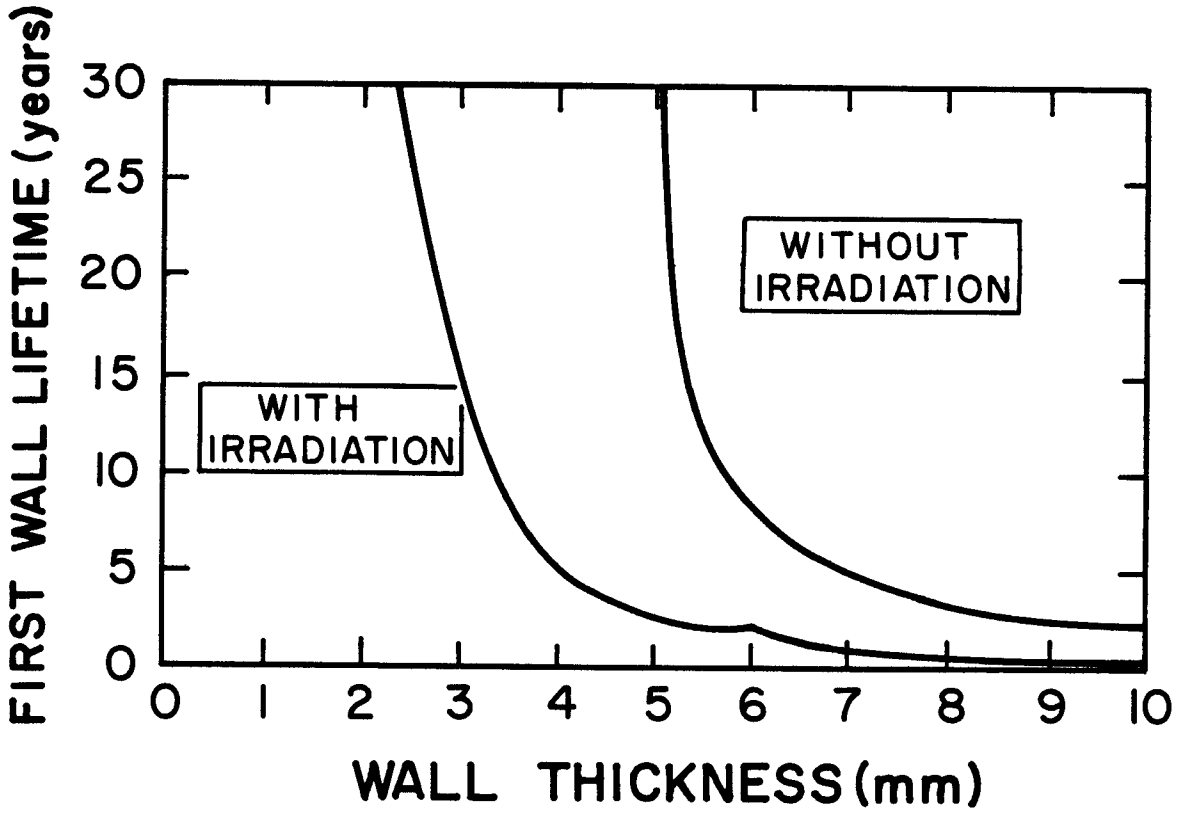

Figure 129. Comparison of effects of irradiation on first wall lifetime as a function of wall thickness.

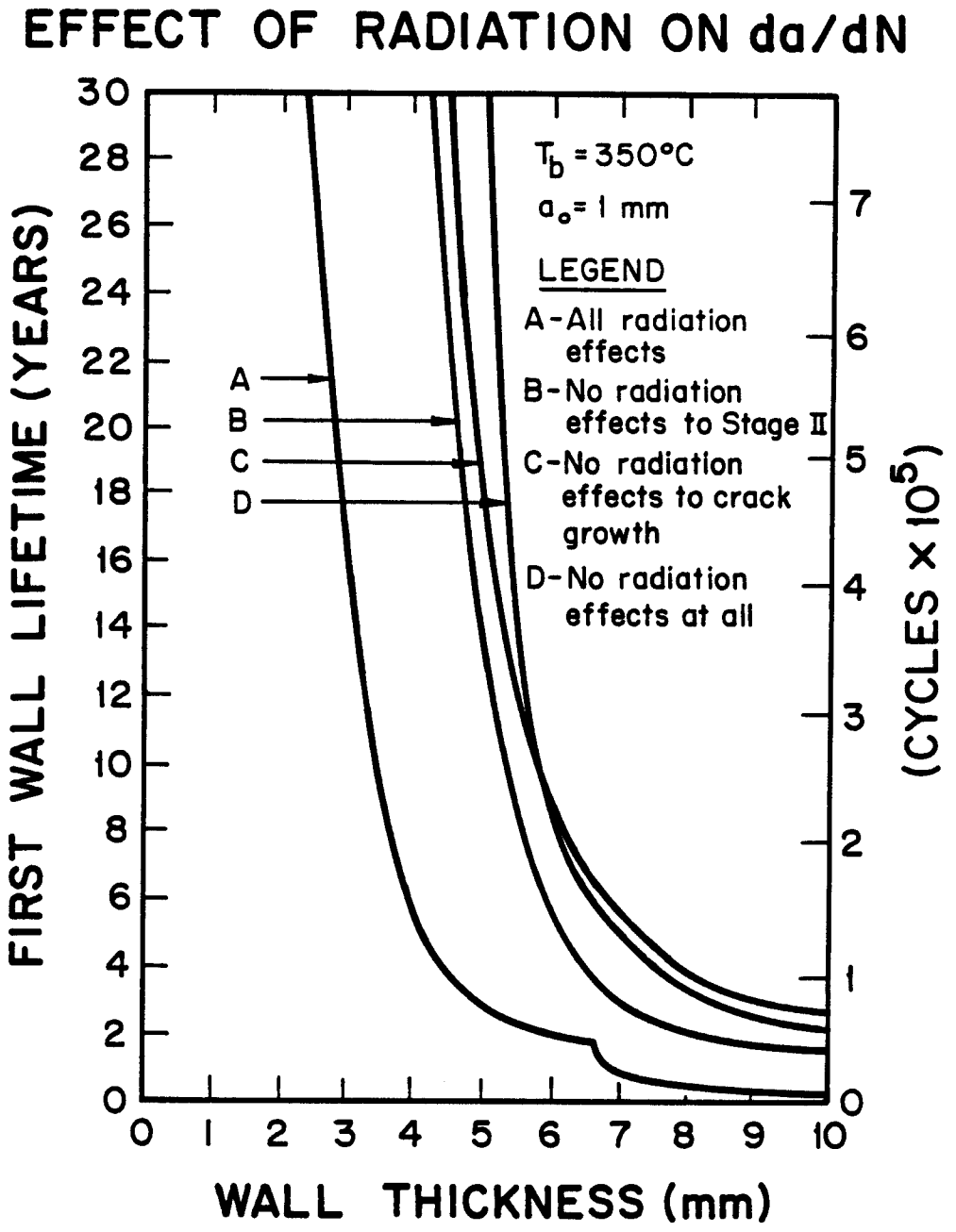

Figure 130. Effect of various assumptions on the severity of radiation effects to fatigue crack growth rates as a function of wall thickness.

reference design case. Curve B is where we allow K_{Ic} to drop, but do not allow the stage II portion of da/dN to be affected (see Fig. 91, IDADN=3). The dramatic increase in life is evident and indicates that our modelling of the entire problem is very sensitive to this particular assumption. Clearly, more data is needed for this regime, i.e. high dpa.

The curve marked "C" assumes no changes in either K_{Ic} or da/dN, but permits swelling and creep to occur. Comparing B and C, then, isolates the effect of a reduction in K_{Ic}. As can be seen, the effect is only large for thick walls, e.g. h > 6 mm. Finally, curve D shows the life for no radiation effects including no creep or swelling. This provides an upper bound for the lifetime.

Effect of Embrittlement

In the preceeding section, it was shown that changes in da/dN significantly affect the lifetime. These changes were assumed to have been caused by the reduction in K_{Ic} to 30 MPa$\sqrt{m}$ due to embrittlement. Since no data has been published on irradiated K_{Ic} values in austenitic stainless steels, we have assumed a range of possible values; from 10 to 150 MPa$\sqrt{m}$. Figure 131 shows the effect of changes in this parameter on lifetime. We observe that the lower the toughness, the shorter the lifetime is. For thin walls, e.g. h < 5 mm, the effect is stronger than for thick walls. Although the choice of K_{Ic} = 30 MPa$\sqrt{m}$ for the reference design may turn out to be too low, we can see from this figure that even for values in the range of 100 MPa$\sqrt{m}$ embrittlement can reduce the life

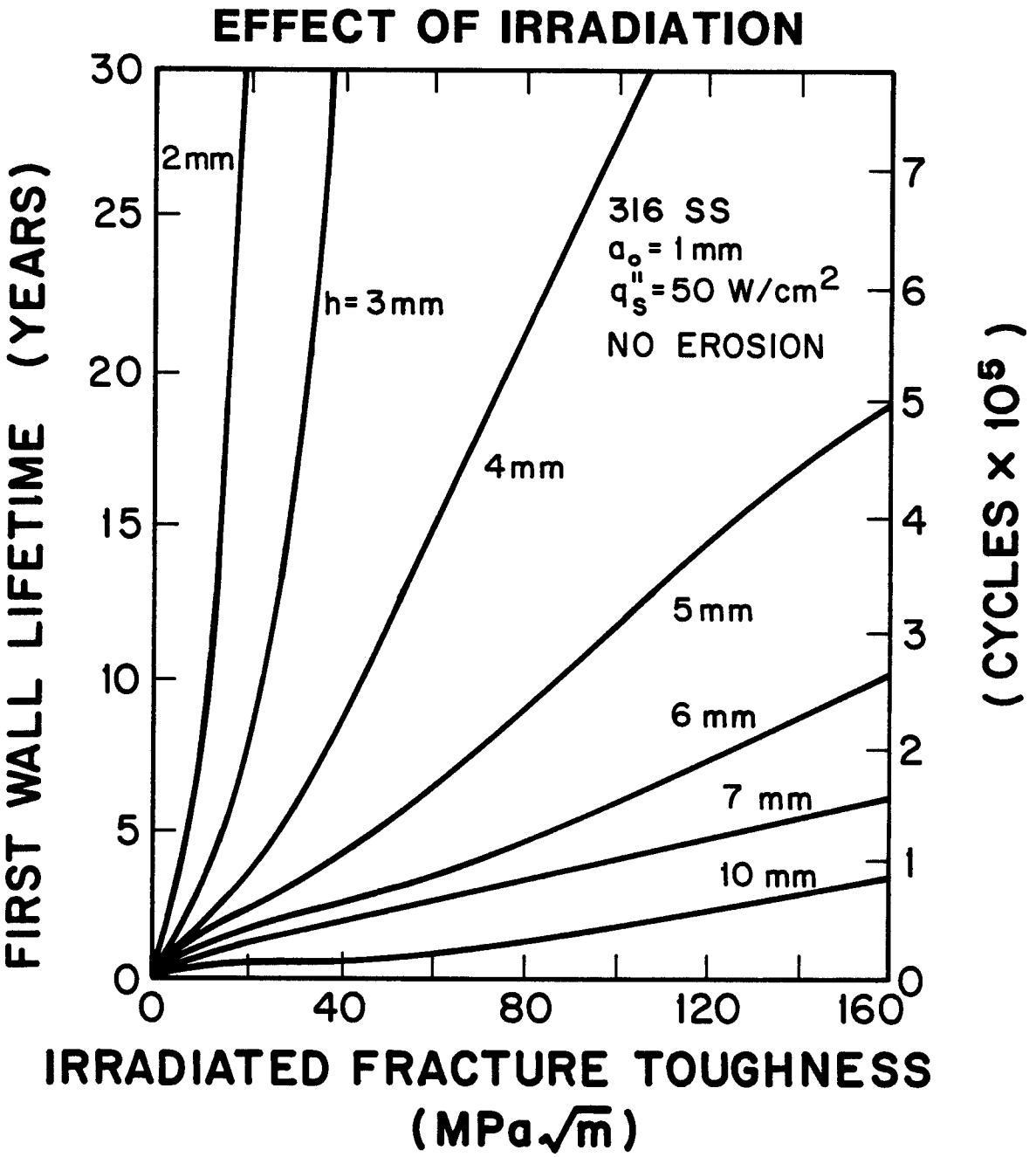

Figure 131. Effect of the minimum irradiated fracture toughness level on first wall lifetime for various wall thicknesses.

of the thin walls by at least a factor of two. In conclusion, the reduction of K_{Ic} due to embrittlement can seriously reduce the lifetime, and further experiments are needed to measure exactly how low K_{Ic} will drop.

If we take all of the data used to generate Fig. 131 and determine whether failure was due to leak-through or fracture, then a plot, such as the one in Fig. 132, can be drawn that shows the locus of points where both failure modes occur simultaneously. By this, we mean that a leak-through crack also fractures the wall. This figure tells us what the governing failure mode is for a given combination of wall thickness and irradiated fracture toughness.

Depending on the particular value of K_{Ic}, a designer could use such a plot as this to choose a wall thickness that would leak before fracturing. This leak-before-break concept is highly desireable in a fusion reactor because of radioactive coolants.

Summary of Effects

Figure 133 plots all of the lifetime curves that have appeared in this chapter in order to provide an overall comparison between all of the effects and assumptions that were considered. The curves fall into three distinct groupings. The major difference between curves 1-5 and 7-10 is due to either the effect of irradiation on K_{Ic} and da/dN or the use of a 1-D flaw growth model. Curve #6 is a special set of calculations that assumed no radiation effects to anything and a 1-D flaw growth model. The predicted lifetimes were

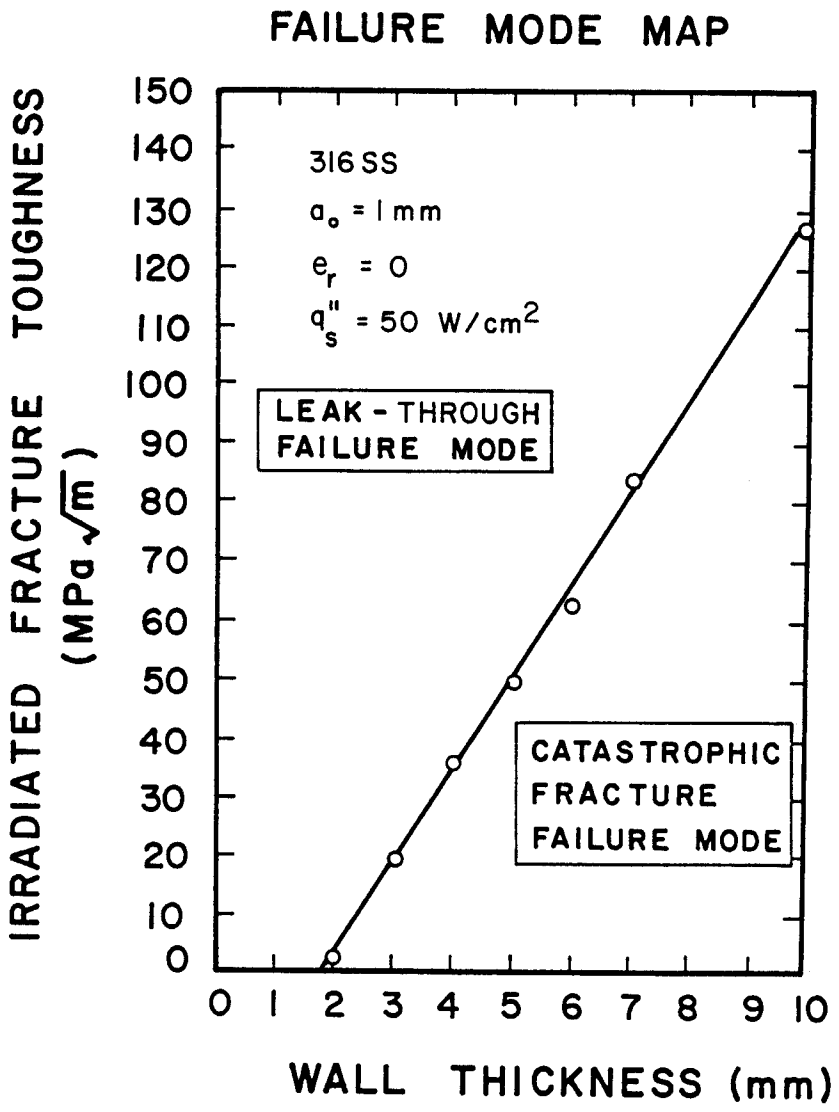

Figure 132. Failure mode map. The locus of points represents a combination of wall thickness and irradiated fracture toughness such that a leak-through failure mode is as equally probable as a catastrophic fracture failure mode.

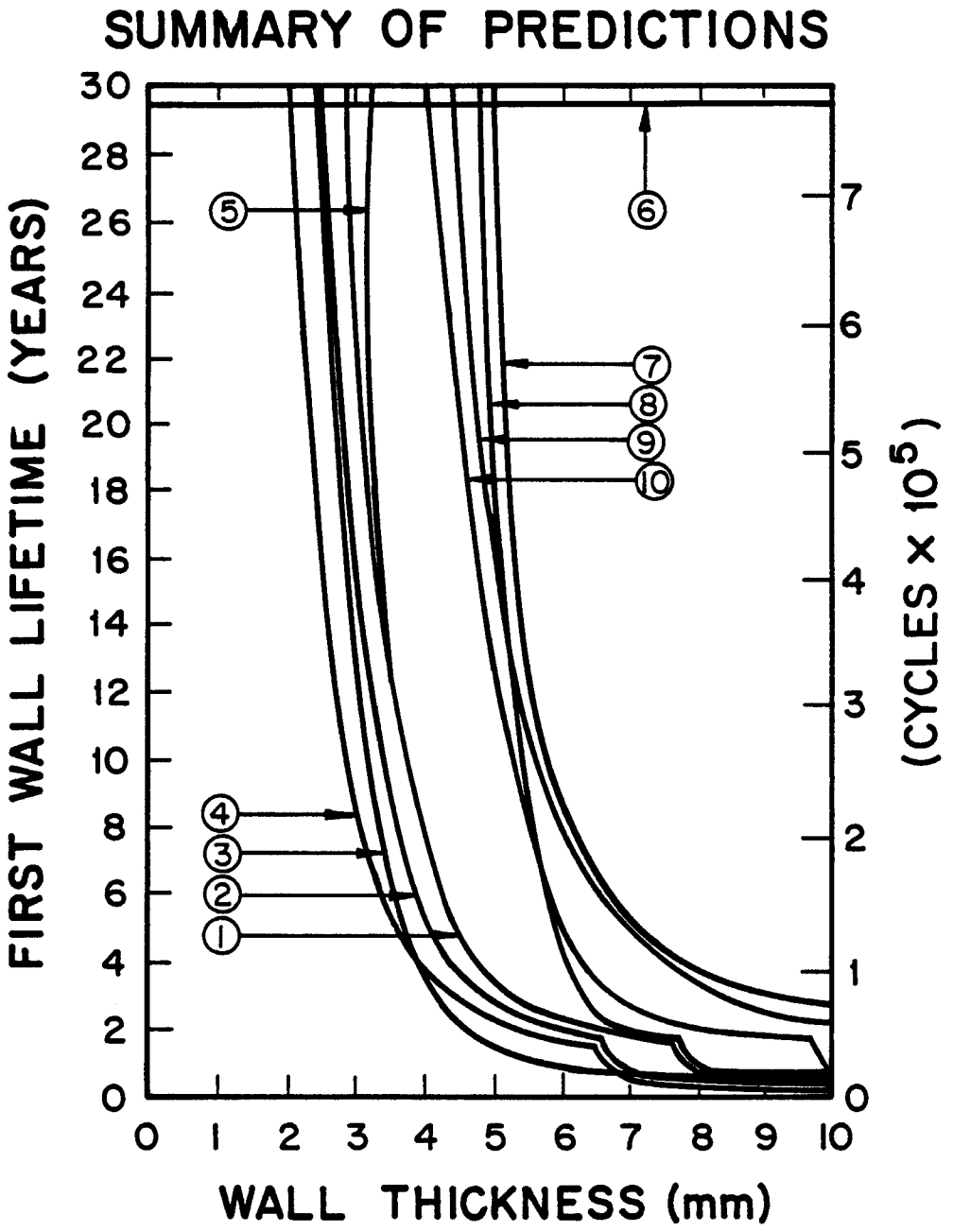

Figure 133. Overall summary of lifetime predictions for various assumptions, plotted as a function of wall thickness. Refer to Table 18 for explanation of each curve.

all greater than 30 years. Therefore by making both of these simplifying assumptions, unrealistically long lifetimes result. Fortunately, by comparing the nine other curves in this figure, it is possible to at least provide upper and lower bounds on the lifetime.

Table 18. Assumptions for Figure 133.

Curve Number	Assumptions
1	Upper bound for da/dN
2	Reference Design parameters (see Table 7)
3	T_b = 100°C
4	Lower bound for da/dN
5	a_o = 0.5 mm
6	No radiation effects and 1-D flaw growth model
7	No radiation effects to anything
8	1-D flaw growth model
9	No radiation effects to da/dN
10	No radiation effects to stage II da/dN

Design Guidelines

Although the primary objective of this research was not to develop a set of design guidelines, nevertheless, some comments are appropriate. Clearly, by picking a thinner wall, a longer life design is possible. A coolant temperature that is neither too hot nor too cold is also desirable. Reducing the surface heat flux, obviously, will help. Allowing some wall erosion will enhance lifetimes, if the rate is not too large.

Although the initial flaw cannot be controlled by design,

the stresses can be chosen to control the fracture mechanics aspects of the problem. From Fig. 132 we saw that catastrophic failure could be avoided by the appropriate choice of wall thickness. Figure 134 illustrates an example of a "fracture map" that could be used to avoid fracture. For a toughness of 30 MPa$\sqrt{m}$ we have plotted the stress required for fracture for various combinations of h and a_o. This stress could arise from any source, including off-normal loads as well.

At the other extreme, if we wish to prevent any crack growth, then ΔK must be below the threshold for fatigue crack growth, ΔK_o. Figure 135 shows a "threshold map" for 316 S.S. Plotted are lines of constant R-ratio that indicate a threshold stress range, $\Delta\sigma$, below which no flaw growth can occur. Of course, this stress depends on the initial flaw depth. Ideally, the stress history can be chosen so that neither of the two failure modes would occur during the service life of the component.

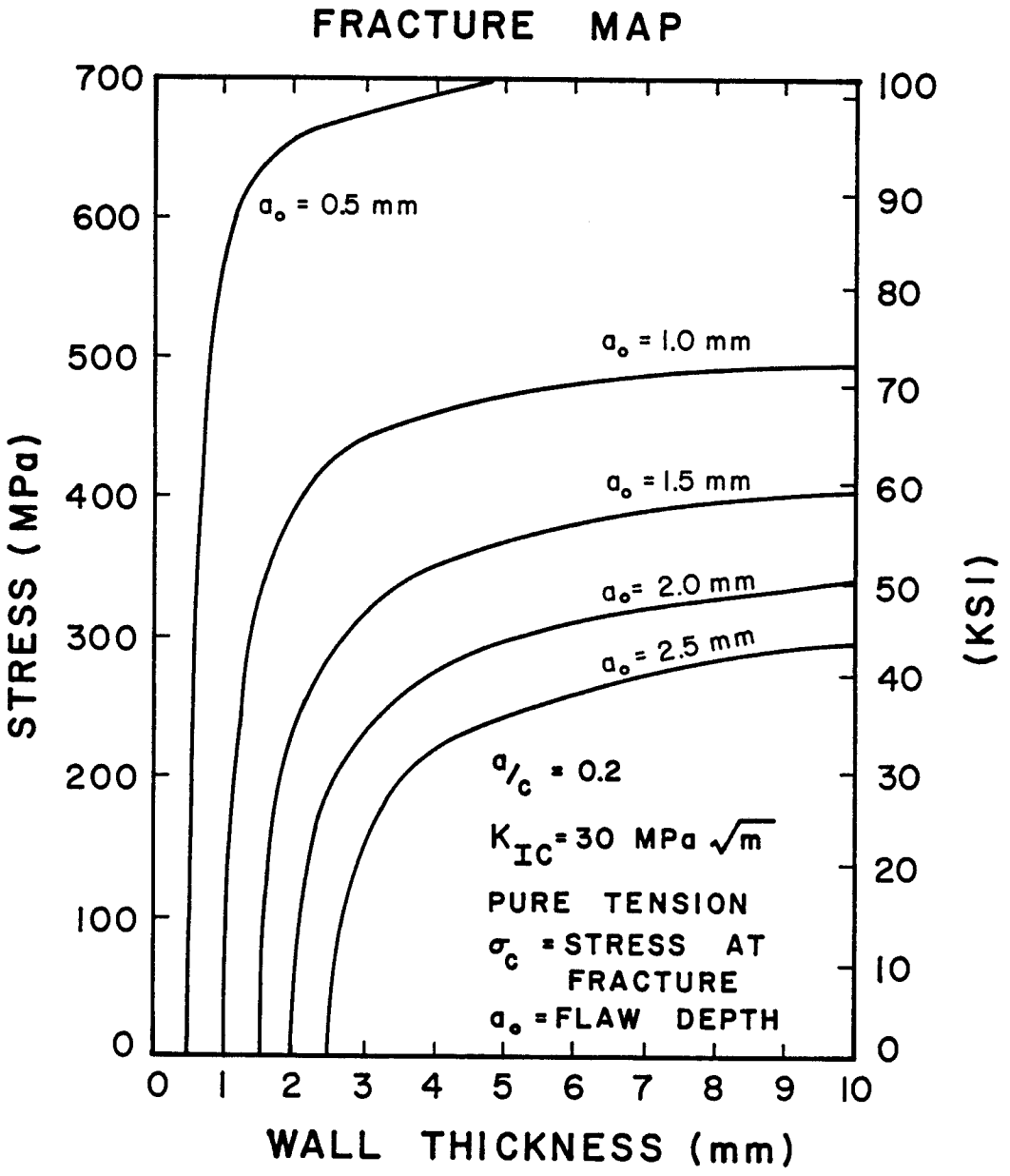

Figure 134. Catastrophic fracture map. For a given wall thickness and flaw depth, the critical stress can be identified that would cause fracture for K_{Ic} = 30 MPa$\sqrt{m}$.

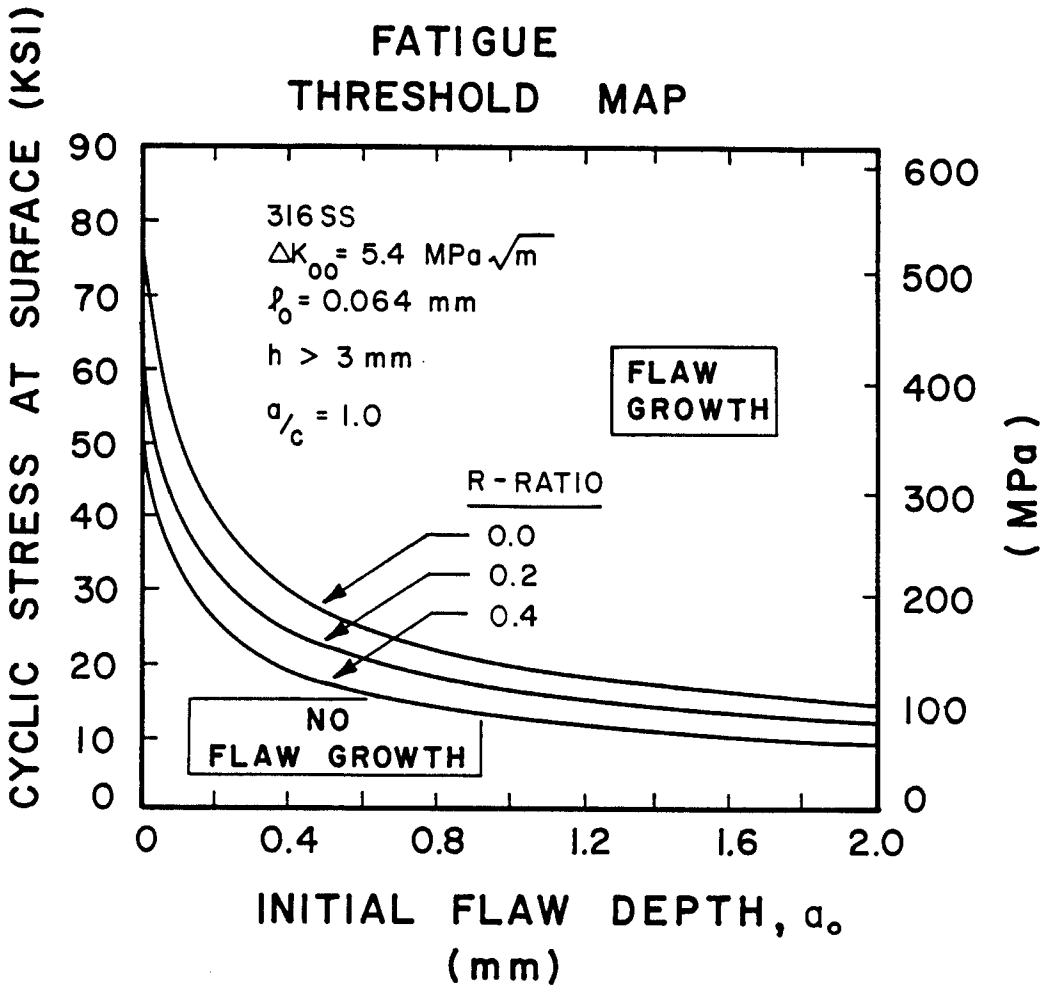

Figure 135. Fatigue threshold map. Given an initial flaw depth, then for a specific R-ratio the cyclic stress at the surface can be determined so that no fatigue crack growth would occur.

CHAPTER 9

Summary and Conclusions

This thesis documents the development of an integrated methodology for lifetime analysis of fusion reactor first wall components. A self-consistent approach is necessary because of the synergistic effects that exist between the materials response to neutron irradiation, the structural response, and the damage processes that occur in a fusion environment. The basic method of solution consists of an inelastic stress analysis coupled to a crack growth calculation. The structural analysis is performed by the computer code TSTRESS which calculates the long-term redistribution of stresses through the thickness of the wall by modelling the inelastic deformation of a generic thin-walled plate element. Four independent sources of stress are included in TSTRESS. They are; (1) membrane loads from coolant pressure, (2) temperature gradients through the wall from surface heat flux, (3) radiation induced swelling gradients through the wall, and (4) residual stress gradients through the wall caused by stress relaxation due to thermal and irradiation creep. In addition, TSTRESS allows the wall to thin down over a period of time due to surface erosion processes.

The stress history which is computed by TSTRESS provides the input for WISECRACK, a linear elastic fracture mechanics code that calculates the two-dimensional growth of a semi-elliptical surface

flaw. Failure is assumed to occur when either the crack penetrates to the other side of the wall, thus causing a leak, or when the maximum stress intensity factor at the crack tip exceeds the material's irradiated fracture toughness, giving rise to catastrophic fracture. WISECRACK uses a sophisticated model for crack growth that accounts for the following effects on crack growth: temperature, mean stress (R-ratio), threshold ΔK_o, short crack correction, aggressive environment, wall thinning and crack erosion, creep crack growth with a linear creep-fatigue interaction law, and neutron induced embrittlement which is modelled as a reduction in the fracture toughness with increasing displacement damage (dpa). Flaw shape changes are followed in the code by using a two-dimensional growth model.

When the two codes are coupled together they form a powerful tool for studying the effects of various correlations for radiation effects assumptions on the response of the first wall.

The major application of the two coupled codes was a study of the sensitivity of the lifetime to different parameters and assumptions. A specific first wall design, namely the cylindrical blanket module with a hemispherical end cap was chosen for this study. The machine is assumed to be a tokamak power reactor with a neutron wall loading of 2 MW/m^2 and a first wall made of 316 stainless steel.

The design parameters that were studied included: the wall thickness, surface heat flux, coolant temperature, and wall erosion rate. By comparing the results, various optimum combinations of

the variables were identified as giving longer lifetimes. In addition to this study, a sensitivity analysis was also performed to investigate the effect on lifetime of the following fracture mechanics parameters: the initial flaw depth, initial flaw aspect ratio, scatter in the fatigue crack growth rate data, and the assumption of either one-dimensional or two-dimensional flaw growth.

Last, but not least, the effects of neutron irradiation were systematically studied by assuming different values of the final irradiated fracture toughness. The effect of radiation on fatigue crack growth was treated with different models and their impact on wall lifetime was investigated.

The major conclusions regarding the lifetime analyses can be summarized as follows:

1. The lifetime is approximately inversely proportional to the fourth power of the cyclic stresses at the surface.
2. The critical location depends primarily upon which side has the smaller ratio of swelling rate to creep compliance, $\dot{S}/\psi$. This parameter determines the steady-state stress distribution through the wall.
3. Creep crack growth can be neglected for most of the operating conditions of tokamak reactors.
4. Among various assumptions investigated in this study, the two that caused the greatest variation in lifetime

were the choice of either a 1-D or 2-D flaw growth model, and the amount of radiation-induced reduction in the fracture toughness.

5. Because of the complex and often subtle synergisms of radiation effects, crack growth, and stress redistribution, misleading or incorrect predictions can result if some, but not all, of the radiation effects are included.
6. For a constant surface heat flux, the lifetime decreases rapidly with increasing wall thickness because of the increasing cyclic thermal stresses. Conversely, for a constant wall thickness, decreasing the surface heat flux significantly increases the lifetime by reducing the cyclic thermal stresses.
7. If the proper combination of wall thickness and surface heat flux is chosen then the cyclic thermal stresses will be sufficiently low so that the stress intensity factor range will be less than the threshold stress intensity. Consequently, no fatigue crack growth will occur. However, swelling and creep may change the mean stresses and thereby influence the R-ratio, which in turn effects the threshold stress intensity factor, thus requiring an inelastic analysis.
8. The proper combination of wall thickness and maximum tensile stress at the surface will insure that a leak-through failure would occur before catastrophic fracture in an embrittled structure.

9. Lifetimes vary inversely proportional to the initial flaw depth, except for the case of very short cracks, e.g. $a_o < 0.2$ mm.

10. The lifetime decreases with decreasing initial flaw aspect ratio. Consequently, the assumption of an initially semi-circular surface flaw is not conservative because it gives a longer life than would be obtained with a long, thin scratch; the latter may be the more probable defect in a first wall structure.

11. The two-dimensional flaw growth model gives shorter lifetimes than the one-dimensional model because of two factors. First, bending stresses cause surface flaws to grow into long, thin shapes, regardless of their initial shapes. And second, the stress intensity factors for long, thin cracks are greater than a semi-circular crack with the same depth. This causes the fatigue crack growth rates for small aspect ratio cracks to be faster, thus reducing the lifetime.

12. The scatter which is inherent in the data for fatigue crack growth rates causes an uncertainty in the lifetime predictions that can be as large as a factor of 2. However, the uncertainty decreases with increasing wall thickness.

13. For a wide range of parameters and assumptions, the effects of radiation damage to the structural materials always causes a significant reduction in the lifetime, when com-

pared to the case of no irradiation.

14. The primary cause of this degradation in the life is due to radiation-induced hardening and the subsequent loss-of-ductility, which may manifest itself in a substantial reduction of the fracture toughness, a fundamental measure of the ability of the material to tolerate a flaw.

15. The fatigue crack growth rate equation used in the WISECRACK models incorporate radiation effects by allowing the fracture toughness to decrease with dose, thereby increasing da/dN. This results in both a downward shift in K_{Ic} for the stage III regime and an increase in the slope of da/dN in stage II. No effects of irradiation on the threshold were modelled, although it can be argued that ΔK_o should decrease with increasing displacement damage. The predicted increase in da/dN therefore reduces the lifetime. Experimental confirmation of the changes in da/dN due to radiation damage is needed.

Finally, this research has identified some critical materials properties which need to be measured in order to improve the accuracy of lifetime determinations. These properties are:

1. The fracture toughness of specimens irradiated to high displacement doses.

2. Fatigue crack growth rates during and after irradiation to high displacement doses.

3. Fatigue crack growth rates in the threshold regime for elevated temperatures and aggressive environments, such as liquid lithium, hydrogen, and steam.
4. Static crack growth in the same aggressive environments.
5. Effect of very long hold-times on fatigue crack growth rates.
6. Effect of irradiation on the threshold stress intensity factor.
7. Measurement of the ratio $\dot{S}/\psi$, for different temperatures, displacement rates, and appropriate He/dpa ratios.

Although a specific design was used to investigate the effects of radiation damage, wall erosion, fracture mechanics, and various design parameters, the conclusions presented here are of a generic nature and are applicable to other first wall designs characterized by the thin-wall assumptions.

One very general conclusion that can be made from the study of this problem is that with present structural materials such as stainless steels, the anticipated severe effects of radiation damage to the mechanical properties and fracture behavior will limit the first wall lifetime to some fraction of the plant life, thereby requiring at least one replacement cycle. As a result, there exists a great incentive to develop both better structural materials (which retain good fracture toughness and fatigue properties) as well as alternate fusion reactor and first wall concepts. The methodology and the codes developed in the present

thesis will allow a better assessment of the improvements that can be achieved in the future, both in the materials area and in fusion reactor technology.

Appendix

A Simple Closed-Form Expression for the Fatigue Lifetime of a Cracked Solid

Given certain assumptions, it is possible to derive a simple expression for the fatigue life of a cracked solid that can be useful for understanding the results predicted by more accurate solutions to the following general equation for crack growth:

$$a_f = a_o + \int_o^{N_f} \frac{da}{dN}\, dN \,. \tag{A1}$$

To solve this equation in closed form, let us exchange the limits of integration, which yields

$$N_f = \int_{a_o}^{a_f} \left(\frac{da}{dN}\right)^{-1} da \,. \tag{A2}$$

We proceed by assuming the Paris equation is valid over the entire range of crack growth, therefore

$$\frac{da}{dN} = C\,(\Delta K)^n \,. \tag{A3}$$

Furthermore, we assume that the stress intensity factor range, ΔK, is given by

$$\Delta K = M\ \Delta\sigma\ \sqrt{\pi a} \tag{A4}$$

where

$$M = \text{geometric factor.}$$

Substituting this equation back into the expression for da/dN yields

$$\frac{da}{dN} = C\, M^n\, (\Delta\sigma)^n\, \pi^{n/2}\, a^{n/2}\,. \tag{A5}$$

The final step involves substituting this equation for da/dN back into equation (A2), thus giving

$$N_f = \int_{a_o}^{a_f} C^{-1} M^{-n}\, \pi^{-n/2} (\Delta\sigma)^{-n} a^{-n/2} da\,. \tag{A6}$$

The constants C and π can be taken outside of the integral. Likewise, if we assume $\Delta\sigma$ is constant, then it can be taken outside as well.

In general, the geometry factor, M, is a function of the crack size, a. However, for certain geometries M is a constant, as in the case of an edge crack in a semi-infinite body. Assuming that M is constant, Equation (A6) becomes

$$N_f = \frac{1}{\pi^{n/2} C M^n (\Delta\sigma)^n} \int_{a_o}^{a_f} a^{-n/2}\, da \tag{A7}$$

Solving the integral in closed-form yields

$$N_f = \frac{2}{\pi^{n/2} (n-2) C M^n (\Delta\sigma)^n} \left[a_o^{(1-n/2)} - a_f^{(1-n/2)}\right] \tag{A8}$$

For many metals, including austenitic stainless steels, $n \cong 4$, therefore Equation (A8) reduces to

$$N_f = \frac{1}{\pi^2 C M^4 (\Delta\sigma)^4} \left[\frac{1}{a_o} - \frac{1}{a_f} \right] \tag{A9}$$

Finally, if we assume that the final crack size is much larger than the initial size, then $a_f >> a_o$ and Equation (A9) is approximated by

$$N_f \cong \frac{1}{\pi^2 C M^4 (\Delta\sigma)^4 a_o} \quad . \tag{A10}$$

Therefore, we find that the fatigue lifetime is inversely proportional to C, a_o, M^4, and $(\Delta\sigma)^4$.

Let us rewrite Equation (A5) with n = 4:

$$\frac{da}{dN} = C M^4 (\Delta\sigma)^4 \pi^2 a^2 \quad . \tag{A11}$$

Now, if we substitute this equation evaluated at $a = a_o$ into Equation (A10), we find

$$N_f \cong \frac{a_o}{(da/dN)\Big|_{t=o}} \quad . \tag{A12}$$

Therefore, this tells us that the fatigue lifetime is roughly inversely proportional to the initial fatigue crack growth rate, assuming the same flaw size, a_o.

References

1. S.R. Swanson, F. Cicci and W. Hoppe, ASTM STP 415, p. 312 (1967).

2. P.C. Paris and F.Erdogan, "A Critical Analysis of Crack Propagation Laws," Journal of Basic Engineering Transactions, ASME, Series D, 85(4), p. 528-534 (1963).

3. H. Liebowitz, ed., Fracture: An Advanced Treatise, Academic Press, New York (1968).

4. R.W. Hertzberg, Deformation and Fracture Mechanics of Engineering Materials, John Wiley & Sons, New York (1976).

5. S.T. Rolfe and J.M. Barsom, Fracture and Fatigue Control in Structures: Application of Fracture Mechanics, Prentice-Hall Englewood Cliffs, NJ (1977).

6. R.G. Forman, H.C. Kavanaugh and B. Stuckey, "Computer Analysis of Two-Dimensional Fatigue Flaw-Growth Problems," NASA Technical Memorandum TM-X-58086 (1972).

7. P.M. Besuner, D.C. Peters and R.C. Cipolla, "BIGIF-Fracture Mechanics Code for Structures," EPRI Report NP-838, Manual 1 (1978).

8. J. Weertman, "Theory of Irradiation Growth of Fatigue Cracks," Journal of Nuclear Materials 55, 253-258 (1975).

9. J. Weertman, "Potential Fatigue Problems in First-Wall Laser-Controlled Fusion Reactors," Los Alamos Scientific Laboratory Report LA-5664-MS (1974).

10. R.A. Krakowski, R.L. Hagenson and G.E. Cort, "First Wall Thermal-Mechanical Analysis of the Reference Theta-Pinch Reactor," Nuclear Technology 34, 217-241 (1976).

11. M. Abdou et al., "The Establishment of Alloy Development Goals Important To Commercialization of Tokamak-Based Fusion Reactors," Argonne Report ANL/FPP/TM-99, MDCE-1743, 88-101 (1977).

12. McDonnell Douglas staff, "Fusion Reactor First Wall/Blanket Systems Analysis Tokamak Concepts," interim report, EPRI-472-1 (1977).

13. B.A. Cramer, J.W. Davis, R.C. Kinder, D.A. Bowers, "An Approach For Determining the Lifetime of a First Wall Structure in a Tokamak Reactor," CONF-760935-P4, Proceedings of the Second Topical Meeting on the Technology of Controlled Nuclear Fusion, Richland, WA (1976).

14. G.M. Fuller et al., "Fusion Reactor First Wall/Blanket Systems Analysis of Tokamak Concepts," Final Report, EPRI ER-582 (1977).

15. B.A. Cramer and J.W. Davis, "Fracture Mechanics Aspects of Irradiated Blanket Structures," Transactions of the Fifth International Conference on Structural Mechanics in Reactor Technology (SMIRT-V), Berlin, Germany, Vol. N (1979).

16. B.A. Cramer, "Response and Life Considerations for First Wall Structures in Fusion Reactor Erosion Environemnts," Second Topical Meeting on Fusion Reactor Materials, Seattle, WA (1981).

17. D.W. Kearney et al., "Mechanical and Thermal Design of a Gas-Cooled Fusion Blanket Module," General Atomic GA-A14671 (1977).

18. R.F. Mattas and D.L. Smith, "Model For Life-Limiting Properties of Fusion Reactor Structural Materials," Nuclear Technology 39, 186-198 (1978).

19. T.V. Prevenslick, "Structural Evaluation of a Tokamak Reactor Cylindrical Module Blanket Concept," Westinghouse Report WFPS-TME-096 (1978).

20. M.J. Delaney, B.A. Cramer and C.A. Trachsel, "Structural Performance of Plasma Chamber Materials for a Power Generating Tokamak," Journal of Nuclear Materials 85, 86, 165-169 (1979).

21. S.N. Rosenwasser et al., "The Application of Martensitic Stainless Steels in Long Lifetime Fusion First Wall/Blankets," General Atomic Report GA-A15356 (1979).

22. "STARFIRE - A Commerical Tokamak Fusion Power Plant Study," Argonne Report ANL/FPP-80-1, Vol. 1, Chapter 10 (1980).

23. A.O. Adegbulugbe and J.E. Meyer, "Failure Criteria for Fusion Reactor First Wall Structural Design," Second Topical Meeting on Fusion Reactor Materials, Seattle, WA (1981).

24. R. Matera, C. Ponti and R. Van Heusden, "SMILE - A Computer Program for the Lifetime Evaluation of Fusion Reactors Structural Components," Second Topical Meeting on Fusion Reactor Materials, Seattle, WA (1981).

25. ASME Boiler and Pressure Vessel Code, Section XI, "Rules for In-service Inspection of Nuclear Power Plant Components," Appendix A, "Evaluation of Flaw Indicators," (1977).

26. D.J. Hagemaier, "Nondestructive Methods for Evaluating Materials," Metal Progress Mid-June, 159-164 (1980).

27. RDT Standards (Draft), "Structural Design Criteria for Fast Breeder Reactor Core Components," US Department of Energy, Division of Reactor Research and Technology, RDT F9-7,8,9 (1978).

28. "Space Shuttle Orbiter Fracture Control Plan," Rockwell International, Space Divison report SD73-SH-0082A (1974).

29. J.C. Newman and I.S. Raju, "Analysis of Surface Cracks in Finite Plates Under Tension or Bending Loads," NASA Technical Paper 1578, (1978).

30. P.C. Paris and F. Erdogan, "A Critical Analysis of Crack Propagation Laws," Journal of Basic Engineering 85(4), 528-534 (1963).

31. L.A. James, "Fatigue Crack Propagation in Austenitic Stainless Steels," Hanford Engineering Development Laboratory Report HEDL-SA-1051 (1976).

32. Nuclear Systems Materials Handbook, Hanford Engineering Development Laboratory (1977).

33. S. Pearson, "Fatigue Crack Propagation in Metals," Nature 211, 1077-1078.

34. M.O. Speidel, "Fatigue Crack Growth at High Temperatures," Proceedings of the Symposium on High-Temperature Materials in Gas Turbines, Baden, Switzerland, 207-251 (1974).

35. J.M. Bloom and W.A. Van Der Sluys, "Determination of Stress Intensity Factors for Gradient Stress Fields," Journal of Pressure Vessel Technology, 477-484 (August 1977).

36. K. Sadanada and P. Shahinian, "Effect of Environment on Crack Growth Behavior in Austenitic Stainless Steels Under Creep and Fatigue Conditions," Mettalurgical Transactions A 11A, 267-276 (1980).

37. P. Shahinian, H.H. Smith and H.E. Watson, "Fatigue Crack Propagation in Type 316 Stainless Steel at High Temperature," Journal of Engineering for Industry, 976-980 (November 1971).

38. E.K. Walker, Air Force Flight Dynamics Laboratory Report AFFDL-TR-70-144, 225 (1970).

39. E. Tschegg and S. Stanzl, "Fatigue Crack Propagation and Threshold in b.c.c. and f.c.c. Metals at 77 K and 293 K," Acta Metallurgica 29, 33-40 (1981).

40. G. Lucas and R. Ritchie, private communications.

41. R.O. Richie, "Near-Threshold Fatigue-Crack Propagation in Steels," International Metals Reviews, No. 5 and 6, Review 245, 205-230 (1979).

42. V. Weiss and D.N. Lal, "A Note on the Threshold Condition for Fatigue Crack Propagation," Metallurgical Transactions 5, 1946-1949 (1974).

43. S. Stanzl and E. Tschegg, "Fatigue Crack Growth and Threshold Measured at Very High Frequencies," Metal Science, 137-143 (April 1980).

44. S. Stanzl and E. Tschegg, "Influence of Environment on Fatigue Crack Growth in the Threshold Region," Acta Metallurgica 29, 21-32 (1981).

45. B. Mukherjee and M.L. Vanderglass, "Fatigue Threshold Stress Intensity and Life Estimation of ASTM A106B Piping Steel," Journal of Pressure Vessel Technology 102, 294-302 (1980).

46. A.T. Stewart, "The Influence of Environemnt and Stress Ratio on Fatigue Crack Growth at Near Threshold Stress Intensities in Low-Alloy Steels," Engineering Fracture Mechanics 13, 463-478 (1980).

47. M. Klesnil and P. Lukas, "Effect of Stress Cycle Asymmetry on Fatigue Crack Growth," Materials Science and Engineering 9, 231-240 (19720.

48. M.W. Brown and K.J. Miller, "Initiation and Growth of Cracks in Biaxial Fatigue," Fatigue of Engineering Materials and Structures 1, 231-246 (1979).

49. R.J. Donahue, H. McI. Clark, P. Atanmo, R. Kumble, and A.J. McEvily, "Crack Opening Displacement and the Rate of Fatigue Crack Growth," International Journal of Fracture Mechanics 8(2), 209-219 (1972).

50. J.M. Barsom, "Fatigue Behavior of Pressure-Vessel Steels," Welding Research Council Bulletin 194, 1-22 (1974).

51. O. Vosikovsky, "The Effect of Stress Ratio on Fatigue Crack Growth Rates in Steels," Engineering Fracture Mechanics 11, 595-602 (1979).

52. S. Pearson, "Initiation of Fatigue Cracks in Commercial Aluminum Alloys and the Subsequent Propagation of Very Short Cracks," Engineering Fracture Mechanics 7, 235-247 (1975).

53. T.H. Topper and M.H. El Haddad, "Fracture Mechanics For Short Fatigue Cracks," Canadian Metallurgical Quarterly 18, 207-213 (1979).

54. H. Kitagawa and S. Takahashi, "Applicability of Fracture Mechanics to Very Small Cracks or the Cracks in the Early Stage," Proceedings of the Second International Conference on Mechanical Behavior of Materials, Boston, MA 627-631 (1976).

55. H. Kitagawa, S. Takahashi, C.M. Suh, S. Miyashita, "Quantitative Analysis of Fatigue Process - Microcracks and Slip Lines Under Cyclic Strains," ASTM STP 675, 420-449 (1979).

56. A. Talug and K. Reifsnider, "Analysis and Investigation of Small Flaws," ASTM STP 637, 81-96 (1977).

57. M.H. El Haddad, K.N. Smith and T.H. Topper, "Fatigue Crack Propagation of of Short Cracks," Journal of Engineering Materials and Technology 101 42-46 (1979).

58. M.H. El Haddad, T.H. Topper and K.N. Smith, "PRediction of Non Propagating Cracks," Engineering Fracture Mechanics 11, 573-584 (1979).

59. S.J. Hudak, Jr., "Small Crack Behavior and the Prediction of Fatigue Life," Journal of Engineering Materials and Technology 103, 26-35 (1981).

60. H.H. Smith, P. Shahinian and M.R. Achter, "Fatigue Crack Growth Rates in Type 316 Stainless Steel at Elevated Temperature as a Function of Oxygen Pressure," Transactions of the Metallurgical Society of AIME 245, 947-953 (1969).

61. T. Ericsson, "Review of Oxidation Effects on Cyclic Life at Elevated Temperature," Canadian Metallurgical Quarterly 18, 177-195 (1979).

62. M.W. Mahoney and N.E. Paton, "The Influence of Gas Environments on Fatigue Crack Growth Rates in Type 316 and 321 Stainless Steels," Nuclear Technology 23, 290-297 (1974).

63. E.K. Priddle, F. Walker and C. Wiltshire, "The Effects of Helium, Sodium and Other Environments on the Fatigue Crack Propagation Characteristics of a Stainless Steel," Proceedings of the Conference on Influence of Invironemnt on Fatigue, London, 137-144 (1977).

64. L.A. James and R.L. Knecht, Metallurgical Transactions 6A, 109 (1975).

65. L.A. James and R.L. Knecht, Hanford Engineering Development Laboratory Report HEDL-TME-74-4, C13 (1975).

66. A.G. Pineau and R.M. Pelloux, "Influence of Strain-Induced Martensitic Transformations on Fatigue Crack Growth Rates in Stainless Steels," Metallurgical Transactions 5, 1103-1112 (1974).

67. P. Shahinian, "Influence of Section Thickness on Fatigue Crack Growth in Type 316 Stainless Steel," Nuclear Technology 30, 390-397 (1976).

68. H. Liebowitz, J.D. Lee and J. Eftis, "Biaxial Load Effects in Fracture Mechanics," Engineering Fracture Mechanics 10, 315-335 (1978).

69. D.L. Hammon, G.J. Coubrough, D.K. Matlock, and D.L. Olson, "The Influence of Cyclic Loading on the Lithium Corrosion Behavior of Reactor Materials," Second Topical Meeting on Fusion Reactor Materials, Seattle, WA (1981).

70. D.C. Hammon, D.K. Matlock and D.L. Olson, "The Effect of Liquid Lithium of Fatigue Crack Propagation in 304L Stainless Steel at Elevated Temperatures," Liquid Metals Symposium, NACE Task Group T2-1, Corrosion/81, Toronto, Canada (1981).

71. R.E. Spencer, S.K. DeWeese, D.K. Matlock, and D.L. Olson, "Fatigue Crack Propagation Characteristics of 2 1/4 Cr-1Mo Steel in Liquid Lithium at 773 K," Metallurgical Transactions A, 11A, 1758-1761 (1980).

72. W.H. Bamford, "Fatigue Crack Growth of Stainless Steel Piping in a Pressurized Water Reactor Environment," Journal of Pressure Vessel Technology 101, 73-79 (1979).

73. W.H. Bamford and D.H. Moon, "Some Mechanistic Observations on the Crack Growth Characteristics of Pressure Vessel and Piping Steels in PWR Environments," Corrosion-NACE 36(6), 289-298 (1980).

74. N. Matsuda et al., "Fatigue Crack Propagation in High Temperature Steam Environment," Society of Material Science, Japan (1975).

75. M. Habashi, J. Galland, P. Azou, and P. Bastien, "Effect of Induced Hydrogen on Fatigue Crack Propagation of an Austenitic Stainless (316L) and Fe-Ni-C Alloys," Second International Congress on Hydrogen in Metals, paper 3 B-7, Paris France (1977).

76. D.W. Hoeppner and W.E. Krupp, "Prediction of Component Life by Application of Fatigue Crack Growth Knowledge," Engineering Fracture Mechanics 6, 47-70 (1974).

77. H. Nordberg, "The Effect of Microstructure on Fatigue-Crack Growth in a 12% Chromium Steel," Scandinavian Journal of Metallurgy 1, 23-25 (1972).

78. R.G. Forman, V.E. Kearney and R.M. Engle,"Numerical Analysis of Crack Propagation in Cyclic-Loaded Structures," Journal of Basic Engineering, 459-464 (August 1967).

79. A.M. Sullivan and T.W. Crooker, "Analysis of Fatigue-Crack Growth in a High Strength Steel - Part I: Stress Level and Stress Ratio Effects at Constant Amplitude," Journal of Pressure Vessel Technology, 1979-184 (May 1976).

80. T.W. Crooker, "Effect of Tension-Compression Cycling on Fatigue Crack Growth in High Strength Alloys," Journal of Engineering for Industry, 893-896 (November 1971).

81. Etsuo Sasaki, Akihiko Ohta, and Michio Kosuge, "Fatigue Crack Propagation Rate and Stress Intensity Threshold Level of Several Structural Materials at Varying Stress Ratios (-1 0.8)," Transactions of National Research Institute For Metals 19(4), 183-199 (1977).

82. M.R. Louthan, Jr., J.A. Donovan, and D.E. Rawl, Jr., "Effect of High Dislocation Density on Stress Corrosion Cracking and Hydrogen Embrittlement of Type 304L Stainless Steel," Corrosion-NACE 29(3), 108-111 (1973).

83. D.J. Michel and H.H. Smith, "Neutron Irradiation Effects on Fatigue Crack Propagation in AUstenitic Stainless Steels and Nickel-Base Alloys," Journal of Nuclear Materials 85, 86, 845-849 (1979).

84. D.J. Michel and H.H. Smith, "Fatigue Crack Propagation in Type 316 Stainless Steel in Vacuum and Air Environments," Second Topical Meeting on Fusion Reactor Materials, Seattle, WA (1981).

85. D.J. Michel and H.H. Smith, "Fatigue Crack Propagation in Neutron Irradiated Type 304 and Type 308 Stainless Steel Plate and Weld Materials," Journal of Nuclear Materials 71, 173-177 (1977).

86. D.J. Michel and G.E. Korth, "Effects of Irradiation on Fatigue and Crack Propagation in Austenitic Stainless Steels," Radiation Effects in Breeder Reactor Structural Materials, AIME, New York, 117-137 (1977).

87. L.A. James, "The Effect of Fast Neutron Irradiation Upon the Fatigue-Crack Propagation Behavior of Two Austenitic Stainless Steels," Journal of Nuclear Materials 59, 183-191 (1976).

88. E.E. Bloom, "Mechanical Properties of Materials in Fusion Reactor First-Wall and Blanket Systems," Journal of Nuclear Materials 85, 86, 795-804 (1979).

89. J.L. Straalsund and E.E. Bloom, "Swelling-Creep and Mechanical Properties of First Wall and Structural Alloys," Second Topical Meeting on Fusion Reactor Materials, Seattle, WA (1981).

90. W.G. Wolfer and R.H. Jones, "Flow and Fracture of Alloys in the Fusion Environment," University of Wisconsin Report UWFDM-429 (August 1981).

91. R.L. Simons, "Strength/Ductility Correlations for 20% CW AISI 316 Stainless Steel," Second Topical Meeting on Fusion Reactor Materials, Seattle, WA (1981).

92. M.O. Speidel, "Corrosion Fatigue in Fe-Ni-Cr Alloys," Proceedings of the Conference on Stress Corrosion Cracking and Hydrogen Embrittlement of Iron Base Alloys, Unieux-Firminy, France (June 1973).

93. R.O. Ritchie, "Influence of Microstructure on Near-Threshold Fatigue Crack Propagation in Ultra-High Strength Steel," Metal Science, 368-381 (August/September 1977).

94. F.R. Stonesifer, "Effect of Grain Size and Temperature on Fatigue Crack Propagation in A533 B Steel," Engineering Fracture Mechanics 10, 305-314 (1978).

95. W.W. Gerberich and N.R. Moody, "A Review of Fatigue Fracture Topology Effects on Threshold and Growth Mechanisms," ASTM STP-675, 292-341 (1979).

96. K. Tanaka, "A Correlation of K_{th}-Value with the Exponent, m, in the Equation of Fatigue Crack Growth for Various Steels," International Journal of Fracture 15(1), 57-68 (1979).

97. R.O. Ritchie and J.F. Knott, "Mechanisms of Fatigue Crack Growth in Low Alloy Steel," Acta Metallurgica 21, 639-648 (1973).

98. T.V. Prevenslick, "Structural Evaluation of a Tokamak Reactor Cylindrical module Blanket Concept," Westinghouse Report WFPS-TME-096 (1978).

99. P. Shahinian, "Crack Propagation in Cold-Worked Austenitic Stainless Steel at Elevated Temperature," Nuclear Technology 38, 415-426 (1978).

100. T. Kawasaki, M. Horiguchi, "Creep Crack Propagation in Austenitic Stainless Steel at Elevated Temperature," Engineering Fracture Mechanics 9, 879-889 (1977).

101. T. Yokobori, H. Sakata and T. Yokobori, Jr., "A New Parameter for Prediction of Creep Crack Growth Rate at High Temperature," Engineering Fracture Mechanics 13, 533-539 (1979).

102. T. Yokobori and H. Sakata, "Studies on Crack Growth Rate Under High Temperature Creep, Fatigue and Creep-Fatigue Interaction-I," Engineering Fracture Mechanics 13, 509-522 (1979).

103. T. Yokobori, H. Sakata and A.T. Yokobori, Jr., "Studies on Crack Growth Rate Under High Temperature Creep, Fatigue and Creep-Fatigue Interaction-II," Engineering Fracture Mechanics 13, 523-532 (1979).

104. L.S. Fu, "Creep Crack Growth in Technical ALloys at Elevated Temperature - A Review," Engineering Fracture Mechanics 13, 307-330 (1980).

105. W.G. Wolfer, R.W. Conn, "New ANalysis of First Wall Lifetime Considerations For Fusion Reactors," University of Wisconsin Report UWFDM-212 (March 1977).

106. G.R. Odette and D. Frey, "Development of Mechanical Property Correlation Methodology for Fusion Environments," Journal of Nuclear Materials 85, 86, 817-822 (1979).

107. B. Cramer and J.W. Davis, "Fracture Mechanics Aspects of Irradiated Blanket Structures," Transactions of the Fifth International Conference on Structural Mechanics in Reactor Technology, Volume N, Berlin, West Germany (1979).

108. G.T. Hahn and A.R. Rosenfield, "Sources of Fracture Toughness: The Relation Between K_{Ic} and the Ordinary Tensile Properties of Metals," ASTM STP 432, 5-31 (1968).

109. P.L. Jones and A.S. Tetelman, "Characterization of the Elevated Temperature Static Load Crack Extension Behavior of Type 304 Stainless Steel", Engineering Fracture Mechanics 12, 79-97 (1979).

110. S. Taira, R. Ohtani, T. Kitamura, "Application of J-Integral to High Temperature Crack Propagation: Part I - Creep Crack Propagation," Journal of Engineering Materials and Technology 101, 154-161 (1979).

111. P. Shahinian, "Fatigue and Creep Crack Propagation in Stainless Steel Weld Metal," Welding Research Supplement, 87-s-92-s (1978).

112. K. Sadananda and P. Shahinian, "Application of Fracture Mechanics to High Temperature Crack Growth," Fracture Mechanics, H Liebowitz, ed., University Press of Virginia, Charlottesville (1978).

113. J.R. Haigh and W. Laidler, "Creep Crack Growth in a Type 316 Austenitic Stainless Steel Weld Metal, Part I: Effects of Metallurgical Variables and Temperature," Central Electricity Research Laboratories Report CEGB/RD/L/N-174/77 (1977).

114. R. Koterazawa and T. Mori, "Applicability of Fracture Mechanics Parameters to Crack Propagation Under Creep Conditions," Journal of Engineering Materials and Technology 298-305 (1977).

115. R.D. Nicholson, "The Effect of Temperature on Creep Crack Propagation in AISI 316 Stainless Steel," Materials Science and Engineering 22, 1-6 (1976).

116. R. Koterazawa and Y. Iwata, "Fracture Mechanics and Fractography of Creep and Fatigue Crack Propagation at Elevated Temperature," Journal of Engineering Materials and Technology, 296-305 (1976).

117. P. Shahinian, "Creep-Fatigue Crack Propagation in Austenitic Stainless Steel," Journal of Pressure Vessel Technology, 166-172 (1976).

118. R.D. Nicholson and C.L. Formby, "The Validity of Various Fracture Mechanics Methods at Creep Temperatures," International Journal of Fracture 11(4), 595-604 (1975).

119. P.S. Chopra, "Finite Element Fracture Mechanics Analysis of Creep Rupture of Fuel ELement Cladding," Nuclear Engineering and Design 29, 7-21 (1974).

120. L.A. James, "Some Preliminary Observations on the Extension of Cracks Under Static Loading at Elevated Temperature," International Journal of Fracture Mechanics 8, 347-349 (1972).

121. J.J. McGowan and H.W. Liu, "A Design Approach for Correlating High Temperature Fatigue Crack Growth Over a Wide Range of Parameters," Journal of Engineering Materials and Technology 103, 246-252 (1981).

122. R.P. Wei and J.D. Landes, "Correlation Between Sustained-Load and Fatigue Crack Growth in High Strength Steels," Materials Research and Standards, 25-46 (1969).

123. E.E. Bloom and W.G. Wolfer, "In-Reactor Deformation and Fracture of Austenitic Stainless Steels," ASTM STP 683, 656-672 (1979).

124. L.K.L. Tu and B.B. Seth, "Threshold Corrosion Fatigue Crack Growth in Steels," Journal of Testing and Evaluation 6(1), 66-74 (1978).

125. G.L. Kulcinski, "Critical Materials Problems in INTOR," University of Wisconsin Report UWFDM-374 (1980).

126. M. Biggio, G. Casini, F. Farfaletti-Casali, M. Riegar, J. van Renterghem, and G. Rubinacci, "Structural Engineering Problems in FINTOR, Conceptual Designs," SMIRT V Conf., N, Berlin (1979).

127. K. Sako and A. Minato, "Blanket Structure Design for JAERI Experimental Fusion Reactor," SMIRT V Conference, Volume N, Berlin, West Germany (1979).

128. B. Streibel and P. Bourrier, "Mechanical Static Analysis of the JET Vacuum Vessel," SMIRT V Conference, Volume N, West Germany (1979).

129. W. Daenner, "The Mechanical Performance of the Fusion Reactor First Wall, Part I: Steady-State Analysis Without Irradiation Effects," Max Planck IPP 4/143 (1976).

130. W. Daenner and J. Raeder, "The Mechanical Performance of the Fusion Reactor First Wall, Part II: Behavior Under Pulsed Load Conditions," Max Planck IPP 4/149 (1977).

131. W. Daenner and J. Raeder, "FWLTB - A Mathematical Model to Calculate the Lifetime of the Fusion Reactor First Wall," Third ANS Topical Meeting on the Technology of Controlled Nuclear Fusion, Santa Fe, NM (1978).

132. W. Daenner and J. Raeder, "Latest Results from the FWLTB Computer Code: The Influence of Swelling and Irradiation Creep on the Stainless Steel First Wall of a Fusion Reactor," Journal of Nuclear Materials 85, 86, 147-151 (1979).

133. W. Daenner, "First Wall and Blanket Structure Performance," SMIRT V Conference, Berlin, West Germany (1979).

134. W.H. Kohler, "Comparison of Technological Problems in Stainless Steel Fusion Reactor Blankets and Fast Breeder Reactor Cores," Proceedints of the Seventh Symposium on Fusion Technology (1972).

135. W.G. Wolfer and R.D. Watson, "Structural Performance of a Graphite Blanket in Fusion Reactors," University of Wisconsin Report UWFDM-258 (1978).

136. R.D. Watson and W.G. Wolfer, "Mechanical Constitutive Laws for the Irradiation Behavior of Graphite," Journal of Nuclear Materials 85, 86, 159-164 (1979).

137. R. Mattas, private communication.

138. R. Szilard, Theory and Analysis of Plates Classical and Numerical Methods, Prentice-Hall, New Jersey (1974).

139. S.P. Timoshenko and J.N. Goodier, Theory of Elasticity, McGraw-Hill, New York (1934).

140. T.H. Lin, Theory of Inelastic Structures, John Wiley and Sons, New York

141. B.B. Glasgow et al., "Helium Bubble Formation and Swelling in Materials," University of Wisconsin Report UWFDM-430 (August 1981).

142. E.R. Gilbert and J.F. Bates, "Dependence of Irradiation Creep on Temperature and Atom Displacements in 20% Cold Worked Type 316 Stainless Steel," Journal of Nuclear Materials 65, 204-209 (1977).

143. W.G. Wolfer and R.W. Conn, "New Analysis of first Wall Lifetime Considerations for Fusion Reactors," University of Wisconsin Report UWFDM-212 (1977).

144. A.Y. Lee, "Thermal and Hydraulic Analysis of a Cylindrical Blanket Module Design for a Tokamak Reactor," Westinghouse Report WFPS-TME-78-103 (1978).

145. A.M. Hassanein and G.L. Kulcinski, "A *THERMAL Code Description," University of Wisconsin Report UWFDM-461 (to be published).

146. R.R. Peterson et al., "TSTRESS - A Transient Stress Computer Code," University of Wisconsin Report UWFDM-382 (1980).

147. J.S. Karbowski et al., "Tokamak Blanket Design Study: FY 78 Summary Report," Oak Ridge National Laboratory Report ORNL/TM-6847 (1979).

148. ASME Boiler and Pressure Vessel Code, Code Case 1592, "Class 1 Components in Elevated Temperature Service," Section III, Division 1; Appendix T, "Rules for Strain, Deformation and Fatigue Limits at Elevated Temperatures" (1977).

149. D.V. Nelson, M.M. Abo-El-Ata, J.D. Stephen and R.G. Sim, "Development of Structural Design Criteria for Highly Irradiated Core Components," ASME paper 78-PVP-78 (1978).

150. B.F. Langer, "Design Aspects of Elevated Temperature Technology," Institution of Mechanical Engineers Conference on Creep and Fatigue in Elevated Temperature Applications, Philadelphia, PA (1973).

151. ASME Boiler nad Pressure Vessel Code, Section III, Subsection NA, Appendix G. "Protection Against Nonductile Failure" (1977).

152. ASME Boiler and Pressure Vessel Code, Section III, "Nuclear Power Plant Components, Division 1"; Subsection NA (General Requirements); Subsection NB (Class 1 Components) (1977).

153. D.R. Olander, Fundamental Aspects of Nuclear Reactor Fuel Elements, DOE Technical Information Center report TID-26711-P1 (1976).

154. "STARFIRE - A Commercial Tokamak Fusion Power Plant Study," Argonne Report ANL/FPP-80-1 (1980).

155. "US Contribution to the International Tokamak Reactor Phase-1 Workshop: Conceptual Design," USA INTOR/81-1 (1981).

156. The Ninth Symposium on the Engineering Problems of Fusion Research, Chicago (1981).

157. S.D. Harkness and B.A. Cramer, "A Review of Lifetime Analysis for Tokamaks," Journal of Nuclear Materials 85, 86, 135-145 (1979).

158. C.K. Youngdahl and D.L. Smith, "Stress and Lifetime Limitations of First Wall Structural Materials," Journal of Nuclear Materials, 85, 86, 153-157 (1979).

159. M. Abdou et al., "The Establishment of Alloy Development Goals Important to Commercialization of Tokamak-Based Fusion Reactors," Argonne report ANL/FPP TM-99, MDCE-1743 (1977).

160. R.W. Conn et al., "Preliminary Conceptual Design of a Tokamak Reactor," University of Wisconsin Report UWFDM-36 (1972).

161. B. Badger et al., "UWMAK-I, A Wisconsin Toroidal Fusion Reactor Design," University of Wisconsin UWFDM-68 (1973).

162. B.M. Ma, "Irradiation Swelling, Creep, Thermal Shock and Thermal Cycling Fatigue Analysis of Cylindrical Controlled Thermonuclear Reactor First Wall," Nuclear Engineering and Design 28, 1-30 (1974).

163. J.R. Standbridge et al., "Design of a Stainless Steel Blanket Cells for a Fusion Reactor," Culham Laboratory Report CLM-R127 (1974).

164. B. Badger et al., "UWMAK-II, A Conceptual D-T Fueled, Helium-Cooled, Tokamak Fusion Power Reactor Design," University of Wisconsin Report UWFDM-112 (1975).

165. B. Badger et al., "UWMAK-III, A Noncircular Tokamak Power Reactor Design," Electric Power Research Institute Report ER-368 EPRI (1976).

166. W.M. Stacey et al., "Tokamak Experimental Power Reactor Conceptual Design," Argonne Report ANL/CTR-76-3 (1976).

167. R.F. Borque, "First Wall Conceptual Designs Using Low Z Atomic Number Materials," Second Topical Meeting on the Technology of Controlled Nuclear Fusion

168. R.W. Conn, "Studies of the Technological Problems of Laser Driven Fusion Reactors," University of Wisconsin Report UWFDM-190 (1976).

169. R.W. Conn et al., "SOLASE - A Conceptual Laser Fusion Reactor Design," University of Wisconsin Report UWFDM-220 (1977).

170. F.W. Wiffen ed., Proceedings of the First Topical Meeting on Fusion Reactor Materials, Journal of Nuclear Materials 85, 86 (1979).

171. SMIRT V,Transactions of the Fifth International Conference on "Structural Mechanics in Reactor Technology:, Volume N: Thermal, Materials Engineering and Structural Mechanics Problems of Future Reactor Power Plants," Berlin, West Germany (1979).

172. J.R. Powell and M. Reich, "A Review of S-ructure [sic] Mechanics Aspects of Fusion Blankets," Nuclear Engineering and Design 58, 247-265 (1980).

173. E.P. Popov, Introduction to Mechanics of Solids, Prentice-Hall, New Jersey (1968).

174. K. Sadananda and P. Shahinian, "Critical Assessment of Creep Crack Growth Behavior and Theoretical Modelling," Metal Science (to be published).

175. K. Sadananda and P. Shahinian, "Review of Fracture Mechanics Approach to Creep Crack Growth in Structural Alloys," Engineering Fracture Mechanics (to be published).

176. "US Contribution to the International Tokamak Reactor Phase-I Workshop: Conceptual Design," Chapter 7, "First Wall and Limiter Systems," USA INTOR/81-1 (1981).

177. K. Plute, private communication.

178. G.L. Kulcinski, R.G. Brown, R.G. Lott, and P.A. Sanger, "Radiation Damage Limitations in the Design of the Wisconsin Tokamak Fusion Reactor," Nuclear Technology 22, 20-35 (1974).

179. R.W. Conn, "First Wall and Divertor Plate Material Selection in Fusion Reactors," University of Wisconsin Report UWFDM-237 (1978).

180. G.L. Kulcinski et al., "TASKA - A Fusion Engineering Facility for the 1990's," University of Wisconsin Report UWFDM-427 (1981).

181. R.W. Weeks, V.Z. Jankus and R.B Poeppel, "The Fuel Element Life Code, an Ultimate Application of Constitutive Equations to a High Technology Problem," Constitutive Equations in Plasticity, A.S. Argon, ed., MIT Press, Cambridge, MA, 549-569 (1975).

182. R.D. Watson, R.R. Peterson and W.G. Wolfer, "The Effect of Irradiation Creep, Swelling, Wall Erosion and Embrittlement on the Fatigue Life of a Tokamak First Wall," University of Wisconsin Report UWFDM-433 (August 1981).

183. R.D. Watson and W.G. Wolfer, "WISECRACK - A Fracture Mechanics Code for Lifetime Analysis of High Heat Flux Components in Fusion Reactors," University of Wisconsin Report UWFDM-440 (1981).

184. B. Mukherjee and D.J. Burns, "Growth of Part-Through Thickness Fatugue Cracks in Sheet Polymethylmethacrylate," Engineering Fracture Mechanics 4, 675-685 (1972).

185. G.G. Sih and R.J. Hartranft, "Growth Characteristics of Surface Flaws in Pressure Vessels," Third Conference on Structural Mechanics in Reactor Technology, SMIRT-III, London (1975).

186. A.F. Grandt, Jr. and G.M. Sinclair, "Stress Intensity Factors for Surface Cracks in Bending," ASTM STP 513, 37-58 (1972).

187. A. Nagai, M. Toyosada and T. Okamoto, "A Study on the Fatigue Crack Growth in 9% Ni Steel Plate," Engineering Fracture Mechanics 7, 481-490 (1975).

188. L.H. Burck, "Fatigue Growth of Surface Cracks in Bending," Engineering Fracture Mechanics 9, 389-395 (1977).

189. P.K. Nair, "Fatigue Crack Growth Model for Part-Through Flaws in Plates and Pipes," Journal of Engineering Materials and Technology 101, 53-58, 153 (1979).

190. D.L. Corn, "A Study of Cracking Techniques for Obtaining Partial Thickness Cracks of Pre-Selected Depths and Shapes," Engineering Fracture Mechanics 3, 45-52 (1971).

191. Masanori Kawahara and Masayoshi Kurihara, "Fatigue Crack Growth From a Surface Flaw," Fourth International Conference on Fracture, ICF4, Waterloo, Canada, 1361-1373 (1977).

192. W.S. Pierce and J.L. Shannon, Jr. "Surface-Crack Shape Change in Bending Fatigue Using an Inexpensive Resonant Fatiguing Apparatus," Journal of Testing and Evaluation 6(3), 183-188 (1978).

193. J.B. Chang, ed., "Part-Through Crack Fatigue Life Prediction," ASTM STP 687 (1977).

194. A.F. Grandt, "A Fracture Mechanics ANalysis of Surface Cracks in Bending," PhD Thesis, University of Illinois, Champaign-Urbana (1971).

195. A. Nagai, M. Toyosada, T. Okamoto, "Growth Rate of Surface Crack in a Plate Under Arbitrarily Combined Tension and Bending," Engineering Fracture Mechanics 7, 481-490 (1975).

196. J.N. Brooks, "Redeposition of the Sputtered Surface in Limiters," Ninth Symposium on the Engineering Problems of Fusion Research, Chicago (1981).

197. D.K. Sze, "Thermal, Mechanical and Neutronic Design Considerations for a Graphite Structure Li_2O Cooled Blanket," University of Wisconsin Report UWFDM-223 (1977).

198. D.L. Smith et al., "Fusion Reactor Blanket/Shield Design Study," Argonne National Laboratory Report ANL-FPP-79-1 (1979).

199. N.M. Ghoniem and R.W. Conn, "Assessment of Ferritic Steels for Steady-State Fusion Reactors," UCLA Report PGG-587 (1981).

200. G.G. Tratina and J.P.D. Wilkinson, "Structural Design Methods for Ceramics in Fusion Reactors," Fifth International Conference on Structural Mechanics in Reactor Technology, SMIRT-V, Volume N, Berlin, West Germany (1979).

201. K. Sadananda and P. Shaninian, "Crack Growth Under Creep and Fatigue Conditions," Proceedings of the AIME Symposium on Creep-Fatigue-Environment Interactions (September 1979).

202. C. Beevers, "Fatigue Crack Growth Characteristics at Low Stress Intensities of Metals and Alloys," Metal Science, 362-367 (August/September 1977).

203. A.P. Fraas, "Comparative Study of the More Promising Combinations of Blanket Materials, Power Conversion Systems, and Tritium Recovery and Containment Systems for Fusion Reactors," Oak Ridge National Lab report ORNL-TM-4999 (1975).

204. G.A. Carlson et al., "Tandom Mirror Reactor With Thermal Barriers," Lawrence Livermore Laboratory report UCRL-52836 (1979).

VITA

Robert D. Watson was born in Kansas City, Missouri on September 1, 1954. He attended the University of Illinois at Champaign-Urbana from 1972 to 1976 where he received a B.S. in Theoretical & Applied Mechanics with Highest Honors and a B.S. in General Engineering with High Honors. He was given the Fred B. Seely award for "Outstanding Senior in the Engineering Mechanics Department". In the summer of 1976 he worked for the Los Alamos National Laboratory. He then attended the University of Wisconsin-Madison from 1976 to 1981 where he received a M.S. in Nuclear Engineering in 1977 and a M.S. in Engineering Mechanics in 1979. In the summer of 1979 he worked for the McDonnell Douglas Astronautics Company. He is a member of the Phi Kappa Phi and Tau Beta Pi honor societies, as well as the Lambda Chi Alpha fraternity. He currently lives in Albuquerque, New Mexico where he is employed by the Sandia National Laboratory.